UNIVERSITY OF SOUTHAMPTON

Faculty of Engineering and Physical Sciences
School of Aerodynamic & Flight Mechanics

The application of optimal control techniques to the Shadowing approach for time averaged sensitivity analysis of chaotic systems

by

Rhys Edward Gilbert
MEng

A thesis for the degree of
Doctor of Philosophy

November 2023

University of Southampton

Abstract

Faculty of Engineering and Physical Sciences
School of Aerodynamic & Flight Mechanics

Doctor of Philosophy

The application of optimal control techniques to the Shadowing approach for time averaged sensitivity analysis of chaotic systems

by Rhys Edward Gilbert

Sensitivity analysis of non-linear systems is performed by finding solutions to the tangent/adjoint equations when the sensitivity of a function of interest is required with respect to single/multiple parameter(s). For chaotic systems, the simulation of the tangent/adjoint equations produces an unstable solution which leads to inaccurate sensitivities. There have been two main methods developed in the literature to overcome this limitation. The first are Shadowing methods, where their main feature is to find a tangent solution which remains bounded and shadows the original non-linear trajectory. This is achieved through modification of the initial condition to the tangent equation typically through a minimisation routine. These methods are typically computationally expensive whilst producing accurate sensitivity values. The second are the computationally cheap but potentially inaccurate numerical viscosity (NV) methods. NV methods stabilise the tangent/adjoint solution through incorporation of an additional control term into the tangent/adjoint equation that dissipates excess energy. Additional work is required when determining and tuning this additional control term, which leads to these methods being potentially inaccurate. The benefit of the NV method is that only one non-linear solution and one tangent/adjoint solution is required making them computationally cheap. There is, currently, a large gap in understanding of how these two methods relate and it is this question that this thesis attempts to answer. This thesis proposes a novel method to answer this question through introducing a generic control term into the tangent equation and finding its structure using optimal control techniques. This is referred to as Optimal Control Shadowing and abbreviated to OCS. The optimal control approach utilises a control term, similar to the control term in the NV methods, and finds its structure using a minimisation procedure, similar to the minimisation procedures used in the Shadowing approaches. Therefore, OCS can be seen as bridging the Shadowing and NV methods. Both tangent and adjoint forms of OCS have been developed for single and multiple parameters of interest, respectively. Computational methods are developed for solving the optimality equations in a matrix free sense which reduces the memory requirements of the

algorithms. The result of this is that these methods become more tractable to large systems. Development of time parallel algorithms and preconditioning methods enabled the solution to be distributed in a parallel manner enabling distribution across multiple compute nodes further increasing tractability to large systems.

One of the main findings of this thesis was that OCS finds a tangent solution very similar in structure to that of Multiple Shooting Shadowing (MSS), which is a leading Shadowing method. The NV methods investigated, on the other hand, did not produce any similarity with MSS suggesting the Shadowing direction was not found. Further, it was found that OCS predominantly targets the wavenumbers where production of tangent/adjoint energy dominated dissipation. This suggests that OCS applies control on the unstable sub-space and is minimal in the neutral and stable sub-space. The NV methods investigated here did not have this behaviour and were applying large amounts of control across all sub-spaces. The ramification of this is that for an NV method to be optimal, control should be applied mainly in the unstable sub-space. Further, the adjoint formulation applied significantly lower amounts of control than the tangent form. This was due to the terminal boundary condition being identical to that of MSS, and closer to the stabilised solution which required smaller amounts of control. The significance of this is that if an initial condition that is closer to the Shadowing direction for the tangent solution can be found than a smaller amount of control could be applied.

A second major finding was that the Shadowing solution was primarily composed of near neutral covariant Lyapunov vectors (CLVs), ones whose Lyapunov exponent was close to zero. This suggests that these near neutral CLVs play an important role in the sensitivity of the system. This thesis also found that the solution generated by OCS is also mainly composed of the near neutral CLVs. This implies, again, that OCS and MSS are finding similar solutions and behave in a comparable manner. NV, on the other hand, did not show as large dominance of the near neutral CLVs suggesting that these methods are applying control in a less than optimal manner and are not targeting the unstable sub-space as well as OCS. A further result discovered in this thesis was that the expected gain, the ratio of the output to input, of the tangent/adjoint solution is proportional to the inverse of the Lyapunov exponent. The significance of this is that CLV modes whose exponents are close to zero will dominate the solution and, as discovered previously, these relate to the near neutral CLVs. This suggests that selecting a control term in the NV method that has these features could produce a more accurate solution with minimal tuning.

Contents

List of Figures

List of Tables

Acknowledgements

First and foremost I would like to extend my deepest gratitude to my supervisor Dr. Davide Lasagna. Without his guidance, perseverance and trust in me this thesis would not have been possible, I am forever grateful. I have thoroughly enjoyed the various discussions we have had over the past few years. I would also like to extend my gratitude to everyone in the Department of Aeronautics & Astronautics for the various discussions we have had along the way. Specifically to Dr. Jack Tyler for the in depth discussions we have had on both of our work, you did it!, Thomas Burton, Gerardo Zampino, Teja Ala, for distracting me with various CFD related questions, Dr. Ben Hoddy, Edmar Silva and Yaseen Reza for all the various discussions we have had over the years, I have learned a lot. I'm sure I have missed a few, please forgive me.

I also wish to thank my family and friends for their continued support and motivation in these trying times. Thanks to my parents, Ruth and Jamie (in no particular order), for all the support they have given, making me take regular breaks and for all that they have done for me up until this point and, no doubt, will continue to provide in the future. My brother, Dan, his wife, Laura, for their continued support and my cheeky little nephew, Ben, for always bringing a smile to my face whenever we meet. To my grandparents, on both sides, I say for everything that you have done, thank you. Finally, my uncle, Kim, auntie, Lynda, and cousins, Samantha and Emma, for being a part of my life.

To my parents.
I hope I have made you proud.

Chapter 1

Introduction

Designing components is a very common activity in the engineering sector. Traditionally, the design has been undertaken by engineers by hand, but since the development of computers, designs have been largely automated. This automation typically involves the minimisation or maximisation of a certain function of interest relevant to the design, and to compute the function of interest generally involves the solution of some governing equations which are usually controlled by certain parameter(s). A common method in the automated design of components is the gradient descent method. This approach starts with a given parameter set, a solution of the governing equations, a computation of the gradient of the function of interest with respect to the parameter(s), and a step that updates the values of the parameter(s) by a certain amount based on the gradient value. This is repeated until a stopping criterion is reached. Locally optimal designs can be found as a result. These gradients of the function of interest are computed using the tangent (forward) or adjoint (backward) equations for a single parameter and multiple parameters, respectively. The tangent equation is found through linearisation of the non-linear governing equations and the adjoint is found using Lagrange multipliers, Ref. [68].

This thesis focuses on the aerospace sector and examples of the function of interest are the lift or drag produced by a body. Similarly, the parameter(s) could be the shape of the body or angle of attack of a wing. The governing equations in the aerospace sector are the Navier-Stokes equations which are typically very computationally expensive and time-consuming. The majority of the design process has been undertaken on the steady state Reynolds-Averaged Navier-Stokes (RANS) equations, Refs. [68, 105, 130]. Therefore, the reason why the methods of Ref. [68] have gained traction is that the solution of the steady state RANS is comparatively cheap and achievable. Consider, for example, a wing at a certain angle of attack for a given flow velocity. These design methods optimise the wing profile for this given flow regime. It is, therefore, unlikely that the wing, in flight, will be at this exact design point for the majority of its life. The

reason for this is that the wing will experience, for example, fouling or wind gusts. Therefore, the design will not be optimal for a large proportion of its working life and is the main limitation of these steady state methods.

With the current advancements and improvements of the computing sector access to high performance computing (HPC) is becoming more readily available. This results in a larger amount of computing power being available to the designer and, as such, problems that were not previously feasible are becoming more approachable. Direct Numerical Simulation (DNS) of the Navier-Stokes equations is currently reserved for academic test cases and is still unfeasible for real world geometries. The result of this is that URANS or Large Eddy Simulation of the Navier-Stokes equations becoming realisable. These methods are inherently transient and, therefore, time averaged sensitivity values should be computed.

The application of the approach taken in Ref. [68] for transient systems fails if that system is chaotic. This is a well known phenomenon as the tangent/adjoint space has an unstable sub-space, Ref. [72]. The result of this is that the solution generated from simulation of the tangent/adjoint equation is unstable and unbounded. Further, these solutions exhibit exponential growth of perturbations which has been referred to as the "butterfly effect", Ref. [125]. This exponential growth of the solution leads to the sensitivities calculated being unphysical and inaccurate. The Navier-Stokes equations are an example of a chaotic system and, therefore, a method to overcome this limitation is required.

To overcome this limitation, two main classes of time averaged sensitivity analysis have been developed in the literature. The first class comprises methods based on the Shadowing lemma, Refs. [84, 101]. This class of methods essentially find a perturbation to the original non-linear governing equations that remains close to, or shadows, the original solution trajectory. The first instance of this approach, Ref. [125], utilised the covariant Lyapunov vectors (CLVs), Refs. [6, 7, 50, 51, 72, 95, 112, 131] and Appendix A. The interpretation of the CLVs are that they describe long-term perturbations of a solution of the dynamical system. The CLVs/adjoint CLVs also form a basis of the tangent/adjoint space, respectively, and, along with the Lyapunov exponents (LEs), can determine their stable, neutral and unstable sub-spaces. Further, the same way that eigenvalues denote how much scaling is applied to an eigenvector under a linear transformation the LEs and CLVs are analogous for dynamical systems. CLVs have also been utilised in prediction of rare events, Refs. [4, 5, 26, 46, 47, 108, 123].

This initial approach, Ref. [125], has not seen significant traction as the computation of these CLVs and LEs is very memory intensive and computationally time-consuming. Therefore, alternative approaches have been derived in the literature. The first of these is the Least Squares Shadowing (LSS) approach, Refs. [16, 17, 18, 21, 35, 124,

128]. The LSS approach solves a minimisation problem where the L_2 norm of the tangent solution is minimised through the relaxation of the initial conditions on the tangent equation. The LSS formulation results in a large linear system being solved and can be computationally expensive. To reduce the size of the LSS system, the Multiple Shooting Shadowing (MSS) approach has been developed, Refs. [19, 110, 111], which minimises the tangent solutions at selected checkpoints. This formulation adds additional constraints on the solution, reducing the size of the linear system generated. There are two main limitations of the MSS method. Firstly, the linear system being solved is proportional to the dimension of the problem under investigation times by the number of time segments which results in the memory requirement of the method scaling linearly with the number of variables of the system. Secondly, the co-state equations are required which can be difficult to derive limiting the ease of utilising MSS.

A limitation of the LSS/MSS approaches is that additional equations are required to be implemented. Many of the existing scientific software may not be able to compute the Jacobian required by LSS/MSS, Ref. [92]. To overcome this limitation, the non-intrusive LSS (NILSS) method was developed, Refs. [14, 22, 65, 88, 91, 92, 93]. This class of methods computes one inhomogeneous linearised solution and M homogeneous linearised solutions where M is larger than the number of positive Lyapunov exponents of the system. The tangent solution is then formed from the inhomogeneous tangent solution and a linear combination of the homogeneous tangent solutions. A minimisation problem is formed that minimises the norm of the tangent solution by altering the linear combination of homogeneous tangent solutions. The current main limitation of NILSS is not the size of the problem being investigated but the number of positive Lyapunov exponents. The minimisation problem scales with the number of positive Lyapunov exponents. It is well known for spatially distributed systems, Figure 7 in Ref. [118], that as the domain size of a system is increased so too does the dimension of the system and, hence, the number of positive Lyapunov exponents. An alternative to LSS/MSS is Periodic Shadowing, Refs. [77, 78]. The Periodic Shadowing method, instead of solving the LSS/MSS linear system, finds a tangent solution which is periodic in time utilising appropriate numerical techniques.

The second class of methods for time averaged sensitivity analysis of chaotic systems is the numerical viscosity (NV) methods, Refs. [12, 23, 49, 120, 121]. These methods have been primarily developed on the adjoint equation. The additional control term is found by determining which terms in the adjoint equation contribute to dissipation of energy, Refs. [23, 120]. These terms are then scaled using a tuning parameter. The value of the tuning parameter selected impacts the accuracy of the method and can be thought of as impacting the amount of control applied. Too little control leads to an under-damped solution and inaccurate sensitivity values. Therefore, these methods

can produce inaccurate sensitivity values if tuned incorrectly. A large amount of work is required in determining the value of the tuning parameter. Typically, the value is selected such that the sensitivity produced is similar to that of the expected sensitivity, limiting their use in industrial applications. Further, no *a priori* recommendations or rules of thumb have been provided for the value of the tuning parameter. The reason for this is that the additional control term and tuning parameter are system dependent and links between systems have not been made. Finally, the vast majority of the method has been developed on the Navier-Stokes equations. NV methods have not been compared with Shadowing approach and their relationship to the CLVs has not been investigated.

1.1 Aims of this thesis

The main limitation of the Shadowing approaches is that they can be very computationally expensive. This is because either the CLV modes are required, an expensive minimisation problem is solved for LSS, MSS and NILSS, or a boundary value problem is solved for Periodic Shadowing. The benefit of these methods is that accurate sensitivities can be calculated for a range of different systems without any tuning and without *a priori* information of the expected sensitivity values.

The NV approaches, on the other hand, are computationally cheap, as only one non-linear solution and one linearised solution is required. The expected value of the sensitivity is required to be able to tune these methods correctly. Currently, there is no best practice in finding these values without *a priori* knowing the sensitivity. Further, additional work is required to find which terms should be added to the linearised equations and usually involves deriving which terms contribute to the dissipation of tangent/adjoint energy.

Several questions arise from analysing these various approaches. The first main question is how optimal are the current NV methods that have been proposed in the literature? This relates to the amount of control that is required to be applied to stabilise the tangent/adjoint solution. Also, is there an alternative approach that could apply less and still stabilise the solution? Further, are there specific structures or characteristics of control that could be utilised to provide a better, more selective NV term in stabilising the solution? The current NV literature select terms which dissipate energy. It is unclear if this is the best strategy or is, for example, targeting production of energy terms more effective? Another question that arises is how similar or dissimilar are the solutions generated by the Shadowing approach to NV? It is clear that the two methods can produce the same sensitivities but how do the solutions compare? It is currently unclear if there are certain features of Shadowing that can be utilised to generate a more optimal NV term. As all the current NV method are

reactive, *i.e.* the application of control is proportional to the linearised solution, is there an approach that is proactive, for example a NV term that can apply control based on the future dynamics of the non-linear solution?

This thesis aims to answer these questions through derivation of a method that bridges the gap between the Shadowing and NV methods. The key idea and novel contribution proposed is to introduce a generic control term to the tangent equation with no *a priori* limitations on its structure. Instead, optimal control techniques, Refs. [96, 103], will be leveraged to find its structure which minimises the norm of the tangent solution. Optimal control techniques are chosen as they provide the "best" control available in stabilising the tangent solution. This approach will be referred to as Optimal Control Shadowing (OCS). It can be seen that, through the addition of the control term, OCS is similar to NV methods and solving the optimal control minimisation problem is similar to the minimisation problem in the Shadowing methods. OCS can be thought of as a bridge between the Shadowing and NV methods. It is worth noting that the control found by OCS is the "best" solution that can be found using NV methods.

This thesis also makes use of covariant Lyapunov vectors (CLVs) as a tool to answer some of the open questions. It is well known that the CLVs span the tangent/adjoint space, Refs. [6, 7, 50, 51, 72, 95, 112, 131], and along with their Lyapunov exponents help determine the unstable, neutral and stable sub-spaces. Currently, NV methods are derived from terms which contribute to dissipation of tangent/adjoint energy. It is unclear which sub-spaces these control terms act. Further, it is unclear on which sub-space an optimal application of control would act on. Decomposing the solutions generated by MSS, OCS and NV onto these modes could show in more detail how these methods behave, what the structure of the solutions look like along with what are the dominant sub-spaces in the solutions. This information could then be utilised in the development of future NV methods that targets specific features or structures and apply control in a more optimal manner.

Chapters 3 through to 5 of this thesis have been accepted for publication in the SIADS journal in the paper, "On the application of optimal control techniques to the Shadowing approach for time averaged sensitivity analysis of chaotic systems" by R. E. Gilbert and D. Lasagna. Another paper is, at the time of writing, being drafted containing Chapters 7 and 8.

1.2 Thesis outline

To provide justification as to why the Shadowing and NV methods are required, mathematical details outlining the current steady state approach to sensitivity

analysis, and an explanation of why transient sensitivity analysis fails for chaotic systems is presented in chapter 2. Mathematical details of the Shadowing and NV methods are also provided in chapter 2, so that the reader can easily see the connection between OCS and the Shadowing and NV methods that OCS is proposed to bridge.

Mathematical derivation of Optimal Control Shadowing (OCS), the novel method developed here in linking the Shadowing and NV methods, is presented in chapter 3 initially for the tangent (single parameter) formulation. As multiple parameters are common in industry, two approaches for the adjoint formulation of OCS are also developed in chapter 3 where they are shown to be identical. Matrix-free methods to solve the optimality conditions are developed in this methodology chapter. This results in the OCS having a reduced computational memory over the alternative solution approaches, Ref. [98], which makes the method more tractable to industrially relevant systems. Finally, a method for decomposing the time domain into segments is developed along with various preconditioning methods. This has the benefit of conditioning the system, Ref. [52], leading to more favourable convergence rates. An added benefit is that these methods can make use of HPC architectures and be distributed across multiple compute nodes leading to investigations into more industrially relevant systems.

Initially, no knowledge of the computational behaviour of OCS is known. Generating an understanding of this behaviour is useful when applying OCS to larger systems that are computationally expensive. This leads to lower amounts of trial and error and saves compute resources and time. Computational aspects such as the impact the tuning parameter has on the accuracy of the method, the time horizon, preconditioning method, number of segments, the stopping criteria for the various linear solvers used in the matrix-free methods, and how these methods scale with domain size, are investigated in chapter 4. This is primarily undertaken on the Lorenz 1963 system, Ref. [80], while the investigation into scaling the domain is undertaken on the Kuramoto-Sivashinsky (KS) system, Refs. [73, 74, 113, 114].

Once an understanding of the computational behaviour of OCS is achieved, a comparison in solutions generated with MSS, OCS and NV can be undertaken. The tangent formulations of MSS, OCS and NV are investigated on the KS system in chapter 5. A large proportion of the development of NV methods are on the Navier-Stokes equations and, therefore, their development on the KS system is required. Two NV terms are developed for the KS system. The first is from terms which produce tangent energy and the second from terms which dissipate tangent energy. Comparison of the tangent solutions generated by MSS, OCS and NV is undertaken and conclusions about their behaviour is drawn. A similar comparison is conducted between the control terms in OCS and NV which provides recommendations as to the structure that NV terms should take. This chapter concludes with a spectral analysis investigation again providing features which the

NV methods should incorporate which could potentially lead to NV methods, through application of control in a more targeted manner, having increased accuracy.

Chapter 6 repeats the analysis undertaken in chapter 5 for the adjoint formulation of MSS, OCS and NV on the KS system. The rationale is to show that the behaviour of the method is common between formulations and that all analysis drawn is applicable to the adjoint formulation also. The adjoint solutions are compared between MSS, OCS and NV to provide deeper insight into the methods. In the adjoint MSS formulation, an equivalent control term in the adjoint equation is present which enables comparison with the control found by OCS and NV. The added benefit of this MSS control term is in providing additional insight into the method along with recommendations for features and structures that NV methods should target. Finally, spectral analysis is performed on the solutions producing similar features and structures to the tangent formulation.

The CLVs, which span the tangent/adjoint space, along with their Lyapunov exponents, help determine the unstable, neutral and stable sub-spaces, Refs. [6, 7, 50, 51, 72, 95, 112, 131]. To gain a deeper understanding of the MSS, OCS and NV methods the solutions generated for the KS system are decomposed onto the KS system CLVs in chapter 7. This is performed to gain deeper insight along with providing details as to what features and structures NV therms should include. The majority of this work is undertaken on the tangent formulation and only the differences between the adjoint and tangent formulations are presented. This involves decomposing the tangent and control solutions which provides additional insight in addition to that presented in chapters 5 and 6. Analysis is presented while varying the domain size to show that there are common features between domain sizes. Further analysis is provided through varying which parameter is investigated to show that the analysis already provided is general and not system or parameter specific. Finally, the adjoint solution decomposition analysis is undertaken to show that conclusions drawn are common between the formulations.

The systems investigated in chapters 4, 5, 6 and 7 are small systems. Industrially relevant systems are larger. Therefore, to show that the analysis that have been presented also translates to larger systems a comparison between OCS, MSS and NV is undertaken on the Kolmogorov system, Refs. [29, 81, 102], in chapter 8. This is mainly a repetition of results and findings showing the analysis is system agnostic and the key features and structures can be translated between systems without loss of generality.

Finally, chapter 9 provides a details summary of findings along with a critical analysis. Suggestions of further research that arises from this thesis is also provided in this chapter.

Chapter 2

Mathematical Preliminaries

This chapter provides mathematical details of the steady state sensitivity analysis that is currently used in industry, Ref. [68]. This is provided to give the reader an initial starting point for moving towards time averaged sensitivity analysis. Development of the time averaged sensitivities and an explanation as to why these methods fail for chaotic systems is then provided. This is undertaken to provide the rationale for development of the Shadowing and NV methods. An introduction to the Shadowing method is provided as the initial approach, Ref. [125], rely on the covariant Lyapunov vectors (CLVs) along with the Shadowing lemma, which is a foundation of these methods. Finally, details of NV method is provided for the purpose of context and highlights the difference in the approaches taken between NV and Shadowing methods in overcoming the limitation in time averaged sensitivity analysis. This chapter is an overview of the literature where no additional insight or development is produced, and is used to provide details and background.

In general, the computer simulations used as a basis in sensitivity analysis solve chaotic non-linear governing equations of the form

$$\frac{\mathrm{d}\mathbf{u}(t,p)}{\mathrm{d}t} = \mathbf{f}(\mathbf{u}(t,p),p), \tag{2.1}$$

where $\mathbf{u}(t,p) \in \mathbb{R}^{n_u}$ is the state vector, $p \in \mathbb{R}$ is a parameter, $t \in (t_s, t_f)$, t_s and t_f are the start and end times of the simulation, respectively, and $\mathbf{f}(\mathbf{u}(t,p),p) : \mathbb{R}^{n_u} \times \mathbb{R} \to \mathbb{R}^{n_u}$ are the governing equations. These functions of interest generally have the form

$$J\left(\mathbf{u}(t,p),p\right), \tag{2.2}$$

where $J\left(\mathbf{u}(t,p),p\right) : \mathbb{R}^{n_u} \times \mathbb{R} \to \mathbb{R}$.

2.1 Current approaches to sensitivity analysis

In the aerospace sector, it is common to perform sensitivity analysis on steady state solutions, *i.e.* finding a solution $\mathbf{u}(p)$ that satisfies $\mathbf{f}(\mathbf{u}(p), p) = \mathbf{0}$, of Equation (2.1), Refs. [68, 105, 130]. Therefore, the function of interest becomes $J(\mathbf{u}(p), p)$. There is high demand for the derivative of the function of interest with respect to parameter(s), which is denoted $\frac{\mathrm{d}J(\mathbf{u}(p),p)}{\mathrm{d}p}$, commonly known as sensitivity analysis. There are two main uses of sensitivity analysis in the engineering sector. The first use is the generation of designs that are robust to perturbations in certain parameter(s). Take, for example, an airfoil that produces a certain amount of lift for a given flow regime. Designers require that this lift remains relatively constant for a perturbation in either shape, due to fouling, or flow conditions, due to gusts. Therefore, $\frac{\mathrm{d}J(\mathbf{u}(p),p)}{\mathrm{d}p}$ must be relatively constant over a large range of p such that perturbations do not significantly impact $J(\mathbf{u}(p), p)$. The second use is to utilise $\frac{\mathrm{d}J(\mathbf{u}(p),p)}{\mathrm{d}p}$ in some optimisation routine, where the derivatives are used to alter the parameters to minimise or maximise the function of interest, typically utilising a gradient descent algorithm.

A common approach to sensitivity analysis is to find the finite difference between the function of interest with two solutions each with slightly perturbed parameters

$$\begin{aligned}\frac{\mathrm{d}J(\mathbf{u}(p), p)}{\mathrm{d}p} &= \lim_{\Delta p \to 0} \frac{J(\mathbf{u}'(p+\Delta p), p+\Delta p) - J(\mathbf{u}(p), p)}{\Delta p} \\ &= \left\langle \frac{\partial J(\mathbf{u}(p), p)}{\partial \mathbf{u}(p)}, \frac{\partial \mathbf{u}(p)}{\partial p} \right\rangle + \frac{\partial J(\mathbf{u}(p), p)}{\partial p},\end{aligned} \tag{2.3}$$

where Δp is a perturbation in the parameter and is typically small, $\mathbf{u}'(p + \Delta p)$ is the solution of $\mathbf{f}(\mathbf{u}'(p + \Delta p), p + \Delta p) = \mathbf{0}$, and $\langle \cdot, \cdot \rangle$ is an appropriately defined inner product with $\| \cdot \| = \sqrt{\langle \cdot, \cdot \rangle}$ as the norm. It is common that the term $\frac{\partial \mathbf{u}(p)}{\partial p}$ is referred to as the tangent solution or variable, Ref. [125], and is often denoted $\mathbf{v} \in \mathbb{R}^{n_v}$. The terms $\frac{\partial J(\mathbf{u}(p),p)}{\partial \mathbf{u}(p)}$ and $\frac{\partial J(\mathbf{u}(p),p)}{\partial p}$ are usually known whereas the tangent solution is unknown. Therefore, an equation is required to compute its value. This is achieved through linearisation of Equation (2.1) which results in

$$\frac{\partial \mathbf{f}(\mathbf{u}(p), p)}{\partial \mathbf{u}(p)} \frac{\partial \mathbf{u}(p)}{\partial p} + \frac{\partial \mathbf{f}(\mathbf{u}(p), p)}{\partial p} = \mathbf{0}, \tag{2.4}$$

where $\frac{\partial \mathbf{f}(\mathbf{u}(p),p)}{\partial \mathbf{u}(p)}$ is the Jacobian, $\frac{\partial \mathbf{u}(p)}{\partial p}$ is the tangent solution and $\frac{\partial \mathbf{f}(\mathbf{u}(p),p)}{\partial p}$ is a forcing term. Equation (2.4) is also known as the tangent equation and forms a linear system that is solved for the tangent variable. Once the tangent solution has been found the sensitivity is calculated with Equation (2.3). This approach is known as the tangent or forwards method.

The tangent method outlined above is valid for a single parameter. It is common in industry, however, that there are multiple parameters. Therefore, the adjoint, Refs. [68,

105, 130], method is utilised. Firstly, let $\hat{\boldsymbol{\lambda}} \in \mathbb{R}^{n_{\hat{\lambda}}}$ be a Lagrange multiplier which is known as the adjoint solution. Equation (2.4) can be incorporated into Equation (2.3) as follows

$$\begin{aligned}\frac{\mathrm{d}J(\mathbf{u}(p),p)}{\mathrm{d}p} = \left\langle \frac{\partial J(\mathbf{u}(p),p)}{\partial \mathbf{u}(p)}, \frac{\partial \mathbf{u}(p)}{\partial p} \right\rangle + \frac{\partial J(\mathbf{u}(p),p)}{\partial p} + \\ \left\langle \hat{\boldsymbol{\lambda}}, \frac{\partial \mathbf{f}(\mathbf{u}(p),p)}{\partial \mathbf{u}(p)} \frac{\partial \mathbf{u}(p)}{\partial p} + \frac{\partial \mathbf{f}(\mathbf{u}(p),p)}{\partial p} \right\rangle.\end{aligned} \tag{2.5}$$

This is possible because the second inner product adds zero to Equation (2.3) which does not impact the value of the sensitivity generated. After integration by parts Equation (2.5) becomes

$$\begin{aligned}\frac{\mathrm{d}J(\mathbf{u}(p),p)}{\mathrm{d}p} = \left\langle \hat{\boldsymbol{\lambda}}, \frac{\partial \mathbf{f}(\mathbf{u}(p),p)}{\partial p} \right\rangle + \frac{\partial J(\mathbf{u}(p),p)}{\partial p} + \\ \left\langle \frac{\partial J(\mathbf{u}(p),p)}{\partial \mathbf{u}(p)} + \frac{\partial \mathbf{f}(\mathbf{u}(p),p)}{\partial \mathbf{u}(p)}^{\dagger} \hat{\boldsymbol{\lambda}}, \frac{\partial \mathbf{u}(p)}{\partial p} \right\rangle,\end{aligned} \tag{2.6}$$

where $\frac{\partial \mathbf{f}(\mathbf{u}(p),p)}{\partial \mathbf{u}(p)}^{\dagger}$ is the adjoint of the Jacobian. The value of $\hat{\boldsymbol{\lambda}}$ can be selected arbitrarily and, therefore, it is chosen such that

$$\frac{\partial J(\mathbf{u}(p),p)}{\partial \mathbf{u}(p)} + \frac{\partial \mathbf{f}(\mathbf{u}(p),p)}{\partial \mathbf{u}(p)}^{\dagger} \hat{\boldsymbol{\lambda}} = \mathbf{0}, \tag{2.7}$$

which results in $\frac{\partial \mathbf{u}(p)}{\partial p}$ never being computed. Equation (2.7) is referred to as the adjoint equation. The sensitivity equation then becomes

$$\frac{\mathrm{d}J(\mathbf{u}(p),p)}{\mathrm{d}p} = \left\langle \hat{\boldsymbol{\lambda}}, \frac{\partial \mathbf{f}(\mathbf{u}(p),p)}{\partial p} \right\rangle + \frac{\partial J(\mathbf{u}(p),p)}{\partial p}. \tag{2.8}$$

The adjoint solution, $\hat{\boldsymbol{\lambda}}$, is independent of the parameter under investigation and only $\frac{\partial \mathbf{f}(\mathbf{u}(p),p)}{\partial p}$ and $\frac{\partial J(\mathbf{u}(p),p)}{\partial p}$ depend on the parameter of interest. Therefore, to compute the sensitivity with respect to different parameters only $\frac{\partial \mathbf{f}(\mathbf{u}(p),p)}{\partial p}$ and $\frac{\partial J(\mathbf{u}(p),p)}{\partial p}$ need to be re-computed, which is computationally cheap and is the main benefit of this formulation. This approach to sensitivity analysis is known as the adjoint or backward approach.

2.2 Towards time averaged sensitivity analysis methods

Recent improvements and advancements in the computing sector means that high performance computing (HPC) is becoming more powerful. This leads to methods that have been previously reserved for academic test cases are increasingly becoming utilised in industry. Examples of these methods include URANS and LES which are inherently transient. The result of this is that time average sensitivity values should be

used. This section follows a similar form to section 2.1 except with the restriction of a steady state solution removed. Also presented in this section is the reason time averaged sensitivity fails for chaotic systems and is the rationale for the development of Shadowing and NV methods.

Firstly, let the time average of the function of interest be

$$\bar{J} = \frac{1}{T}\int_{t_s}^{t_f} J\left(\mathbf{u}(t,p),p\right)\mathrm{d}t, \tag{2.9}$$

where $T = t_f - t_s$ is the time horizon. The infinite time averaged sensitivity is found again by computing the finite difference between time averaged functions of interest

$$\begin{aligned}\frac{\mathrm{d}\bar{J}}{\mathrm{d}p} = \lim_{\Delta p\to 0}\frac{1}{\Delta p}\left(\lim_{T\to\infty}\frac{1}{T}\int_{t_s}^{t_f} J(\mathbf{u}'(t,p+\Delta p),p+\Delta p)\mathrm{d}t - \right.\\ \left.\lim_{T\to\infty}\frac{1}{T}\int_{t_s}^{t_f} J(\mathbf{u}(t,p),p)\mathrm{d}t\right).\end{aligned} \tag{2.10}$$

For the limits in Equation 2.10 to commute $\mathbf{u}(t,p)$ and $\mathbf{u}'(t,p+\Delta p)$ must remain uniformly close to each other forever. If this is the case then

$$\begin{aligned}\frac{\mathrm{d}\bar{J}}{\mathrm{d}p} &= \lim_{T\to\infty}\frac{1}{T}\int_{t_s}^{t_f}\lim_{\Delta p\to 0}\frac{J(\mathbf{u}'(t,p+\Delta p),p+\Delta p)-J(\mathbf{u}(t,p),p)}{\Delta p}\mathrm{d}t\\ &= \lim_{T\to\infty}\frac{1}{T}\int_{t_s}^{t_f}\left\langle\frac{\partial J(\mathbf{u}(t,p),p)}{\partial\mathbf{u}(t,p)},\frac{\partial\mathbf{u}(t,p)}{\partial p}\right\rangle+\frac{\partial J(\mathbf{u}(t,p),p)}{\partial p}\mathrm{d}t.\end{aligned} \tag{2.11}$$

It is worth reiterating this point in that the solutions must remain uniformly close to each other for the limits to commute. If this is not the case then the sensitivity analysis generated using Equation (2.11) is inaccurate. It is worth noting that for URANS these two solutions do remain close to each other as the URANS solution averages out the impact of small scales and is not chaotic. For LES, which contains the small scales and is, therefore, chaotic, these solutions do not remain close to each other and the limits do not commute.

Similar to the steady state case, section 2.1, the terms $\frac{\partial J(\mathbf{u}(t,p),p)}{\partial\mathbf{u}(t,p)}$ and $\frac{\partial J(\mathbf{u}(t,p),p)}{\partial p}$ are known whereas the tangent solution $\mathbf{v}(t)\equiv\frac{\partial\mathbf{u}(t,p)}{\partial p}$ is unknown. The tangent equation is found through linearisation of Equation (2.1) which results in

$$\frac{\mathrm{d}\mathbf{v}(t)}{\mathrm{d}t} = \frac{\partial\mathbf{f}(\mathbf{u}(t,p),p)}{\partial\mathbf{u}(t,p)}\mathbf{v}(t)+\frac{\partial\mathbf{f}(\mathbf{u}(t,p),p)}{\partial p}. \tag{2.12}$$

Equation (2.12) is simulated to give the tangent solution which can then be substituted into Equation (2.11) to compute the sensitivity. It is common to solve the two trajectories $\mathbf{u}'(t,p+\Delta p)$ and $\mathbf{u}(t,p)$ from the same initial condition, Ref. [92]. This leads to $\frac{\partial\mathbf{u}(t_s,p)}{\partial p}\equiv\mathbf{v}(t_s)=\mathbf{0}$.

It is well known that when the system is chaotic, such as turbulent flows, the tangent space has an unstable sub-space, Ref. [72]. The tangent solutions generated by Equation (2.12) become unstable and unbounded. This means that $\mathbf{u}'(t, p+\Delta p) - \mathbf{u}(t,p) \sim e^{\Lambda_{MAX} t}$, Ref. [19], where Λ_{MAX} is the largest Lyapunov exponent. For chaotic systems it is well known that $\Lambda_{MAX} > 0$, Ref. [72]. This results in $\mathbf{u}'(t, p+\Delta p)$ and $\mathbf{u}(t,p)$ no longer remaining uniformly close forever. Since this was required for the limits to commute (Equation (2.10) to (2.11)), for chaotic systems the sensitivity generated by Equation (2.11), therefore, becomes inaccurate and unphysical. The implication of this is that without any modification this approach will not produce accurate sensitivity. This is the justification as to why Shadowing and NV methods have been developed. Shadowing and NV methods have been developed to find solutions to Equation (2.12) that remain bounded. This then means the limits do commute and Equation (2.11) produces accurate sensitivity values.

The adjoint formulation follows in a similar manner to that presented in section 2.1 where $\hat{\boldsymbol{\lambda}}(t) \in \mathbb{R}^{n_\lambda}$ is a Lagrange multiplier, also known as the adjoint solution, which can be used to incorporate Equation (2.12) through the addition of zero into Equation (2.11), which results in

$$\begin{aligned} \frac{\mathrm{d}\bar{J}}{\mathrm{d}p} = \frac{1}{T}\int_{t_s}^{t_f} \left\langle \frac{\partial J(\mathbf{u}(t,p),p)}{\partial \mathbf{u}(t,p)}, \mathbf{v}(t) \right\rangle + \frac{\partial J(\mathbf{u}(t,p),p)}{\partial p} + \\ \left\langle \hat{\boldsymbol{\lambda}}(t), \frac{\mathrm{d}\mathbf{v}(t)}{\mathrm{d}t} - \frac{\partial \mathbf{f}(\mathbf{u}(t,p),p)}{\partial \mathbf{u}(t,p)}\mathbf{v}(t) - \frac{\partial \mathbf{f}(\mathbf{u}(t,p),p)}{\partial p} \right\rangle \mathrm{d}t. \end{aligned} \tag{2.13}$$

Integration by parts in time of Equation (2.13) results in

$$\begin{aligned} \frac{\mathrm{d}\bar{J}}{\mathrm{d}p} = \int_{t_s}^{t_f} \frac{1}{T}\frac{\partial J(\mathbf{u}(t,p),p)}{\partial p} - \left\langle \frac{\partial \mathbf{f}(\mathbf{u}(t,p),p)}{\partial p}, \hat{\boldsymbol{\lambda}}(t) \right\rangle + \\ \left\langle \mathbf{v}(t), -\frac{\mathrm{d}\hat{\boldsymbol{\lambda}}(t)}{\mathrm{d}t} - \frac{\partial \mathbf{f}(\mathbf{u}(t,p),p)}{\partial \mathbf{u}(t,p)}^{\dagger} \hat{\boldsymbol{\lambda}}(t) + \frac{1}{T}\frac{\partial J(\mathbf{u}(t,p),p)}{\partial \mathbf{u}(t,p)} \right\rangle \mathrm{d}t + \left\langle \mathbf{v}(t), \hat{\boldsymbol{\lambda}}(t) \right\rangle \Big|_{t_s}^{t_f}, \end{aligned} \tag{2.14}$$

where $\frac{\partial \mathbf{f}(\mathbf{u}(t,p),p)}{\partial \mathbf{u}(t,p)}^{\dagger}$ is defined as before. The value of $\hat{\boldsymbol{\lambda}}(t)$ is free to be selected and is chosen in such a way that the explicit computation of $\mathbf{v}(t)$ is removed. This is achieved through selecting

$$\mathbf{0} = -\frac{\mathrm{d}\hat{\boldsymbol{\lambda}}(t)}{\mathrm{d}t} - \frac{\partial \mathbf{f}(\mathbf{u}(t,p),p)}{\partial \mathbf{u}(t,p)}^{\dagger} \hat{\boldsymbol{\lambda}}(t) + \frac{1}{T}\frac{\partial J(\mathbf{u}(t,p),p)}{\partial \mathbf{u}(t,p)}, \tag{2.15}$$

which is referred to as the adjoint equation, see Refs. [119, 126] for details. There still is a reliance on $\mathbf{v}(t)$ in $\left\langle \mathbf{v}(t), \hat{\boldsymbol{\lambda}}(t) \right\rangle \Big|_{t_s}^{t_f}$. Since the adjoint solution is free to be selected $\left\langle \mathbf{v}(t), \hat{\boldsymbol{\lambda}}(t) \right\rangle \Big|_{t_s}^{t_f} = 0$ is used which , in combination with $\mathbf{v}(t_s) = \mathbf{0}$, leads to $\hat{\boldsymbol{\lambda}}(t_f) = \mathbf{0}$. This terminal condition on the adjoint equation means that Equation (2.15) is solved backwards in time from t_f to t_s with $\hat{\boldsymbol{\lambda}}(t_f) = \mathbf{0}$ as the terminal condition. Finally, the

adjoint sensitivity equation becomes

$$\frac{\mathrm{d}\bar{J}}{\mathrm{d}p} = \int_{t_s}^{t_f} \frac{1}{T} \frac{\partial J(\mathbf{u}(t,p),p)}{\partial p} - \left\langle \frac{\partial \mathbf{f}(\mathbf{u}(t,p),p)}{\partial p}, \hat{\boldsymbol{\lambda}}(t) \right\rangle \mathrm{d}t. \tag{2.16}$$

2.3 The Shadowing approach to time averaged sensitivity analysis

The failure of the method presented in section 2.2 can be caused by the trajectories $\mathbf{u}'(t, p+\Delta p)$ and $\mathbf{u}(t,p)$ not remaining uniformly close forever. It was presented that the difference between these two solutions is proportional to $e^{\Lambda_{MAX} t}$. The Shadowing lemma, where details are provided in section 2.3.1, describes a pseudo-orbit that remains uniformly near a true orbit, Refs. [84, 101]. This suggests that the pseudo-orbit can be utilised as $\mathbf{u}'(t, p+\Delta p)$ and the true orbit as $\mathbf{u}(t,p)$ resulting in Equation (2.11) producing accurate sensitivity values. The downside of this Shadowing lemma is that no indication as to how to find this pseudo-orbit is given. One such approach, Ref. [125], to find the Shadowing direction, or pseudo-orbit, is to use the covariant Lyapunov vectors (CLVs), Refs. [6, 7, 50, 51, 72, 95, 112, 131], and is referred to as Shadowing. Details and algorithms in the computation of CLVs are provided in Appendix A. Details, recapped from the literature, of this Shadowing approach, Ref. [125], are provided in section 2.3.2 for the tangent formulation. The limitations of these Shadowing methods involve the computation of the CLVs which is computationally expensive. Therefore, alternative reformulations of the Shadowing approach are outlined from literature in sections 2.3.3, 2.3.4 and 2.3.5.

2.3.1 The Shadowing lemma

In this section the details of the Shadowing lemma, which is used in time averaged sensitivity of chaotic systems, is outlined. Further, details are given in Refs. [84, 101]. This section is a overview of the literature where no new insight is provided and is provided purely for context. The Shadowing lemma exists for both discrete and continuous dynamical systems, but is provided here for a discrete system of the form

$$x_i = \Phi(x_{i-1}),$$

where $\Phi : \mathbb{R} \to \mathbb{R}$ and $x_i \in \mathbb{R}$. A β-pseudo-orbit for Φ is a sequence of points $\{x_i\}$ where this sequence obeys the following inequality

$$\|x_{i+1} - \Phi(x_i)\| < \beta,$$

shown in Figure 2.1. Typically, this β-pseudo-orbit is the result of using a numerical

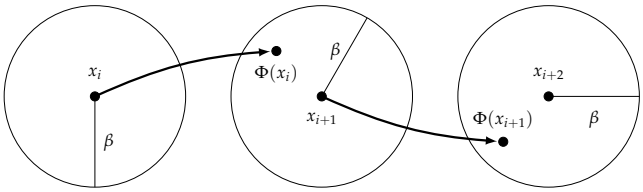

FIGURE 2.1: A β-pseudo-orbit.

method to solve the dynamical system Φ and the error is due to round off error. An orbit $\{y_i\}$, where $y_i = \Phi^i(y_0)$, is said to α-shadow a β-pseudo-orbit, $\{x_i\}$, if

$$\|y_i - x_i\| < \alpha,$$

shown in Figure 2.2. The Shadowing lemma is

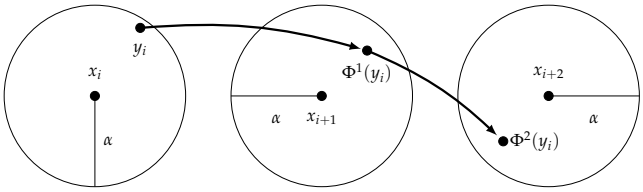

FIGURE 2.2: An α-shadow.

Lemma 2.1. *If Γ is a compact, hyperbolic attractor for Φ, then, for all $\alpha > 0$, there exists a $\beta > 0$ such that every β-pseudo-orbit in Γ is α-shadowed by the actual orbit of some point $z \in \Gamma$.*

The implication of this is the pseudo-orbit remains uniformly close to the true orbit. This then means that these two orbits, the true and pseudo-orbits, can be utilised in the derivation for time-averaged sensitivity values (section 2.2), resulting in the sensitivity produced by Equation (2.11) being accurate. The limitation of the Shadowing lemma is that no details are provided as to the method to find the pseudo-orbit.

2.3.2 A tangent formulation for sensitivity analysis

The Shadowing lemma states that there is, for a given initial condition, a solution that α-shadows a β-pseudo-orbit. Rather than starting from $\mathbf{v}(t_s) = \mathbf{0}$ as in the traditional approach, a method that has been introduced finds an initial condition to the tangent equation that results in an α-shadow, Ref. [125]. This method relies on the Shadowing lemma which is shown in section 2.3.1, and further details are provided in Ref. [125].

Linearisation of Equation (2.1) leads to the following tangent equation

$$\frac{\mathrm{d}\mathbf{v}(t)}{\mathrm{d}t} = \frac{\partial \mathbf{f}(\mathbf{u}(t,p),p)}{\partial \mathbf{u}(t,p)}\mathbf{v}(t) + \frac{\partial \mathbf{f}(\mathbf{u}(t,p),p)}{\partial p}. \tag{2.17}$$

By defining the Shadowing operator as $S_f(t) = \frac{\mathrm{d}}{\mathrm{d}t} - \frac{\partial \mathbf{f}(\mathbf{u}(t,p),p)}{\partial \mathbf{u}(t,p)}$, Equation (2.17) can be re-written resulting in

$$S_f(t)\mathbf{v}(t) = \frac{\partial \mathbf{f}(\mathbf{u}(t,p),p)}{\partial p}.$$

There is a need to invert this shadow operator because in general $\frac{\partial \mathbf{f}(\mathbf{u}(t,p),p)}{\partial p}$ is known but $\mathbf{v}(t)$ is unknown. It is well known that the CLVs span the tangent space, Ref. [72]. An introduction to covariant Lyapunov vectors (CLVs) and Lyapunov exponents (LEs) is given in Ref. [131] and the reader is referred to Appendix A for details. One interpretation of the CLVs and LEs is that LEs denote the growth/decay rate and the CLVs the directions along which perturbations grow/decay for a dynamical system. This is analogous to eigenvector-eigenvalue pairs for linear operators. A positive Lyapunov exponent implies that perturbations grow along its corresponding CLV denoting an unstable direction. Similarly, a negative exponent implies perturbations decay along the CLV and is a stable direction. A netural direction is one in which the exponent is zero. Typical examples of a neutral mode is a shift in time, or space. Systems can have multiple neutral modes corresponding to a shift in time and space. Therefore, the tangent solution, $\mathbf{v}(t)$, can be constructed from a linear combination of CLVs, $\gamma_k(t)$, resulting in

$$\mathbf{v}(t) = \sum_{k=0}^{n_v-1} a_k(t)\gamma_k(t), \tag{2.18}$$

where $a_k(t) \in \mathbb{R}$ is a weighting factor. The same decomposition is undertaken for the forcing term, resulting in

$$\frac{\partial \mathbf{f}(\mathbf{u}(t,p),p)}{\partial p} = \sum_{k=0}^{n_v-1} a_k^f(t)\gamma_k(t), \tag{2.19}$$

where $a_k^f(t) \in \mathbb{R}$. Substitution of these into Equation (2.17) leads to

$$\sum_{k=0}^{n_v-1} \frac{\mathrm{d}a_k(t)\gamma_k(t)}{\mathrm{d}t} = \frac{\partial \mathbf{f}(\mathbf{u}(t,p),p)}{\partial \mathbf{u}(t,p)} \sum_{k=0}^{n_v-1} a_k(t)\gamma_k(t) + \sum_{k=0}^{n_v-1} a_k^f(t)\gamma_k(t). \tag{2.20}$$

After the application of the chain rule on the left hand side, Equation (2.20) results in

$$\sum_{k=0}^{n_v-1} \frac{\mathrm{d}a_k(t)}{\mathrm{d}t}\boldsymbol{\gamma}_k(t) = -\sum_{k=0}^{n_v-1}\left[a_k(t)\left(\underbrace{\frac{\mathrm{d}\boldsymbol{\gamma}_k(t)}{\mathrm{d}t} - \frac{\partial \mathbf{f}(\mathbf{u}(t,p),p)}{\partial \mathbf{u}(t,p)}\boldsymbol{\gamma}_k(t)}_{A}\right)\right] + \sum_{k=0}^{n_v-1} a_k^f(t)\boldsymbol{\gamma}_k(t). \tag{2.21}$$

The equation for the CLVs, Ref.[50], is

$$\frac{\mathrm{d}\boldsymbol{\gamma}_k(t)}{\mathrm{d}t} = \frac{\partial \mathbf{f}(\mathbf{u}(t,p),p)}{\partial \mathbf{u}(t,p)}\boldsymbol{\gamma}_k(t) - \Lambda_k\boldsymbol{\gamma}_k(t) \quad k = 0,1,\ldots,n_v-1, \tag{2.22}$$

where Λ_k is the Lyapunov exponent. Using Equation (2.22), it can be seen that the term labelled A in Equation (2.21) is the Lyapunov exponent term, $-\Lambda_k\boldsymbol{\gamma}_k$, and using this substitution results in

$$\sum_{k=0}^{n_v-1}\left[\left(\underbrace{\frac{\mathrm{d}a_k(t)}{\mathrm{d}t} - \Lambda_k a_k(t) - a_k^f(t)}_{B}\right)\boldsymbol{\gamma}_k(t)\right] = \mathbf{0}. \tag{2.23}$$

The method for finding the tangent solution begins with computing the CLVs and Lyapunov exponents. Next, the forcing term is then decomposed onto each CLV mode, Equation (2.19). Once these have been computed the terms $a_k(t)$ for $k = 0,1,\ldots,n_v-1$ are found by solving the scalar ODE using the term labelled B in Equation (2.23). Finally, the tangent solution is found using Equation (2.18). This tangent solution can then be used in Equation (2.11) to compute the sensitivity of the system

Special considerations are required when $\Lambda_k = 0$ as this results in the corresponding

$$\mathbf{v}(t) = S_f(t)^{-1}\frac{\partial \mathbf{f}(\mathbf{u}(t,p),p)}{\partial p}$$

not existing, Ref. [125]. This results in the scalar ODE for this mode becoming

$$\frac{\mathrm{d}a_k(t)}{\mathrm{d}t} = a_k^f(t)$$

and the corresponding covariant Lyapunov vector is $\boldsymbol{\gamma}_k(t) = \mathbf{f}(\mathbf{u}(t,p),p)$, Ref. [125]. Taking the infinite time average of this leads to

$$\lim_{T\to\infty}\frac{a_k(T)-a_k(0)}{T} = \overline{a_k^f(t)} = 0.$$

This is not always guaranteed to be true and one example that contradicts this is when

$\frac{\partial \mathbf{f}(\mathbf{u}(t,p),p)}{\partial p} \equiv \mathbf{f}(\mathbf{u}(t,p),p)$ leads to $\overline{a_k^f(t)} \neq 0$. To overcome this limitation, a time dilation variable, $\eta \in \mathbb{R}$, is added to handle this case. The value of

$$\eta + \overline{a_k^f(t)} = 0$$

is selected which leads to the ODE becoming

$$\frac{\mathrm{d}a_k(t)}{\mathrm{d}t} = a_k^f(t) + \eta, \tag{2.24}$$

when $\Lambda_k = 0$.

This approach to time averaged sensitivity analysis has been shown on the Lorenz 1963 system, Ref. [125], where there are three CLVs. For larger spatially distributed systems, such as turbulent flow, computation of the CLVs may be infeasible due to the limitation in current computational resources. This limitation reduces the tractability and adoption of the method into an industrial setting. There has been work undertaken in the literature to overcome this limitation and these are recapped in sections 2.3.3, 2.3.4 and 2.3.5.

The adjoint formulation of this method follows a very similar form to that shown here, Ref. [125]. Adjoint forms of the tangent variables are denoted with $\hat{\square}$. For clarity, the adjoint scalar ODE is found by satisfying

$$\sum_{k=0}^{n_v-1} \left[\left(\frac{\mathrm{d}\hat{a}_k(t)}{\mathrm{d}t} + \hat{a}_k(t)\Lambda_k - \hat{a}_k^f(t) \right) \hat{\boldsymbol{\gamma}}_k(t) \right] = \mathbf{0}, \tag{2.25}$$

in a similar manner to the tangent form. The scalar $\hat{a}_k^f(t) \in \mathbb{R}$ is found using

$$\frac{1}{T} \frac{\partial J(\mathbf{u}(t,p),p)}{\partial \mathbf{u}(t,p)} = \sum_{k=0}^{n_v-1} \hat{a}_k^f(t) \hat{\boldsymbol{\gamma}}_k(t). \tag{2.26}$$

The scalar $\hat{a}_k(t) \in \mathbb{R}$ for each mode is found using the adjoint scalar ODE. Following this, its value is used in

$$\hat{\boldsymbol{\lambda}}(t) = \sum_{k=0}^{n_v-1} \hat{a}_k(t) \hat{\boldsymbol{\gamma}}_k(t), \tag{2.27}$$

to compute the adjoint solution which is then used in Equation 2.16 to compute the sensitivity.

2.3.3 A least squares method to the Shadowing approach for sensitivity analysis

One of the first approaches to remove the computation of the CLVs in the method derived in section 2.3.2 was Least Squares Shadowing (LSS), Refs. [16, 17, 18, 21, 35,

124, 128]. The Shadowing approach is reformulated, Ref. [128], to a minimisation problem resulting in

$$\min_{\tau(t),\mathbf{u}(\tau(t),p+\Delta p)} \frac{1}{T}\int_{t_s}^{t_f} \|\mathbf{u}(\tau(t),p+\Delta p)-\mathbf{u}_r(t,p)\|^2+\beta^2\left(\frac{\mathrm{d}\tau(t)}{\mathrm{d}t}-1\right)^2\mathrm{d}t, \tag{2.28a}$$

$$s.t. \quad \frac{\mathrm{d}\mathbf{u}(\tau(t),p+\Delta p)}{\mathrm{d}\tau}=\mathbf{f}(\mathbf{u}(\tau(t),p+\Delta p),p+\Delta p), \tag{2.28b}$$

where $\tau(t)\in\mathbb{R}$ is a time transformation term, $\mathbf{u}_r(t,p)\in\mathbb{R}^{n_u}$ is a reference trajectory and $\beta\in\mathbb{R}$ is selected such that the two terms in the integral have a similar magnitude. The term $\mathbf{u}_r(t,p)$ is analogous to $\mathbf{u}(t,p)$ and $\mathbf{u}(\tau(t),p+\Delta p)$ is analogous to $\mathbf{u}'(t,p+\Delta p)$ in section 2.2. In this instance $\mathbf{u}_r(t,p)$ is known and $\mathbf{u}(\tau(t),p+\Delta p)$ is unknown and is found by the minimisation. Further, the reference trajectory can be thought of as the true orbit in the Shadowing lemma and $\mathbf{u}(\tau(t),p+\Delta p)$ to be the pseudo-orbit. The minimisation problem was reformulated through linearisation of Equation (2.1), Ref. [128], resulting in

$$\min_{\eta(t),\mathbf{v}(t)} \frac{1}{T}\int_{t_s}^{t_f} \|\mathbf{v}(t)\|^2+\beta^2\eta(t)^2\mathrm{d}t, \tag{2.29a}$$

$$s.t. \quad \frac{\mathrm{d}\mathbf{v}(t)}{\mathrm{d}t}=\frac{\partial\mathbf{f}(\mathbf{u}(t,p),p)}{\partial\mathbf{u}(t,p)}\mathbf{v}(t)+\frac{\partial\mathbf{f}(\mathbf{u}(t,p),p)}{\partial p}+\eta(t)\mathbf{f}(\mathbf{u}(t,p),p). \tag{2.29b}$$

The main benefit of the linearised formulation is that there is no requirement to compute the CLVs or LEs. Instead, a minimisation problem is solved. Manipulation of the minimisation problem results in a linear system and all the numerical tools associated with the field can be leveraged. One limitation of the method is that the minimisation problem can be very large and memory intensive, Ref. [15]. To improve the tractability of this method, improvements such as preconditioning and multi-grid approaches have been developed and implemented, Ref. [18]. The linearised approach has been applied to the Lorenz 1963 system, the van der Pol oscillator, and an aero-elastic limit cycle oscillator, Refs. [125, 128], and the Dowell's plate, Ref. [15]. The development of the Shadowing approach relied on the infinite time horizon sensitivity, Equation (2.10). This is clearly impossible in practice, and as a result long finite time horizons are utilised. It has been shown that as the time horizon increases the accuracy of the sensitivity increases, Ref. [128]. Further, the sensitivity standard deviation is proportional to the inverse of the time horizon, Ref. [128], suggestin that as the time horizon increases a better approximation to the true Shadowing direction is found. LSS has also been applied to larger spatially distributed systems such as the Kuramoto-Sivashinsky (KS) system, Ref. [17], turbulent flow, Ref [16], and flow around an airfoil, Ref. [21].

Increasing the time horizon, which increases accuracy, has the impact of increasing the memory requirements of the system and decreasing convergence of the method. A

sufficient 'spin up' time is required to ensure that the solution is on the attractor and, therefore, ergodic. The error between the analytical Shadowing direction and the approximate Shadowing direction generated by LSS is shown on the Smale-Williams solenoid system, Refs. [35, 124], and is shown to decrease as the time horizon is increased. The main limitation is that LSS relies on a uniformly hyperbolic attractor whereas not all real world systems are uniformly hyperbolic, Ref. [35]. Further, it was shown that LSS can produce non-physical results, Ref. [31].

Lasagna, Sharma, and Meyers developed a modification of the LSS algorithm for systems that exhibit periodicity. The main feature is that a boundary value problem is solved, using appropriate numerical methods, and a periodic Shadowing direction is found, Refs. [77, 78], which is in contrast to the minimisation problem of LSS. This approach is referred to as Periodic Shadowing. An error analysis is also provided showing that Periodic Shadowing has the same requirements for the time horizon as that of the standard LSS method. Further, it has been shown on the Lorenz attractor, Refs. [77, 78].

2.3.4 A multiple shooting reformulation of LSS

The main size of the linear system derived in the LSS formulation comes from the minimisation of the integral of the tangent solution over the entire time horizon. An approach to reduce the size of the linear system generated by LSS, section 2.3.3, is to use a multiple shooting approach, Ref. [19]. Utilising a multiple shooting approach seeks to minimise the tangent solution at a discrete number of checkpoints. This reduces the size of the linear system making the multiple shooting approach more tractable to industrial applications. This formulation is known in the literature as Multiple Shooting Shadowing (MSS). One other method to reduce the size of the linear system is to constrain the tangent solution to be orthogonal to $\mathbf{f}(\mathbf{u}(t,p),p)$ at all times. This has the result of removing the explicit computation of $\eta(t)$ from the linear system, Ref. [19]. The minimisation problem for MSS is

$$\min_{\mathbf{v}_j(t_{j+1})} \sum_{j=0}^{N-1} \left\langle \mathbf{v}_j(t_{j+1}), \mathbf{v}_j(t_{j+1}) \right\rangle, \tag{2.30a}$$

$$s.t. \quad \mathbf{v}_j(t_{j+1}) = \mathbf{v}_{j+1}(t_{j+1}) \quad j = 0, 1, \ldots, N-2, \tag{2.30b}$$

$$\frac{\mathrm{d}\mathbf{v}_j(t)}{\mathrm{d}t} = \frac{\partial \mathbf{f}(\mathbf{u}(t,p),p)}{\partial \mathbf{u}(t,p)} \mathbf{v}_j(t) + \frac{\partial \mathbf{f}(\mathbf{u}(t,p),p)}{\partial p} + \eta_j(t)\mathbf{f}(\mathbf{u}(t,p),p) \quad j = 0, 1, \ldots, N-1, \tag{2.30c}$$

$$\left\langle \mathbf{f}(\mathbf{u}(t,p),p), \mathbf{v}_j(t) \right\rangle = 0 \quad j = 0, 1, \ldots, N-1, \tag{2.30d}$$

where the time domain is split into N segments. Equation (2.30a) is the cost of the tangent solution at the end of each segment. Equation (2.30b) ensures that the tangent

solution is continuous across consecutive segments. Equation (2.30c) is the modified tangent equation with $\eta_j(t)\mathbf{f}(\mathbf{u}(t,p),p)$ term for handling the neutral CLV. Equation (2.30d) constrains the tangent solution to be orthogonal to $\mathbf{f}(\mathbf{u}(t,p),p)$ and is used to remove the explicit computation of $\eta_j(t)$ in Equation (2.30c). The MSS formulation is based on the initial Shadowing approach, Ref. [125], and, therefore, the MSS tangent solution also decomposes on the CLVs in a similar way. Equation 2.30d is derived from solving Equation 2.29 when $\beta = 0$, Ref. [13].

For the remainder of this thesis, MSS is utilised to compute the sensitivity for the Shadowing approaches for the various dynamical systems investigated. MSS has been applied to the KS system, Ref. [19]. An alternative application is to utilise MSS to compute gradients that are used in a gradient descent approach in finding an optimal feedback kernel to control a chaotic system, Ref. [111].

It is recognised in Ref. [19] that there are convergence issues of the minimisation problem due to the large difference in eigenvalues of the linear operator that is formed. To overcome this, the authors introduced a filtering parameter which improves conditioning which results in better convergence. Further advancements in improving the conditioning of the linear operator were achieved through preconditioning, Ref. [110]. It was shown, Ref. [19], that when the filtering parameter is large the MSS approach is an ensemble average of solutions similar to alternative ensemble average approaches, Refs. [45, 79].

2.3.5 A non-intrusive approach to LSS

Both LSS and MSS require additional equations to be implemented into software. Current scientific software may not have the ability to compute the Jacobian required for LSS/MSS and therefore alternatives are required, Ref. [92]. To overcome this the non-intrusive LSS (NILSS) method was developed, Refs. [14, 22, 65, 88, 91, 92, 93]. NILSS finds the solution to one inhomogeneous tangent equation and M homogeneous tangent equations where M is larger than the number of positive LEs of the system. The tangent solution is then formed from the inhomogeneous tangent solution and of a linear combination of homogeneous tangent solutions. A minimisation problem is formed that minimises the norm of the tangent solution by altering the linear combination of homogeneous tangent solutions. The main limitation of this method is that the number of LEs of the system must be known *a priori* to ensure that M is large enough. As in the LSS and MSS methods, the time horizon must also be large for accurate sensitivites, Ref. [20]. Adjoint approaches to NILSS have also been developed, Refs. [14, 88]. The NILSS approach also requires the derivation of the tangent equation and to overcome this finite difference NILSS (FDNILSS) has been developed where the tangent solutions are approximated by finite differences, Ref. [93].

NILSS has been shown on the Lorenz 1963 system, the KS system and a fluid flow problem, Refs. [14, 90, 91, 92]. Ensemble averages for adjoint solutions, Refs. [45, 79], have been approximated by NILSS, Ref. [89]. Chaotic acoustic oscillations in a cavity have been controlled using the NILSS approach, Ref. [65]. Further to this, NILSS has been used for sensitivity analysis of weakly turbulent flow over a 3D cylinder, Refs. [91, 93].

2.4 A numerical viscosity approach to time averaged sensitivity analysis

The time averaged sensitivity derived in section 2.2 requires that the two trajectories, $\mathbf{u}'(t, p + \Delta p)$ and $\mathbf{u}(t, p)$, remain uniformly close forever. The Shadowing approach presented in section 2.3 utilised the Shadowing lemma. An alternative approach is also possible. In this section a method for keeping the two trajectories uniformly close is to apply a control term that damps excess energy, Refs. [23, 49, 120, 121], resulting in accurate sensitivity values. These methods are referred to, in this thesis, as numerical viscosity (NV) methods.

The main focus of these methods is to find terms that contribute to the dissipation of adjoint energy and to use those terms as additional control terms in the adjoint equation, Refs. [23, 120]. While these methods have been predominantly focussed on the adjoint formulation, they are also applicable to the tangent formulation. A tuning parameter is added to control term that determines the amount of control that is applied. This has been predominantly developed on the Navier-Stokes equations where the additional control term was $\nabla \cdot (\mu_s \nabla \hat{\boldsymbol{\lambda}}(t))$, Ref. [23], where $\mu_s \in \mathbb{R}^+$ is the tuning parameter. This results in Equation (2.15) becoming

$$\mathbf{0} = -\frac{\mathrm{d}\hat{\boldsymbol{\lambda}}(t)}{\mathrm{d}t} - \frac{\partial \mathbf{f}(\mathbf{u}(t,p),p)}{\partial \mathbf{u}(t,p)}^{\dagger} \hat{\boldsymbol{\lambda}}(t) + \frac{1}{T}\frac{\partial J(\mathbf{u}(t,p),p)}{\partial \mathbf{u}(t,p)} - \nabla \cdot (\mu_s \nabla \hat{\boldsymbol{\lambda}}(t)), \tag{2.31}$$

This tuning parameter can be thought of as damping additional adjoint energy. Too small a value leads to inadequate damping and the solutions being unstable and unbounded. The determination of the tuning parameter is selected such that the sensitivity produced by the method matches the expected sensitivity, Refs. [23, 120]. This limits the application of these methods into industry as the required sensitivity is unknown. These NV methods have been shown on quasi-2D annular jet, Ref. [23], 2D turbine blades, Ref. [121], trailing edge of a turbine blade, Ref. [120], and channel flow, Ref. [49]. The main benefit of these NV methods is that one non-linear and one linear solution is required. Therefore, these methods are significantly computationally cheaper than the Shadowing approach.

Numerical damping has also been introduced through the careful selection of the time step, Ref. [12], as opposed to introduction of an additional term. The numerical dissipation introduced in the time stepping scheme is utilised to stabilise the adjoint solution. Using this approach removes the numerical inconsistency between the adjoint and non-linear systems when utilising the control term, Ref. [49].

2.5 Summary

This chapter initially presented the steady state sensitivity analysis approach. Recent developments in computational hardware means that a larger amount of computing power is available which means that methods that have previously been reserved for academic test cases have started to be utilised in industrial applications. Examples of such methods are URANS and LES which are inherently transient. Therefore, time averaged sensitivity values should be used. A method for time averaged sensitivity values was presented and its limitations were outlined. The main limitation was that the tangent/adjoint solution must remain bounded *i.e.* two trajectories under the non-linear system with perturbed parameters must remain uniformly close forever, and not diverge away from the unperturbed solution. If this was not satisfied the sensitivity values produced will be inaccurate and unphysical. This limitation arises in chaotic systems of which turbulent flow is one example. The reason for this is that the initial value problem is ill-conditioned for chaotic systems, Ref. [128]. The physical manifestation of this is that the tangent space has an unstable sub-space, Refs. [6, 7, 112], meaning perturbations grow exponentially in time.

There has been two main classes of methods developed in the literature to overcome this limitation in sensitivity analysis. The first class of methods is derived from the Shadowing lemma, Refs. [84, 101]. The Shadowing lemma essentially states that for a given true trajectory of a system that there exists a pseudo-orbit that remains uniformly close. This then implies that this method can be utilised in time-averaged sensitivity analysis. The limitation of the Shadowing lemma is that no information as to the method to find this pseudo-orbit is provided. The first approach to utilise the Shadowing lemma in sensitivity analysis, Ref. [125], utilised the covariant Lyapunov vectors (CLVs) and Lyapunov exponents (LEs), Refs. [6, 7, 50, 51, 72, 95, 112, 131]. The key focus of industry is generation of solutions in a fast manner. The main limitation in the adoption of this approach into industry is the computational expense of finding the CLVs. One of the limiting factors causing a large computational expense is that all the CLVs are required for this method. The number of CLVs is porportional to the dimension of the system. For Lorenz there are three, but for turbulence there could be many millions. Each CLV is then marched under the tangent equation and are re-orthogonalised after n time steps resulting in a large computational cost. Further

details of the algoithms required to compute the CLVs are presented in Ref. [72] and in Appendix A. For larger systems, which are common in industry, computation of the CLVs may even be infeasible given the current computing resources.

Therefore, alternative developments have been made in the literature. The first development was the Least Squares Shadowing (LSS), Refs. [16, 17, 18, 21, 35, 124, 128]. These approaches reformulate the Shadowing approach into a minimisation problem where the integral of the tangent solution is minimised. This results in a large linear system being solved. Consequently, for large industrially relevant systems the LSS approach may be too time and memory intensive which limits its traction in industry.

The second development is Multiple Shooting Shadowing (MSS), Ref. [19, 110], which utilise multiple shooting methods to minimise the tangent solution at a discrete number of checkpoints. This reduces the size of the linear system solved making this method more appealing to industrial applications. Finally, non-intrusive methods, Refs. [14, 22, 65, 88, 91, 92, 93], have been developed. These methods solve one inhomogeneous tangent equation and M homogeneous tangent equations. The limitation is that M must be larger than the number of positive Lyapunov exponents, which generally is unknown *a priori*. An approximation to the Shadowing direction is then found by combining the inhomogeneous tangent solution a linear combination of homogeneous tangent solutions. The tangent solution is minimised by altering the combination of homogeneous tangent solutions.

The implications of the Shadowing method is that a minimisation problem is solved which can be computationally expensive. Large solution times of the linear systems generated from the Shadowing approach limits the uptake of these methods into industry. The benefit of these methods is that accurate sensitivity values are produced with no tuning.

The second class of time averaged sensitivity analysis methods are numerical viscosity approaches. While the Shadowing approaches utilise the Shadowing lemma the numerical viscosity methods either add an additional control term to the adjoint equations, Refs. [23, 49, 120, 121], or use the dissipation of the time stepping scheme, Ref. [12], to stabilise the linearised solution. The methods that apply additional control determine its structure by finding which terms contribute to dissipation of adjoint energy. An additional tuning parameter is added that controls the amount of control added. When the control added is too small the control is unable to stabilise the adjoint solution which results in inaccurate and unphysical sensitivity values. Currently, the tuning parameter is selected such that the sensitivity produced by the NV method matches the expected sensitivity. One approach is to compute the sensitivity across a wide range of values and find which range of values matches the expected sensitivity, similar to a design of experiments. This implies that the

sensitivity is already known thus meaning NV methods would not be required. The benefit of these methods is that only one non-linear solution and one linear solution is required resulting in these methods being computationally cheaper than the Shadowing approach. This implies that, provided the tuning parameter can be selected accurately, these methods would be more likely to be adopted into an industrial setting than Shadowing.

The result of this analysis suggest for time-averaged sensitivity analysis to be adopted into industry either cheaper numerical methods for solving the Shadowing direction or improvements in understanding in the NV methods are required. Current literature has kept both of these approaches separate and there has been no connection between Shadowing and NV methods. The main reason for this is that the Shadowing methods have mainly been developed and tested on small systems whereas the NV methods have been developed and tested on the Navier-Stokes equations. Comparison of the two methods could be mutually beneficial and this thesis performs this analysis.

Chapter 3

Applying optimal control techniques to the Shadowing approach

It was shown in chapter 2 that the traditional approach to sensitivity analysis fails for chaotic systems. Further, there have been two main approaches presented in the literature to find stabilised solutions to the tangent/adjoint equations. Those being the Shadowing approach and the numerical viscosity (NV) approaches. These approaches either find a bounded solution through finding an initial condition to Equation 2.1 that shadows the original trajectory (Shadowing) or through the addition of a damping term in the tangent/adjoint equations that damps excess energy. Due to their formulation differences there has been little comparison between these approaches.

The chapter aims to bridge this gap in understanding and presents a novel approach. The original contribution proposed utilises optimal control theory, Refs [2, 9, 27, 97], to find an appropriate stabilising control for the tangent/adjoint equations. This approach will be referred to as Optimal Control Shadowing and abbreviated to OCS. OCS provides the link between the Shadowing and NV approaches. This is because optimal control techniques add additional control to the tangent/adjoint equations, similar to that of NV, and find its value/structure utilising minimisation procedures, similar to some Shadowing methods. This chapter provides the derivation for OCS along with pseudocode/algorithms for computing the optimal tangent/adjoint solution. Detailed implementation details are provided in section 3.8 Some notation used previously is repeated here for clarity and to ensure this chapter is stand alone.

As shown in section 2.2 there are two approaches used in computing sensitivities. Those are the tangent and adjoint methods which are utilised for single and multiple parameters, respectively. This leads to two possible approaches for OCS. The first of

these is to apply control to the tangent equation, derived in section 3.2, and is known as tangent OCS. Following this, the adjoint of tangent OCS can be derived which is detailed in section 3.4. Alternatively, the adjoint equation can be directly controlled is presented in section 3.5.

3.1 Problem set-up

Firstly, consider a non-linear chaotic dynamical system of the form

$$\frac{\mathrm{d}\mathbf{u}(t,p)}{\mathrm{d}t} = \mathbf{f}(\mathbf{u}(t,p),p), \tag{3.1}$$

where $\mathbf{u}(t,p) \in \mathbb{R}^{n_u}$ is the state vector, which in the aerospace sector typically is the fluid velocity, pressure and temperature, $p \in \mathbb{R}$ is a parameter of interest, typically the surface geometry, $t \in (t_s, t_f)$, and t_s and t_f are the start and end times of the simulation, respectively, and $\mathbf{f}(\mathbf{u}(t,p),p) : \mathbb{R}^{n_u} \times \mathbb{R} \to \mathbb{R}^{n_u}$ are the governing equations, typically the Navier-Stokes equations. In general, the function of interest is $J(\mathbf{u}(t,p),p) : \mathbb{R}^{n_u} \times \mathbb{R} \to \mathbb{R}$ and its time average is

$$\bar{J} = \frac{1}{T}\int_{t_s}^{t_f} J(\mathbf{u}(t,p),p)\,\mathrm{d}t, \tag{3.2}$$

where $T = t_f - t_s$ is the time horizon. A common example of the function of interest in the aerospace sector is the lift or drag produced by a body.

3.2 Derivation of the tangent OCS formulation

To derive OCS, first Equation (3.1) is linearised. A time dilation term $\eta(t)\mathbf{f}(\mathbf{u}(t,p),p)$ is introduced to invert the Shadowing operator for the covariant Lyapunov vector (CLV) that corresponds to a Lyapunov exponent (LE) of zero. The reader is referred to section 2.3.2 for details on inverting the Shadowing operator and Appendix A for details on CLVs and LEs. This results in

$$\frac{\mathrm{d}\mathbf{v}(t)}{\mathrm{d}t} = \frac{\partial \mathbf{f}(\mathbf{u}(t,p),p)}{\partial \mathbf{u}(t,p)}\mathbf{v}(t) + \frac{\partial \mathbf{f}(\mathbf{u}(t,p),p)}{\partial p} + \eta(t)\mathbf{f}(\mathbf{u}(t,p),p), \tag{3.3}$$

where $\mathbf{v}(t) \in \mathbb{R}^{n_v}$ and $\mathbf{v}(t) \equiv \frac{\partial \mathbf{u}(t)}{\partial p}$, $\frac{\partial \mathbf{f}(\mathbf{u}(t,p),p)}{\partial \mathbf{u}(t,p)}$ is the Jacobian and $\frac{\partial \mathbf{f}(\mathbf{u}(t,p),p)}{\partial p}$ is a forcing term. The addition of the time dilation term is common in the LSS, MSS and NILSS approaches, Refs. [14, 16, 17, 18, 19, 21, 22, 35, 65, 88, 91, 92, 93, 124, 128], but is not utilised in NV approaches due to the presence of the control term. To remove explicit calculation of the $\eta(t)\mathbf{f}(\mathbf{u}(t,p),p)$ term, $\mathbf{v}(t)$ is constrained to be orthogonal to

$\mathbf{f}(\mathbf{u}(t,p),p)$ or simply $\langle \mathbf{v}(t), \mathbf{f}(\mathbf{u}(t,p),p)\rangle = 0$ where $\langle\cdot,\cdot\rangle$ is an inner product and $\|\cdot\| = \sqrt{\langle\cdot,\cdot\rangle}$ is the norm.

In the Shadowing approach the tangent solution is stabilised by minimisation of the norm of the tangent solution through modification of the tangent initial condition. Unlike the Shadowing approaches, the tangent solution is stabilised in the NV approach with the additional control term. This control term utilised in the NV approach is defined *a priori* and the tuning parameter requires further work to find its value. It is worth noting that the author did combine both approaches to stabilising the tangent solution, *i.e.* allowing both the tangent initial condition to vary and application of control, but found that the term that was most significant in stabilising the tangent solution was the initial condition and control was minimal which resulted in there being similar computational effort to MSS. This did not provide significant understanding between the methods. To overcome this, and gain a better knowledge between the Shadowing and NV methods, the initial condition is constrained to $\mathbf{v}(t_s) = \mathbf{0}$. NV methods usually consist of addition of a pre-defined control term. It is currently unclear how optimal these terms are. The novelty of this thesis is to introduce a generic control term whose structure is found utilising optimal control techniques, Refs. [2, 9, 27, 97]. These optimal control techniques find a control term which minimises the integral of the norms of the tangent solution and control solution. This generic control term denoted $\mathbf{q}(t) \in \mathbb{R}^{n_q}$ is introduced into Equation (3.3) and results in the tangent equation

$$\frac{\mathrm{d}\mathbf{v}(t)}{\mathrm{d}t} = \frac{\partial \mathbf{f}(\mathbf{u}(t,p),p)}{\partial \mathbf{u}(t,p)}\mathbf{v}(t) + \frac{\partial \mathbf{f}(\mathbf{u}(t,p),p)}{\partial p} + \eta(t)\mathbf{f}(\mathbf{u}(t,p),p) + \mathbf{q}(t), \tag{3.4a}$$

$$\mathbf{v}(t_s) = \mathbf{0}. \tag{3.4b}$$

Following the control techniques, which are typically used to compute the structure of the control term $\mathbf{q}(t)$, leads to the following minimisation problem

$$\min_{\mathbf{v}(t),\mathbf{q}(t)} \int_{t_s}^{t_f} \langle \mathbf{v}(t), \mathbf{v}(t)\rangle + \alpha \langle \mathbf{q}(t), \mathbf{q}(t)\rangle \,\mathrm{d}t \tag{3.5a}$$

$$s.t.\ \frac{\mathrm{d}\mathbf{v}(t)}{\mathrm{d}t} = \frac{\partial \mathbf{f}(\mathbf{u}(t,p),p)}{\partial \mathbf{u}(t,p)}\mathbf{v}(t) + \frac{\partial \mathbf{f}(\mathbf{u}(t,p),p)}{\partial p} + \eta(t)\mathbf{f}(\mathbf{u}(t,p),p) + \mathbf{q}(t), \tag{3.5b}$$

$$\langle \mathbf{v}(t), \mathbf{f}(\mathbf{u}(t,p),p)\rangle = 0, \tag{3.5c}$$

$$\mathbf{v}(t_s) = \mathbf{0}, \tag{3.5d}$$

where $\alpha \in \mathbb{R}$ can thought of as modifying the cost of applying control. Small values of α mean control is cheap to apply and the tangent solution is over-damped, and large values mean control is expensive to apply and the tangent solution is under-damped. The effects of varying α will be discussed later on each system investigated, for example in section 4.3. Introduction of the control term is assumed to be small and

does not significantly alter the attractor of the dynamical system, thus removing the issues outlined in Ref. [49].

It is worth noting the difference between OCS and other Shadowing methods. Shadowing methods do not "kill off" the unstable subspace. Instead they find a linear combination of covariant Lyapunov vectors which results in a stable solution. Through the introduction of the control term, OCS can "kill off" the unstable subspace resulting in a stable solution, because the control term can negate the unstable covariant Lyapunov vectors. These two approaches, while achieveing the same outcome of a stable solution, are completely different in terms of the approach used to achieve this objective.

For the structure of $\mathbf{q}(t)$ to be optimal, the Pontryagin minimisation principle, Refs. [96, 103], is used. Firstly, a set of Lagrange multipliers, $\boldsymbol{\lambda}(t) \in \mathbb{R}^{n_\lambda}$ and $\omega(t) \in \mathbb{R}$, are introduced for each of the constraints, Equation (3.5b) and Equation (3.5c), respectively. Utilising $\boldsymbol{\lambda}(t)$ and $\omega(t)$ means that the constraints can be incorporated to form the Hamiltonian, $\mathcal{H}$, of Equation (3.5), resulting in

$$\begin{aligned} \mathcal{H} = \int_{t_s}^{t_f} \langle \mathbf{v}(t), \mathbf{v}(t) \rangle + \alpha \langle \mathbf{q}(t), \mathbf{q}(t) \rangle + \\ \left\langle \boldsymbol{\lambda}(t), \frac{\mathrm{d}\mathbf{v}(t)}{\mathrm{d}t} - \frac{\partial \mathbf{f}(\mathbf{u}(t,p),p)}{\partial \mathbf{u}(t,p)} \mathbf{v}(t) - \frac{\partial \mathbf{f}(\mathbf{u}(t,p),p)}{\partial p} - \eta(t)\mathbf{f}(\mathbf{u}(t,p),p) - \mathbf{q}(t) \right\rangle + \\ \omega(t) \langle \mathbf{f}(\mathbf{u}(t,p),p), \mathbf{v}(t) \rangle \, \mathrm{d}t. \end{aligned} \tag{3.6}$$

Integration of Equation (3.6) by parts leads to

$$\begin{aligned} \mathcal{H} = \int_{t_s}^{t_f} \langle \mathbf{v}(t), \mathbf{v}(t) \rangle + \alpha \langle \mathbf{q}(t), \mathbf{q}(t) \rangle + \\ \left\langle \mathbf{v}(t), -\frac{\mathrm{d}\boldsymbol{\lambda}(t)}{\mathrm{d}t} - \frac{\partial \mathbf{f}(\mathbf{u}(t,p),p)}{\partial \mathbf{u}(t,p)}^{\dagger} \boldsymbol{\lambda}(t) \right\rangle - \\ \left\langle \boldsymbol{\lambda}(t), \frac{\partial \mathbf{f}(\mathbf{u}(t,p),p)}{\partial p} + \eta(t)\mathbf{f}(\mathbf{u}(t,p),p) + \mathbf{q}(t) \right\rangle + \\ \omega(t) \langle \mathbf{f}(\mathbf{u}(t,p),p), \mathbf{v}(t) \rangle \, \mathrm{d}t + \langle \boldsymbol{\lambda}(t), \mathbf{v}(t) \rangle |_{t_s}^{t_f}, \end{aligned} \tag{3.7}$$

where $\frac{\partial \mathbf{f}(\mathbf{u}(t,p),p)}{\partial \mathbf{u}(t,p)}^{\dagger}$ is the adjoint of the Jacobian. Pontryagin's minimisation principle defines the minimum of Equation (3.5) to be when all partial derivatives of $\mathcal{H}$ with respect to $\mathbf{v}(t)$, $\boldsymbol{\lambda}(t)$, $\mathbf{q}(t)$, $\omega(t)$ and $\eta(t)$ are zero. This leads to the set of first order

optimality conditions

$$\frac{\partial \mathcal{H}}{\partial \mathbf{v}(t)} = \mathbf{0} = -\frac{\mathrm{d}\boldsymbol{\lambda}(t)}{\mathrm{d}t} - \frac{\partial \mathbf{f}(\mathbf{u}(t,p),p)}{\partial \mathbf{u}(t,p)}^{\dagger} \boldsymbol{\lambda}(t) + 2\mathbf{v}(t) + \omega(t)\mathbf{f}(\mathbf{u}(t,p),p), \tag{3.8a}$$

$$\frac{\partial \mathcal{H}}{\partial \boldsymbol{\lambda}(t)} = \mathbf{0} = \frac{\mathrm{d}\mathbf{v}(t)}{\mathrm{d}t} - \frac{\partial \mathbf{f}(\mathbf{u}(t,p),p)}{\partial \mathbf{u}(t,p)}\mathbf{v}(t) - \frac{\partial \mathbf{f}(\mathbf{u}(t,p),p)}{\partial p} - \eta(t)\mathbf{f}(\mathbf{u}(t,p),p) - \mathbf{q}(t), \tag{3.8b}$$

$$\frac{\partial \mathcal{H}}{\partial \mathbf{q}(t)} = \mathbf{0} = 2\alpha\mathbf{q}(t) - \boldsymbol{\lambda}(t), \tag{3.8c}$$

$$\frac{\partial \mathcal{H}}{\partial \omega(t)} = 0 = \langle \mathbf{f}(\mathbf{u}(t,p),p), \mathbf{v}(t) \rangle , \tag{3.8d}$$

$$\frac{\partial \mathcal{H}}{\partial \eta(t)} = 0 = \langle \boldsymbol{\lambda}(t), \mathbf{f}(\mathbf{u}(t,p),p) \rangle . \tag{3.8e}$$

The Hamiltonian Hessian matrix is positive-definite, which means the minimisation problem, Equation (3.5a), will be convex if the second order sufficient condition

$$\frac{\partial^2 \mathcal{H}}{\partial \mathbf{q}(t)^2} = 2\alpha, \tag{3.9}$$

is greater than zero. This leads to the constraint $\alpha > 0$.

To find the optimal control, Equation (3.8) need to be solved. Once the optimal solution has been found the sensitivity of the system, due to the time dilation term $\eta(t)$, is

$$\frac{\mathrm{d}\bar{J}}{\mathrm{d}p} = \frac{1}{T}\int_{t_s}^{t_f} \left\langle \frac{\partial J(\mathbf{u}(t,p),p)}{\partial \mathbf{u}(t,p)}, \mathbf{v}(t) \right\rangle + \frac{\partial J(\mathbf{u}(t,p),p)}{\partial p} + \eta(t)\left(J(\mathbf{u}(t,p),p) - \bar{J}\right)\mathrm{d}t. \tag{3.10}$$

Details of the derivation of Equation (3.10) are presented in Ref. [19].

There are some terms, $\boldsymbol{\lambda}(t)$, $\eta(t)$ and $\omega(t)$, in the derivation which, currently, are free variables and are eliminated using the state transition matrix. To overcome this each term is handled in turn. As the Lagrange multipliers are free to be selected the following constraint, $\langle \boldsymbol{\lambda}(t), \mathbf{v}(t) \rangle|_{t_s}^{t_f} = 0$, is used. This results in the terminal condition on the co-state equation being $\boldsymbol{\lambda}(t_f) = \mathbf{0}$.

3.2.1 Derivation for the closed form expression of $\eta(t)$

So far in the OCS derivation the time dilation term, $\eta(t)$, has been introduced to overcome the limitation in inverting the Shadowing operator for CLV modes corresponding to $\Lambda_k = 0$, but has not been explained as to what values it should take. LSS solves for this term at each time step, Ref. [128], whereas MSS, Ref. [19], utilises a closed form solution and finds a projection operator to remove the explicit computation of $\eta(t)$. This section computes the closed form solution of $\eta(t)$ such that

its explicit calculation is removed, reducing the size of the linear system formed and, therefore, improving convergence of the numerical method.

Firstly, the solution at time t to Equation (3.8b) can be written utilising the state transition matrix, $\mathbf{\Phi}(t_1, t_2)$, which results in

$$\begin{aligned}\mathbf{v}(t) = \boldsymbol{A}\mathbf{v}(t_s) + \left(\int_{t_s}^{t} \eta(\tau)\mathrm{d}\tau\right)\mathbf{f}(\mathbf{u}(t,p),p) + \\ \int_{t_s}^{t} \mathbf{\Phi}(\tau,t)\frac{\partial \mathbf{f}(\mathbf{u}(\tau,p),p)}{\partial p}\mathrm{d}\tau + \int_{t_s}^{t}\mathbf{\Phi}(\tau,t)\mathbf{q}(\tau)\mathrm{d}\tau,\end{aligned} \tag{3.11}$$

where the operator $\mathbf{A}$ is defined as

$$\boldsymbol{A}\mathbf{v}(t_s) = \mathbf{\Phi}(t_s,t)\mathbf{v}(t_s). \tag{3.12}$$

An introduction to the state transition matrix can be found in Ref. [57] and details are provided in Appendix B. To ease notation the terms

$$\int_{t_s}^{t} \mathbf{\Phi}(\tau,t)\frac{\partial \mathbf{f}(\mathbf{u}(\tau,p),p)}{\partial p}\mathrm{d}\tau \quad \text{and} \quad \int_{t_s}^{t}\mathbf{\Phi}(\tau,t)\mathbf{q}(\tau)\mathrm{d}\tau$$

are denoted using the simplified notation

$$\boldsymbol{B}\square = \int_{t_s}^{t}\mathbf{\Phi}(\tau,t)\square(\tau)\mathrm{d}\tau \quad \text{to give} \quad \boldsymbol{B}\frac{\partial \mathbf{f}(\mathbf{u}(t,p),p)}{\partial p} \quad \text{and} \quad \boldsymbol{B}\mathbf{q}(t).$$

By defining the solution to the tangent equation without the influence of the $\eta(t)\mathbf{f}(\mathbf{u}(t,p),p)$ term as

$$\mathbf{v}'(t) = \boldsymbol{A}\mathbf{v}(t_s) + \boldsymbol{B}\frac{\partial \mathbf{f}(\mathbf{u}(t,p),p)}{\partial p} + \boldsymbol{B}\mathbf{q}(t), \tag{3.13}$$

Equation (3.11) can be re-written as follows

$$\mathbf{v}(t) = \mathbf{v}'(t) + \left(\int_{t_s}^{t}\eta(\tau)\mathrm{d}\tau\right)\mathbf{f}(\mathbf{u}(t,p),p). \tag{3.14}$$

Taking the inner product of Equation (3.14) with $\mathbf{f}(\mathbf{u}(t,p),p)$ and utilising the constraint, Equation (3.8d), results in

$$\begin{aligned}\langle \mathbf{v}(t), \mathbf{f}(\mathbf{u}(t,p),p)\rangle = 0 \\ = \langle \mathbf{v}'(t), \mathbf{f}(\mathbf{u}(t,p),p)\rangle + \left(\int_{t_s}^{t}\eta(\tau)\mathrm{d}\tau\right)\langle \mathbf{f}(\mathbf{u}(t,p),p), \mathbf{f}(\mathbf{u}(t,p),p)\rangle .\end{aligned} \tag{3.15}$$

Manipulation of Equation (3.15) leads to the closed form expression of $\eta(t)$,

$$\int_{t_s}^{t}\eta(\tau)\mathrm{d}\tau = -\frac{\langle \mathbf{v}'(t), \mathbf{f}(\mathbf{u}(t,p),p)\rangle}{\langle \mathbf{f}(\mathbf{u}(t,p),p), \mathbf{f}(\mathbf{u}(t,p),p)\rangle}, \tag{3.16}$$

which can be combined with Equation (3.14) to give the solution to the tangent solution at time t

$$\mathbf{v}(t) = \mathbf{v}'(t) - \frac{\langle \mathbf{v}'(t), \mathbf{f}(\mathbf{u}(t,p),p)\rangle}{\langle \mathbf{f}(\mathbf{u}(t,p),p), \mathbf{f}(\mathbf{u}(t,p),p)\rangle}\mathbf{f}(\mathbf{u}(t,p),p). \tag{3.17}$$

Finally, Equation (3.10) still has reliance on $\eta(t)$. To remove its influence, $\mathbf{v}'(t)$ and Equation (3.15) can be utilised to give

$$\begin{aligned}\frac{\mathrm{d}\bar{J}}{\mathrm{d}p} = \frac{1}{T}\int_{t_s}^{t_f}\left\langle \frac{\partial J(\mathbf{u}(t,p),p)}{\partial \mathbf{u}(t,p)}, \mathbf{v}'(t)\right\rangle + \frac{\partial J(\mathbf{u}(t,p),p)}{\partial p}\mathrm{d}t + \\ \frac{1}{T}\frac{\langle \mathbf{v}'(t_f), \mathbf{f}(\mathbf{u}(t_f,p),p)\rangle}{\langle \mathbf{f}(\mathbf{u}(t_f,p),p), \mathbf{f}(\mathbf{u}(t_f,p),p)\rangle}\left(\bar{J} - J(\mathbf{u}(t_f,p),p)\right).\end{aligned} \tag{3.18}$$

Further details of this manipulation are given in Appendix C of Ref. [19].

3.2.2 Derivation for the closed form expression of $\omega(t)$

The $\omega(t)$ term was introduced as a method of incorporating the orthogonality constraint into the Hamiltonian. There, so far, has been no description on what value this should take and it, therefore, requires constraining. The closed form expression for $\omega(t)$ is found by following a similar procedure to that of the derivation for the closed form expression for $\eta(t)$.

Firstly, the solution to Equation (3.8a) at time t can be written in terms of the adjoint state transition matrix, $\hat{\mathbf{\Phi}}(t_1,t_2)$, which results in

$$\boldsymbol{\lambda}(t) = -\mathbf{C}\left[2\mathbf{v}(t)\right] + \mathbf{D}\boldsymbol{\lambda}(t_f) + \left(\int_t^{t_f}\omega(\tau)\mathrm{d}\tau\right)\mathbf{f}(\mathbf{u}(t,p),p), \tag{3.19}$$

where

$$\mathbf{C}\left[2\mathbf{v}(t)\right] = \int_t^{t_f}\hat{\mathbf{\Phi}}\left(t,\tau\right)^{-1}\left[2\mathbf{v}(\tau)\right]\mathrm{d}\tau, \tag{3.20}$$

and

$$\mathbf{D}\boldsymbol{\lambda}(t_f) = \hat{\mathbf{\Phi}}\left(t,t_f\right)^{-1}\boldsymbol{\lambda}(t_f). \tag{3.21}$$

Defining the solution to the co-state equation without the influence of $\omega(t)\mathbf{f}(\mathbf{u}(t,p),p)$ as

$$\boldsymbol{\lambda}'(t) = -\mathbf{C}\left[2\mathbf{v}(t)\right] + \mathbf{D}\boldsymbol{\lambda}(t_f), \tag{3.22}$$

leads to Equation (3.19) being

$$\boldsymbol{\lambda}(t) = \boldsymbol{\lambda}'(t) + \left(\int_t^{t_f}\omega(\tau)\mathrm{d}\tau\right)\mathbf{f}(\mathbf{u}(t,p),p). \tag{3.23}$$

Taking the inner product of Equation (3.23) with $\mathbf{f}(\mathbf{u}(t,p),p)$ and using the co-state constraint, Equation (3.8e), results in

$$\begin{aligned} &\langle \boldsymbol{\lambda}(t), \mathbf{f}(\mathbf{u}(t,p),p)\rangle = 0 \\ &= \langle \boldsymbol{\lambda}'(t), \mathbf{f}(\mathbf{u}(t,p),p)\rangle + \left(\int_t^{t_f} \omega(\tau)\mathrm{d}\tau\right) \langle \mathbf{f}(\mathbf{u}(t,p),p), \mathbf{f}(\mathbf{u}(t,p),p)\rangle . \end{aligned} \tag{3.24}$$

Manipulation of Equation (3.24) leads to the closed form expression of ω,

$$\int_t^{t_f} \omega(\tau)\mathrm{d}\tau = -\frac{\langle \boldsymbol{\lambda}'(t), \mathbf{f}(\mathbf{u}(t,p),p)\rangle}{\langle \mathbf{f}(\mathbf{u}(t,p),p), \mathbf{f}(\mathbf{u}(t,p),p)\rangle}, \tag{3.25}$$

and can be substituted into Equation (3.23) to give the co-state solution at time t

$$\boldsymbol{\lambda}(t) = \boldsymbol{\lambda}'(t) - \frac{\langle \boldsymbol{\lambda}'(t), \mathbf{f}(\mathbf{u}(t,p),p)\rangle}{\langle \mathbf{f}(\mathbf{u}(t,p),p), \mathbf{f}(\mathbf{u}(t,p),p)\rangle}\mathbf{f}(\mathbf{u}(t,p),p). \tag{3.26}$$

3.3 A matrix-free method for the solution to the optimality conditions of tangent OCS

The first order optimality conditions were derived in the previous section with no information about how to solve them computationally. This section provides algorithms for the computation of these optimality conditions. A common method for generating a solution that satisfies the optimality conditions, Equation (3.8), is the differential Riccati equation (DRE), Refs. [10, 64, 85, 104]. The DRE generates a differential equation for the feedback kernel, a matrix $n_q \times n_q$ in size, between $\mathbf{v}(t)$ and $\mathbf{q}(t)$ that ensures all of the optimality conditions are satisfied. This DRE becomes unfeasible for systems with a large number of degrees of freedom, such as unsteady turbulent flows, due to memory requirements. The rationale is that memory requirements of the DRE square with number of solution variables. Further, the cost of solving the DRE scales with the cube of the number of degrees of freedom of the system. This soon becomes unfeasible for large systems and the required storage for the matrix becomes larger than the available compute resources. Further, it has been shown, Ref. [100], that the control term relates to the tangent term via $\mathbf{v}(t) = -\mathbf{K}\mathbf{q}(t) + \mathbf{q}'(t)$, where $\mathbf{K}$ is a feedback kernel and $\mathbf{q}'(t)$ is a feed forward term. This solutions requires the backward marching of two Riccati equations. The feedback kernel relates to the terms in the tangent equations that are to be supressed or kept. Selecting terms within the feedback kernel could help also select a better tuning parameter of NV term for the NV method. Further, utilising the DRE would remove the requirement for iterative solvers removing the requirement for time domain decomposition in section 3.6. While the DRE and feedback kernel have their benefits the author determined, that through the use of CLVs, that similar information from the

solution could be gained and that the memory requirements of storing the feedback kernel at each time step would become problematic. An example of this would be a simple 1D mesh with 100 grid points in the x direction simulated for 500 time units with a time step of 1×10^{-4} using double precision would result in 400Gb of memory.

One of the simplest and earliest methods to overcome the memory requirements of the DRE is the matrix-free approach, Ref. [98]. This approach casts the optimality conditions as a linear system and utilises conjugate gradient (CG) methods, Refs. [39, 48, 117], to solve the system. An alternative to the matrix-free method, Ref. [98], is the reduced space method, Ref. [86], which solves the reduced Hessian system. Alternatives also include various types of preconditioning, Refs. [3, 109], where Schur complement and Schwarz preconditioning are utilised to increase convergence rates. The methods proposed here compute the solution of the control at every time step. An approach to increasing performance is the multi-grid in time method, Ref. [56], where through restriction the control solution is solved on a coarser time step and then prolongated down onto a finer one. All of these approaches have been utilised on stable systems whereas the tangent equation investigated here is linear and unstable. Therefore, it is unclear how these methods perform on such systems. The vast majority of the alternatives to the DRE require manipulation of the Hessian matrix, which for large spatially distributed systems such as unsteady turbulence, is not feasible due, again, to memory requirements. Here matrix-free methods, Ref. [98], are utilised so that the Hessian or DRE matrices are not computed, which reduces memory requirements. In this section the notation is kept general for reasons that will become clear when undertaking the time domain decomposition technique, section 3.6.

Initially, there is no knowledge of what the control term should be and, therefore, here $\mathbf{q}(t) = \mathbf{0}$ is arbitrarily selected as an initial estimate for the control terms. The tangent solution is found by solving Equation (3.8b) from t_s to t_f from the initial condition $\mathbf{v}(t_s) = \mathbf{0}$, the initial guess for $\mathbf{q}(t)$, and Equation (3.17). Finding the tangent solution in this way ensures that Equation (3.8b) and Equation (3.8d) of the optimality conditions are always satisfied. Similarly, the co-state solution is found by solving Equation (3.8a) backwards in time from t_f to t_s with $\boldsymbol{\lambda}(t_f) = \mathbf{0}$ as the terminal condition along with using the tangent solution, $\mathbf{v}(t)$, and Equation (3.26). Finding the co-state solution in this way ensures that Equation (3.8a) and Equation (3.8e) of the optimality conditions are always satisfied.

The only remaining unsatisfied optimality constraint is $\frac{\partial \mathcal{H}}{\partial \mathbf{q}(t)} = \mathbf{0}$ because the initial guess for the control is not guaranteed to satisfy this equation. To show this, the analytical solutions of the tangent and co-state solutions are required.

Substitution of the analytical tangent solution, Equations (3.11), into the analytical co-state solution, Equation (3.19), leads to

$$\boldsymbol{\lambda}(t) = -\mathbf{C}\left(2\left[\boldsymbol{A}\mathbf{v}(t_s) + \left(\int_{t_s}^{\tau}\eta(s)\mathrm{d}s\right)\mathbf{f}(\mathbf{u}(\tau,p),p) + \boldsymbol{B}\frac{\partial\mathbf{f}(\mathbf{u}(t,p),p)}{\partial p} + \boldsymbol{B}\mathbf{q}(t)\right]\right) + \mathbf{D}\boldsymbol{\lambda}(t_f) + \left(\int_{t}^{t_f}\omega(\tau)\mathrm{d}\tau\right)\mathbf{f}(\mathbf{u}(t,p),p). \tag{3.27}$$

Substitution of Equation (3.27) into Equation (3.8c) and grouping term in $\mathbf{q}(t)$ gives

$$\left[2\alpha\mathbf{I} + \mathbf{C}\left(2\mathbf{B}\right)\right]\mathbf{q}(t) + \mathbf{C}\left(2\left[\mathbf{A}\mathbf{v}(t_s) + \left(\int_{t_s}^{\tau}\eta(s)\mathrm{d}s\right)\mathbf{f}(\mathbf{u}(\tau,p),p) + \mathbf{B}\frac{\partial\mathbf{f}(\mathbf{u}(t,p),p)}{\partial p}\right]\right) - \left(\int_{t}^{t_f}\omega(\tau)\mathrm{d}\tau\right)\mathbf{f}(\mathbf{u}(t,p),p) - \mathbf{D}\boldsymbol{\lambda}(t_f) = \mathbf{0}, \tag{3.28}$$

where $\mathbf{I}$ is the identity. This represents a linear system of the form

$$\frac{\partial\mathcal{H}}{\partial\mathbf{q}(t)} = \mathbf{G}\mathbf{q}(t) = \mathbf{E}\mathbf{q}(t) - \mathbf{b}(t) = \mathbf{0},$$

where $\mathbf{G}\mathbf{q}(t)$ represents the value of the gradient given a certain value of $\mathbf{q}(t)$, $\mathbf{E}\mathbf{q}(t)$ the impact that the control has on the solution, and $\mathbf{b}(t)$ the growth of the solution without control. This linear system can be solved using a conjugate gradient method as the linear operator is positive-definite, Ref. [98]. Algorithm 1 shows how to compute $\mathbf{G}\mathbf{q}(t)$ in a matrix-free sense which can then be utilised to compute $\mathbf{b}(t)$. This is achieved by computing $\mathbf{G}\mathbf{q}(t)$ with $\mathbf{q}(t) = \mathbf{0}$ and $\mathbf{E}\mathbf{q}(t)$ is computed by evaluating $\mathbf{G}\mathbf{q}(t)$ and adding $\mathbf{b}(t)$. Finally, the optimal control, tangent and co-state solutions are

Algorithm 1: A matrix-free method for the calculation of $\mathbf{G}\mathbf{q}(t)$.

Input: $\mathbf{q}(t)$
Output: $\mathbf{G}\mathbf{q}(t)$
1 $\mathbf{v}(t) \leftarrow$ Solve Equation (3.8b) from t_s to t_f using $\mathbf{v}(t_s)$ and $\mathbf{q}(t)$
2 $\boldsymbol{\lambda}(t) \leftarrow$ Solve Equation (3.8a) from t_f to t_s using $\boldsymbol{\lambda}(t_f)$ and $\mathbf{v}(t)$
3 $\mathbf{G}\mathbf{q}(t) \leftarrow 2\alpha\mathbf{q}(t) - \boldsymbol{\lambda}(t)$

found using Algorithm 2.

Algorithm 2: A matrix-free method for solution of the optimality conditions.

1 $\mathbf{b}(t) \leftarrow -\mathbf{G}\mathbf{0}(t)$
2 $\mathbf{E}\mathbf{q}(t) \leftarrow \mathbf{G}\mathbf{q}(t) + \mathbf{b}(t)$
3 Solve $\mathbf{E}\mathbf{q}(t) = \mathbf{b}(t)$ using conjugate gradient to compute $\mathbf{q}(t)$
4 $\mathbf{v}(t) \leftarrow$ Solve Equation (3.8b) from t_s to t_f using $\mathbf{v}(t_s)$ and $\mathbf{q}(t)$
5 $\boldsymbol{\lambda}(t) \leftarrow$ Solve Equation (3.8a) from t_f to t_s using $\boldsymbol{\lambda}(t_f)$ and $\mathbf{v}(t)$

The operators $\mathbf{G}$ and $\mathbf{E}$ are never actually formed in practice and only their action on vectors is computed. This method requires the storage of $\mathbf{v}(t)$, $\boldsymbol{\lambda}(t)$ and $\mathbf{q}(t)$ at each time step in the time horizon. Storage requirements scale linearly with problem size, time horizon and time step.

It is well known that the convergence rate of the conjugate gradient algorithm is determined by the condition number of $\mathbf{E}$, Ref. [98]. The value chosen for α, through the $2\alpha\mathbf{I}$ term, controls the condition number of the operator $\mathbf{E}$ which is composed of two terms, $2\alpha\mathbf{I}$ and $\mathbf{C}\left(2\mathbf{B}\right)$. These terms can be thought of as the cost in applying control and how well the control stabilises the solution, respectively. If $\alpha \approx 0$, then the $\mathbf{C}\left(2\mathbf{B}\right)$ term dominates the condition number and as such a control is applied such that

$$\mathbf{q}(t) \approx \left[\mathbf{C}\left(2\mathbf{B}\right)\right]^{-1}\left(-\mathbf{C}\left(2\left[\mathbf{A}\mathbf{v}(t_s)+\left(\int_{t_s}^{\tau}\eta(s)\mathrm{d}s\right)\mathbf{f}(\mathbf{u}(\tau,p),p)+\mathbf{B}\frac{\partial\mathbf{f}(\mathbf{u}(t,p),p)}{\partial p}\right]\right)+\left[\int_{t}^{t_f}\omega(\tau)\mathrm{d}\tau\right]\mathbf{f}(\mathbf{u}(t,p),p)+\mathbf{D}\boldsymbol{\lambda}(t_f)\right),$$

which implies that the control applied is exactly the negative of the tangent equation and leads to a tangent solution that is over-damped. Conversely, if α is large then $2\alpha\mathbf{I}$ dominates the conditioning of $\mathbf{E}$ and the control applied results in

$$\mathbf{q}(t) \approx \frac{1}{2\alpha}\left(-\mathbf{C}\left(2\left[\mathbf{A}\mathbf{v}(t_s)+\left(\int_{t_s}^{\tau}\eta(s)\mathrm{d}s\right)\mathbf{f}(\mathbf{u}(\tau,p),p)+\mathbf{B}\frac{\partial\mathbf{f}(\mathbf{u}(t,p),p)}{\partial p}\right]\right)+\left[\int_{t}^{t_f}\omega(\tau)\mathrm{d}\tau\right]\mathbf{f}(\mathbf{u}(t,p),p)+\mathbf{D}\boldsymbol{\lambda}(t_f)\right),$$

which implies the control applied is negligible and the solution is under-damped. Therefore, selecting α in between these values leads to an adequately controlled solution.

3.4 Derivation of the adjoint OCS formulation

It is common in engineering applications that the sensitivity of the function of interest is required with respect to multiple parameters. Typically, this is achieved using the adjoint approach. To derive the adjoint of OCS, additional Lagrange multipliers, $\hat{\boldsymbol{\lambda}}(t) \in \mathbb{R}^{n_{\hat{\lambda}}}$, $\hat{\mathbf{v}}(t) \in \mathbb{R}^{n_{\hat{v}}}$, $\hat{\mathbf{q}}(t) \in \mathbb{R}^{n_{\hat{q}}}$, $\hat{\eta}(t) \in \mathbb{R}$ and $\hat{\omega}(t) \in \mathbb{R}$, one for each optimality condition in Equation (3.8), are introduced. These, again, allow the incorporation of the optimality conditions, Equation (3.8), into Equation (3.10), through the addition of

zero, which results in

$$\begin{aligned}
\frac{\mathrm{d}\bar{J}}{\mathrm{d}p} = \int_{t_s}^{t_f} \frac{1}{T}\left\langle \frac{\partial J(\mathbf{u}(t,p),p)}{\partial \mathbf{u}(t,p)}, \mathbf{v}(t)\right\rangle + \frac{1}{T}\eta(t)\left(J(\mathbf{u}(t,p),p)-\bar{J}\right) + \\
\frac{1}{T}\frac{\partial J(\mathbf{u}(t,p),p)}{\partial p} + \\
\left\langle \hat{\boldsymbol{\lambda}}(t), \frac{\mathrm{d}\mathbf{v}(t)}{\mathrm{d}t} - \frac{\partial \mathbf{f}(\mathbf{u}(t,p),p)}{\partial \mathbf{u}(t,p)}\mathbf{v}(t) - \frac{\partial \mathbf{f}(\mathbf{u}(t,p),p)}{\partial p} - \eta(t)\mathbf{f}(\mathbf{u}(t,p),p) - \mathbf{q}(t)\right\rangle + \\
\left\langle \hat{\mathbf{v}}(t), -\frac{\mathrm{d}\boldsymbol{\lambda}(t)}{\mathrm{d}t} - \frac{\partial \mathbf{f}(\mathbf{u}(t,p),p)}{\partial \mathbf{u}(t,p)}^{\dagger}\boldsymbol{\lambda}(t) + 2\mathbf{v}(t) + \omega(t)\mathbf{f}(\mathbf{u}(t,p),p)\right\rangle + \\
\left\langle \hat{\mathbf{q}}(t), 2\alpha\mathbf{q}(t) - \boldsymbol{\lambda}(t)\right\rangle + \\
\hat{\omega}(t)\left\langle \mathbf{f}(\mathbf{u}(t,p),p), \mathbf{v}(t)\right\rangle - \hat{\eta}(t)\left\langle \mathbf{f}(\mathbf{u}(t,p),p), \boldsymbol{\lambda}(t)\right\rangle \mathrm{d}t.
\end{aligned} \tag{3.29}$$

Integration by parts of Equation (3.29) and grouping terms in $\mathbf{v}(t)$, $\mathbf{q}(t)$, $\boldsymbol{\lambda}(t)$, $\omega(t)$ and $\eta(t)$ leads to

$$\begin{aligned}
\frac{\mathrm{d}\bar{J}}{\mathrm{d}p} = \int_{t_s}^{t_f} \frac{1}{T}\frac{\partial J(\mathbf{u}(t,p),p)}{\partial p} - \left\langle \frac{\partial \mathbf{f}(\mathbf{u}(t,p),p)}{\partial p}, \hat{\boldsymbol{\lambda}}(t)\right\rangle + \\
\left\langle \mathbf{v}(t), \frac{1}{T}\frac{\partial J(\mathbf{u}(t,p),p)}{\partial \mathbf{u}(t,p)} - \frac{\mathrm{d}\hat{\boldsymbol{\lambda}}(t)}{\mathrm{d}t} - \frac{\partial \mathbf{f}(\mathbf{u}(t,p),p)}{\partial \mathbf{u}(t,p)}^{\dagger}\hat{\boldsymbol{\lambda}}(t) + 2\hat{\mathbf{v}}(t) + \hat{\omega}(t)\mathbf{f}(\mathbf{u}(t,p),p)\right\rangle + \\
\left\langle \boldsymbol{\lambda}(t), \frac{\mathrm{d}\hat{\mathbf{v}}(t)}{\mathrm{d}t} - \frac{\partial \mathbf{f}(\mathbf{u}(t,p),p)}{\partial \mathbf{u}(t,p)}\hat{\mathbf{v}}(t) - \hat{\eta}(t)\mathbf{f}(\mathbf{u}(t,p),p) - \hat{\mathbf{q}}(t)\right\rangle + \\
\left\langle \mathbf{q}(t), 2\alpha\hat{\mathbf{q}}(t) - \hat{\boldsymbol{\lambda}}(t)\right\rangle + \\
\eta(t)\left(\frac{1}{T}\left(J(\mathbf{u}(t,p),p)-\bar{J}\right) - \left\langle \hat{\boldsymbol{\lambda}}(t), \mathbf{f}(\mathbf{u}(t,p),p)\right\rangle\right) + \\
\omega(t)\left\langle \hat{\mathbf{v}}(t), \mathbf{f}(\mathbf{u}(t,p),p)\right\rangle \mathrm{d}t + \left\langle \hat{\boldsymbol{\lambda}}(t), \mathbf{v}(t)\right\rangle\Big|_{t_s}^{t_f} + \left\langle \boldsymbol{\lambda}(t), \hat{\mathbf{v}}(t)\right\rangle\Big|_{t_s}^{t_f}.
\end{aligned} \tag{3.30}$$

By careful selection of the terms in Equation (3.30) to be zero, one removes the explicit calculation of $\mathbf{v}(t)$, $\mathbf{q}(t)$, $\boldsymbol{\lambda}(t)$, $\omega(t)$ and $\eta(t)$ and obtains the following adjoint optimality conditions

$$\mathbf{0} = \frac{\mathrm{d}\hat{\mathbf{v}}(t)}{\mathrm{d}t} - \frac{\partial \mathbf{f}(\mathbf{u}(t,p),p)}{\partial \mathbf{u}(t,p)}\hat{\mathbf{v}}(t) - \hat{\eta}(t)\mathbf{f}(\mathbf{u}(t,p),p) - \hat{\mathbf{q}}(t), \tag{3.31a}$$

$$\mathbf{0} = \frac{1}{T}\frac{\partial J(\mathbf{u}(t,p),p)}{\partial \mathbf{u}(t,p)} - \frac{\mathrm{d}\hat{\boldsymbol{\lambda}}(t)}{\mathrm{d}t} - \frac{\partial \mathbf{f}(\mathbf{u}(t,p),p)}{\partial \mathbf{u}(t,p)}^{\dagger}\hat{\boldsymbol{\lambda}}(t) + 2\hat{\mathbf{v}}(t) + \hat{\omega}(t)\mathbf{f}(\mathbf{u}(t,p),p), \tag{3.31b}$$

$$\mathbf{0} = 2\alpha\hat{\mathbf{q}}(t) - \hat{\boldsymbol{\lambda}}(t), \tag{3.31c}$$

$$0 = \left\langle \hat{\mathbf{v}}(t), \mathbf{f}(\mathbf{u}(t,p),p)\right\rangle, \tag{3.31d}$$

$$0 = \frac{1}{T}\left(J(\mathbf{u}(t,p),p)-\bar{J}\right) - \left\langle \hat{\boldsymbol{\lambda}}(t), \mathbf{f}(\mathbf{u}(t,p),p)\right\rangle. \tag{3.31e}$$

Finally, the remaining terms that are non-zero from Equation (3.30) lead to the adjoint sensitivity equation

$$\frac{\mathrm{d}\bar{J}}{\mathrm{d}p} = \int_{t_s}^{t_f} \frac{1}{T}\frac{\partial J(\mathbf{u}(t,p),p)}{\partial p} - \left\langle \frac{\partial \mathbf{f}(\mathbf{u}(t,p),p)}{\partial p}, \hat{\boldsymbol{\lambda}}(t) \right\rangle \mathrm{d}t. \tag{3.32}$$

Once $\hat{\boldsymbol{\lambda}}(t)$ has been found, it is trivial to modify Equation (3.32) for multiple parameters.

There is still some reliance on $\mathbf{v}(t)$ and $\boldsymbol{\lambda}(t)$ and as in the tangent OCS formulation there are still some free variables, $\hat{\eta}(t)$ and $\hat{\omega}(t)$, that require constraining. Following a similar procedure of constraints to that presented in the tangent OCS formulation, $\left\langle \hat{\boldsymbol{\lambda}}(t), \mathbf{v}(t) \right\rangle\Big|_{t_s}^{t_f} = 0$ and $\langle \boldsymbol{\lambda}(t), \hat{\mathbf{v}}(t) \rangle|_{t_s}^{t_f} = 0$, leads to $\hat{\mathbf{v}}(t_s) = \mathbf{0}$ and

$$\hat{\boldsymbol{\lambda}}(t_f) = \frac{1}{T}\frac{J(\mathbf{u}(t_f,p),p) - \bar{J}}{\langle \mathbf{f}(\mathbf{u}(t_f,p),p), \mathbf{f}(\mathbf{u}(t_f,p),p) \rangle}\mathbf{f}(\mathbf{u}(t_f,p),p),$$

as the initial and terminal constraints for Equations (3.31a) and (3.31b), respectively. The closed form expressions for $\hat{\eta}(t)$ and $\hat{\omega}(t)$, using a similar procedure to their tangent counterparts, result in

$$\hat{\mathbf{v}}(t) = \hat{\mathbf{v}}'(t) - \frac{\langle \hat{\mathbf{v}}'(t), \mathbf{f}(\mathbf{u}(t,p),p) \rangle}{\langle \mathbf{f}(\mathbf{u}(t,p),p), \mathbf{f}(\mathbf{u}(t,p),p) \rangle}\mathbf{f}(\mathbf{u}(t,p),p).$$

and

$$\hat{\boldsymbol{\lambda}}(t) = \hat{\boldsymbol{\lambda}}'(t) - \frac{\left\langle \hat{\boldsymbol{\lambda}}'(t), \mathbf{f}(\mathbf{u}(t,p),p) \right\rangle}{\langle \mathbf{f}(\mathbf{u}(t,p),p), \mathbf{f}(\mathbf{u}(t,p),p) \rangle}\mathbf{f}(\mathbf{u}(t,p),p) + \frac{1}{T}\frac{J(\mathbf{u}(t,p),p) - \bar{J}}{\langle \mathbf{f}(\mathbf{u}(t,p),p), \mathbf{f}(\mathbf{u}(t,p),p) \rangle}\mathbf{f}(\mathbf{u}(t,p),p).$$

Details of these derivations can be found in Appendices C and D, respectively. The approach for solving the first order optimality conditions, section 3.3, are equally viable for the adjoint optimality conditions, Equation (3.31), but are not presented here for brevity.

3.5 An alternative derivation for adjoint OCS

This section shows that directly controlling the unstable and unbounded adjoint equation produces an identical set of optimality conditions to that presented in section 3.4. First, the unbounded and unstable adjoint equation is found. Let the Lagrange multipliers $\hat{\boldsymbol{\lambda}}(t) \in \mathbb{R}^{n_{\hat{\lambda}}}$ and $\hat{\omega}(t) \in \mathbb{R}$ be utilised to incorporate

Equation (3.3) and $\langle \mathbf{v}(t), \mathbf{f}(\mathbf{u}(t,p),p)\rangle = 0$ into Equation (3.10) which results in

$$\begin{aligned}\frac{\mathrm{d}\bar{J}}{\mathrm{d}p} = \int_{t_s}^{t_f} \frac{1}{T}\left\langle \frac{\partial J(\mathbf{u}(t,p),p)}{\partial \mathbf{u}(t,p)}, \mathbf{v}(t)\right\rangle + \frac{1}{T}\frac{\partial J(\mathbf{u}(t,p),p)}{\partial p} + \\ \frac{1}{T}\eta(t)(J(\mathbf{u}(t,p),p)-\bar{J}) + \\ \left\langle \hat{\boldsymbol{\lambda}}(t), \frac{\mathrm{d}\mathbf{v}(t)}{\mathrm{d}t} - \frac{\partial \mathbf{f}(\mathbf{u}(t,p),p)}{\partial \mathbf{u}(t,p)}\mathbf{v}(t) - \frac{\partial \mathbf{f}(\mathbf{u}(t,p),p)}{\partial p} - \eta(t)\mathbf{f}(\mathbf{u}(t,p),p)\right\rangle + \\ \hat{\omega}(t)\left\langle \mathbf{f}(\mathbf{u}(t,p),p), \mathbf{v}(t)\right\rangle \mathrm{d}t.\end{aligned} \tag{3.33}$$

Again, performing integration by parts and grouping terms in $\mathbf{v}(t)$ and $\eta(t)$ results in

$$\begin{aligned}\frac{\mathrm{d}\bar{J}}{\mathrm{d}p} = \int_{t_s}^{t_f} \frac{1}{T}\frac{\partial J(\mathbf{u}(t,p),p)}{\partial p} - \left\langle \frac{\partial \mathbf{f}(\mathbf{u}(t,p),p)}{\partial p}, \hat{\boldsymbol{\lambda}}(t)\right\rangle + \\ \left\langle \mathbf{v}(t), \frac{1}{T}\frac{\partial J(\mathbf{u}(t,p),p)}{\partial \mathbf{u}(t,p)} - \frac{\mathrm{d}\hat{\boldsymbol{\lambda}}(t)}{\mathrm{d}t} - \frac{\partial \mathbf{f}(\mathbf{u}(t,p),p)}{\partial \mathbf{u}(t,p)}^{\dagger}\hat{\boldsymbol{\lambda}}(t) + \hat{\omega}(t)\mathbf{f}(\mathbf{u}(t,p),p)\right\rangle + \\ \eta(t)\left(\frac{1}{T}(J(\mathbf{u}(t,p),p)-\bar{J}) - \left\langle \hat{\boldsymbol{\lambda}}(t), \mathbf{f}(\mathbf{u}(t,p),p)\right\rangle\right)\mathrm{d}t + \left\langle \hat{\boldsymbol{\lambda}}(t), \mathbf{v}(t)\right\rangle\Big|_{t_s}^{t_f}.\end{aligned} \tag{3.34}$$

Careful selection of the Lagrange multiplier terms in Equation (3.34) removes the explicit calculation of $\mathbf{v}(t)$ and $\eta(t)$ and results in the adjoint co-state equation and adjoint co-state orthogonality constraint

$$\mathbf{0} = \frac{1}{T}\frac{\partial J(\mathbf{u}(t,p),p)}{\partial \mathbf{u}(t,p)} - \frac{\mathrm{d}\hat{\boldsymbol{\lambda}}(t)}{\mathrm{d}t} - \frac{\partial \mathbf{f}(\mathbf{u}(t,p),p)}{\partial \mathbf{u}(t,p)}^{\dagger}\hat{\boldsymbol{\lambda}}(t) + \hat{\omega}(t)\mathbf{f}(\mathbf{u}(t,p),p), \tag{3.35}$$

and

$$0 = \frac{1}{T}(J(\mathbf{u}(t,p),p)-\bar{J}) - \left\langle \hat{\boldsymbol{\lambda}}(t), \mathbf{f}(\mathbf{u}(t,p),p)\right\rangle. \tag{3.36}$$

Again, setting $\left\langle \hat{\boldsymbol{\lambda}}(t), \mathbf{v}(t)\right\rangle\Big|_{t_s}^{t_f} = 0$ and using Equation (3.36) leads to the terminal condition

$$\hat{\boldsymbol{\lambda}}(t_f) = \frac{1}{T}\frac{J(\mathbf{u}(t_f,p),p)-\bar{J}}{\left\langle \mathbf{f}(\mathbf{u}(t_f,p),p), \mathbf{f}(\mathbf{u}(t_f,p),p)\right\rangle}\mathbf{f}(\mathbf{u}(t_f,p),p)$$

and Equation (3.35) is solved backwards in time. Equation (3.35) shares the same behaviour as the tangent equation, Equation (3.3), in that it experiences exponential growth of perturbations and requires controlling. Introducing a control term

$\hat{\boldsymbol{\zeta}}(t) \in \mathbb{R}^{n_{\hat{\zeta}}}$ into Equation (3.35) and forming the minimisation problem results in

$$\min_{\hat{\boldsymbol{\lambda}}(t),\hat{\boldsymbol{\zeta}}(t)} \int_{t_s}^{t_f} \hat{\beta} \left\langle \hat{\boldsymbol{\lambda}}(t), \hat{\boldsymbol{\lambda}}(t) \right\rangle + \hat{\delta} \left\langle \hat{\boldsymbol{\zeta}}(t), \hat{\boldsymbol{\zeta}}(t) \right\rangle \mathrm{d}t, \tag{3.37a}$$

$$s.t. \ \frac{\mathrm{d}\hat{\boldsymbol{\lambda}}(t)}{\mathrm{d}t} = \frac{1}{T}\frac{\partial J(\mathbf{u}(t,p),p)}{\partial \mathbf{u}(t,p)} - \frac{\partial \mathbf{f}(\mathbf{u}(t,p),p)}{\partial \mathbf{u}(t,p)}^{\intercal} \hat{\boldsymbol{\lambda}}(t) + \hat{\omega}(t)\mathbf{f}(\mathbf{u}(t,p),p) + \hat{\boldsymbol{\zeta}}(t), \tag{3.37b}$$

$$\frac{1}{T}(J(\mathbf{u}(t,p),p) - \bar{J}) - \left\langle \hat{\boldsymbol{\lambda}}(t), \mathbf{f}(\mathbf{u}(t,p),p) \right\rangle = 0, \tag{3.37c}$$

$$\hat{\boldsymbol{\lambda}}(t_f) = \frac{1}{T}\frac{J(\mathbf{u}(t_f,p),p) - \bar{J}}{\left\langle \mathbf{f}(\mathbf{u}(t_f,p),p), \mathbf{f}(\mathbf{u}(t_f,p),p) \right\rangle}\mathbf{f}(\mathbf{u}(t_f,p),p), \tag{3.37d}$$

where $\hat{\beta}$ and $\hat{\delta}$ control the relative importance of each term. As before, introducing additional Lagrange multipliers $\hat{\mathbf{v}}(t) \in \mathbb{R}^{n_\phi}$ and $\hat{\eta}(t) \in \mathbb{R}$ to incorporate Equation (3.37b) and Equation (3.37c) into Equation (3.37a) leads to the Hamiltonian, $\hat{\mathcal{H}}$, and performing integration by parts results in

$$\begin{aligned}
\hat{\mathcal{H}} = \int_{t_s}^{t_f} \hat{\beta} \left\langle \hat{\boldsymbol{\lambda}}(t), \hat{\boldsymbol{\lambda}}(t) \right\rangle + \hat{\delta} \left\langle \hat{\boldsymbol{\zeta}}(t), \boldsymbol{\zeta}(\hat{t}) \right\rangle + \\
\left\langle \hat{\boldsymbol{\lambda}}(t), \frac{\mathrm{d}\hat{\mathbf{v}}(t)}{\mathrm{d}t} - \frac{\partial \mathbf{f}(\mathbf{u}(t,p),p)}{\partial \mathbf{u}(t,p)}\hat{\mathbf{v}}(t) - \hat{\eta}(t)\mathbf{f}(\mathbf{u}(t,p),p) \right\rangle + \\
\left\langle \hat{\mathbf{v}}(t), \frac{1}{T}\frac{\partial J(\mathbf{u}(t,p),p)}{\partial \mathbf{u}(t,p)} + \hat{\omega}(t)\mathbf{f}(\mathbf{u}(t,p),p) + \hat{\boldsymbol{\zeta}}(t) \right\rangle + \\
\hat{\eta}(t)\left(\frac{1}{T}(J(\mathbf{u}(t,p),p) - \bar{J}) - \left\langle \hat{\boldsymbol{\lambda}}(t), \mathbf{f}(\mathbf{u}(t,p),p) \right\rangle\right)\mathrm{d}t + \left\langle \hat{\boldsymbol{\lambda}}(t), \hat{\mathbf{v}}(t) \right\rangle\Big|_{t_s}^{t_f}.
\end{aligned} \tag{3.38}$$

Pontryagin's minimisation principle defines the minimum of Equation (3.37) to be when all partial derivatives of $\hat{\mathcal{H}}$ with respect to $\hat{\mathbf{v}}(t)$, $\hat{\boldsymbol{\lambda}}(t)$, $\hat{\boldsymbol{\zeta}}(t)$, $\hat{\omega}(t)$ and $\hat{\eta}(t)$ are zero. This leads to the first order adjoint optimality conditions

$$\frac{\partial \hat{\mathcal{H}}}{\partial \hat{\boldsymbol{\lambda}}(t)} = \mathbf{0} = \frac{\mathrm{d}\hat{\mathbf{v}}(t)}{\mathrm{d}t} - \frac{\partial \mathbf{f}(\mathbf{u}(t,p),p)}{\partial \mathbf{u}(t,p)}\hat{\mathbf{v}}(t) - \hat{\eta}(t)\mathbf{f}(\mathbf{u}(t,p),p) + 2\hat{\beta}\hat{\boldsymbol{\lambda}}(t), \tag{3.39a}$$

$$\begin{aligned}
\frac{\partial \hat{\mathcal{H}}}{\partial \hat{\mathbf{v}}(t)} = \mathbf{0} = \frac{1}{T}\frac{\partial J(\mathbf{u}(t,p),p)}{\partial \mathbf{u}(t,p)} - \frac{\mathrm{d}\hat{\boldsymbol{\lambda}}(t)}{\mathrm{d}t} - \frac{\partial \mathbf{f}(\mathbf{u}(t,p),p)}{\partial \mathbf{u}(t,p)}^{\intercal} \hat{\boldsymbol{\lambda}}(t) + \\
\hat{\omega}(t)\mathbf{f}(\mathbf{u}(t,p),p) + \hat{\boldsymbol{\zeta}}(t),
\end{aligned} \tag{3.39b}$$

$$\frac{\partial \hat{\mathcal{H}}}{\partial \hat{\boldsymbol{\zeta}}(t)} = \mathbf{0} = 2\hat{\delta}\hat{\boldsymbol{\zeta}}(t) + \hat{\mathbf{v}}(t), \tag{3.39c}$$

$$\frac{\partial \hat{\mathcal{H}}}{\partial \hat{\omega}(t)} = 0 = \left\langle \mathbf{f}(\mathbf{u}(t,p),p), \hat{\mathbf{v}}(t) \right\rangle, \tag{3.39d}$$

$$\frac{\partial \hat{\mathcal{H}}}{\partial \hat{\eta}(t)} = 0 = \frac{1}{T}(J(\mathbf{u}(t,p),p) - \bar{J}) - \left\langle \hat{\boldsymbol{\lambda}}(t), \mathbf{f}(\mathbf{u}(t,p),p) \right\rangle. \tag{3.39e}$$

Selecting $\hat{\delta} = -\frac{1}{4}$ and substituting Equation (3.39c) into Equation (3.39b) to eliminate $\hat{\boldsymbol{\zeta}}(t)$ leads to Equation (3.31b). Similarly, selecting $\hat{\beta} = -\frac{1}{4\alpha}$ in Equation (3.39a) leads to the same equation when Equation (3.31c) is substituted into Equation (3.31a) to

eliminate $\mathbf{q}(t)$. Again, $\hat{\eta}(t)$ and $\hat{\omega}(t)$ can be handled as in Appendices C and D respectively. Therefore, it can be concluded that taking the adjoint of the minimisation problem or minimisation of the adjoint problem result in methods that are identical, given careful selection of $\hat{\beta}$ and $\hat{\delta}$.

3.6 Decomposition of the time horizon into segments

A matrix-free method for solving the optimality conditions for the tangent OCS formulation was presented in section 3.3 where the time horizon was considered as a whole. The runtimes of these standard algorithms can be large, Ref. [52], and, therefore, there has been a large development in parallel-in-time or time domain decomposition methods for optimal control problems, Refs. [37, 38, 42, 52, 53, 60, 71, 76, 82, 83, 122]. Further to this, the splitting of the time horizon into segments acts to condition the system, Ref. [75], where the convergence rates of these algorithms are related to the condition number of the linear operator. A solution of the tangent equation still exhibits exponential growth but is limited to the growth in one segment. The growth is reduced due to the smaller segment time resulting in better conditioning.

One further benefit for splitting the time horizon into segments is that, for large systems, the method outlined in section 3.2 may require more memory than the compute node has. Therefore, the time domain is split into segments so that the memory requirements are reduced and each segment can be solved on a separate compute node.

The splitting, Ref. [37, 38, 42, 60, 71], is derived for the tangent OCS formulation in this section. However, this is easily modified for the equations derived for the adjoint OCS formulation, section 3.4. Various alternatives to Refs. [37, 38, 42, 60, 71] are available. One alternative method is the single shooting formulation Ref [25], which estimates the initial condition for the tangent and co-state equation that satisfy the terminal condition on the co-state. This shooting approach is also undertaken on multiple time segments, Ref. [24], which is the single shooting method but reformulated on multiple segments with continuity conditions applied between consecutive segments. This multiple shooting approach is also undertaken utilising gradient descent, Ref. [1], to impose continuity between consecutive segments. Finally, a receding horizon optimal control, Ref. [55], formulation which approximates the long time horizon control by solving iteratively smaller finite horizon control problems.

The time horizon (t_s, t_f) is split into N equal segments where each has a local time span, (t_j, t_{j+1}), $j = 0, 1, \ldots, N-1$ and $t_s = t_0 < t_1 < \ldots < t_{N-1} < t_N = t_f$. Next, a locally defined tangent solution $\mathbf{v}_j(t) \in \mathbb{R}^{n_v}$ and control $\mathbf{q}_j(t) \in \mathbb{R}^{n_q}$ on each segment j

are introduced. For this splitting to be identical to the method presented in section 3.2, continuity in both control and tangent solutions between consecutive segments is required. This results in the following constraints $\mathbf{v}_{j-1}(t_j) = \mathbf{v}_j(t_j)$ for $j = 1, \ldots, N-1$ and $\mathbf{q}_{j-1}(t_j) = \mathbf{q}_j(t_j)$ for $j = 1, \ldots, N-1$. A graphical representation of this can be seen in Figure 3.1. These conditions leads to the following minimisation problem

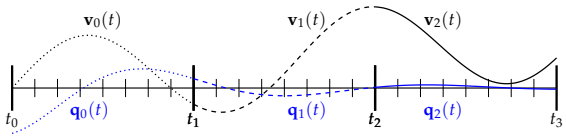

FIGURE 3.1: Example time domain decomposition where the dotted lines represent the solution in segment 0, dashed in segment 1 and solid segment 2. Black solutions represent the tangent solution and blue the control.

$$\min_{\mathbf{v}_j(t), \mathbf{q}_j(t)} \sum_{j=0}^{N-1} \int_{t_j}^{t_{j+1}} \left\langle \mathbf{v}_j(t), \mathbf{v}_j(t) \right\rangle + \alpha \left\langle \mathbf{q}_j(t), \mathbf{q}_j(t) \right\rangle \mathrm{d}t \tag{3.40a}$$

$$\text{s.t.} \quad \frac{\mathrm{d}\mathbf{v}_j(t)}{\mathrm{d}t} = \frac{\partial \mathbf{f}(\mathbf{u}(t,p),p)}{\partial \mathbf{u}(t,p)} \mathbf{v}_j(t) + \frac{\partial \mathbf{f}(\mathbf{u}(t,p),p)}{\partial p} + \eta_j(t) \mathbf{f}(\mathbf{u}(t,p),p) + \mathbf{q}_j(t) \quad j = 0, 1, \ldots, N-1, \tag{3.40b}$$

$$\left\langle \mathbf{v}_j(t), \mathbf{f}(\mathbf{u}(t,p),p) \right\rangle = 0 \quad j = 0, 1, \ldots, N-1, \tag{3.40c}$$

$$\mathbf{v}(t_s) = \mathbf{0}, \tag{3.40d}$$

$$\mathbf{v}_{j-1}(t_j) = \mathbf{v}_j(t_j) \quad j = 1, \ldots, N-1, \tag{3.40e}$$

$$\mathbf{q}_{j-1}(t_j) = \mathbf{q}_j(t_j) \quad j = 1, \ldots, N-1. \tag{3.40f}$$

The Hamiltonian, $\mathcal{H}$, for this minimisation problem is formed through the introduction of locally defined Lagrange multipliers $\boldsymbol{\lambda}_j(t) \in \mathbb{R}^{n_\lambda}$ for $j = 0, 1, \ldots, N-1$ for the tangent equation, $\omega_j(t) \in \mathbb{R}$ for $j = 0, 1, \ldots, N-1$ for the tangent orthogonality constraint, $\boldsymbol{\kappa}_j \in \mathbb{R}^{n_\kappa}$ for $j = 1, \ldots, N-1$ for the tangent continuity constraints, and $\boldsymbol{\iota}_j \in \mathbb{R}^{n_\iota}$ for $j = 1, \ldots, N-1$ for the control continuity constraint. For optimality the derivatives of the Hamiltonian with respect to $\mathbf{v}_j(t)$, $\boldsymbol{\lambda}_j(t)$, $\mathbf{q}_j(t)$, $\eta_j(t)$, $\omega_j(t)$, $\boldsymbol{\iota}_j$ and $\boldsymbol{\kappa}_j$, using Pontryagin's minimisation principle, are zero. This leads to the

set of first order optimality conditions

$$\frac{\partial \mathcal{H}}{\partial \boldsymbol{\lambda}_j(t)} = \mathbf{0} = \frac{\mathrm{d}\mathbf{v}_j(t)}{\mathrm{d}t} - \frac{\partial \mathbf{f}(\mathbf{u}(t,p),p)}{\partial \mathbf{u}(t,p)}\mathbf{v}_j(t) - \frac{\partial \mathbf{f}(\mathbf{u}(t,p),p)}{\partial p} - \eta_j(t)\mathbf{f}(\mathbf{u}(t,p),p) - \mathbf{q}_j(t) \quad j = 0,1,\ldots,N-1, \tag{3.41a}$$

$$\frac{\partial \mathcal{H}}{\partial \mathbf{v}_j(t)} = \mathbf{0} = -\frac{\mathrm{d}\boldsymbol{\lambda}_j(t)}{\mathrm{d}t} - \frac{\partial \mathbf{f}(\mathbf{u}(t,p),p)}{\partial \mathbf{u}(t,p)}^{\dagger} \boldsymbol{\lambda}_j(t) + 2\mathbf{v}_j(t) + \omega_j(t)\mathbf{f}(\mathbf{u}(t,p),p) \quad j = 0,1,\ldots,N-1, \tag{3.41b}$$

$$\frac{\partial \mathcal{H}}{\partial \mathbf{q}_j(t)} = \mathbf{0} = 2\alpha\mathbf{q}_j(t) - \boldsymbol{\lambda}_j(t) \quad j = 0,1,\ldots,N-1, \tag{3.41c}$$

$$\frac{\partial \mathcal{H}}{\partial \omega_j(t)} = 0 = \left\langle \mathbf{f}(\mathbf{u}(t,p),p), \mathbf{v}_j(t) \right\rangle \quad j = 0,1,\ldots,N-1, \tag{3.41d}$$

$$\frac{\partial \mathcal{H}}{\partial \eta_j(t)} = 0 = \left\langle \boldsymbol{\lambda}_j(t), \mathbf{f}(\mathbf{u}(t,p),p) \right\rangle \quad j = 0,1,\ldots,N-1, \tag{3.41e}$$

$$\frac{\partial \mathcal{H}}{\partial \boldsymbol{\kappa}_j} = \mathbf{0} = \mathbf{v}_{j-1}(t_j) - \mathbf{v}_j(t_j) \quad j = 1,\ldots,N-1, \tag{3.41f}$$

$$\frac{\partial \mathcal{H}}{\partial \boldsymbol{\iota}_j} = \mathbf{0} = \mathbf{q}_{j-1}(t_j) - \mathbf{q}_j(t_j) \quad j = 1,\ldots,N-1. \tag{3.41g}$$

The control continuity constraint, Equation (3.41g), can be cast onto the co-state through the use of the control equation, Equation (3.41c), resulting in

$$\mathbf{0} = \boldsymbol{\lambda}_{j-1}(t_j) - \boldsymbol{\lambda}_j(t_j) \quad j = 1,\ldots,N-1. \tag{3.42}$$

The initial condition for the tangent equation in segment 0 is $\mathbf{v}(t_s) = \mathbf{v}_0(t_0) = \mathbf{0}$ and the terminal condition for the co-state equation in segment $N-1$ is $\boldsymbol{\lambda}(t_f) = \boldsymbol{\lambda}_{N-1}(t_N) = \mathbf{0}$. Again, removing the explicit computation of $\eta_j(t)$ using Equation (3.41d) results in

$$\mathbf{v}_j(t) = \mathbf{v}'_j(t) - \frac{\left\langle \mathbf{v}'_j(t), \mathbf{f}(\mathbf{u}(t,p),p) \right\rangle}{\left\langle \mathbf{f}(\mathbf{u}(t,p),p), \mathbf{f}(\mathbf{u}(t,p),p) \right\rangle}\mathbf{f}(\mathbf{u}(t,p),p). \tag{3.43}$$

Similarly, removal of the explicit computation of $\omega_j(t)$ using Equation (3.41e) results in

$$\boldsymbol{\lambda}_j(t) = \boldsymbol{\lambda}'_j(t) - \frac{\left\langle \boldsymbol{\lambda}'_j(t), \mathbf{f}(\mathbf{u}(t,p),p) \right\rangle}{\left\langle \mathbf{f}(\mathbf{u}(t,p),p), \mathbf{f}(\mathbf{u}(t,p),p) \right\rangle}\mathbf{f}(\mathbf{u}(t,p),p). \tag{3.44}$$

The sensitivity equation, Equation (3.10), is an integral over the whole time horizon with an additional modification for the time dilation therm, $\eta(t)$. Due to performing the time domain decomposition the sensitivity equation is decomposed into the sum of integrals on each segment, This is because the solution may not be exactly continuous between segments and small discontinuities could be present due to how accurately the optimality conditions are solved. This leads to the following sensitivity

equation

$$\frac{\mathrm{d}\bar{J}}{\mathrm{d}p} = \frac{1}{T}\sum_{j=0}^{N-1}\int_{t_j}^{t_{j+1}} \left\langle \frac{\partial J(\mathbf{u}(t,p),p)}{\partial \mathbf{u}(t,p)}, \mathbf{v}_j'(t) \right\rangle + \frac{\partial J(\mathbf{u}(t,p),p)}{\partial p}\mathrm{d}t + \frac{1}{T}\sum_{j=0}^{N-1} \frac{\left\langle \mathbf{v}'(t_{j+1}), \mathbf{f}(\mathbf{u}(t_{j+1},p),p)\right\rangle}{\left\langle \mathbf{f}(\mathbf{u}(t_{j+1},p),p), \mathbf{f}(\mathbf{u}(t_{j+1},p),p)\right\rangle} \left(\bar{J} - J(\mathbf{u}(t_{j+1},p),p)\right). \tag{3.45}$$

The derivation of this equation is not reported here but further details of this derivation can be found in Appendix C of Ref. [19].

3.7 A matrix-free method for solving the optimality conditions for time domain decomposition

The matrix-free methods used in section 3.3 can also be used for the first order optimality conditions, Equation 3.41. The previous work on the matrix-free methods for the time domain decomposition has been undertaken on advection-diffusion problems and heat equations, Refs. [37, 38, 60]. The systems that are being solved here are linear and unstable. The authors of Refs. [37, 38, 60] make no discussion on the impact of these methods for unstable systems. Therefore, it is unclear if the unstable system causes any additional requirements on the length of the segments and the impact the growth of the solution in the time horizon has on convergence of these methods. To aid in the distributed computation, the initial values of $\mathbf{v}_j(t_j) = \mathbf{0}$ and $\boldsymbol{\lambda}_{j-1}(t_j) = \mathbf{0}$ for $j = 1, \ldots, N-1$ are used. Further, $\mathbf{q}_j(t) = \mathbf{0}$ for $j = 0, 1, \ldots, N-1$ is used. The local tangent solution is found by marching Equation (3.41a) forwards in time from t_j to t_{j+1} using the initial condition $\mathbf{v}_j(t_j)$ for $j = 0, 1, \ldots, N-1$, the control $\mathbf{q}_j(t)$ and making use of Equation (3.43) to remove the explicit computation of $\eta_j(t)$. Using this approach ensures that the time domain decomposition optimality constraints Equation (3.41a) and Equation (3.41d) are satisfied. The same procedure is used for the co-state solution by solving Equation (3.41b) backwards in time from t_{j+1} to t_j using the terminal condition $\boldsymbol{\lambda}_j(t_{j+1})$ for $j = 0, 1, \ldots, N-1$, the tangent solution $\mathbf{v}_j(t)$ and Equation (3.44) to remove the explicit calculation of $\omega_j(t)$. Again, this approach ensures that the constraints Equation (3.41b) and Equation (3.41e) are satisfied. Therefore, the only constraints not satisfied are the control equation, Equation (3.41c), the continuity constraint on the tangent solution, Equation (3.41f), and the continuity on the control solution, Equation (3.41g).

In practice, substitution of Equation (3.41g) for Equation (3.42) is undertaken. With this approach the unknowns are

$$\mathbf{x} = \left(\mathbf{v}_1(t_1), \mathbf{q}_0(t), \ldots, \mathbf{v}_{j+1}(t_{j+1}), \mathbf{q}_j(t), \boldsymbol{\lambda}_{j-1}(t_j), \ldots, \mathbf{q}_{N-1}(t), \boldsymbol{\lambda}_{N-2}(t_{N-1})\right)^T$$

Making use of the analytical form of the tangent and co-state solutions leads to

$$\begin{pmatrix} \frac{\partial \mathcal{H}}{\partial \boldsymbol{\kappa}_0} \\ \frac{\partial \mathcal{H}}{\partial \mathbf{q}_0(t)} \\ \vdots \\ \frac{\partial \mathcal{H}}{\partial \boldsymbol{\kappa}_j} \\ \frac{\partial \mathcal{H}}{\partial \mathbf{q}_j(t)} \\ \frac{\partial \mathcal{H}}{\partial \boldsymbol{\iota}_j} \\ \vdots \\ \frac{\partial \mathcal{H}}{\partial \mathbf{q}_{N-1}(t)} \\ \frac{\partial \mathcal{H}}{\partial \boldsymbol{\iota}_{N-1}} \end{pmatrix} = \mathbf{H}\mathbf{x} = \begin{pmatrix} \mathbf{v}_1(t_1) - \mathbf{v}_0(t_1) \\ 2\alpha\mathbf{q}_0(t) - \boldsymbol{\lambda}_0(t) \\ \vdots \\ \mathbf{v}_{j+1}(t_{j+1}) - \mathbf{v}_j(t_{j+1}) \\ 2\alpha\mathbf{q}_j(t) - \boldsymbol{\lambda}_j(t) \\ \boldsymbol{\lambda}_{j-1}(t_j) - \boldsymbol{\lambda}_j(t_j) \\ \vdots \\ 2\alpha\mathbf{q}_{N-1}(t) - \boldsymbol{\lambda}_{N-1}(t) \\ \boldsymbol{\lambda}_{N-2}(t_{N-1}) - \boldsymbol{\lambda}_{N-1}(t_{N-1}) \end{pmatrix} = \begin{pmatrix} \mathbf{0} \\ \mathbf{0} \\ \vdots \\ \mathbf{0} \\ \mathbf{0} \\ \mathbf{0} \\ \vdots \\ \mathbf{0} \\ \mathbf{0} \end{pmatrix}. \tag{3.46}$$

Using a similar approach to that presented in section 3.3 it can be shown that

$$\mathbf{H}\mathbf{x} = \mathbf{F}\mathbf{x} - \mathbf{c} = \mathbf{0}, \tag{3.47}$$

where the linear operator, $\mathbf{F}$, is block-tridiagonal,

$$\mathbf{F} = \begin{pmatrix} \mathbf{F}_{0,0} & \mathbf{F}_{0,1} & & & & & & \\ \mathbf{F}_{1,0} & \ddots & & & & & & \\ & & \mathbf{F}_{j,j-1} & \mathbf{F}_{j,j} & \mathbf{F}_{j,j+1} & & & \\ & & & & & \ddots & & \mathbf{F}_{N-2,N-1} \\ & & & & & & \mathbf{F}_{N-1,N-2} & \mathbf{F}_{N-1,N-1} \end{pmatrix}, \tag{3.48}$$

and block $\mathbf{F}_{j,j}$ is

$$\mathbf{F}_{j,j} = \begin{pmatrix} \mathbf{I} & -\mathbf{B}_j & 0 \\ 0 & 2\alpha\mathbf{I} + \mathbf{C}_j\left(2\mathbf{B}_j\right) & 0 \\ 0 & \mathbf{C}_j\left(2\mathbf{B}_j\right) & \mathbf{I} \end{pmatrix}, \tag{3.49}$$

where $\mathbf{B}$ and $\mathbf{C}$ are defined as in section 3.3 and the subscript $\square_j$ denotes the operator $\square$ on segment j. The full structure of $\mathbf{F}$ and $\mathbf{c}$ can be found in Appendix E.

The system, Equation (3.47), cannot be solved using conjugate gradient methods because conjugate gradient methods are used on systems whose operators are positive-definite, Refs. [39, 48, 117], and the operator generated by the time domain decomposition is symmetric and indefinite, Refs. [38, 60]. Therefore, GMRES, Refs. [106, 107, 116], a generic linear system solver is used for solving the linear system generated. Algorithm 3 is a matrix-free method for computing $\mathbf{H}\mathbf{x}$ which can then be utilised for computing $\mathbf{c}$ by computing $\mathbf{H}\mathbf{x}$ with $\mathbf{x} = \mathbf{0}$. $\mathbf{F}\mathbf{x}$ is found by computing $\mathbf{H}\mathbf{x}$ and adding $\mathbf{c}$. Algorithm 4 is used for finding the optimal control, tangent and co-state solutions. Parallel computation can be leveraged using this method as all the information required for each segment is contained within $\mathbf{x}$ and,

Algorithm 3: A matrix-free method for the calculation of $\mathbf{Hx}$.

Input: $\mathbf{x}$
Output: $\mathbf{Hx}$

for $j = 0, 1, \ldots, N-1$ **do**
  $\mathbf{v}_j(t) \leftarrow$ Solve Equation (3.41a) from t_j to t_{j+1} using $\mathbf{v}_j(t_j)$ and $\mathbf{q}_j(t)$
  $\boldsymbol{\lambda}_j(t) \leftarrow$ Solve Equation (3.41b) from t_{j+1} to t_j using $\boldsymbol{\lambda}_j(t_{j+1})$ and $\mathbf{v}_j(t)$
  $\mathbf{Hx} \leftarrow 2\alpha\mathbf{q}_j(t) - \boldsymbol{\lambda}_j(t)$
for $j = 1, \ldots, N-1$ **do**
  $\mathbf{Hx} \leftarrow \mathbf{v}_{j-1}(t_j) - \mathbf{v}_j(t_j)$
  $\mathbf{Hx} \leftarrow \boldsymbol{\lambda}_{j-1}(t_j) - \boldsymbol{\lambda}_j(t_j)$

Algorithm 4: A matrix-free method for solution of the optimality conditions.

$\mathbf{c} \leftarrow -\mathbf{H0}$
$\mathbf{Fx} \leftarrow \mathbf{Hx} + \mathbf{c}$
Solve $\mathbf{Fx} = \mathbf{c}$ using GMRES to compute $\mathbf{x}$
for $j = 0, 1, \ldots, N-1$ **do**
  $\mathbf{v}_j(t) \leftarrow$ Solve Equation (3.41a) from t_j to t_{j+1} using $\mathbf{v}_j(t_j)$ and $\mathbf{q}_j(t)$
  $\boldsymbol{\lambda}_j(t) \leftarrow$ Solve Equation (3.41b) from t_{j+1} to t_j using $\boldsymbol{\lambda}_j(t_{j+1})$ and $\mathbf{v}_j(t)$

therefore, computation of the tangent and co-state solutions on each segment along with computation of the constraints between consecutive segments are not reliant on the solutions of other segments.

The main limitation with this method is that the vector of unknowns, $\mathbf{x}$, is larger than $\mathbf{q}(t)$ presented in section 3.3 due to the unknown conditions of the tangent and co-state at the segment interfaces and, therefore, does not reduce the memory limitations. One method to overcome this limitation is to store the vector $\mathbf{x}$ across compute nodes. Using this approach a parallel implementation of GMRES, see Refs. [43, 44, 134], is required for the solution of the optimality conditions. An alternative approach to remove this limitation is through using various preconditioning methods, Refs. [8, 38, 60, 71], that reduce the size of the linear system formed which can then fit on one compute node and parallel GMRES methods are not required. These preconditioning methods are presented in the following sections.

3.7.1 Jacobi preconditioning

To reduce the condition number of the system and to reduce the size of the linear system various preconditioning methods have been developed, Refs. [8, 38, 60, 71], and a benefit of these preconditioning methods is that the convergence rates are improved. Here the Jacobi approach is presented. Firstly, consider the splitting $\mathbf{F} = \mathbf{M} - \mathbf{L} - \mathbf{U}$, where $\mathbf{M}$ is the block diagonal component of $\mathbf{F}$, and $\mathbf{L}$ and $\mathbf{U}$ are the block lower and block upper components, respectively. The intuitive reasoning

behind these components is that $\mathbf{M}$ is related to the constraints $\frac{\partial \mathcal{H}}{\partial \mathbf{q}_j(t)}$, $\mathbf{L}$ is related to the constraint $\frac{\partial \mathcal{H}}{\partial \boldsymbol{\kappa}_j}$ and $\mathbf{U}$ is related to the constraint $\frac{\partial \mathcal{H}}{\partial \boldsymbol{\iota}_j}$. Inverting any of $\mathbf{M}$, $\mathbf{L}$ and $\mathbf{U}$ can be thought of as solving their respective constraints, for example inverting the diagonal blocks of $\mathbf{F}$ is equivalent to solving the optimal control problem on each segment, Ref. [60]. Utilising this splitting, the system, Equation (3.46), can be written as

$$\mathbf{F}\mathbf{x} - \mathbf{c} = \left[\mathbf{M} - (\mathbf{U} + \mathbf{L})\right]\mathbf{x} - \mathbf{c} = \mathbf{0}, \tag{3.50}$$

where left multiplication by $\mathbf{M}^{-1}$ results in

$$\left[\mathbf{I} - \mathbf{M}^{-1}(\mathbf{U} + \mathbf{L})\right]\mathbf{x} - \mathbf{M}^{-1}\mathbf{c} = \mathbf{0}. \tag{3.51}$$

Left multiplication of $\mathbf{M}^{-1}$ always satisfies the constraints $\frac{\partial \mathcal{H}}{\partial \mathbf{q}_j(t)}$ regardless of which $\mathbf{q}_j(t)$ is chosen in $\mathbf{x}$. This leaves the unknowns for the Jacobi preconditioning as

$$\mathbf{x}^{\text{Jac}} = \left(\mathbf{v}_1(t_1), \ldots, \mathbf{v}_{j+1}(t_{j+1}), \boldsymbol{\lambda}_{j-1}(t_j), \ldots, \boldsymbol{\lambda}_{N-2}(t_{N-1})\right)^T,$$

which is significantly smaller than $\mathbf{x}$ and can easily fit onto one compute node to be solved with GMRES. This results in a better conditioned linear operator which reduces the computational cost and time over the non-preconditioned system, Ref. [38]. These unknowns are the initial tangent conditions at the beginning of each segment and the co-state terminal conditions at the end of each segment. Further, the entries from $\mathbf{F}$ and $\mathbf{c}$ relating to the constraint $\frac{\partial \mathcal{H}}{\partial \mathbf{q}_j(t)}$ can be removed which leads to the simplified Jacobi preconditioned system

$$\begin{pmatrix} \frac{\partial \mathcal{H}}{\partial \boldsymbol{\kappa}_0} \\ \vdots \\ \frac{\partial \mathcal{H}}{\partial \boldsymbol{\kappa}_j} \\ \frac{\partial \mathcal{H}}{\partial \boldsymbol{\iota}_j} \\ \vdots \\ \frac{\partial \mathcal{H}}{\partial \boldsymbol{\iota}_{N-1}} \end{pmatrix} = \mathbf{H}^{\text{Jac}}\mathbf{x}^{\text{Jac}} = \begin{pmatrix} \mathbf{v}_1(t_1) - \mathbf{v}_0(t_1) \\ \vdots \\ \mathbf{v}_{j+1}(t_{j+1}) - \mathbf{v}_j(t_{j+1}) \\ \boldsymbol{\lambda}_{j-1}(t_j) - \boldsymbol{\lambda}_j(t_j) \\ \vdots \\ \boldsymbol{\lambda}_{N-2}(t_{N-1}) - \boldsymbol{\lambda}_{N-1}(t_{N-1}) \end{pmatrix} = \begin{pmatrix} \mathbf{0} \\ \vdots \\ \mathbf{0} \\ \mathbf{0} \\ \vdots \\ \mathbf{0} \end{pmatrix}. \tag{3.52}$$

Again, it can be shown that

$$\mathbf{H}^{\text{Jac}}\mathbf{x}^{\text{Jac}} = \mathbf{F}^{\text{Jac}}\mathbf{x}^{\text{Jac}} - \mathbf{c}^{\text{Jac}} = \mathbf{0}.$$

Algorithm 5 is a matrix-free method for the computation of $\mathbf{H}^{\text{Jac}}\mathbf{x}^{\text{Jac}}$. The term $\mathbf{c}^{\text{Jac}}$ is computed using $\mathbf{H}^{\text{Jac}}\mathbf{x}^{\text{Jac}}$ using zero for $\mathbf{x}^{\text{Jac}}$. Similarly, $\mathbf{F}^{\text{Jac}}\mathbf{x}^{\text{Jac}}$ is computed using $\mathbf{H}^{\text{Jac}}\mathbf{x}^{\text{Jac}}$ and adding $\mathbf{c}^{\text{Jac}}$. An algorithm for computing the optimal control, tangent and co-state solutions using Jacobi preconditioning is given Algorithm 6. One benefit of this approach is that all the optimal control problems on each segment can be solved

Algorithm 5: A matrix-free method for the calculation of $\mathbf{H}^{\text{Jac}}\mathbf{x}^{\text{Jac}}$.

Input: $\mathbf{x}^{\text{Jac}}$
Output: $\mathbf{H}^{\text{Jac}}\mathbf{x}^{\text{Jac}}$
for $j = 0, 1, \ldots, N-1$ **do**
  Solve Algorithm 2 on (t_j, t_{j+1}) from $\mathbf{v}_j(t_j)$ and $\boldsymbol{\lambda}_j(t_{j+1})$
for $j = 1, \ldots, N-1$ **do**
  $\mathbf{H}^{\text{Jac}}\mathbf{x}^{\text{Jac}} \leftarrow \mathbf{v}_{j-1}(t_j) - \mathbf{v}_j(t_j)$
  $\mathbf{H}^{\text{Jac}}\mathbf{x}^{\text{Jac}} \leftarrow \boldsymbol{\lambda}_{j-1}(t_j) - \boldsymbol{\lambda}_j(t_j)$

Algorithm 6: A matrix-free method for solution of the optimality conditions.

$\mathbf{c}^{\text{Jac}} \leftarrow -\mathbf{H}^{\text{Jac}}\mathbf{0}$
$\mathbf{F}^{\text{Jac}}\mathbf{x}^{\text{Jac}} \leftarrow \mathbf{H}^{\text{Jac}}\mathbf{x}^{\text{Jac}} + \mathbf{c}^{\text{Jac}}$
Solve $\mathbf{F}^{\text{Jac}}\mathbf{x}^{\text{Jac}} = \mathbf{c}^{\text{Jac}}$ using GMRES to compute $\mathbf{x}^{\text{Jac}}$
for $j = 0, 1, \ldots, N-1$ **do**
  Solve Algorithm 2 on (t_j, t_{j+1}) from $\mathbf{v}_j(t_j)$ and $\boldsymbol{\lambda}_j(t_{j+1})$

in parallel, even distributed across multiple compute nodes, thus distributing computational resources and reducing the per-node memory requirements.

3.7.2 Forward Gauss-Seidel preconditioning

The same splitting of $\mathbf{F} = \mathbf{M} - \mathbf{L} - \mathbf{U}$ presented in section 3.7.1 is utilised for this preconditioning approach. Left multiplying Equation (3.50) by $(\mathbf{M} - \mathbf{L})^{-1}$ results in

$$\left[\mathbf{I} - (\mathbf{M} - \mathbf{L})^{-1}\,\mathbf{U}\right]\mathbf{x} - (\mathbf{M} - \mathbf{L})^{-1}\,\mathbf{c} = \mathbf{0}. \tag{3.53}$$

Left multiplication by $(\mathbf{M} - \mathbf{L})^{-1}$ can be thought of as solving the optimal control on each segment and then applying continuity in the tangent solution between consecutive segments. This approach is referred to as Forward Gauss-Seidel (FGS) preconditioning. The remaining unknown terms are

$$\mathbf{x}^{\text{FGS}} = \left(\boldsymbol{\lambda}_{j-1}(t_j), \ldots, \boldsymbol{\lambda}_{N-2}(t_{N-1})\right)^T.$$

These unknowns are the co-state terminal conditions at the end of each segment. By utilising this left multiplication, the FGS linear system satisfies the constraints $\frac{\partial \mathcal{H}}{\partial \mathbf{q}_j(t)}$ and $\frac{\partial \mathcal{H}}{\partial \boldsymbol{\kappa}_j}$ and, as before, these can be removed from the linear system resulting in

$$\begin{pmatrix} \frac{\partial \mathcal{H}}{\partial \boldsymbol{\iota}_1} \\ \vdots \\ \frac{\partial \mathcal{H}}{\partial \boldsymbol{\iota}_{N-1}} \end{pmatrix} = \mathbf{H}^{\text{FGS}}\mathbf{x}^{\text{FGS}} = \begin{pmatrix} \boldsymbol{\lambda}_0(t_1) - \boldsymbol{\lambda}_1(t_1) \\ \vdots \\ \boldsymbol{\lambda}_{N-2}(t_{N-1}) - \boldsymbol{\lambda}_{N-1}(t_{N-1}) \end{pmatrix} = \begin{pmatrix} \mathbf{0} \\ \vdots \\ \mathbf{0} \end{pmatrix}. \tag{3.54}$$

Again, it can be shown that

$$\mathbf{H}^{\mathrm{FGS}}\mathbf{x}^{\mathrm{FGS}} = \mathbf{F}^{\mathrm{FGS}}\mathbf{x}^{\mathrm{FGS}} - \mathbf{c}^{\mathrm{FGS}} = \mathbf{0}.$$

Algorithm 7 is used for computing $\mathbf{H}^{\mathrm{FGS}}\mathbf{x}^{\mathrm{FGS}}$ in a matrix-free sense. Computation of

Algorithm 7: A matrix-free method for the calculation of $\mathbf{H}^{\mathrm{FGS}}\mathbf{x}^{\mathrm{FGS}}$.

Input: $\mathbf{x}^{\mathrm{FGS}}$
Output: $\mathbf{H}^{\mathrm{FGS}}\mathbf{x}^{\mathrm{FGS}}$
for $j = 0, 1, \ldots, N-1$ **do**
  Solve Algorithm 2 on (t_j, t_{j+1}) from $\mathbf{v}_j(t_j)$ and $\boldsymbol{\lambda}_j(t_{j+1})$
  if $j \neq N-1$ **then**
    $\mathbf{v}_{j+1}(t_{j+1}) \leftarrow \mathbf{v}_j(t_{j+1})$
for $j = 1, \ldots, N-1$ **do**
  $\mathbf{H}^{\mathrm{FGS}}\mathbf{x}^{\mathrm{FGS}} \leftarrow \boldsymbol{\lambda}_{j-1}(t_j) - \boldsymbol{\lambda}_j(t_j)$

Algorithm 7 is commonly referred to as instantaneous control in the literature, Refs. [11, 34, 36, 61, 62, 63]. The term $\mathbf{c}^{\mathrm{FGS}}$ is computed using $\mathbf{H}^{\mathrm{FGS}}\mathbf{x}^{\mathrm{FGS}}$ using zero for $\mathbf{x}^{\mathrm{FGS}}$. Similarly, $\mathbf{F}^{\mathrm{FGS}}\mathbf{x}^{\mathrm{FGS}}$ is computed using $\mathbf{H}^{\mathrm{FGS}}\mathbf{x}^{\mathrm{FGS}}$ and adding $\mathbf{c}^{\mathrm{FGS}}$. An algorithm for computing the optimal control, tangent and co-state solutions using FGS preconditioning is given Algorithm 8. One drawback of the FGS preconditioning

Algorithm 8: A matrix-free method for solution of the optimality conditions.

$\mathbf{c}^{\mathrm{FGS}} \leftarrow -\mathbf{H}^{\mathrm{FGS}}\mathbf{0}$
$\mathbf{F}^{\mathrm{FGS}}\mathbf{x}^{\mathrm{FGS}} \leftarrow \mathbf{H}^{\mathrm{FGS}}\mathbf{x}^{\mathrm{FGS}} + \mathbf{c}^{\mathrm{FGS}}$
Solve $\mathbf{F}^{\mathrm{FGS}}\mathbf{x}^{\mathrm{FGS}} = \mathbf{c}^{\mathrm{FGS}}$ using GMRES to compute $\mathbf{x}^{\mathrm{FGS}}$
for $j = 0, 1, \ldots, N-1$ **do**
  Solve Algorithm 2 on (t_j, t_{j+1}) from $\mathbf{v}_j(t_j)$ and $\boldsymbol{\lambda}_j(t_{j+1})$

method is that the parallel computation of segments is removed due to the continuity constraint between segments. The solution of FGS preconditioning can be distributed across the compute nodes, for systems where memory is a limitation, in the same way that the Jacobi preconditioning can. However, unlike Jacobi the solution of the optimal control on each compute node cannot be computed in parallel. This is because the initial condition of a segment relies on the optimal solution of the previous segment and the solution becomes serialised and no longer computationally parallel. The result of this is that compute nodes are sat idle waiting for their respective initial conditions to be updated.

3.7.3 Backward Gauss-Seidel preconditioning

An alternative to the FGS preconditioning approach is to left multiply Equation (3.50) by $(\mathbf{M}-\mathbf{U})^{-1}$, which results in

$$\mathbf{0} = \left[\mathbf{I} - (\mathbf{M}-\mathbf{U})^{-1}\mathbf{L}\right]\mathbf{x} - (\mathbf{M}-\mathbf{U})^{-1}\mathbf{c}. \tag{3.55}$$

Left multiplication by $(\mathbf{M}-\mathbf{U})^{-1}$ can be thought of as solving the optimal control problem on a segment and then applying continuity in the co-state solution and is referred to as Backward Gauss-Seidel (BGS) preconditioning. The remaining unknowns in using this approach are

$$\mathbf{x}^{\mathrm{BGS}} = \left(\mathbf{v}_1(t_1), \ldots, \mathbf{v}_{N-1}(t_{N-1})\right)^T.$$

These unknowns are the initial tangent conditions at the beginning of each segment. Using this approach results in the constraints $\frac{\partial \mathcal{H}}{\partial \mathbf{q}_j(t)}$ and $\frac{\partial \mathcal{H}}{\partial \boldsymbol{\iota}_j}$ being satisfied and, therefore, can be removed from the linear system which results in the BGS linear system

$$\begin{pmatrix} \frac{\partial \mathcal{H}}{\partial \boldsymbol{\kappa}_1} \\ \vdots \\ \frac{\partial \mathcal{H}}{\partial \boldsymbol{\kappa}_{N-1}} \end{pmatrix} = \mathbf{H}^{\mathrm{BGS}}\mathbf{x}^{\mathrm{BGS}} = \begin{pmatrix} \mathbf{v}_0(t_1) - \mathbf{v}_1(t_1) \\ \vdots \\ \mathbf{v}_{N-2}(t_{N-1}) - \mathbf{v}_{N-1}(t_{N-1}) \end{pmatrix} = \begin{pmatrix} \mathbf{0} \\ \vdots \\ \mathbf{0} \end{pmatrix}. \tag{3.56}$$

As in the FGS case, it can be shown that $\mathbf{H}^{\mathrm{BGS}}\mathbf{x}^{\mathrm{BGS}} = \mathbf{F}^{\mathrm{BGS}}\mathbf{x}^{\mathrm{BGS}} - \mathbf{c}^{\mathrm{BGS}}$, where the structures of $\mathbf{F}^{\mathrm{BGS}}$ and $\mathbf{c}^{\mathrm{BGS}}$ are the matrices $\mathbf{F}$ and $\mathbf{c}$ with the respective rows and columns relating to the $\frac{\partial \mathcal{H}}{\partial \mathbf{q}_j(t)}$ and $\frac{\partial \mathcal{H}}{\partial \boldsymbol{\iota}_j}$ constraints removed. The algorithms for the matrix-free computation of $\mathbf{H}^{\mathrm{BGS}}\mathbf{x}^{\mathrm{BGS}}$ are very similar to that of the FGS approach except that the segments are solved from starting from the final segment and then continuity is applied on the co-state solution. An algorithm for computing $\mathbf{H}^{\mathrm{BGS}}\mathbf{x}^{\mathrm{BGS}}$ in a matrix free sense is provided in Algorithm 9 and an algorithm for the solution of the optimality conditions is given in Algorithm 10.

Algorithm 9: A matrix-free method for the calculation of $\mathbf{H}^{\mathrm{BGS}}\mathbf{x}^{\mathrm{BGS}}$.

Input: $\mathbf{x}^{\mathrm{BGS}}$
Output: $\mathbf{H}^{\mathrm{BGS}}\mathbf{x}^{\mathrm{BGS}}$
for $j = N-1, N-2, \ldots, 0$ **do**
  Solve Algorithm 2 from $\mathbf{v}_j(t_j)$ and $\boldsymbol{\lambda}_j(t_{j+1})$
  if $j \neq 0$ **then**
    $\boldsymbol{\lambda}_{j-1}(t_j) \leftarrow \boldsymbol{\lambda}_j(t_j)$
for $j = 1, \ldots, N-1$ **do**
  $\mathbf{H}^{\mathrm{BGS}}\mathbf{x}^{\mathrm{BGS}} \leftarrow \mathbf{v}_{j-1}(t_j) - \mathbf{v}_j(t_j)$

Algorithm 10: A matrix-free method for solution of the optimality conditions.

$\mathbf{c}^{\mathrm{BGS}} \leftarrow -\mathbf{H}^{\mathrm{BGS}}\mathbf{0}$
$\mathbf{F}^{\mathrm{BGS}}\mathbf{x}^{\mathrm{BGS}} \leftarrow \mathbf{H}^{\mathrm{BGS}}\mathbf{x}^{\mathrm{BGS}} + \mathbf{c}^{\mathrm{BGS}}$
Solve $\mathbf{F}^{\mathrm{BGS}}\mathbf{x}^{\mathrm{BGS}} = \mathbf{c}^{\mathrm{BGS}}$ using GMRES to compute $\mathbf{x}$
for $j = 0, 1, \ldots, N-1$ **do**
    Solve Algorithm 2 from $\mathbf{v}_j(t_j)$ and $\boldsymbol{\lambda}_j(t_{j+1})$

The BGS approach has the same computational limitations as the FGS approach in that solutions can be distributed across compute nodes but due to the reliance on the optimal solution in a segment updating the terminal co-state solution in the preceeding segment means that computational efficiency is reduced.

3.8 Implementation details for solving the OCS optimality conditions

While pseudocode has been provided in sections 3.3 and 3.7 further details of the implementation are provided in this section. The implementation of the algorithms made heavy use of C++ templates along with parallelism from OpenMP and MPI. Utilising C++ templating enabled writing of generic, system agnostic code that could be tested and validated on simple small cases. No modifications were then required in the investigation of more complex systems. This reduced the time spent debugging and bespoke code was not required to be written when changing system. The implementation involved several classes and functions each described here.

The two main functions are the conjugate gradient and GMRES functions. This is called to solve systems of the form $Ax = b$ and takes as input A and b and initial estimate for x. Templating these functions enables the reuse on different operators A and as such the method can be tested on simple known problems and applied to more complicated systems without any additional modification.

The first class is the variable class. This class houses logic for adding, subtracting, multiplication, division, inner products and norms of the variables under investigation. Specific implementations depending on whether the variable is 1D, 2D or the result of a Fourier transform all inherit from the base class and overload the required member functions. Rationale for a variable class is that the return type of C++ functions is required enabling a generic return type (base class) and making use of polymorphism when more complex variables are used.

The second class is the time integration scheme. As with the variable class the base class houses the functions for stepping a generic equation forwards in time. The equations used are inputs to the class meaning, again, maximal code reuse is

achieved. Implementation of a new time stepping scheme is achieved via inheritance and overloading with no additional modifications to alternative classes are required ensuring that maximal flexibility is maintained.

The system class is specific for each system under investigation. This class contains the non-linear, tangent and co-state equations under investigation and is provided by the user. Furthermore, the system class houses storage containers for the non-linear, tangent, co-state and control solutions for the given time horizon.

The previous three classes have been building blocks for the optimal control class. The optimal control class takes, as input, the system and time integration scheme classes along with making use of the conjugate gradient function. This enables the optimal control class to be written in a generic orchestration manner. Member functions include methods for computing Algorithms 1 and 2.

The member function for the operator **G** (Algorithm 1) takes as an input a control term. This input control term is then passed into the system class for use in the marching of the tangent equation. The tangent equation is then marched forwards in time from the initial condition along with control term, Equation (3.8b). Next, the co-state is marched backwards in time from the terminal condition and utilising the tangent solution, Equation (3.8a). Finally, the return of the member function is $2\alpha\mathbf{q}(t) - \boldsymbol{\lambda}(t)$ at every time step.

The member function for Algorithm 2 is as follows. Firstly, the term **b** is computed using a zero input to the member function for the operator **G** (Algorithm 1). Next, the operator function for **E** is created. This wraps the call to member function for the operator **G** (Algorithm 1) and addition of **b** into one function. This operator function for **E** along with **b** and initial guess for **q** are then passed to the conjugate gradient function for solving the linear system. The return of the conjugate gradient function is the optimal control value at each time step. One final call to operator **G** with the optimal control generates the optimal tangent and co-state solutions that are then used to compute the sensitivities.

Finally, the time domain decomposition class takes many optimal control classes (one for each segment) as input. Each segment shares a time instance with its neighbour, referred to as the interface time, t_j. As with the optimal control class the time domain decomposition class is an orchestration manner. This class is responsible for orchestration of the solving of the optimal control problems on each segment. Depending on which preconditioner used results in a different size system solved by the GMRES solver. If Jacobi is used then the continuity constraints for the tangent and co-state between consecutive segments are solved. If FGS is used then only the continuity constraints between consecutive segments for the co-state variable is solved and finally BGS the continuity constraint between consecutive segments for the

tangent solution is solved. These methods work in a very similar way so the algorithm for the preconditioners is described.

The member function $\mathbf{H}^{\text{Jac, FGS or BGS}}$ (Algorithms 5, 7 or 9) takes an input of the $\mathbf{x}^{\text{Jac, FGS or BGS}}$. These contain the initial and terminal conditions for the tangent and co-state solutions on each segment. These values are then set in the optimal control class for each segment. Once this has been undertaken Jacobi preconditioning uses MPI to solve the optimal control problem (Algorithm 2) for each segment in parallel. FGS solves the optimal control problem on the first segment (Algorithm 2) then sets the tangent interface value $\mathbf{v}_{j+1}(t_j)$ using $\mathbf{v}_j(t_j)$ from the current segment. In other words the terminal condition of the current segment is passed onto the proceeding segment for the tangent solution. The optimal control problem (Algorithm 2) is then solved on the next segment. This continues sequentially forwards until all segments are solved. BGS solves the optimal control problem on the final segment (Algorithm 2) then sets the tangent interface value $\boldsymbol{\lambda}_{j-1}(t_{j-1})$ using $\boldsymbol{\lambda}_j(t_{j-1})$ from the current segment. In other words the initial condition of the current segment is passed onto the preceding segment. The optimal control problem (Algorithm 2) is then solved on the penultimate segment. This continues sequentially backwards until all segments are solved. Once the optimal control problem has been solved on each segment then the continuity conditions can be computed resulting in $\mathbf{H}^{\text{Jac, FGS or BG}S}\mathbf{x}^{\text{Jac, FGS or BGS}}$.

The member function for Algorithms 6, 8 or 10 is, again, dependent on the preconditioner used. Even though the methods are preconditioner dependent they all follow a similar format. Firstly, the term $\mathbf{c}^{\text{Jac, FGS or BGS}}$ is calculated by providing $\mathbf{x}^{\text{Jac, FGS or BGS}} = \mathbf{0}$ into the member function for $\mathbf{H}^{\text{Jac, FGS or BGS}}$. Next, a function wrapper for the operator $\mathbf{F}^{\text{Jac, FGS, BGS}}$ is created. This function wrapper takes $\mathbf{x}^{\text{Jac, FGS or BGS}}$ as an input. The wrapper calls the member function for $\mathbf{H}^{\text{Jac, FGS or BGS}}$ and adds $\mathbf{c}^{\text{Jac, FGS or BGS}}$ to the output. It is worth noting that this function wrapper is called at every iteration within the GMRES solver. And in turn this function calls a solve for the optimal control problem on each segment, therefore at each GMRES iteration one CG optimisation is performed. This highlights the nested nature of the OCS method. Having set up the function wrappers GMRES is utilised to solve the linear system $\mathbf{F}^{\text{Jac, FGS or BGS}}\mathbf{x}^{\text{Jac, FGS or BGS}} - \mathbf{c}^{\text{Jac, FGS or BGS}} = \mathbf{0}$ for the optimal continuity conditions between consecutive segments ($\mathbf{x}^{\text{Jac, FGS or BGS}}$). Once these have been computed, then, one final call to the member function for $\mathbf{H}^{\text{Jac, FGS or BGS}}$ which ensures the tangent and co-state solutions are optimal.

3.9 Summary

This chapter presented derivation of the tangent formulation of the Optimal Control Shadowing, OCS, approach. This approach is valid when only a single parameter is of

interest. The minimisation problem was outlined and the first order optimality conditions were derived. Solving these optimality conditions results in an optimal and bounded solution. Further, the equation to compute the sensitivity generated by OCS was also presented.

As multiple parameters are commonly of interest in industry two methods of the adjoint OCS formulation were derived. The first used the adjoint of the tangent OCS formulation. The second approach found the adjoint and then found an appropriate stabilising control for the adjoint equation. It was shown that these two methods are equivalent given careful selection of certain weighting factors.

An approach for decomposing the time horizon into non-overlapping segments was developed. This was undertaken to improve the conditioning of the linear operator generated. This has the benefit of increasing computational efficiency and reducing solving time. The matrix-free methods for solving the tangent OCS optimality conditions require the storage of the non-linear, tangent, control and co-state solutions at each time-step in the time horizon. For large systems this could be larger than the available computational resources. One additional benefit of the time domain decomposition is that each time segment can be distributed across multiple compute nodes, thus reducing per-node memory limitations. Additional constraints were imposed on the solution, namely continuity between consecutive segments, to ensure that the solution generated using the time domain decomposition techniques is identical to the case where no time domain decomposition is used. This approach is also valid for the adjoint OCS formulation.

This chapter also provided implementation details in a matrix-free sense for solving the optimality conditions for the tangent OCS formulation. These were derived using analytical solutions of the tangent and co-state equations along with the optimality conditions. Pseudocode has also been provided to outline the steps taken to compute the optimal solution. These details were provided for the tangent OCS formulation, however, these methods are equally viable and easily translatable to the adjoint OCS formulation. Further, details were provided to explain what the control term would look like for extreme values of α.

A similar approach was taken for the method that decomposes the time domain into segments which resulted in a matrix-free method. It was shown that this decomposition could leverage parallel computation. In addition to this, three different preconditioning methods were presented. The first is Jacobi, which computes the optimal control solution on each segment, and then solves the discontinuity between consecutive segments. The second is Forward Gauss-Seidel, which solves the optimal control problem on the first segment and then applies continuity in the tangent solution, repeating this process on the proceeding segments and solving the discontinuity in the co-state solution. The final method was Backward Gauss-Seidel,

which solves the optimal control problem in the final segment and then applies continuity on the co-state solution, repeating this on the preceding segments and solving the discontinuity in the tangent solution. These methods are, again, equally applicable to the adjoint formulation of the time domain decomposition. The Jacobi preconditioning method still leverages parallel computing. Due to the sequential nature of both Gauss-Seidel methods the solution can be split across compute nodes, however, the compute nodes will be sat idle as the solution of the optimal control problem cannot be computed in parallel.

Chapter 4

Computational aspects of the OCS algorithm

This chapter is focused on the computational aspects of the OCS method. Only the tangent OCS formulation is investigated here as all analysis is identical for the adjoint formulations. The main focus is on the time domain decomposition approach as this is more industrially relevant and the results generated are easily transferable to the case where the whole time domain is investigated. These computational methods will be applied to larger more industrially relevant systems. To avoid trial and error tuning of the methods, a deeper understanding of how the various variables interact and affect convergence rates and accuracy of the method is required. The main variables free to the user are α, the time horizon, the preconditioning method, the number of segments, and the stopping criteria in both CG and GMRES, Refs. [48, 106]. These variables are investigated on two systems that are extensively utilised as a benchmark for sensitivity analysis of chaotic systems. The first is the Lorenz 1963 system, Ref. [80], which has been mainly investigated using the Shadowing approaches using LSS, Refs. [18, 23, 35, 125, 128, 129], MSS, Ref. [110], NILSS, Refs. [14, 20, 65, 91, 92], Periodic Shadowing, Refs. [77, 78], and various other approaches, Ref. [12, 30, 31, 32]. The Lorenz system is of fixed size and, therefore, a system that is spatially distributed, which is common in more industrially relevant systems, is required. Varying the domain size or mesh density is common in industry and information on the algorithm's behaviour is required. This is investigated on the widely used Kuramoto-Sivashinsky system, Refs. [73, 74, 113, 114], for sensitivity analysis of chaotic systems using the Shadowing approach using LSS, Refs. [16, 17, 23, 129], MSS, Refs. [19, 110, 111], NILSS, Ref. [14], Periodic Shadowing, Refs. [77], and by altering the time step, Ref. [12].

4.1 Description of the Lorenz system

The Lorenz system, Ref. [80], was developed as a simplified model for atmospheric convection and is given by the following system of ordinary differential equations

$$\frac{\mathrm{d}x(t)}{\mathrm{d}t} = \sigma\left(y(t) - x(t)\right) \tag{4.1a}$$

$$\frac{\mathrm{d}y(t)}{\mathrm{d}t} = x(t)\left(\rho - z(t)\right) - y(t) \tag{4.1b}$$

$$\frac{\mathrm{d}z(t)}{\mathrm{d}t} = x(t)y(t) - \beta z(t). \tag{4.1c}$$

The state vector is $\mathbf{u}(t) = (x(t), y(t), z(t))^T$, where $x(t) \in \mathbb{R}$ represents the rate of convection of the problem, $y(t) \in \mathbb{R}$ is the horizontal temperature variation, $z(t) \in \mathbb{R}$ is the vertical temperature variation. The parameter σ is proportional to the Prandtl number of the flow, ρ is proportional to the Rayleigh number, and β represents a physical thickness of the fluid layer. Typical values for σ, ρ and β are 10, 28 and $\frac{8}{3}$ respectively, and shall be used here unless otherwise stated. The time step for the numerical simulation of the system is $\Delta t = 0.01$ time units. For numerical stability a fourth order Runge-Kutta time-stepping scheme is used, Refs. [28, 133]. All results are generated using an initial conditions for $x(t)$, $y(t)$ and $z(t)$ drawn from a uniform random distribution between 0 and 1.

4.2 Numerical computation of the Lorenz system sensitivity

The variable ρ is chosen to be the parameter of interest as in other studies and

$$J(\mathbf{u}(t, p), p) = z(t), \tag{4.2}$$

as the function of interest. To aid in the investigation into the accuracy in the time averaged sensitivity generated by OCS the impact that ρ has on $\bar{J}$ is found. The value of $\bar{J}$ is computed for the range $\rho \in (1, 100)$ for 100 equally spaced points with each sample having a random initial conditions for $\mathbf{u}(t_s)$. Each sample has a 'spin up' time of 50 time units to ensure the solution is on the attractor. The time average is computed over 1500 time units.

The results can be seen in Figure 4.1 along with a curve fit of the solution following the discontinuity at $\rho = 24$. The curve fit can then be utilised to compute the derivative of $\bar{J}$ with respect to ρ. The derivative of the curve fit at $\rho = 28$ is $\frac{\mathrm{d}\bar{J}}{\mathrm{d}\rho} \approx 1.006$ and it is this value that will be utilised for comparison throughout the remainder of this system.

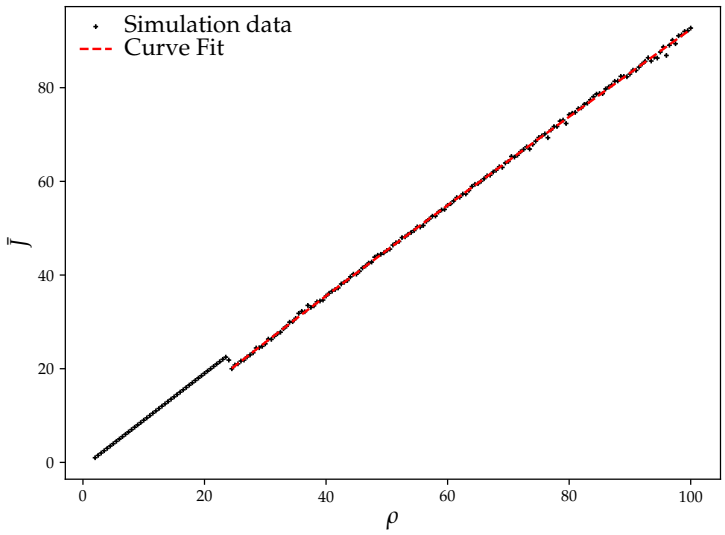

FIGURE 4.1: The value of $\bar{J}$ against ρ for the Lorenz system.

4.3 Influence of α on the sensitivity generated by OCS

The sensitivity generated by OCS is now computed for the range $\alpha \in (1, 1 \times 10^{15})$ when $T = 30$ time units, a 'spin up' time of 50 time units and the same initial conditions are used for Equation (4.1) for each value of α. This analysis is undertaken to investigate how varying the cost of the control applied varies the sensitivity generated. This influence has been undertaken on three different initial conditions and can be seen in Figure 4.2. The first observation to note is that the initial condition

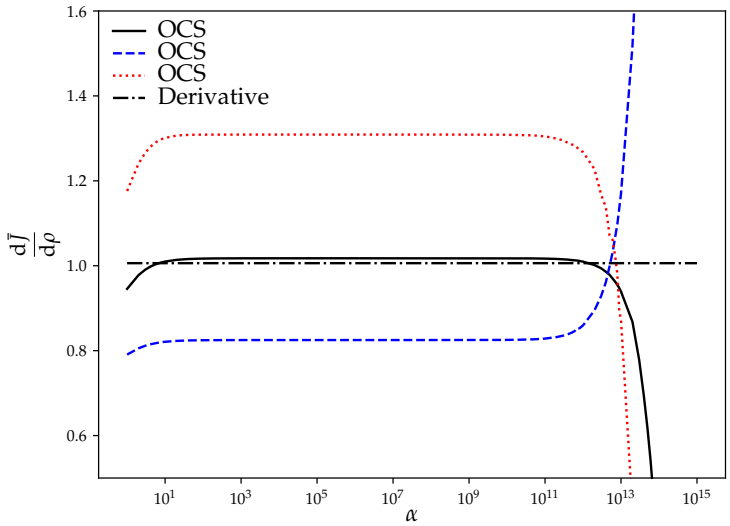

FIGURE 4.2: $\frac{d\bar{J}}{d\rho}$ against α for OCS for three different initial conditions, solid black line, dashed blue line and dotted red line. The derivative of the curve fit derivative of Figure 4.1, black dash dotted line, is also shown for comparison.

chosen impacts the value of the sensitivity generated. However, it is well known that Shadowing methods increase in accuracy as the time horizon is increased, Ref. [78, 124], and, therefore, this bias will reduce. Secondly, taking an average of the sensitivity over a range of initial conditions will also reduce the bias. It is worth noting here that using OCS leads to a larger spread in sensitivity values for given initial conditions than that of MSS. The reason is due to the control term stabilising the solution onto something which is not the exact Shadowing solution. To investigate these claims, the mean and standard error, $\frac{\sigma}{\sqrt{n}}$ where σ is the standard deviation and n the number of samples, are computed for $T \in \{5, 10, 15, 20, 25, 30, 35, 40, 45, 50\}$ time units from 100 different initial conditions. This is shown in Figure 4.3 for a 'spin up' time of 50 time units, $\alpha = 500$. This value of α is selected as it is in the "flat" region of Figure 4.2 and is neither under- or over-damped and provides good sensitivity values. The first observation to note is that the oscillations in average solution above $T = 30$

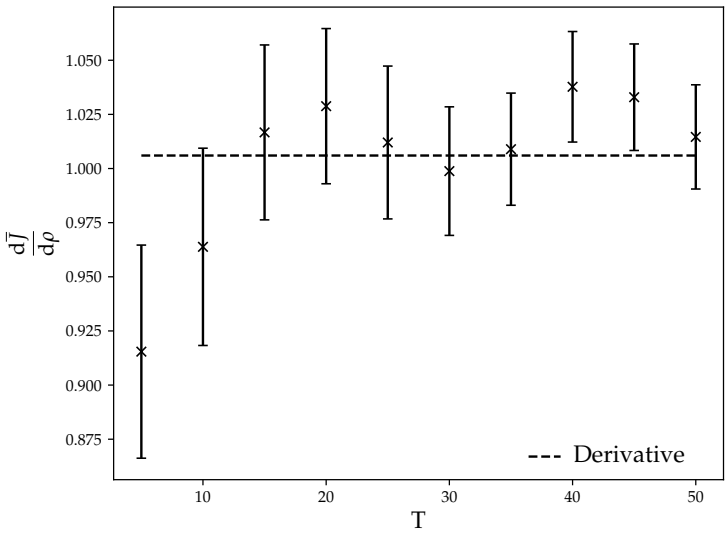

FIGURE 4.3: Mean and standard error of $\frac{d\bar{J}}{d\rho}$ computed over 100 different samples for $T \in \{5, 10, 15, 20, 25, 30, 35, 40, 45, 50\}$. The derivative of the curve fit derivative of Figure 4.1, black dash dotted line, is also shown for comparison.

are due to the small sample size used to generate the averages but general trends can still be found. It can be seen that when T is small the sensitivity generated has the largest error between the curve fit derivative. Furthermore, the standard error associated with the mean is also largest for small T values. As is common in the Shadowing approach, the error of the result is reduced as the time horizon is increased, Refs. [78, 124]. It can be seen that this is the case for OCS also. The reason for this is that when as the time horizon is increased the tangent solution generated tends towards the true Shadowing direction, reducing the error, which results in more accurate sensitivities, Ref. [124].

The physical interpretation of this is that, when the time horizon is small, there is a large number of different trajectories that remain bounded and the numerical methods, due to round off error, could find any one of these. These solutions are not the Shadowing direction which lead to inaccurate sensitivity values. If, however, these trajectories are simulated for a larger time they will no longer remain bounded and, therefore, the solutions that do remain bounded are better approximations of the true Shadowing direction. This is compounded as T increases. It can be concluded, that, for accurate simulations large time horizons, as in all Shadowing methods, should be utilised.

It can be observed that when $\alpha \leq 10$ the sensitivity is under-predicted. This is because the control in this region is considered cheap to apply and a large amount is applied. Large amounts of control damps the tangent solution significantly (over-damping) which results in the inaccurate sensitivity, that tends towards zero. By contrast, when $\alpha \geq 1 \times 10^{11}$ the control applied is unable to stabilise the tangent solution which leads to inaccurate sensitivities, and an under-damped solution. In between these regions the control applied is large enough to control the exponential growth of perturbations but small enough not to damp the entire solution. Comparisons not reported here with solutions obtained with MSS suggest that, excluding the initial fraction of the time horizon, the tangent solution generated by OCS converges to a solution which is very close to the true Shadowing direction. This is a bounded, but unstable, solution of the linearised equations which many Shadowing methods find approximations for. In the present approach, such an approximation is found by finding an appropriate stabilising control using optimal control theory.

It has been argued here that the inaccurate sensitivities below $\alpha \leq 10$ is due to an over-damped solution and $\alpha \geq 1 \times 10^{11}$ form an under-damped solution. To provide additional weight to this argument, the squared norm profiles of the tangent and control solutions are presented to provide additional detail. These are shown in Figure 4.4 where the norms of the optimal tangent and control solutions as a function of time are displayed for $\alpha \in \{1, 1 \times 10^{6}, 1 \times 10^{12}\}$. Panel (A) shows that for all α values investigated the tangent solution is stabilised onto approximations of the Shadowing direction for the initial five sixths of the time horizon. There are slight differences between the tangent solutions generated by each value of α and, therefore, the same approximation to the Shadowing direction is not found between cases.

Panel (B) shows that when $\alpha = 1$ there is a constant amount of control being applied throughout the time horizon which is able to counteract the growth of perturbations. The dip in control applied at the end of the time horizon is due to the terminal condition on the co-state. When $\alpha = 1 \times 10^{6}$ there is significantly less control applied, where the control value decays exponentially for the first two thirds of the time horizon and then reaches a constant value for the remainder. Finally, when $\alpha = 1 \times 10^{12}$, the control follows a similar profile for the previous case except the

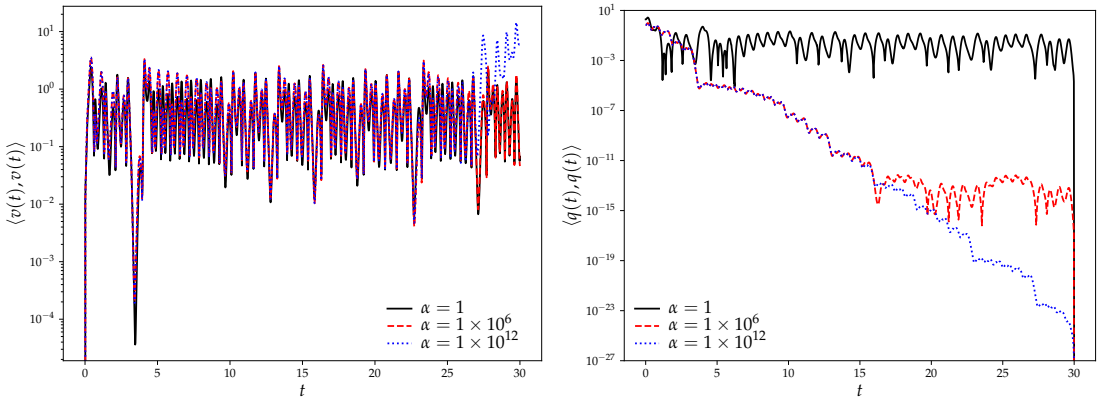

(A) (B)

FIGURE 4.4: Comparison of the squared norms of the tangent solution, panel (A), and control, panel (B), for $\alpha = 1$, solid black line, $\alpha = 1 \times 10^6$, red dotted line, and $\alpha = 1 \times 10^{12}$ blue dotted line.

constant value reached is several orders of magnitude lower. This exponential decay in the first two thirds of the time horizon of the control solution suggests that a solution with exponential growth is being controlled. In the final third of the time horizon there is significant difference between $\alpha = 1 \times 10^{12}$ and the other two cases. This is caused by the small value of control applied which is unable to control exponential growth in the tangent solution. This is the mechanism that causes the sensitivity values to be inaccurate for large values of α.

OCS has been derived to better understand the NV method. The result of the analysis presented in this section is that the control applied in NV methods by the additional term must be large initially. This will have the impact of stabilising the tangent solution onto an approximate Shadowing direction. Once the solution is near the approximate Shadowing direction, an unstable and bounded solution, minimal amounts of control are then required to keep the solution stable.

4.4 Convergence rates of the preconditioning methods

The stopping criteria for the GMRES is based on the value of the residual, $\mathbf{r} = \mathbf{H}\mathbf{x} - \mathbf{c}$, and gives an estimate of how accurately the linear system has been solved. In this analysis the stopping criteria is chosen to be 1×10^{-14} for both CG and GMRES, Refs. [48, 106], as this value is close to machine epsilon in 64-bit double-precision floating-point arithmetic. A large stopping tolerance means that there are discontinuities between segments, and the control will not be optimal, and as such the values generated for the sensitivities will be impacted.

The various preconditioning methods derived, Jacobi, Forward Gauss-Seidel (FGS) and Backward Gauss-Seidel (BGS), are compared to the no preconditioning case in Figure 4.5 for $T = 30$ time units, a 'spin up' time of 50 time units, $\alpha = 500$, $N = 6$ and using the same initial condition for Equation (4.1). It can be seen that applying no

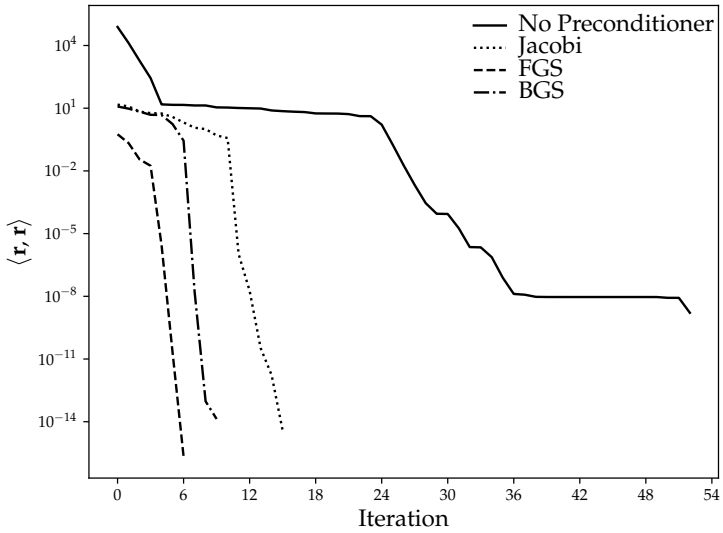

FIGURE 4.5: The squared norm of the residual, $\mathbf{r}$, for no preconditioning, solid line, Jacobi preconditioning, dotted line, FGS, dashed line, and BGS, dash dotted line.

preconditioning has the slowest rate of convergence, followed by Jacobi then BGS and, finally, FGS having the fastest convergence rate of those investigated. These results are in good agreement with those presented in Figure 6 in Ref. [60], Figure 5.6 in Ref. [37] and Tables 5.2 to 5.4 in Ref. [38] despite the difference in system investigated.

When there is no preconditioning applied, the converge rate is slow because all variables, *i.e.* the control and interface values for the tangent and co-state, are solved together. Therefore, at each iteration the control values on each segment and tangent and co-state values at the segment interfaces are not guaranteed to be optimal. Jacobi preconditioning, on the other hand, solves the optimal control problem on each segment at each GMRES iteration with discontinuities in both the tangent and co-state solution between consecutive segments. This results in "information" being propagated between consecutive segments faster than no preconditioning. BGS solves the optimal control problem sequentially backwards in time, meaning the co-state equation always obeys continuity across the segment boundaries. This leads to an increased rate of "information" transfer compared to the Jacobi preconditioning. The reason why the FGS converges quicker than BGS is that the formulation derived in section 3 is to minimise the norm of the tangent solution. By ensuring that there is continuity between consecutive segments in the tangent solution, as the FGS preconditioning does, its growth is known in each segment. By knowing the growth of the tangent solution in each segment the control can be applied in a more

"appropriate" fashion to better stabilise the solution which leads to fewer iterations required.

From these results it is clear that FGS requires the fewest number of iterations, but FGS does not have a favourable parallel efficiency, as the optimal control problems on the segments must be solved sequentially. In this regard, from the perspective of maximising compute resources, Jacobi preconditioning is advantageous over FGS or BGS. This is because the increased parallelism of the Jacobi preconditioning may result in the CPU wall-clock time of a single GMRES iteration being reduced over FGS or BGS and may lead to a faster overall solution in terms of CPU wall-clock time depending on the number of segments and other factors. In this thesis the FGS method is used due to the faster convergence rates and the impact on computational efficiency is disregarded.

4.5 Total cost of the OCS algorithm

For a given preconditioning method, there are two factors that will impact the cost of the OCS algorithm, the first being α, due to its impact on the condition number of the linear system associated with the optimal control problem in each segment and the second being the number of segments, N. The cost of the algorithm, where the total cost is the number of tangent and co-state solutions required, is used here. Providing the cost in terms of the number of tangent and co-state solution leads to results which are agnostic of computer hardware and implementation, and this gives a better understanding of how these methods will behave in general.

The total cost of the algorithm is computed for $N \in \{4, 6, 8, 12, 24\}$ with $\alpha \in (1, 1 \times 10^{19})$ for $T = 30$ time units and a 'spin up' time of 50 time units using the FGS preconditioning method. The number of tangent and co-state solutions is directly tied to the number of CG and GMRES iterations. For a solution of the optimal control problem on each segment a tangent and co-state solution is required for the computation of $\mathbf{b}_j(t)$. A forward and backward solution is then required for each computation of $\mathbf{E}_j\mathbf{q}_j(t)$. Finally, solutions to the tangent and co-state equations are required once the optimal control $\mathbf{q}_j(t)$ has been found. Solving the discontinuities between segments leads to one optimal control solution required for the computation of $\mathbf{c}^{\text{Jac}}$, $\mathbf{c}^{\text{FGS}}$ or $\mathbf{c}^{\text{BGS}}$. An optimal control solution is required every GMRES iteration for the evaluation of $\mathbf{F}^{\text{Jac}}\mathbf{x}^{\text{Jac}}$, $\mathbf{F}^{\text{FGS}}\mathbf{x}^{\text{FGS}}$ or $\mathbf{F}^{\text{BGS}}\mathbf{x}^{\text{BGS}}$. Finally, one more optimal control solution is required once the interface values for the tangent and co-state has been found. Therefore, the total cost of the algorithm in terms of number of tangent and co-state solutions required for convergence through can be found with

$$\text{Total Cost} = (\text{Iters}_{\text{GMRES}} + 2) \times (2 \times \text{Iters}_{\text{CG}} + 4)\,.$$

The change in cost through varying α and the number of segments for one simulation is presented in Figure 4.6. For large values of α, fewer segments are preferred,

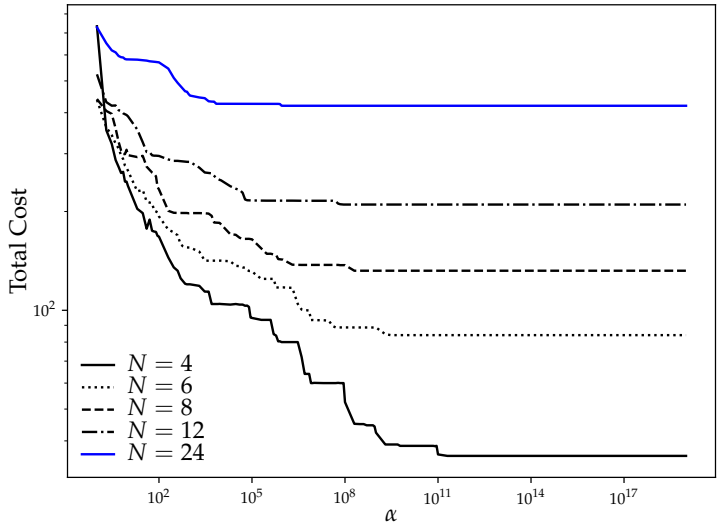

FIGURE 4.6: Total cost of the OCS algorithm against α for 4 segments, solid black line, 6 segments, dotted black line, 8 segments, dashed black line, 12 segments, dash dotted black line, and 24 segments, blue solid line.

however, for small values of α the difference between the cost generated by varying the number of segments is reduced. As can be found in Figure 6 in Ref. [60], Figure 5.6 in Ref. [37] and Tables 5.2 to 5.4 in Ref. [38], fewer segments produce lower computational cost. The number of iterations required for MSS is an order of magnitude lower than OCS. The reason is that per GMRES iteration MSS solves the tangent and co-state equation whereas OCS solves a minimisation problem with multiple solutions of the tangent and co-state equations. Based on this analysis, the fewest number of segments should be used. However, due to memory limitations this may not be feasible and a larger number of segments may be necessary. In practice, the number of segments used are selected such that the memory required for the optimal control problem on each segment is constrained by the memory each compute node has available.

4.6 Description of the Kuramoto-Sivashinsky system

The Kuramoto-Sivashinsky (KS) equation was initially introduced as a method of modelling angular-phase turbulence in a system of reaction-diffusion equations, Refs. [73, 74]. Later, the equations were derived to model how the instabilities of a distributed plane flame front evolve, Refs. [113, 114]. The KS system investigated here

is given by

$$\begin{gathered}\frac{\partial u(x,t)}{\partial t} = -(u(x,t)+c)\frac{\partial u(x,t)}{\partial x} - \frac{\partial^2 u(x,t)}{\partial x^2} - \beta\frac{\partial^4 u(x,t)}{\partial x^4}, \\ x \in [0, L), \\ u(0,t) = u(L,t),\end{gathered} \tag{4.3}$$

where $u(x,t)$ is a spatially distributed variable with L being the length of the domain, $c = 0.5$ the mean convective speed, and $\beta = 1.0$ is used in section 7.5 as an alternative parameter of interest. There have been several investigations into the modified KS system where Neumann and Dirichlet boundary conditions are used, Refs [12, 14, 16, 17, 19, 23, 77, 110, 111, 129], instead of periodic boundary conditions used here. In this thesis, periodic boundary conditions are utilised as this facilitates the use of spectral methods and a wavenumber-by-wavenumber analysis of the tangent/adjoint energy budget derived in sections 5.1 and 6.1. The solution can be expanded as

$$u(x,t) = \sum_{k=-\infty}^{\infty} \tilde{u}_k(t) e^{ik\frac{2\pi}{L}x},$$

but, in practice, a discretisation of $K_x = \frac{6L}{5}$ grid points is used. The reason for this is that the solutions of Equation (4.3) are smooth for long time horizons and the values of $\tilde{u}_k$ decrease with k due to the $\frac{\partial^4 u(x,t)}{\partial x^4}$ term, Ref [41]. As the solution is real valued, this results in $\frac{K_x}{2} + 1$ Fourier modes. A zero mean solution is chosen, *i.e.* $\tilde{u}_0 = 0$, which is commonly performed in the literature, Ref [41]. For the time integration, a Crank-Nicolson scheme, Ref. [40], is used for the linear terms and a second order Runge-Kutta scheme, Ref. [69], is used for the non-linear terms and $\Delta t = 1 \times 10^{-3}$ time units is used for stability. An inner product between two spatially distributed variables, $a(x,t)$ and $b(x,t)$,

$$\langle a(x,t), b(x,t) \rangle = \frac{1}{L}\int_0^L (a(x,t)b(x,t))\,\mathrm{d}x$$

is used and the norm is

$$\|a(x,t)\| = \sqrt{\langle a(x,t), a(x,t)\rangle}.$$

A typical example of the solution to the KS system is given in Figure 4.7.

4.7 Influence of the domain size on the convergence rate of the OCS algorithm

The influence the size of the domain, L, has on the convergence properties of CG and GMRES is now investigated. The spatial resolution, $\Delta x = \frac{L}{K_x} = \frac{5}{6}$, is kept constant between all domain sizes investigated. Each simulation uses a time horizon of

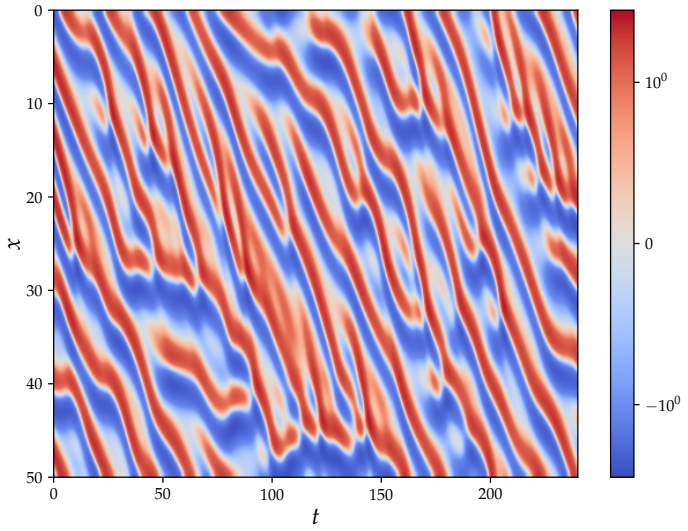

FIGURE 4.7: Example of a typical solution, $u(x,t)$, of the Kuramoto-Sivashinsky equations when convective speed $c = 0.5$.

$T = 240$ time units, following a 'spin up' time of 1000 time units, $N = 20$ and the FGS preconditioning method. Increasing the domain size increases the size of the control variable, $\mathbf{q}(t)$, which results in the size of the linear systems generated by the optimal control problem on each segment and the continuity constraints between consecutive segments becoming larger. The convergence properties of the average number of CG iterations across all segments per GMRES iteration, panel (A), and GMRES, panel (B), for $L \in \{64, 128, 256, 512\}$ and $\alpha \in (1, 1 \times 10^{19})$ are presented in Figure 4.8. In general

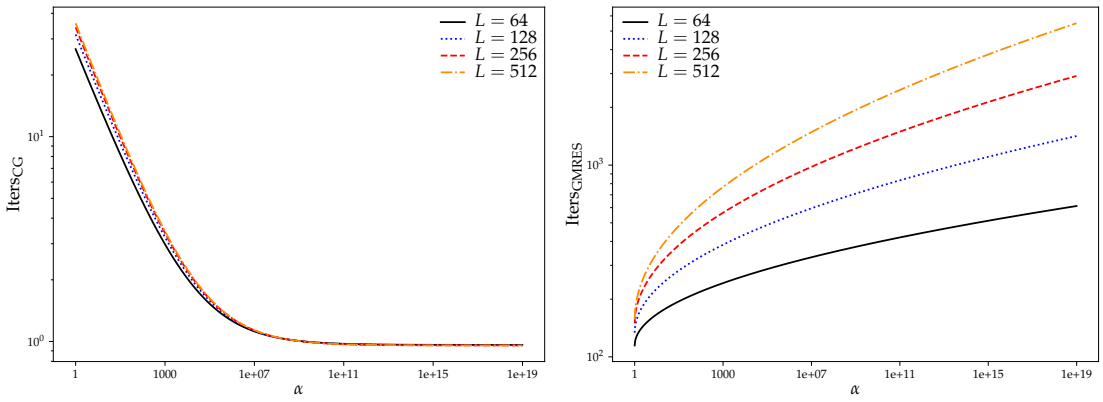

(A) (B)

FIGURE 4.8: Average number CG iterations per GMRES iteration, panel (A), and GMRES iterations, panel (B), for $L = 64$, black solid line, $L = 128$, blue dotted line, $L = 256$, red dashed line, and $L = 512$, orange dash dotted line, for a range of α values.

a small value of α leads to an increase in the number of CG iterations required for all domain sizes, Figure 4.8a. There is a very small influence that domain size has on the

average number of CG iterations. This behaviour is also seen, for a different system, in Table 5.7 in Ref. [38]. In general, increasing α leads to a larger number of GMRES iterations, Figure 4.8b. This is because the discontinuities between segments becomes larger when α is increased which results in more work being required to enforce continuity. Increasing the domain size increases the system solved by GMRES which results in a larger number of GMRES iterations and this relationship can be seen to be linear. From this analysis it is expected that when applying these methods to larger systems, such as fluid flow problems, that the majority of the computational time is dedicated to the GMRES iterations.

4.8 Summary

This chapter investigated the computational aspects of the tangent OCS formulation on two systems. The first was the Lorenz system as it is commonly utilised in sensitivity analysis of chaotic systems as it is a small and simple problem to test the methods on. Unfortunately, the Lorenz system is not spatially distributed and the computational aspects on a spatially distributed system could not be investigated. Spatially distributed systems are common in engineering and to provide details on their performance, the Kuramoto-Sivashinsky system was investigated.

There are several terms available to the user of the OCS algorithm. The first of these is α. The value of α modifies the cost of applying control. Too small a value will result in a large amount of control being applied, which damps the solution significantly (over-damping), and leads to inaccurate sensitivity values and large computational cost. Conversely, a large value means control is expensive to apply and small amounts of control are applied, which does not provide enough control to stabilise the solution (under-damping), leading to inaccurate sensitivity values and small computational cost. Values in between this provides adequate control to stabilise excess tangent/adjoint energy, which results in accurate sensitivity values. The values of α that should be selected are dependent on the system under investigation and general guidelines cannot be developed. However, the range of α that relates to apropriate stabilising control is large and suggests that values around 100 to 1000 may be appropriate for a range of different systems. One approach to automate the finding of this value is to find an α value where the gradient of the sensitivity is small or zero over a range of values. An iterative process could be utilised for determining the appropriate value of α which increases the tractability of the method and reducing the need to evaluate the sensitivity for a large range of α values.

The second term is the time horizon of the simulation. As in all Shadowing methods, the accuracy of the method improves with increasing the time horizon. When the time horizon is small there are a number of different trajectories that are bounded. These

trajectories are different from the Shadowing direction and, therefore, produce inaccurate sensitivity values. Increasing the time horizon leads to fewer of these bounded trajectories, which also tend towards the true Shadowing direction, resulting in more accurate sensitivity values. Therefore, for OCS to produce accurate sensitivity values large time horizons are required. Investigating the role of α on a smaller time horizon could be beneficial in selection of an appropriate value. The reason for this is that investigatinos on smaller time horizons are computatioanlly cheaper and a larger range of α values could be investigated. This would then give better confidence in the range of α values that produce accurate sensitivity which could then be utilised on longer time horizons with minimal modification.

Another variable open to the user is the preconditioning method used. For the tangent OCS formulation, the Forward Gauss-Seidel method provided the fastest convergence rate. This was due to two factors. First the OCS method minimises the norm of the tangent solution and having continuity between segments in this equation means that the growth of the solution is known and control can be applied more "appropriately". Secondly, these methods transfer "information" between segments faster than Jacobi preconditioning which leads to faster convergence. It is expected that for the adjoint OCS formulation that as the adjoint is being controlled that Backward Gauss-Seidel would have faster convergence for a similar reason. The limitation of the Gauss-Seidel methods is that the segments are solved sequentially whereas Jacobi preconditioning allows for parallel computation. Jacobi preconditioning has a slower convergence rate but may, potentially, have a lower CPU wall-clock time due to the parallel computation over Gauss-Seidel methods. This again is highly dependent on the problem investigated as the growth of the tangent/adjoint solution is determined by the largest Lyapunov exponent.

To improve convergence rates of the method, the time horizon was split into a number of segments which has an impact on the computational cost of the algorithm. A small number of segments leads to reduced computational cost for all values of α and is recommended. One limitation of using small number of segments is that the memory requirements per segment increase. For small systems, such as the Lorenz and Kuramoto-Sivashinsky systems investigated here, this was not an issue as the memory required for all variables was smaller than that of the compute node. For larger systems, such as transient turbulent flows, the memory requirements for each segment when few segments are used could be larger than the compute node. One other limitation is that with small number of segments the runtime computing the optimal control on each segment increases. This is compounded by large computational cost for small values of α which may mean that solutions are unfeasible for industry. It is, therefore, recommended that the number of segments is selected on two factors: the first being that the memory required for the solution on each segment

is smaller than the compute node, and secondly the solution of the optimal control problem on each segment is achieved in a "reasonable" time.

The main insight that the Lorenz system has provided is that the control applied by OCS has one important feature. A large amount of control is applied to move the solution onto an approximation of the tangent solution followed by minimal control that is required to keep the solution stable. Implications of this feature are control is applied in a more targeted manner than other NV methods which suggests a smaller amount of control is used. As a smaller amount of control is used this reducs the impact on the attractor of the system which results in sensitivity values that are more representative of the system under investigation.

For spatially distributed systems the domain size is another variable that influences computational cost. This was investigated on the Kuramoto-Sivashinsky system. Large domain sizes lead to increased number of GMRES iterations. This was because the linear system solved by GMRES increases with the number of variables. There is small dependence on the number of iterations of the CG method with domain size. For even larger systems, such as 2D/3D transient turbulent flows, it is expected that the largest factor in the computational cost is the solution of the linear system corresponding to the segment interface values. This could become an issue and reduce the industrial traction of the OCS method.

Chapter 5

Performance of tangent OCS on the Kuramoto-Sivashinsky system

OCS has been proposed to bridge the gap in understanding between MSS and NV methods for sensitivity analysis and this role is invesitgated in this chapter. This analysis is undertaken on the Kuramoto-Sivashinsky (KS) sysytem, Refs. [73, 74, 113, 114], which is a spatially distributed system. The rationale for why the KS system is utilised is that a vast amount of engineering systems are spatially distributed systems, typically in all three spatial dimensions. The KS system, which is a 1D partial differential equation, is utilised as a stepping stone to larger, more industrially relevant systems. Furthermore, while the KS system has been extensively investigated for Shadowing approaches to sensitivity analysis, Refs. [12, 14, 16, 17, 19, 23, 77, 110, 111, 129], there has been little development of NV methods on this system. To be able to compare the OCS with MSS and NV, additional derivation of the NV method for the KS system is required. This is achieved following similar principles to that proposed in previous literature in computing sensitivity analysis using the NV method, Refs. [12, 23, 49, 120, 121], and is found by determining which terms contribute to dissipation of tangent energy.

As with the Lorenz system, the sensitivity computed by OCS and NV are compared to the expected value for a range of their tuning parameters to show the behaviour of OCS and NV on these systems. This analysis is undertaken on the KS system with a domain size of $L = 50$ and $K_x = 60$ solution points, which results in $\frac{K_x}{2} + 1$ Fourier modes. A 'spin up' time of 1000 time units and a total time horizon $T = 240$ time units were used.

The NV and Shadowing methods have been shown to produce similar sensitivity values to the expected values, Refs. [12, 14, 16, 17, 19, 23, 49, 77, 110, 111, 120, 121, 129]. The similarity in solutions generated by the Shadowing and NV methods have

yet to be compared in the literature which is predominantly due to the methods being investigated on different systems. As the solutions generated by the Shadowing approach and NV have not been compared there could be some structure or feature present in Shadowing that could inform the structure of the computationally cheaper NV methods. To overcome this gap in the literature the spatio-temporal structure of the tangent and control solutions generated by MSS, OCS, and NV are compared. The similarity between the methods is investigated through comparison of the angle between solutions generated by MSS and by OCS and NV. Finally, a wavenumber analysis of the solutions generated by MSS, OCS and NV is presented as this could help inform certain structures, features or length scales which numerical viscosity terms should incorporate.

5.1 Derivation of the tangent energy equation

The main development of NV methods has been for fluid flow problems, Ref. [23], and has not been developed for the KS system. Therefore, the derivation of the tangent energy equation is needed for the NV approach. The approach taken to derive the NV method in Ref. [23] consisted of selecting a term which dissipates excess adjoint energy and stabilises the solution. Here, the NV terms for the KS system are derived following a similar approach by finding terms that contribute to the dissipation of tangent energy.

Starting from the KS system, Equation (4.3), the tangent equation when c is the parameter of interest and a control term, $q(x,t)$, is added is

$$\begin{aligned}\frac{\partial v(x,t)}{\partial t} = &\underbrace{-c\frac{\partial v(x,t)}{\partial x} - u(x,t)\frac{\partial v(x,t)}{\partial x} - v(x,t)\frac{\partial u(x,t)}{\partial x} + \eta(t)f(x,t)}_{C(x,t)} - \\ &\underbrace{\frac{\partial^2 v(x,t)}{\partial x^2}}_{P(x,t)} - \underbrace{\frac{\partial^4 v(x,t)}{\partial x^4}}_{D(x,t)} - \underbrace{\frac{\partial u(x,t)}{\partial x}}_{I(x,t)} + \underbrace{q(x,t)}_{Q(x,t)}, \\ &x \in [0, L), \\ &v(0,t) = v(L,t),\end{aligned} \tag{5.1}$$

where $v(x,t)$ is the tangent solution, $C(x,t)$ can be seen as relating to a combination of production and dissipation of tangent energy, $P(x,t)$ purely contributes to production of tangent energy, $D(x,t)$ purely to dissipation of tangent energy, $I(x,t)$ to the contribution to the tangent energy due to the inhomogeneous term, $Q(x,t)$ to the contribution to the tangent energy due to the control term, and $f(x,t)$ is the right hand side of Equation (4.3). Note that $q(x,t)$ is only applicable for OCS and NV and not MSS due to its formulation. The KS system, Equation (4.3), has periodic boundary

conditions, therefore, it follows that the tangent equation also has periodic boundary conditions. This results in the spectral methods being applicable for the tangent equation also. Therefore, the tangent and control variables can be broken down in a similar fashion

$$v(x,t) = \sum_{k=-\infty}^{\infty} \tilde{v}_k(t) e^{ik\frac{2\pi}{L}x} \quad \text{and} \quad q(x,t) = \sum_{k=-\infty}^{\infty} \tilde{q}_k(t) e^{ik\frac{2\pi}{L}x},$$

where $\tilde{v}_k(t), \tilde{q}_k(t) \in \mathbb{C}$.

Let $\epsilon(x,t) = \frac{1}{2}v(x,t)^2$ denote the local tangent energy. This variable is found by multiplication of Equation (5.1) by $v(x,t)$ resulting in

$$\begin{aligned} \frac{\partial \epsilon(x,t)}{\partial t} = \\ -2\epsilon(x,t)\frac{\partial u(x,t)}{\partial x} - (u(x,t)+c)\frac{\partial \epsilon(x,t)}{\partial x} - v(x,t)\frac{\partial^2 v(x,t)}{\partial x^2} + v(x,t)\eta(t)f(x,t) - \\ v(x,t)\frac{\partial^4 v(x,t)}{\partial x^4} - v(x,t)\frac{\partial u(x,t)}{\partial x} + v(x,t)q(x,t). \end{aligned} \tag{5.2}$$

Defining the tangent energy $\mathcal{E}(t) = \frac{1}{L}\int_0^L \epsilon(x,t)\mathrm{d}x$ as the domain average of the local tangent energy results in

$$\begin{aligned} \frac{\mathrm{d}\mathcal{E}(t)}{\mathrm{d}t} = \frac{1}{L}\int_0^L \Bigg(-2\epsilon(x,t)\frac{\partial u(x,t)}{\partial x} - (u(x,t)+c)\frac{\partial \epsilon(x,t)}{\partial x} - v(x,t)\frac{\partial^2 v(x,t)}{\partial x^2} + \\ +v(x,t)\eta(t)f(x,t) - v(x,t)\frac{\partial^4 v(x,t)}{\partial x^4} - v(x,t)\frac{\partial u(x,t)}{\partial x} + v(x,t)q(x,t) \Bigg)\mathrm{d}x. \end{aligned} \tag{5.3}$$

Integration of the third term on the right hand side of Equation (5.3) by parts results in

$$\int_0^L -v(x,t)\frac{\partial^2 v(x,t)}{\partial x^2}\mathrm{d}x = \int_0^L \left(\frac{\partial v(x,t)}{\partial x}\right)^2 \mathrm{d}x,$$

which can be seen to be a production term as it is always positive. Similarly, integration of the fourth term by parts twice leads to

$$\int_0^L -v(x,t)\frac{\partial^4 v(x,t)}{\partial x^4}\mathrm{d}x = \int_0^L -\left(\frac{\partial^2 v(x,t)}{\partial x^2}\right)^2 \mathrm{d}x,$$

which is always negative and is a dissipation term.

The first numerical viscosity term considered here is

$$q(x,t) = \mu_P \frac{\partial^2 v(x,t)}{\partial x^2}$$

which modifies the production of tangent energy where $\mu_P \in \mathbb{R}^+$ is a tuning parameter, and shall henceforth be referred to as NV_P. When $\mu_P > 1$ the control

applied by NV_P counteracts the influence of $P(x,t)$. Similarly, modification of the dissipation of tangent energy leads to

$$q(x,t) = -\mu_D \frac{\partial^4 v(x,t)}{\partial x^4}$$

where $\mu_D \in \mathbb{R}^+$ is a scaling factor for the artificial viscosity term and shall be referred to as NV_D.

5.2 Computation of the sensitivity for the Kuramoto-Sivashinsky system

The parameter chosen for this case is the mean convective speed, c, as is a precedent in the literature, Refs [12, 14, 16, 17, 19, 23, 77, 110, 111, 129], and

$$J\left(u(x,t),p\right) = \|u(x,t)\|^2, \tag{5.4}$$

is the function of interest which represents the energy density of the solution variable $u(x,t)$. The value of $\bar{J}$ is found using a random initial condition for Equation (4.3) for a time horizon of $T \in \{2\times10^3, 2\times10^4\}$ time units following a 'spin up' time of 1000 time units. This is undertaken over 50 samples. The change in mean value $\bar{J}$ and standard deviation as a function of $c \in (0.0, 1.0)$ using 100 equally spaced points is shown in Figure 5.1, where a curve fit through the data is also shown. It is worth

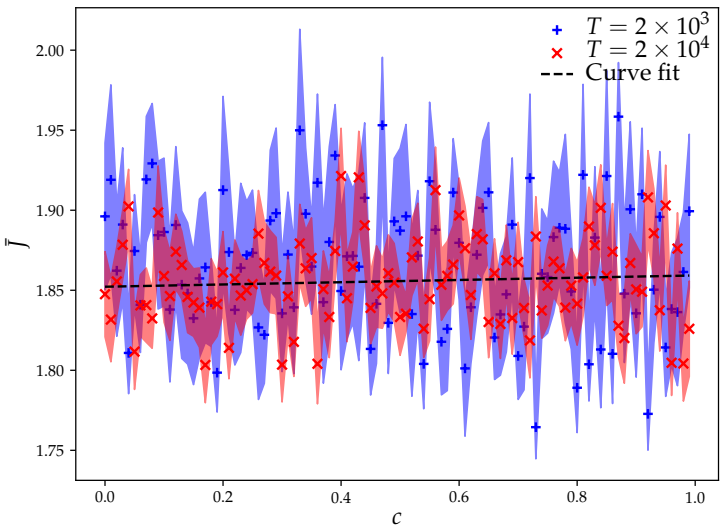

FIGURE 5.1: Mean and standard deviation of $\bar{J}$ against c for the KS system from numerical simulation when $T = 2\times10^3$, blue crosses, $T = 2\times10^4$, red crosses, and a curve fit through when $T = 2\times10^4$, black dashed line.

noting that the literature uses Neumann and Dirichlet boundary conditions and the

resulting correlation between c and $\bar{J}$ is strong, see Figure 7 in Ref. [19]. Figure 5.1 indicates that as the time horizon increases the average value of $\bar{J}$ is approximately constant in this range of c values. This is shown by the mean converging to the curve fit as T increases along with the standard deviation decreasing. The derivative of the curve fit when $c = 0.5$ is $\frac{\mathrm{d}\bar{J}}{\mathrm{d}c} \approx 6.725 \times 10^{-2}$, which shall be used for comparison throughout the investigation into this system.

The tangent OCS problem is solved for $\alpha \in (10, 1 \times 10^{10})$ using $T = 240$ time units, preceded by a 'spin up' time of 1000 time units, $L = 50$ and $K_x = 60$. This procedure is repeated for $\mu_P \in (0, 5)$ and $\mu_D \in (0, 50)$ using the same conditions. In Figure 5.2, the sensitivity generated by tangent OCS, NV_P and NV_D are shown in the left column for the range of tuning parameters along with, in the right column, $\|v(x,t)\|^2$. There is some bias with the OCS solution and the curve fit derivative, Figure (5.2a), which is caused by the selection of the initial condition of $u(x, t_s)$ as discussed in section 4.3. Although there is little correlation between c and $\bar{J}$ the influence of α still shows similar features as those presented for the Lorenz case and this lack of correlation is not a major limitation in the analysis. Further, the values of α that determine the under and over-damping regions are different to that of the Lorenz system and can be concluded that each system will have a different range of values. This reduces ability to transfer OCS between systems as one value which produces accurate sensitivity on one system may not produce accurate sensitivity on a different system. The result of this is that additional work is required to find a value which is inbetween the under and over-damped regions. When $\alpha < 1 \times 10^2$ the solution is over-damped and when $\alpha > 1 \times 10^4$ the solution is under-damped. In between these values the sensitivities are in good agreement with the curve fit derivative. Above this value the sensitivities become inaccurate. This, as will be shown later, is due to the control applied being too small and allowing the tangent solution to experience exponential growth, Figure (5.2b). One interesting feature to note is that the norm of the tangent solution can be quite large, and still produce sensitivity values in good agreement with the curve fit derivative.

When $\mu_P < 1$ the sensitivities generated by NV_P are inaccurate, Figure (5.2c), which is due to the control being inadequate and not able to stabilise the tangent solution. When μ_P is increased above 2, on the other hand, the sensitivity generated becomes in better agreement with the curve fit derivative which is due to the control being adequate and tangent solution norm does not exhibit exponential growth. This behaviour is similar for the NV_D case. In both of these NV cases it is unclear if there is an over-damped region as the range of tuning parameters investigated is relatively small.

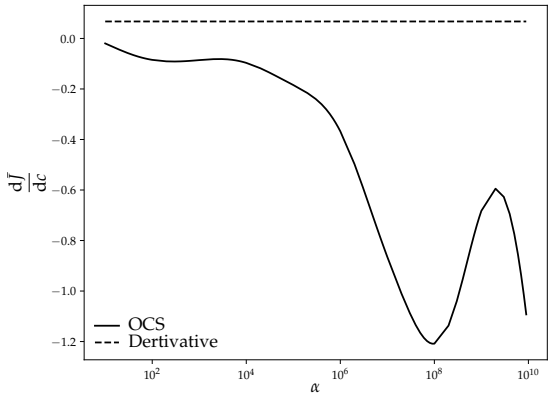

(A) $\frac{d\bar{J}}{dc}$ against α generated by OCS, solid line, and the curve fit derivative, dashed line.

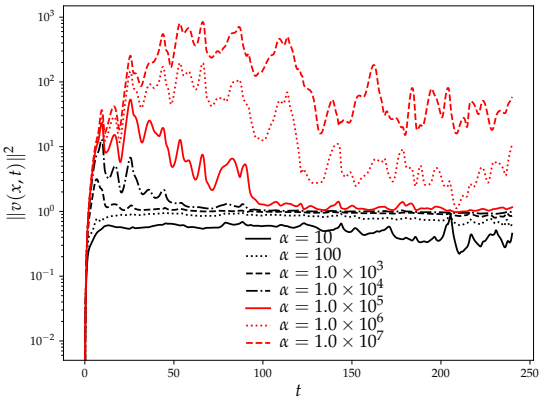

(B) $\|v(x,t)\|^2$ for $\alpha \in \{10, 100, 1 \times 10^3, 1 \times 10^4, 1 \times 10^5, 1 \times 10^6, 1 \times 10^7\}$

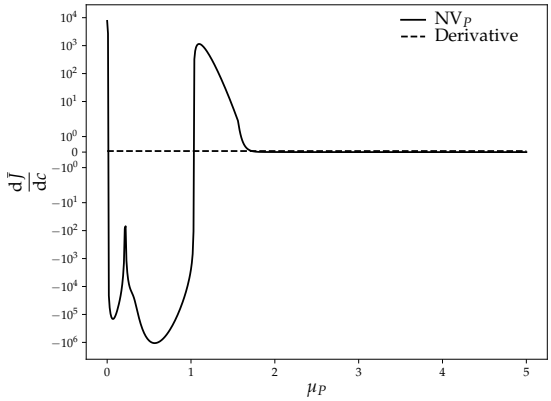

(C) $\frac{d\bar{J}}{dc}$ against μ_P generated by NV$_P$, solid line, and the curve fit derivative, dashed line.

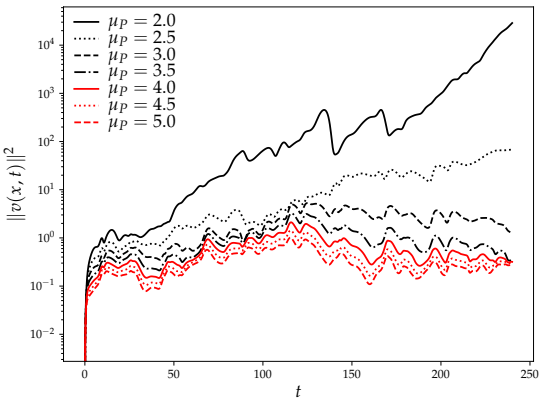

(D) $\|v(x,t)\|^2$ for $\mu_P \in \{2, 2.5, 3, 3.5, 4, 4.5, 5\}$

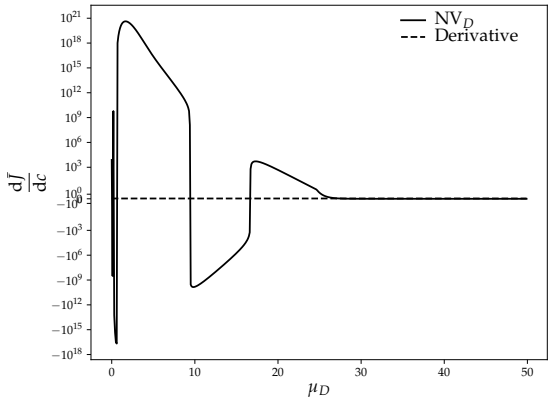

(E) $\frac{d\bar{J}}{dc}$ against μ_D generated by NV$_D$, solid line, and the curve fit derivative, dashed line.

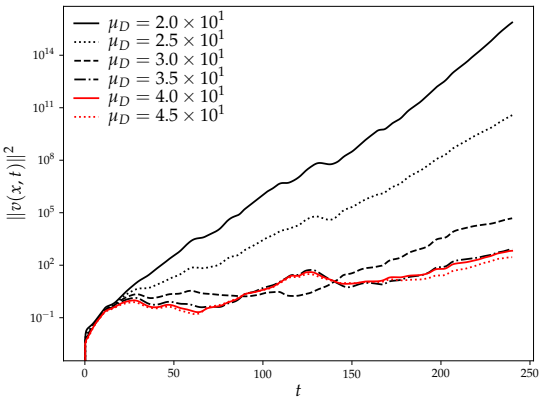

(F) $\|v(x,t)\|^2$ for $\mu_D \in \{20, 25, 30, 35, 40, 45\}$

FIGURE 5.2: $\frac{d\bar{J}}{dc}$, left column, and $\|v(x,t)\|^2$, right column, for different values of tuning parameters generated by OCS, top row, NV$_P$, middle row, and NV$_D$, bottom row.

5.3 Analysis of the optimal tangent spatial structures generated by MSS, OCS and NV

In this section MSS, OCS and NV are compared. An MSS solution, panel (A), on a time horizon of 240 time units following a 'spin up' time of 1000 time units using $K_x = 60$ and $N = 20$ from a random initial condition $u(x, t_s)$ is shown in Figure 5.3 along with the norm of the tangent solution, panel (B), for comparison. The main features of

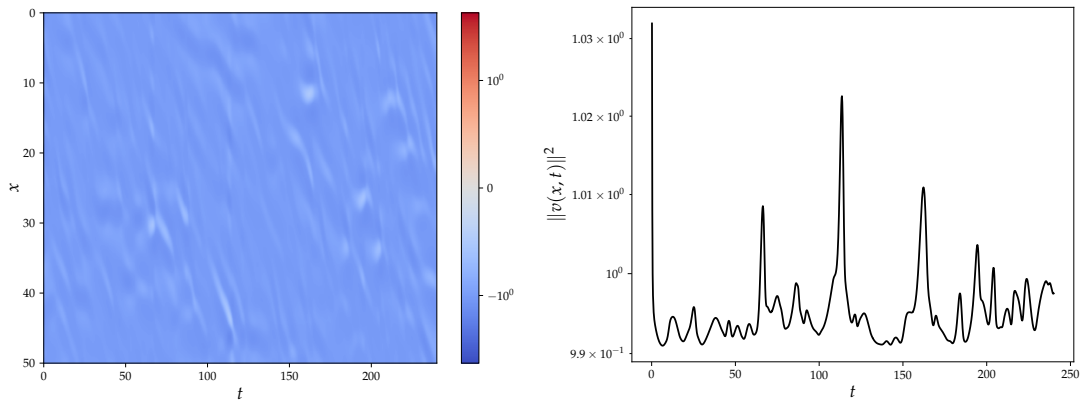

(A) (B)

FIGURE 5.3: $v(x, t)$, panel (A), and $\|v(x, t)\|^2$, panel (B), of the tangent solution generated by MSS.

Figure 5.3 is that the solution exhibits a large amount of dissipation in the initial 5 time units. It is unclear if this is due to dissipation leverged by the MSS method or if this is due to physical phenomena within the primal solution. Further, a large amount of features present in the tangent solution, Figure 5.3, have direct comparison to those in primal solution, Figure 4.7, suggesting that the tangent solution is tightly coupled with the primal solution. Regions of interest within the primal solution, such as vortex bursting in turbulent flows, impact the tangent solution and ultimately the sensitivity of the system. The large spikes in tangent energy around $t = 60$, $t = 120$ and $t = 160$ time units are due to the "merging" of features in the primal solution at these instances also, Figure 4.7 reiterating the importance of physical phenomena on the tangent solution. This "merging" process causes a lot of mixing and "turbulence" which is inherrantly chaotic leading to a tangent solution with larger energy than regions without "merging".

The tangent solutions generated by OCS for the same conditions when $\alpha \in \{50, 5000, 5 \times 10^6\}$ are shown in Figure 5.4 in the left column along with $\|v(x, t)\|^2$, right column. When $\alpha = 50$ there are some similarities between MSS, Figure 5.3a, and the OCS, Figure 5.4a. One thing to note is that OCS produces a tangent solution with a smaller norm, Figure 5.4b, than MSS, Figure 5.3b. It is argued

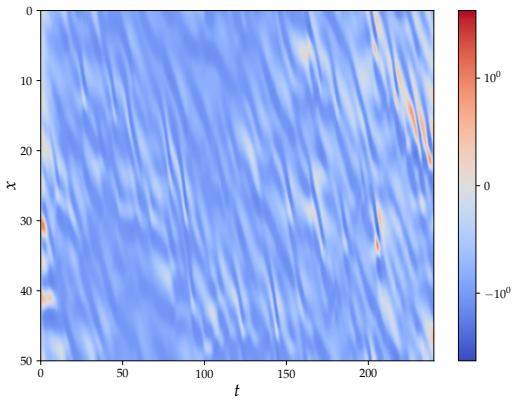

(A) $v(x,t)$ generated by OCS for $\alpha = 50$.

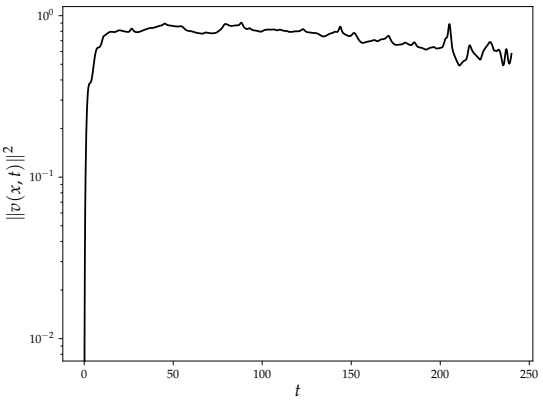

(B) $\|v(x,t)\|^2$ generated by OCS for $\alpha = 50$.

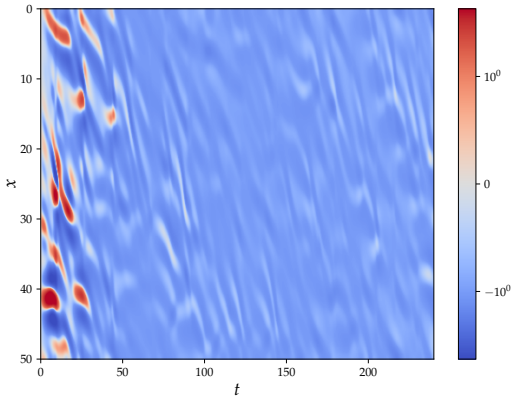

(C) $v(x,t)$ generated by OCS for $\alpha = 5000$.

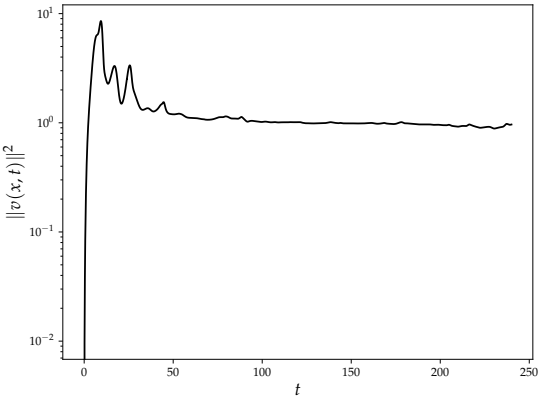

(D) $\|v(x,t)\|^2$ generated by OCS for $\alpha = 5000$.

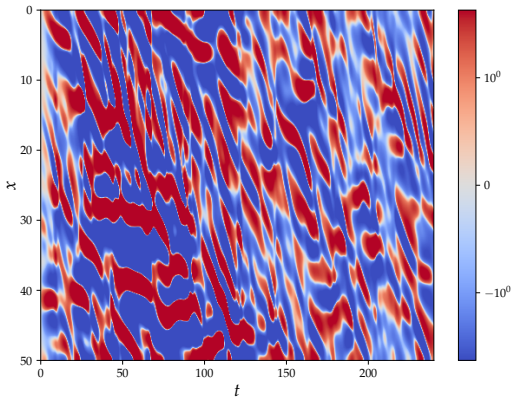

(E) $v(x,t)$ generated by OCS for $\alpha = 5 \times 10^6$.

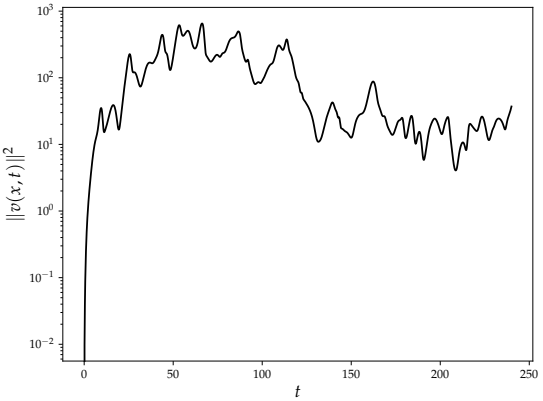

(F) $\|v(x,t)\|^2$ generated by OCS for $\alpha = 5 \times 10^6$.

FIGURE 5.4: $v(x,t)$, left column, and $\|v(x,t)\|^2$, right column, of the tangent solution generated by OCS for $\alpha = 50$, top row, $\alpha = 5000$, middle row, and $\alpha = 5 \times 10^6$, bottom row.

that this is because the small value of α leads to a large amount of control being applied which damps the solution. OCS has zero norm which then rises, which is common between all OCS solutions due to the control stabilising the solution onto the approximate Shadowing direction. Increasing α to 5000 results in a larger solution norm, Figure 5.4d. The large initial fluctuations in the tangent solution are caused by the reduced amount of control being applied when $\alpha = 5000$ compared to the previous case. The tangent solution for $\alpha = 5 \times 10^6$, Figure 5.4c, is found to not resemble that of MSS initially, Figure 5.3a, but following the transient period does show similar features. Finally, when $\alpha = 5 \times 10^6$ it is seen that the solution norm is significantly larger than MSS. This is caused by the control term being too small. This results in the tangent solution, Figure 5.4e, having no resemblance to MSS.

The behaviour that increasing α leads to a larger norm is not seen in the literature. This is because the equations that optimal control have been applied to in the literature, Refs. [10, 11] for example, do not exhibit exponential growth whereas the tangent equation, in this case, does. From this analysis it can be seen that OCS, given adequate selection of α, produces a tangent solution which is visually similar to that generated by MSS. This suggests that OCS, a NV method, can find the approximate Shadowing direction found by MSS.

The same analysis is repeated for $\mu_P \in \{1, 2.5, 5\}$ using the same conditions as before. Results are shown in Figure 5.5. When $\mu_P = 1$, it can be seen the control term is unable to stabilise the tangent solution, which results in the solution norm growing exponentially, Figure 5.5b. One other impact of this is that this solution, Figure 5.5a, has no similarities with that generated by MSS. Increasing μ_P to 2.5 leads to a solution where the control applied results in a better stabilised tangent solution, Figure 5.5b, shown by the reduced norm. For this value of μ_P, the tangent solution is better controlled, Figure 5.5c, and is starting to exhibit some features that resemble that of MSS. Increasing μ_P to 5 leads to a solution that has been stabilised, Figure 5.5f. Further, this norm is smaller than that generated by MSS, Figure 5.3b. When $\mu_P = 5$ the tangent solution, Figure 5.5e, has some features of the MSS solution, Figure 5.3a, but there is still a large difference, seen in the large diagonal banding in the solution. Similar behaviour is found for NV_D. This analysis suggests that utilising the NV approaches that are derived from finding terms which dissipate tangent energy may not be able to find the approximate Shadowing direction found by the Shadowing methods.

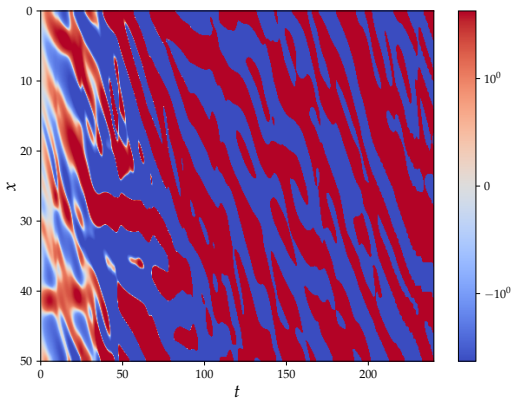

(A) $v(x,t)$ generated by NV_P for $\mu_P = 1$.

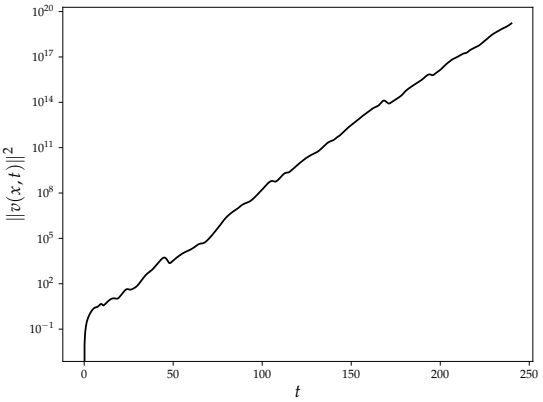

(B) $\|v(x,t)\|^2$ generated by NV_P for $\mu_P = 1$.

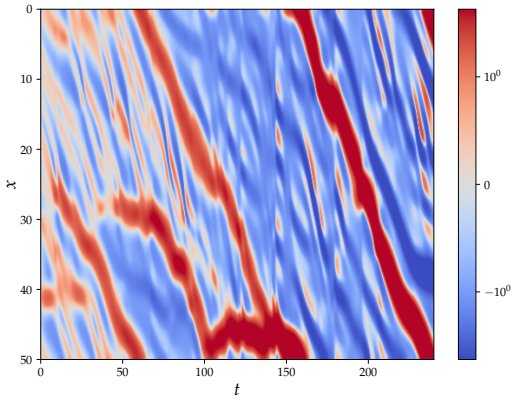

(C) $v(x,t)$ generated by NV_P for $\mu_P = 2.5$.

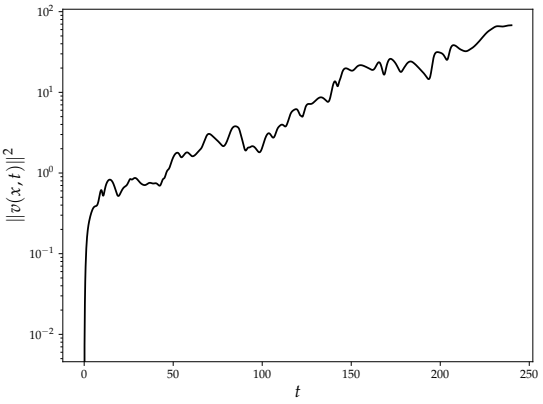

(D) $\|v(x,t)\|^2$ generated by NV_P for $\mu_P = 2.5$.

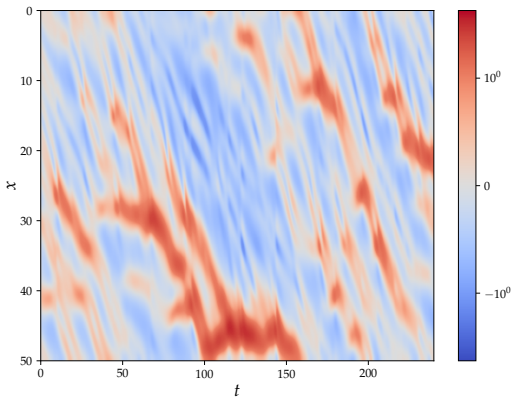

(E) $v(x,t)$ generated by NV_P for $\mu_P = 5$.

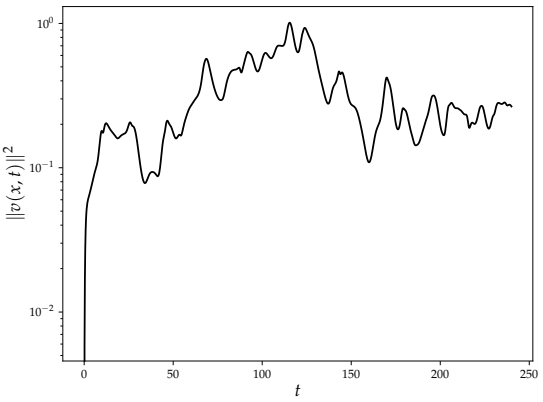

(F) $\|v(x,t)\|^2$ generated by NV_P for $\mu_P = 5$.

FIGURE 5.5: $v(x,t)$, left column, and $\|v(x,t)\|^2$, right column, of the tangent solution generated by NV_P for $\mu_P = 1$, top row, $\mu_P = 2.5$, middle row, and $\mu_P = 5$, bottom row.

5.3.1 Quantifying the similarities between tangent solutions

To gain a better understanding of the similarities between the tangent solutions generated by OCS and NV with MSS the metric

$$\theta_X(t) = \arccos\left(\frac{\langle v_{\text{MSS}}(x,t), v_X(x,t)\rangle}{\|v_{\text{MSS}}(x,t)\|\|v_X(x,t)\|}\right),$$

is used where $v_X(x,t)$ is the tangent solution generated by OCS or NV_P and $v_{\text{MSS}}(x,t)$ by MSS. The solution generated by MSS is used as a reference for the approximate Shadowing direction. Similar behaviour is seen between the NV_P and NV_D methods. A value of $\theta_X(t)$ close to zero shows that the solutions are well aligned with each other and are similar whereas values close to $\frac{\pi}{2}$ indicates the solutions are dissimilar. The comparison between MSS and OCS, $\theta_{\text{OCS}}(t)$, for a range of α values in panel (A) and the comparison between NV_P and MSS, $\theta_{\text{NV}_P}(t)$, for a range of μ_P values in panel (B), are shown in Figure 5.6.

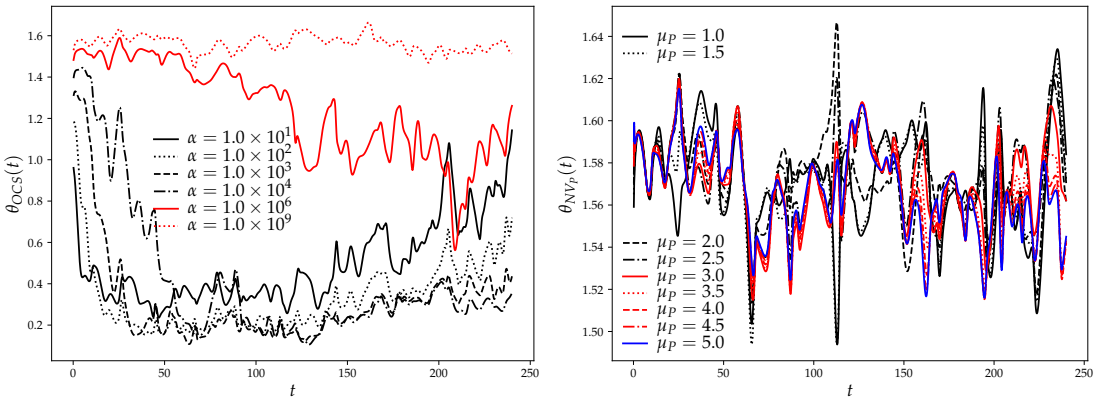

(A) (B)

FIGURE 5.6: $\theta_{\text{OCS}}(t)$ for $\alpha = 1.0 \times 10^1$, solid black line, $\alpha = 1.0 \times 10^2$, dotted black line, $\alpha = 1.0 \times 10^3$, dashed black line, $\alpha = 1.0 \times 10^4$, dash dotted black line, $\alpha = 1.0 \times 10^5$, solid red line, and $\alpha = 1.0 \times 10^9$, dotted red line, panel (A), and $\theta_{\text{NV}_P}(t)$ for $\mu_P = 1$, solid black line, $\mu_P = 1.5$, dotted black line, $\mu_P = 2$, dashed black line, $\mu_P = 2.5$, dash dotted black line, $\mu_P = 3$, solid red line, $\mu_P = 3.5$, dotted red line, $\mu_P = 4$, dashed red line, $\mu_P = 4.5$, dash dotted red line, and $\mu_P = 5$, solid blue line, panel (B).

When $\alpha \in \{1.0 \times 10^1, 1.0 \times 10^2, 1.0 \times 10^3, 1.0 \times 10^4\}$ there is initially little similarity between the tangent solution generated by MSS and OCS. This is because there is a difference in the initial conditions between the two methods. Following this initial period, the tangent solutions become more similar, shown by the reduction in the value of $\theta_{\text{OCS}}(t)$. This suggests that OCS stabilises the tangent solution to one similar to MSS. When $\alpha = 1.0 \times 10^1$, the tangent solution gets close to the MSS solution rapidly and throughout the time horizon diverges away. This is because the

exponential growth of perturbations are damped, yet control is continued to be applied throughout the time horizon meaning the solution is controlled further. Increasing α to 1.0×10^2 leads to an increased time the OCS solution takes to get close to MSS. Once the solution reaches something resembling MSS, little control is applied and the solution stays close and, therefore, diverges less. This behaviour is seen when increasing α to 1.0×10^3 or 1.0×10^4. If α is increased further then there is no resemblance between the tangent solutions generated by OCS and MSS. This is because the control applied is unable to control the growth of perturbations. As OCS is an NV method it can be seen that these methods, with appropriate selection of control term, can produce solutions similar to those produced by Shadowing.

To gain a deeper understaning panel (A) of Figure 5.6 is reproduced for a time horizon of 380 time units. The results of this are shown in Figure 5.7. It can be seen that there

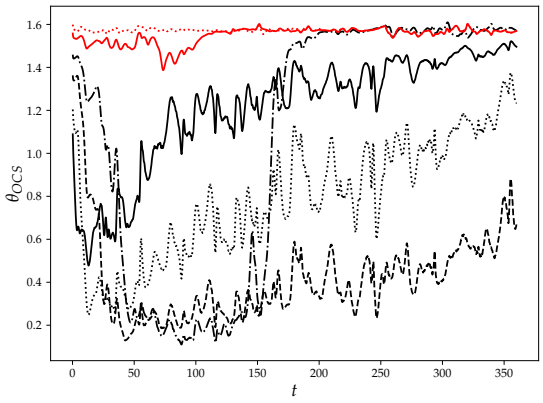

FIGURE 5.7: $\theta_{\text{OCS}}(t)$ for $\alpha = 1.0 \times 10^1$, solid black line, $\alpha = 1.0 \times 10^2$, dotted black line, $\alpha = 1.0 \times 10^3$, dashed black line, $\alpha = 1.0 \times 10^4$, dash dotted black line, $\alpha = 1.0 \times 10^5$, solid red line, and $\alpha = 1.0 \times 10^9$, dotted red line for $T = 380$ time units.

are very similar features between Figure 5.6a and Figure 5.7 implying the solutions generated for the smaller time horzon are valid. It is, again, argued that small values of α move the solution towards the Shadowing direction initially yet as more control is applied this increases the difference between the solution and the Shadowing direction. Increasing α means the solution takes longer to become similar to the Shadowing direction but stays closer for longer, again due to the large control applied initially and reduced amount later in the time horizon being applied to keep the solution stable. Finally, when too little control is applied the solution does not resemble the Shadowing direction. One interesting observation is that for $T = 240$ time units the solution generated by $\alpha = 1.0 \times 10^4$ remains similar to the tangent solution for the entire time horizon, yet when $T = 380$ this solution diverges. One explanation for this is that increasing the time horizon reduces the space of control solutions that can adequately stabilise the tangent solution. This value of α is appropriate for small values but is outside the space of adequate control for larger

time horizons. The implication is that as the time horizon is increased the range of stabilising α values decreases.

For NV_P, it can be seen that regardless of which value of μ_P chosen there is no similarity with the tangent solution generated by MSS, as the angle between solutions is on average $\frac{\pi}{2}$. This result is surprising even though the sensitivity values generated with both methods are in good agreement with each other. One possible explanation of this behaviour is that the NV methods, due to their simple control strategy, find a trajectory that resembles an approximate Shadowing direction which is different from the true Shadowing direction.

5.4 Spatio-temporal structures of the control produced by OCS and NV

The control solution is now shown to aid in the explanation of the analysis derived for the tangent solutions. The spatio-temporal structures of $q(x,t)$ and its squared norm generated by OCS for $\alpha \in \{50, 5000, 5 \times 10^6\}$ are shown in the left and right columns, respectively, of Figure 5.8. When $\alpha = 50$, it can be seen that the amount of control applied is constant throughout the time horizon, Figure 5.8b. The drop towards the end of the time horizon is due to the control being related to the co-state solution which has zero terminal condition. The control also has very similar spatio-temporal structures in the entire time domain, as observed in the tangent solution, Figure 5.4a. When increasing α to 5000, there is exponential decay in the amount of control applied over the first half of the time horizon, Figure 5.8d. Following this, the amount of control applied is constant. The majority of the control is found to be applied in the first half of the time horizon, Figure 5.8c. Finally, increasing α to 5×10^6 the control applied is several orders of magnitude lower than the other cases. It is argued that the large amount of control applied initially stabilises the solution onto the approximate Shadowing direction. The results of the control term are in good agreement with the analysis presented in section 5.3. Small values of α lead to a large amount of control being applied throughout the time horizon which, while initially driving the solution towards the approximate Shadowing direction, leads to the solution becoming dissimilar to MSS towards the end of the time horizon. Large values, on the other hand, are unable to control the solution meaning the Shadowing direction is not found. Finally, values in between these extremes lead to a solution which is stabilised onto the Shadowing direction and minimal control is applied to keep the solution bounded.

The same analysis is repeated for $\mu_P \in \{1, 2.5, 5\}$ using the same conditions as before. These results can be seen in Figure 5.9. As the control term, $q(x,t) = \mu_P \frac{\partial^2 v(x,t)}{\partial x^2}$, is linked to the tangent solution it is found that when $\mu_P = 1$ the control is unable to

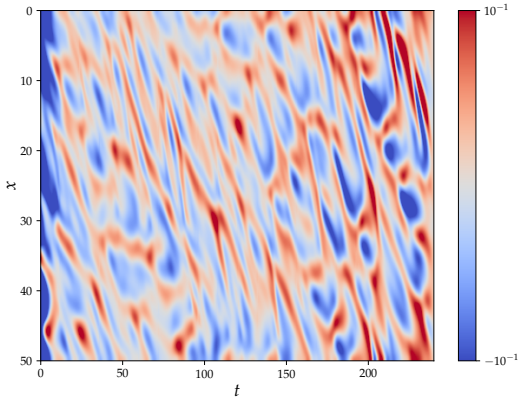

(A) $q(x,t)$ generated by OCS for $\alpha = 50$.

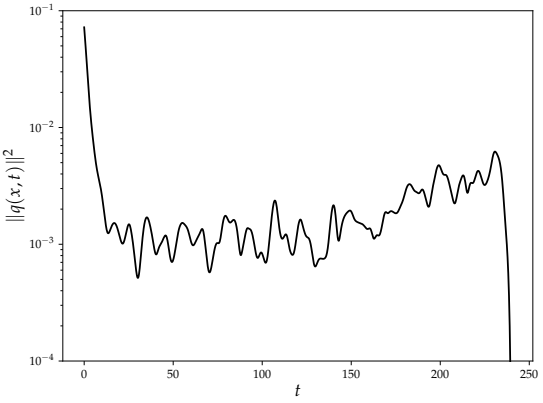

(B) $\|q(x,t)\|^2$ generated by OCS for $\alpha = 50$.

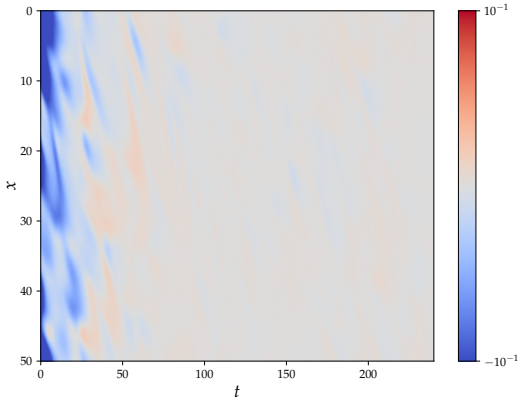

(C) $q(x,t)$ generated by OCS for $\alpha = 5000$.

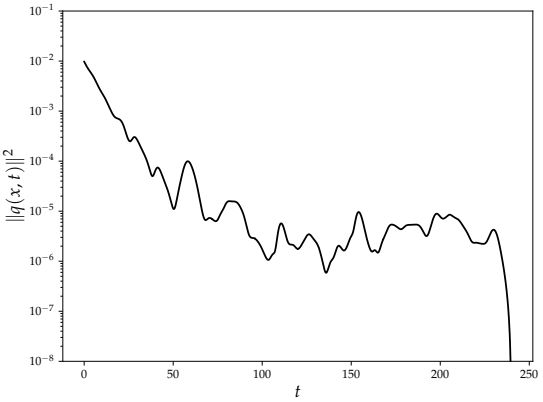

(D) $\|q(x,t)\|^2$ generated by OCS for $\alpha = 5000$.

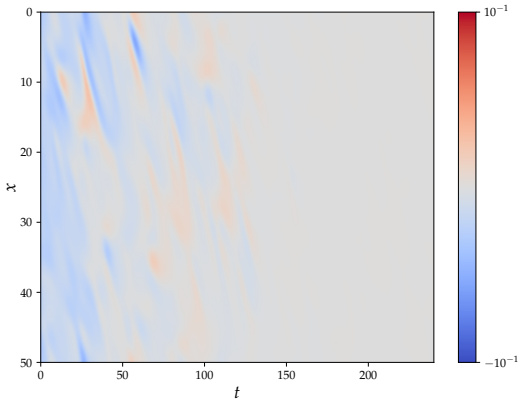

(E) $q(x,t)$ generated by OCS for $\alpha = 5 \times 10^6$.

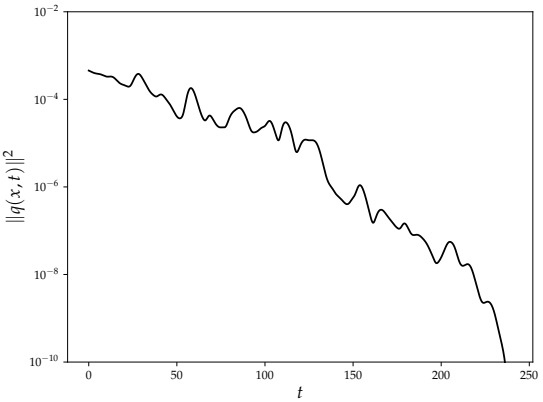

(F) $\|q(x,t)\|^2$ generated by OCS for $\alpha = 5 \times 10^6$.

FIGURE 5.8: $q(x,t)$, left column, and $\|q(x,t)\|^2$, right column, of the control solution generated by OCS for $\alpha = 50$, top row, $\alpha = 5000$, middle row, and $\alpha = 5 \times 10^6$, bottom row.

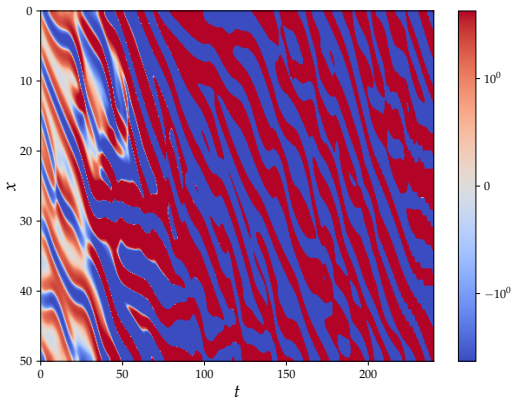

(A) $q(x,t)$ generated by NV_P for $\mu_P = 1$.

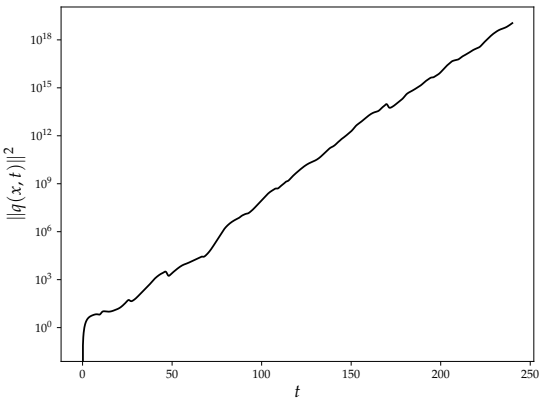

(B) $\|q(x,t)\|^2$ generated by NV_P for $\mu_P = 1$.

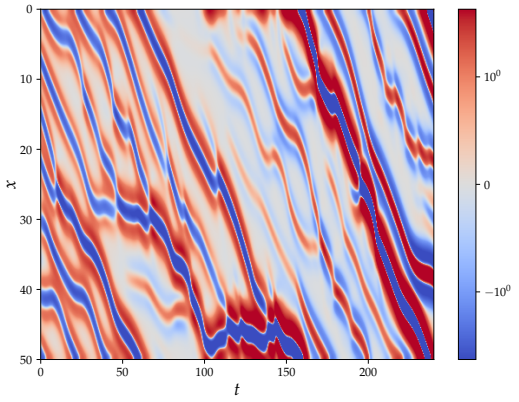

(C) $q(x,t)$ generated by NV_P for $\mu_P = 2.5$.

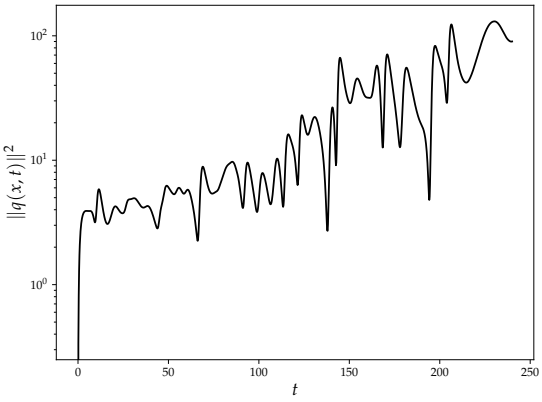

(D) $\|q(x,t)\|^2$ generated by NV_P for $\mu_P = 2.5$.

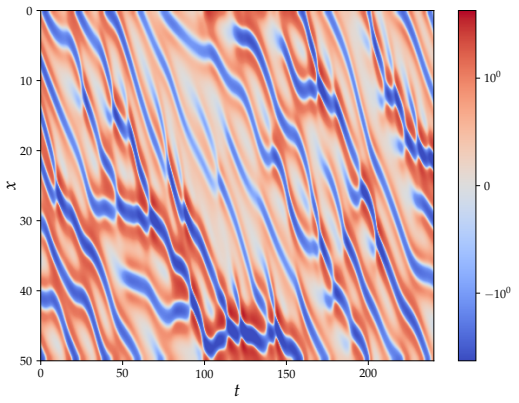

(E) $q(x,t)$ generated by NV_P for $\mu_P = 5$.

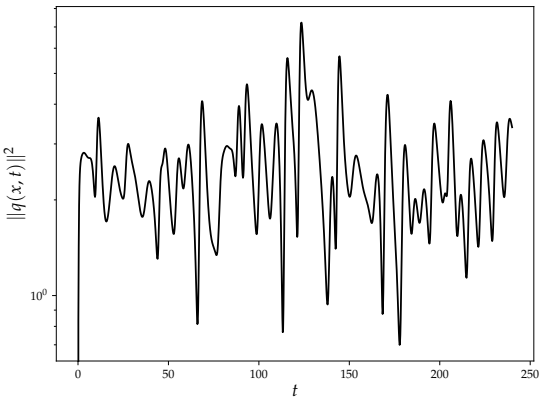

(F) $\|q(x,t)\|^2$ generated by NV_P for $\mu_P = 5$.

FIGURE 5.9: $q(x,t)$, left column, and $\|q(x,t)\|^2$, right column, of the tangent solution generated by NV_P for $\mu_P = 1$, top row, $\mu_P = 2.5$, middle row, and $\mu_P = 5$, bottom row.

stabilise the solution and the amount applied increases exponentially throughout the time horizon, Figure 5.9b. The control is also applied at shorter wavelengths, Figure 5.9a, compared to the tangent solution, Figure 5.5a. Increasing μ_P to 2.5 applies smaller amount of control than $\mu_P = 1$, Figure 5.9d. This may seem counter-intuitive, but as $q(x,t)$ is directly related to the tangent solution a control term that is able to stabilise the solution will result in less control being applied. Finally, increasing μ_P to 5 reduces the control applied even more, Figure 5.9f. When $\mu_P = 5$, Figure 5.9e, the resulting control being applied has similar features as that of $\alpha = 50$, Figure 5.8a. Further, NV_P applies orders of magnitude more control than OCS.

As a final remark, the magnitude of the control applied by NV_P has high amplitude oscillations, Figure 5.9f, whereas that applied by OCS, Figure 5.8d, does not exhibit this behaviour. This behaviour is also seen for the NV_D case. This analysis shows that the NV terms derived from the tangent equation produce results which are dissimilar to MSS as the amount of control is significant. The results in the tangent system are altered significantly and an alternative Shadowing direction is found which, in essence, relates to a slightly modified non-linear system, Ref. [49]. The conclusion is that the NV method is too simple to be able to find the correct Shadowing direction. It can be concluded that an NV method should utilise minimal control to stabilise the tangent solution to ensure that the tangent solution is as similar to the true Shadowing direction as possible.

5.5 Spectral analysis of the tangent equation

It has been shown in previous sections that the control term applied should have minimal influence while still stabilising the solution. To aid in this understanding, the tangent equation, section 5.1, is investigated on a wavenumber by wavenumber basis for the solutions generated by MSS, OCS, and the two NV methods. Investigating the wavenumber decomposition of the solution could lead to a deeper understanding of the structure required by NV methods. The tangent equation is solved using spectral methods and, therefore, each term in Equation (5.1) can be represented in terms of its spectral decomposition. The time average of the absolute value of these terms is computed on a wavenumber by wavenumber basis, *i.e.* $\overline{|P_l|}$. This analysis is repeated for 50 samples from different initial conditions, $L = 50$, $K_x = 60$, $T = 240$ and a 'spin up' time of 1000 time units. An observation is that results on different domain sizes collapse when the wavenumbers are scaled by $\frac{l}{L}$. This behaviour is shown in Figure 5.10 for three domain sizes $L \in \{50, 75, 100\}$. It is worth noting that these decompositions are computed for a single simulation and the values are impacted by the initial condition selected. To mitigate this averages over multiple simulations should be undertaken. Therefore, the analysis drawn for $L = 50$ is applicable to all

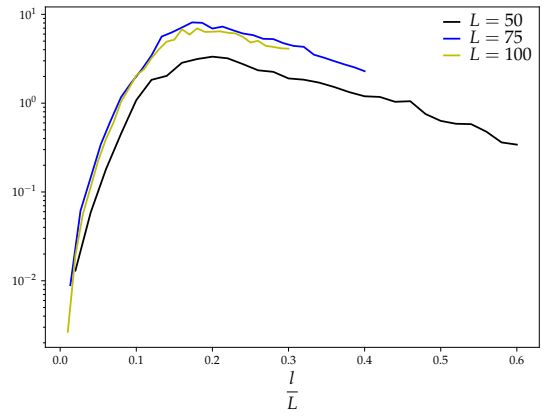

(A) Power spectra for $\overline{|P_l|}$.

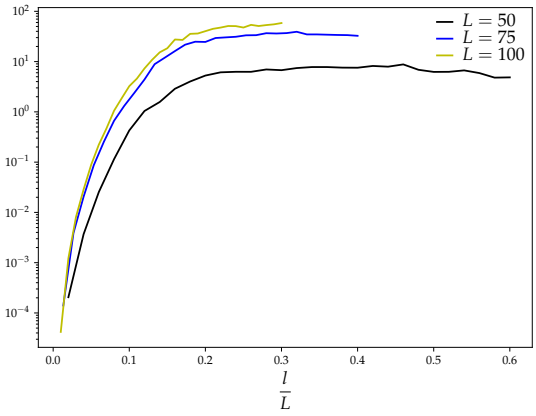

(B) Power spectra for $\overline{|D_l|}$.

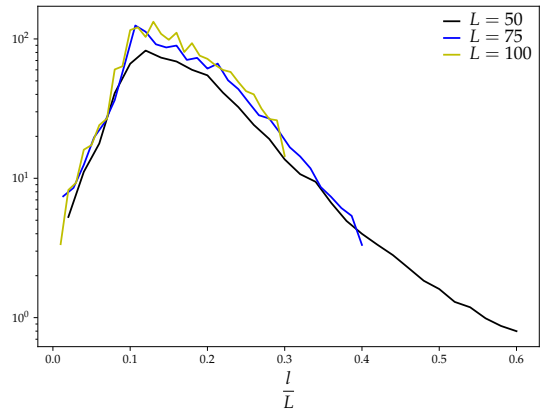

(C) Power spectra for $\overline{|C_l|}$.

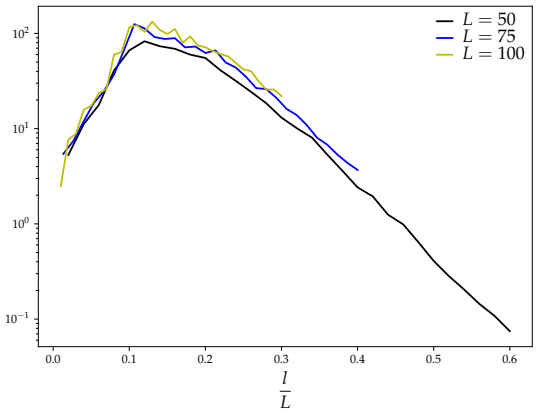

(D) Power spectra for $\overline{|I_l|}$.

FIGURE 5.10: Comparison of the power spectra of the tangent equation produced by MSS over different domain lengths $L = 50$ black line, $L = 75$, blue line and $L = 100$.

domain sizes under the correct scaling. A restriction imposed here is that one value of the tuning parameters in OCS and the NV methods which are $\alpha = 500$, $\mu_P = 2.5$ and $\mu_D = 31.0$ is used. These values are chosen as the sensitivity values generated are in good agreement with the expected value and are in the adequately damped region. The mean and standard error, $\frac{\sigma}{\sqrt{(n)}}$ where σ is the standard deviation and n the number of samples, of these results is computed for 50 different initial conditions which is shown in Figure 5.11 for MSS, panel (A), OCS, panel (B), NV_P, panel (C), and NV_D, panel (D). Some general trends that are observed are production of tangent energy is dominated by the longest wavelengths. For dissipation of tangent energy the dominant wavelengths are of medium wavelength. Dissipation of tangent energy dominates production around wavenumber $l = 8$. It is well known that the stable CLVs have stronger signatures at high wavenumbers, see Figure 3 in Ref. [118], and more stable CLVs have higher wavenumbers. It is argued that the wavenumber at which dissipation dominates production is related to the most dominant wavenumber of the CLV with the smallest negative (closest to zero) LE. Inhomogeneous and $C(x,t)$

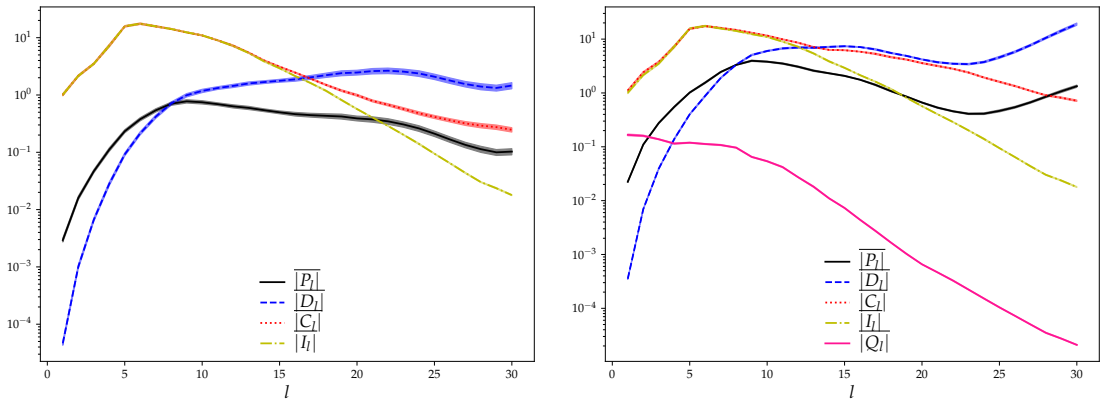

(A) Mean and standard error of the power spectra of the tangent equation terms produced by MSS.

(B) Mean and standard error of the power spectra of the tangent equation terms produced by OCS.

(C) Mean and standard error of the power spectra of the tangent equation terms produced by NV_P.

(D) Mean and standard error of the power spectra of the tangent equation terms produced by NV_D.

FIGURE 5.11: Comparison of the mean and standard error of the power spectra of the tangent equation produced by various methods over 50 samples. Panel (A) is produced by MSS, panel (B) by OCS, panel (C) by NV_P and panel (D) by NV_D.

terms both act on the longest length scales of the system and are reduced at shorter length scales for all cases.

The main difference between OCS and the two NV methods investigated is the length scales at which the control term acts. It can be seen that for OCS the control term acts predominantly in wavenumbers where production dominates dissipation and is reduced elsewhere. Further, the magnitude of the control term is several orders of magnitude lower than the other terms. This suggests that OCS applies control at length scales that require stabilising. The same argument that these long wavelengths are related to the unstable CLVs of the system, see Figure 3 in Ref. [118], is made. Both NV methods, on the other hand, have a large amount of control applied across all wavenumbers, peaking at $l = 8$ and damping across a large range of length scales, even when dissipation dominates production. This behaviour suggests that NV

applies control that does not consider the unstable, neutral or stable sub-spaces of the tangent space. By contrast, it is argued that OCS applies control only on the unstable sub-space. The wider implications of this is that knowing at what length scales production of tangent energy dominates dissipation or the length scales associated to the unstable sub-space could lead to the selection of a control term with more targeted control.

5.6 Summary

This chapter focussed on a comparison between the tangent formulations of the OCS, NV and MSS methods. NV methods have not been developed in the literature for the KS system. Therefore, the tangent energy equation was derived and its analysis allowed the determination of two NV terms. The first is derived from terms which contribute to production of tangent energy, and the second is derived from terms that contribute to dissipation. The expected value of the sensitivity was computed and the impact that the tuning parameters had on this were presented for OCS and the two NV methods. It was shown that the behaviour of α in the OCS method shared similar characteristics with that of the Lorenz case. Small values led to an over-damped solution, while large values resulted in under-damped solutions. Values inbetween led to an appropriately stabilised tangent solution and accurate sensitivity values. The main difference is that the values of α at which the tangent solution became under or over-damped are system dependent. This results in additional work required to determine the value of α if OCS is to be applied to a new system.

OCS has been developed to bridge the gap between Shadowing and NV methods. To gain a better understanding of this bridge the tangent solutions generated by OCS for a range of α were compared to the solution generated by MSS. It was found that OCS produced solutions which looked visually similar to MSS for smaller values of α. These values of α led to solutions with smaller norms than MSS and is due to the larger control applied damping the solution. Further, the angle between the solutions generated by MSS and OCS initially was $\frac{\pi}{2}$, showing the results are dissimilar, but tended towards an angle close to 0. This suggests that OCS finds a solution that is approximately the Shadowing direction. Increasing α led to solutions which did not visually resemble MSS due to the control applied being smaller and the solutions becoming unbounded. For these values, the angle between OCS and MSS was $\frac{\pi}{2}$ throughout the time horizon suggesting the solutions are not similar. This implies that NV methods, of which OCS is one, can find a solution which is similar to that found by Shadowing methods, when control is appropriately chosen, and is an approximate Shadowing direction. Further, to ensure the solution remains close to the Shadowing direction for the duration of the time horizon, the control applied should be minimal whilst still stabilising the tangent solution.

This analysis was also undertaken for NV methods. The main features were that for smaller values of the tuning parameters the solutions were not stabilised and did not visually resemble MSS. Increasing the tuning parameter stabilised the solution, however, did not visually resemble the MSS solution. For all values of the tuning parameter the angle between MSS and NV was, on average, $\frac{\pi}{2}$ throughout the time horizon implying the solutions are not similar. One possible explanation for this is that these methods derived from the tangent energy equation apply significant amount of control to stabilise the solution and, therefore, are the tangent equations to modified non-linear systems, Ref. [49].

A comparison of the control between OCS and NV was then conducted. The main feature of OCS is that large amounts of control are applied initially and decreased throughout the time horizon. This control, it was argued, stabilised the solution onto the approximate Shadowing direction. Increasing α reduced the amount of control applied where this feature of larger control initially was still present. Following this initial period, the amount of control applied reduced and resulted in there being inadequate control to stabilise the tangent solution. NV, on the other hand, applies control proportional to the tangent solution. Therefore, NV methods apply zero control initially and increase in time. Further, the amount of control applied was significant which supports the analysis that there is a difference between the tangent system and non-linear system, Ref. [49]. This also suggests that the NV methods are non-optimal in the application of the control.

Finally, a wavenumber analysis of the tangent equation was undertaken. It was found that OCS predominantly applies control along wavenumbers where the production of tangent energy dominates dissipation. Outside this region, the control decays quickly with increasing wavenumber. It was argued that this region was related to the power spectra of the unstable covariant Lyapunov vectors and that OCS provides control only in the unstable sub-space of the tangent space. This was not the case for the NV method which applied significant control across all wavenumbers even when dissipation of tangent energy dominates production contrary to OCS. The wider implication of this is that to generate a solution which is similar to the Shadowing direction, control must be applied in minimal amounts to stabilise the solution. This is achieved through application of control only in the unstable sub-space. This leads to the conclusion that NV methods should act predominantly in the unstable subspace region and only provide minimal control required to stabilise the tangent solution.

Chapter 6

Performance of adjoint OCS on the Kuramoto-Sivashinsky system

It is common in the engineering sector that the sensitivity of functions of interest with respect to multiple parameters is required. This led to the development of the adjoint formulation of OCS. This chapter repeats the analysis of chapter 5 for the adjoint formulation through comparison of the co-state and control spatio-temporal structures and the respective angles between solutions along with a wavenumber analysis of the adjoint equation. The rationale for this is to show the analysis presented for the tangent formulation is equally valid for the adjoint form and to aid in determining the link between NV and Shadowing methods along with finding features that are present in Shadowing that should be incorporated into NV methods. The adjoint NV terms are required for comparison and have not been investigated in the literature. Therefore, these terms are found through analysis of the adjoint energy equation. The sensitivity values produced by adjoint OCS are presented and compared to the expected sensitivity and the tangent OCS formulation.

Chapter 5 provided analysis that links the OCS, Shadowing and NV methods for the tangent formulation. This was achieved through comparison of tangent and control structures along with a wavenumber analysis of the solutions. This tangent formulation analysis was undertaken on the KS system with functional of interest $J(u(x,t),p) = \|u(x,t)\|^2$ and a parameter of interest $c = 0.5$. The domain size was $L = 50$, and $K_x = 60$ solution points were used which resulted in $\frac{K_x}{2} + 1$ Fourier modes. A 'spin up' time of 1000 time units and a total time horizon $T = 240$ time units were used. These conditions are, again, used in the analysis of the adjoint formulation of OCS. Further, the adjoint is found under the inner product

$$\langle a(x,t), b(x,t) \rangle = \frac{1}{L} \int_0^L (a(x,t)b(x,t)) \, \mathrm{d}x.$$

6.1 Derivation of the adjoint energy equation

It is common in the NV method, Refs. [12, 23, 49, 120, 121], to introduce a control term into the adjoint equations which dissipates excess adjoint energy. The NV method has not been developed in the literature for the KS system. This section identifies which terms contribute to the production and dissipation of adjoint energy and manipulates them to form the NV terms that dissipate excess adjoint energy. These terms are analogous to those presented in section 5.1.

To undertake this analysis, firstly define the adjoint of Equation (5.1) under the appropriate inner product as

$$\begin{aligned}\frac{\partial \hat{\lambda}(x,t)}{\partial t} = \underbrace{-c\frac{\partial \hat{\lambda}(x,t)}{\partial x} - \frac{\partial\left(u(x,t)\hat{\lambda}(x,t)\right)}{\partial x} + \hat{\lambda}(x,t)\frac{\partial u(x,t)}{\partial x} + \hat{\omega}(t)f(x,t)}_{\hat{C}(x,t)} + \\ \underbrace{\frac{1}{T}\frac{\partial J(u(x,t),p)}{\partial u(x,t)}}_{\hat{I}(x,t)} + \underbrace{\frac{\partial^2 \hat{\lambda}(x,t)}{\partial x^2}}_{\hat{P}(x,t)} + \underbrace{\frac{\partial^4 \hat{\lambda}(x,t)}{\partial x^4}}_{\hat{D}(x,t)} + \underbrace{\hat{\zeta}(x,t)}_{\hat{Q}(x,t)}, \\ x \in [0, L), \\ \hat{\lambda}(0,t) = \hat{\lambda}(L,t),\end{aligned} \tag{6.1}$$

where $\hat{I}(x,t)$, $\hat{C}(x,t)$, $\hat{P}(x,t)$, $\hat{D}(x,t)$, $\hat{Q}(x,t)$, and $\hat{\zeta}(x,t)$ are the adjoint counterparts to $I(x,t)$, $C(x,t)$, $P(x,t)$, $D(x,t)$, $Q(x,t)$ and $q(x,t)$ presented in section 5.1. The term $\hat{\zeta}(x,t) = 2\hat{v}(x,t)$ for MSS and OCS is found from the difference between Equations (2.15) and (3.31b). It follows that as the boundary conditions for the tangent equation are periodic, so too are the boundary conditions for Equation (6.1). Therefore, the co-state and control can be decomposed in a similar fashion

$$\hat{\lambda}(x,t) = \sum_{l=-\infty}^{\infty} \tilde{\hat{\lambda}}_l(t) e^{il\frac{2\pi}{L}x} \quad \text{and} \quad \hat{\zeta}(x,t) = \sum_{l=-\infty}^{\infty} \tilde{\hat{\zeta}}_l(t) e^{il\frac{2\pi}{L}x}.$$

where $\tilde{\hat{\lambda}}_l(t), \tilde{\hat{\zeta}}_l(t) \in \mathbb{C}$.

Defining the adjoint co-state energy as $\hat{\mathcal{E}}(t) = \int_0^L \hat{e}(x,t)\mathrm{d}x$ and multiplication of Equation (6.1) with $\hat{\lambda}(x,t)$ and integration over the domain leads to

$$\begin{aligned}\frac{\mathrm{d}\hat{\mathcal{E}}(t)}{\mathrm{d}t} = \\ \int_0^L \Bigg(-c\hat{\lambda}(x,t)\frac{\partial\hat{\lambda}(x,t)}{\partial x} - \hat{\lambda}(x,t)\frac{\partial\left(u(x,t)\hat{\lambda}(x,t)\right)}{\partial x} + 2\hat{e}(x,t)\frac{\partial u(x,t)}{\partial x} + \\ \hat{\lambda}(x,t)\hat{\omega}(t)f(x,t) + \hat{\lambda}(x,t)\frac{\partial^2\hat{\lambda}(x,t)}{\partial x^2} + \\ +\hat{\lambda}(x,t)\frac{\partial^4\hat{\lambda}(x,t)}{\partial x^4} + \hat{\lambda}(x,t)\frac{1}{T}\frac{\partial J(u(x,t),p)}{\partial u(x,t)} + \hat{\lambda}(x,t)\hat{\zeta}(x,t)\Bigg)\,\mathrm{d}x.\end{aligned} \tag{6.2}$$

Integration of the fourth term of the right hand side of Equation (6.2) by parts leads to

$$\int_0^L \hat{\lambda}(x,t)\frac{\partial^2\hat{\lambda}(x,t)}{\partial x^2}\mathrm{d}x = \int_0^L -\left(\frac{\partial\hat{\lambda}(x,t)}{\partial x}\right)^2\mathrm{d}x,$$

which is always negative. Since the adjoint equations are solved backwards in time, this negative term acts as a production term. Similarly, integration of the fifth term by parts twice leads to

$$\int_0^L \hat{\lambda}(x,t)\frac{\partial^4\hat{\lambda}(x,t)}{\partial x^4}\mathrm{d}x = \int_0^L \left(\frac{\partial^2\hat{\lambda}(x,t)}{\partial x^2}\right)^2\mathrm{d}x,$$

which is always positive, but backwards in time acts as a dissipation term. Following the same approach as the tangent formulation the first adjoint NV term, which modifies the production of adjoint co-state energy, is

$$\hat{\zeta}(x,t) = -\hat{\mu}_P\frac{\partial^2\hat{\lambda}(x,t)}{\partial x^2},$$

where $\hat{\mu}_P \in \mathbb{R}^+$ is a tuning parameter. When this value is larger than one this term counteracts the production due to $\hat{P}(x,t)$, and utilising this control term in the NV method is referred to as adjoint NV_P in this thesis. The second adjoint NV term, which modifies the dissipation of adjoint energy, is

$$\hat{\zeta}(x,t) = \hat{\mu}_D\frac{\partial^4\hat{\lambda}(x,t)}{\partial x^4},$$

where $\hat{\mu}_D \in \mathbb{R}^+$ is a tuning parameter, utilising this control term in the NV method is referred to as adjoint NV_D in this thesis.

	$K_x = 60$		$K_x = 120$		$K_x = 180$	
	Tangent	Adjoint	Tangent	Adjoint	Tangent	Adjoint
$\Delta T = 1 \times 10^{-3}$	0.003037	0.098168	0.003153	0.057134	0.002938	0.002705
$\Delta T = 1 \times 10^{-4}$	0.001031	0.040315	0.001153	0.028382	0.001052	0.001059
$\Delta T = 1 \times 10^{-5}$	0.001029	0.004872	0.001045	0.001691	0.001027	0.001025

TABLE 6.1: Sensitivity generated by Tangent and Adjoint OCS for $\Delta T \in \{1 \times 10^{-3}, 1 \times 10^{-4}, 1 \times 10^{-5}\}$ and $K_x \in \{60, 120, 180\}$

6.2 Sensitivities generated by the adjoint OCS and NV formulations

From the derivation presented in section 3.4 it is expected that α would behave in an identical manner to the tangent form. This is investigated in this section. The values of sensitivity generated by the adjoint formulations as a function of their respective tuning parameters, left column, and the squared norm of the adjoint co-state solution for a range of tuning parameters, right column, are presented in Figure 6.1 for OCS, top row, NV_P, middle row, and NV_D, bottom row.

The first major difference between the tangent and adjoint OCS formulations is the difference in the profile of the sensitivity as a function of α, Figures 5.2a and 6.1a respectively. The tangent profile is always negative and below that of the expected value whereas the adjoint profile starts positive then decreases as α increases until around $\alpha = 1 \times 10^5$ until the sensitivity increases. The main reason for this is to do with discrete and continuous adjoint formulations, where details can be found in Ref. [87]. Essentially, the discrete adjoint approach finds the exact adjoint of the tangent OCS that has been implemented and should reproduce the sensitivity exactly. The continuous adjoint, on the other hand, implements the adjoint equations and is not guaranteed, given the same discretisation, to compute the same sensitivity profile as the discrete adjoint approach or the tangent OCS formulation. The two approaches do compute identical sensitivity values as $\Delta t \to 0$ and $K_x \to \infty$. Table 6.1 shows this. Here the continuous formulation is utilised and, therefore, the sensitivity profiles generated by tangent OCS and adjoint OCS are different.

It can be seen that the behaviour of the adjoint formulation shares features with the tangent formulation presented in section 5.2. The bias in the sensitivity is, again, due to the initial condition of the non-linear solution. When $\alpha < 1 \times 10^2$ the solution is showing signs of being over-damped. Similarly, when $\alpha > 1 \times 10^8$ the solution is under-damped, as seen in the solution norms, Figure 6.1b, and leads to inaccurate sensitivities. In between these values the control applied is able to stabilise the solution and results in accurate sensitivities. These are different to the tangent OCS formulation where under-damping occurs at $\alpha > 5 \times 10^6$, again due to the continuous adjoint formulation being utilised. This analysis can be seen in the squared norm

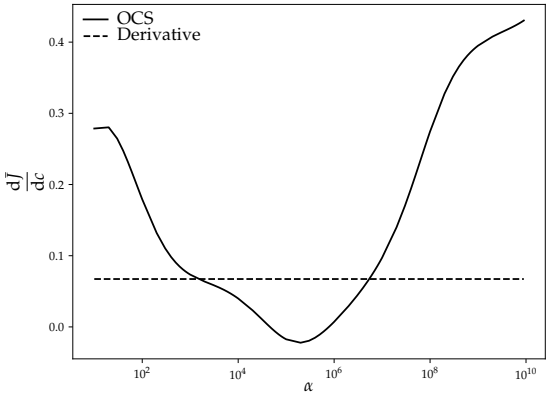

(A) $\frac{d\bar{J}}{dc}$ against α generated by OCS, solid line, and the curve fit derivative, dashed line.

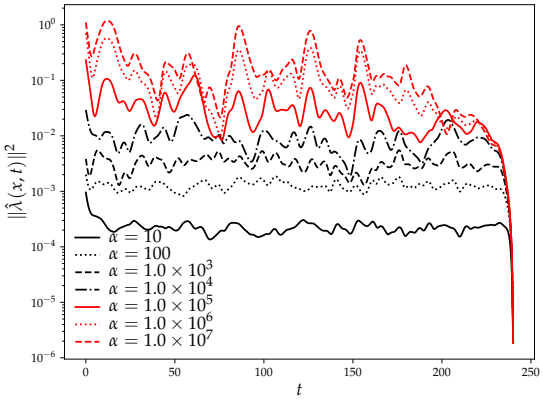

(B) $\|\hat{\lambda}(x,t)\|^2$ for $\alpha \in \{10, 100, 1\times10^3, 1\times10^4, 1\times10^5, 1\times10^6, 1\times10^7\}$

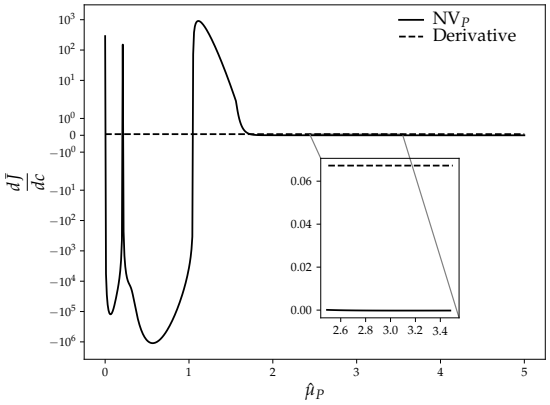

(C) $\frac{d\bar{J}}{dc}$ against $\hat{\mu}_P$ generated by NV_P, solid line, and the curve fit derivative, dashed line.

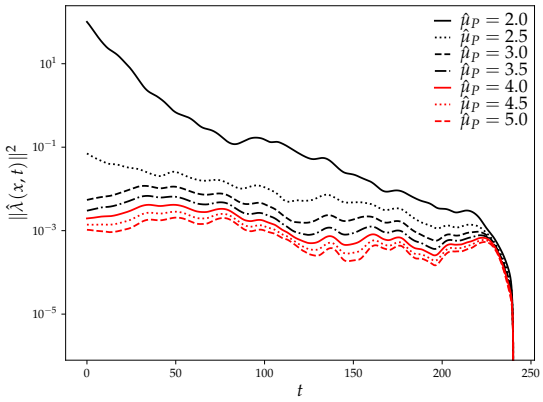

(D) $\|\hat{\lambda}(x,t)\|^2$ for $\hat{\mu}_P \in \{2, 2.5, 3, 3.5, 4, 4.5, 5\}$

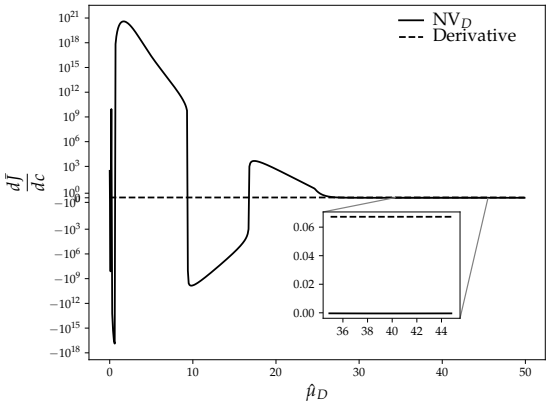

(E) $\frac{d\bar{J}}{dc}$ against $\hat{\mu}_D$ generated by NV_D, solid line, and the curve fit derivative, dashed line.

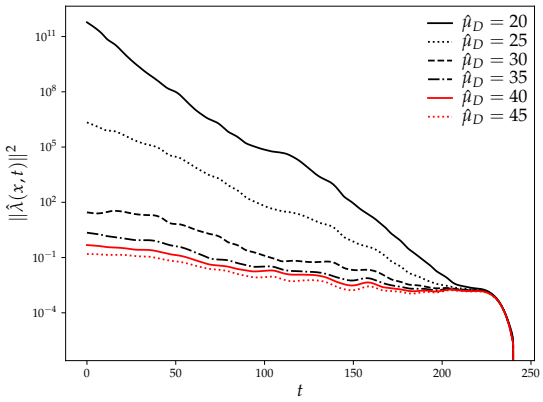

(F) $\|\hat{\lambda}(x,t)\|^2$ for $\hat{\mu}_D \in \{20, 25, 30, 35, 40, 45\}$

FIGURE 6.1: $\frac{d\bar{J}}{dc}$, left column, and $\|\hat{\lambda}(x,t)\|^2$, right column, for different values of tuning parameters generated by adjoint OCS, top row, NV_P, middle row, and NV_D, bottom row.

profiles which have very similar behaviour to the tangent formulation presented previously. With small values of α the solution does not exhibit exponential growth, and increasing the value increases the squared norm.

The behaviour of adjoint NV_P is very similar to that of NV_P. Too small a value for $\hat{\mu}_P$ and the control is unable to stabilise the solution. This leads to the sensitivity value generated being inaccurate. As $\hat{\mu}_P$ is increased the solution is stabilised more and the method produces sensitivity values that are in good agreement with the curve fit derivative of Figure 5.1. This behaviour is also seen for the adjoint NV_D case.

6.3 Adjoint co-state spatio-temporal structures generated by OCS, NV and MSS

This section investigates the similarities in co-state solutions generated by the adjoint formulations of MSS, OCS and NV. This is undertaken to gain a better understanding of the behaviour of the methods and to link to the analysis undertaken on the tangent formulation. In this section, the adjoint co-state spatio-temporal structures generated by adjoint MSS, panel (A), and the squared norm of this value, panel (B), are presented in Figure 6.2. It is worth noting that the adjoint MSS formulation has initial

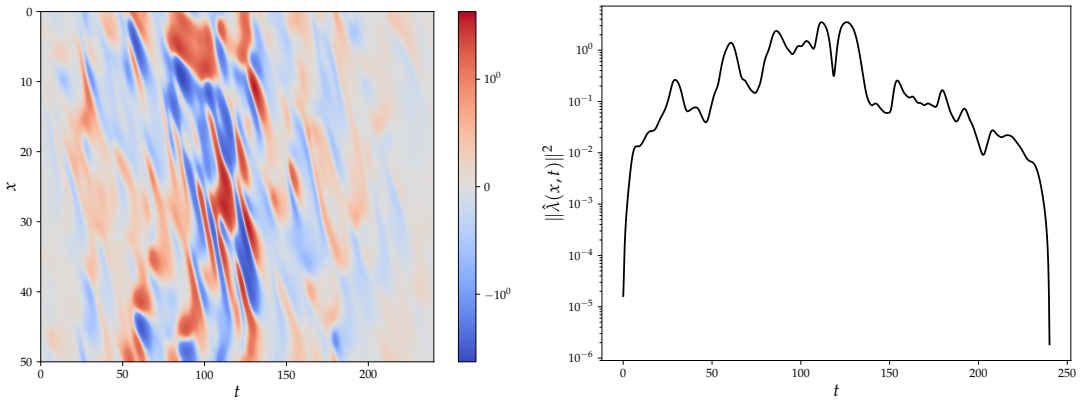

(A) (B)

FIGURE 6.2: $\hat{\lambda}(x,t)$, panel (A), and $\|\hat{\lambda}(x,t)\|^2$, panel (B), of the adjoint solution generated by MSS.

and terminal constraints on $\hat{\lambda}(x,t)$. Further, the solution generated by MSS is of similar order of magnitude to that generated by the tangent formulation along with the sensitivity values generated being similar.

The spatio-temporal structures and squared norm of the solution generated using adjoint OCS are shown in Figure 6.3. It can be seen that when $\alpha = 50$ the solutions

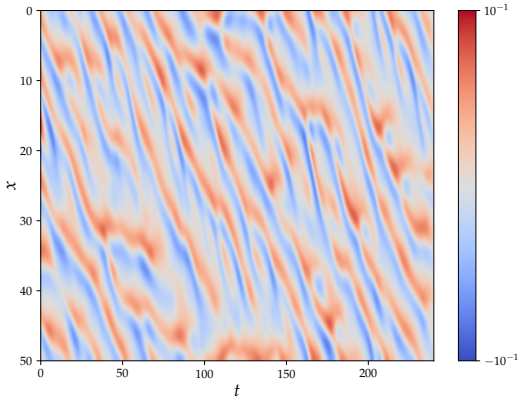

(A) $\hat{\lambda}(x,t)$ generated by OCS for $\alpha = 50$.

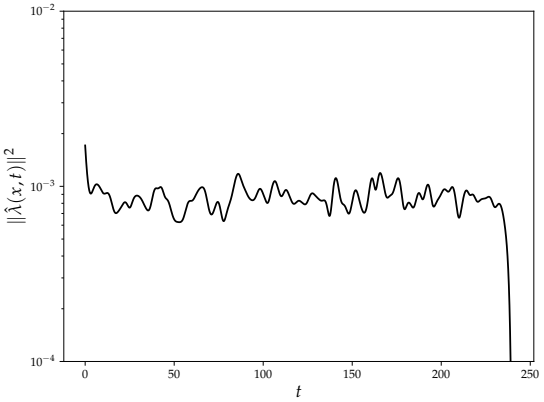

(B) $\|\hat{\lambda}(x,t)\|^2$ generated by OCS for $\alpha = 50$.

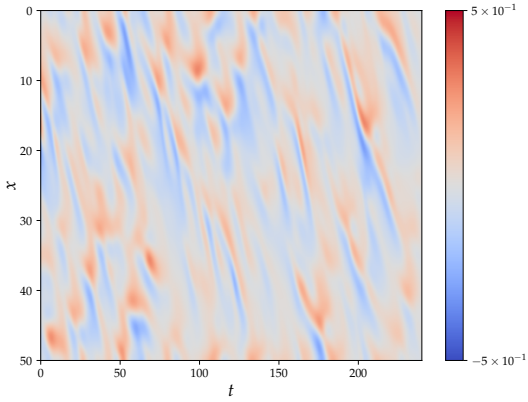

(C) $\hat{\lambda}(x,t)$ generated by OCS for $\alpha = 5000$.

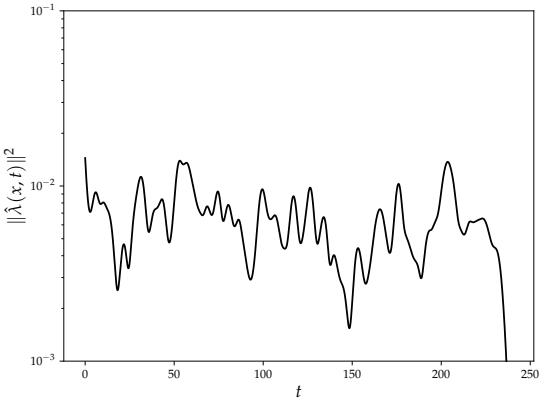

(D) $\|\hat{\lambda}(x,t)\|^2$ generated by OCS for $\alpha = 5000$.

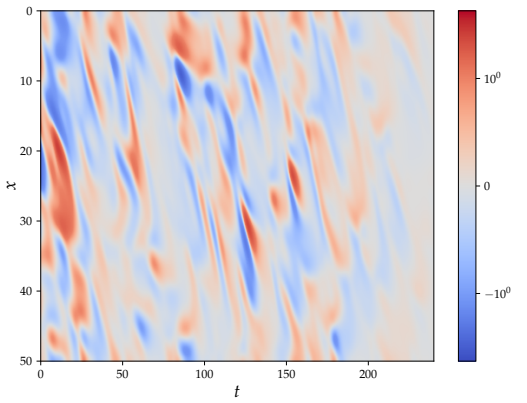

(E) $\hat{\lambda}(x,t)$ generated by OCS for $\alpha = 5 \times 10^6$.

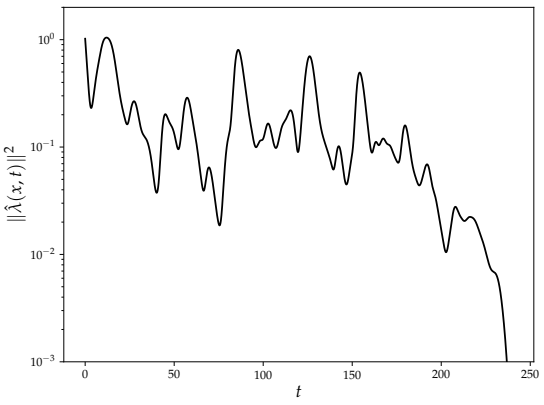

(F) $\|\hat{\lambda}(x,t)\|^2$ generated by OCS for $\alpha = 5 \times 10^6$.

FIGURE 6.3: $\hat{\lambda}(x,t)$, left column, and $\|\hat{\lambda}(x,t)\|^2$, right column, of the adjoint solution generated by OCS for $\alpha = 50$, top row, $\alpha = 5000$, middle row, and $\alpha = 5 \times 10^6$, bottom row.

generated by OCS shares a large similarity with the non-linear solution, Figure 4.7. The explanation for this is that the forcing term in the adjoint formulation is $\frac{2u(x,t)}{T}$ and similarity is expected. This solution shares little similarity with the solution generated by MSS outside of the central quarter of the time horizon. Further, the solution has a constant magnitude throughout the time horizon and is significantly lower than the MSS solution implying the solution is over-damped. Increasing α to 5000 results in a solution that starts to resemble the spatio-temporal features of MSS but at a reduced magnitude. Further, the solution does not exhibit signs of exponential growth as shown in the relatively constant squared norm of the solution. Finally, when $\alpha = 5 \times 10^6$ the solution's spatio-temporal structures are closest to MSS and no longer resemble the non-linear solution. This solution is showing signs of exponential growth as the squared norm of the solution is increasing backwards in time suggesting an under-damped solution.

The wider implication is that, while the tangent formulation of OCS finds a similar approximate Shadowing direction as MSS for a large proportion of the time horizon, this is not necessarily the case when using the adjoint formulation. The MSS, Ref. [19], and OCS, chapter 3, formulations were developed to minimise the tangent norm. Adjoint formulations were then derived from these which leads to a difference in temporal boundary condition between the methods. This difference between the temporal boundary conditions could be an explanation for the visual differences between the solutions generated. One method to test this hypothesis is to formulate the Shadowing minimisation problem for the adjoint equation and allow the adjoint temporal boundary conditions to vary, *i.e.* an "adjoint Shadowing direction". It is argued that this method may produce adjoint solutions which are more similar to those produced by OCS more in line with conclusions drawn from the tangent analysis. Another argument for the difference is that OCS found an approximate Shadowing direction that was similar but not exactly the same as MSS and that this difference is amplified in the adjoint solutions.

The analysis is repeated for $\hat{\mu}_P \in \{1, 2.5, 5\}$ using the same conditions as before. Results are shown in Figure 6.4. The behaviour of adjoint NV_P is again similar to that of the tangent NV_P. When $\hat{\mu}_P = 1.0$, the control is unable to stabilise the solution. This leads to the squared norm of the adjoint co-state solution increasing exponentially backwards in time. Further, the spatio-temporal structures generated share no similarities with MSS and are predominantly composed of long wavelength features. Increasing $\hat{\mu}_P$ to 2.5 provides some better control, however the squared norm of the solution is still increasing backwards in time. The magnitude of the solution is also an order of magnitude smaller than MSS but still shows signs of exponential growth. This suggests that the solution may not be applying control in a targeted or optimal manner. As in the previous case the spatio-temporal structures do not resemble that of MSS. When $\hat{\mu}_P = 5.0$, the squared norm of the adjoint co-state shows adequate

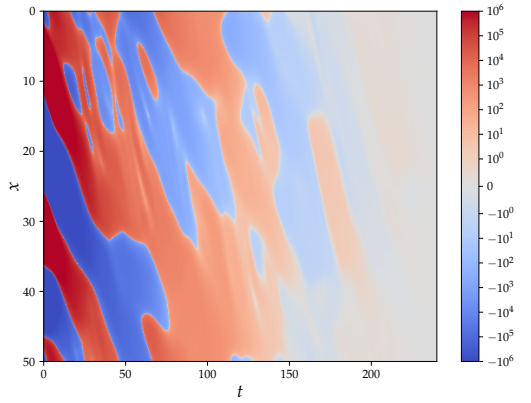

(A) $\hat{\lambda}(x,t)$ generated by adjoint NV$_P$ for $\hat{\mu}_P = 1$.

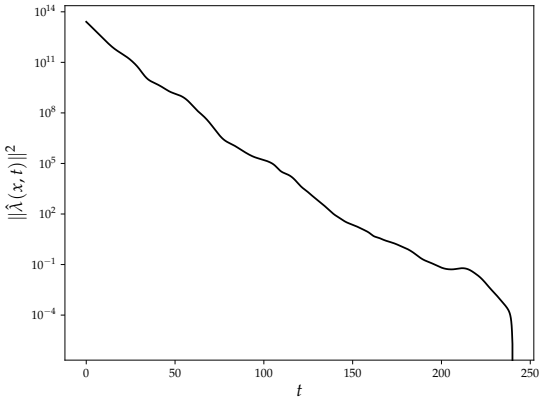

(B) $\|\hat{\lambda}(x,t)\|^2$ generated by adjoint NV$_P$ for $\hat{\mu}_P = 1$.

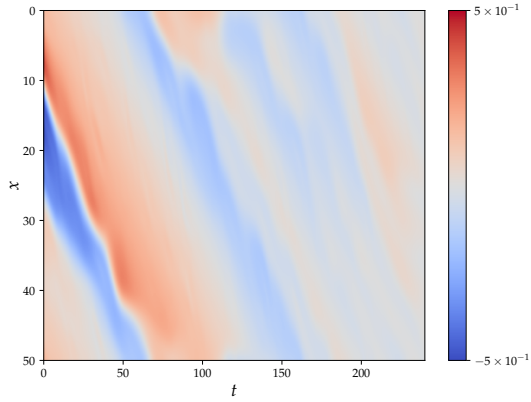

(C) $\hat{\lambda}(x,t)$ generated by adjoint NV$_P$ for $\hat{\mu}_P = 2.5$.

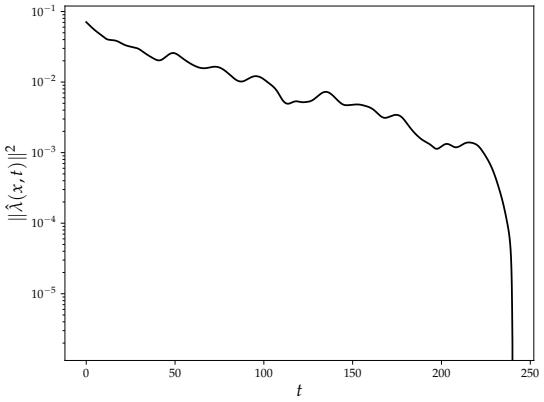

(D) $\|\hat{\lambda}(x,t)\|^2$ generated by adjoint NV$_P$ for $\hat{\mu}_P = 2.5$.

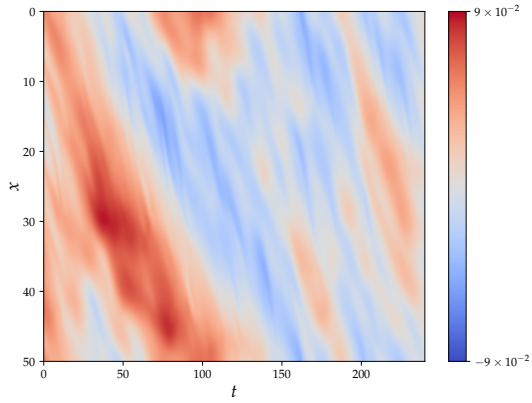

(E) $\hat{\lambda}(x,t)$ generated by adjoint NV$_P$ for $\hat{\mu}_P = 5$.

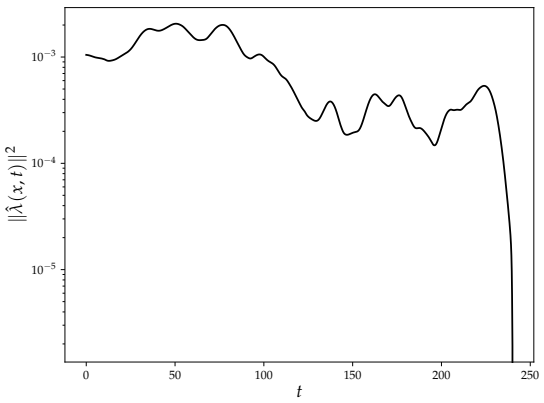

(F) $\|\hat{\lambda}(x,t)\|^2$ generated by adjoint NV$_P$ for $\hat{\mu}_P = 5$.

FIGURE 6.4: $\hat{\lambda}(x,t)$, left column, and $\|\hat{\lambda}(x,t)\|^2$, right column, of the adjoint solution generated by NV$_P$ for $\hat{\mu}_P = 1$, top row, $\hat{\mu}_P = 2.5$, middle row, and $\hat{\mu}_P = 5$, bottom row.

stabilisation of the solution. This suggests that the solution is stabilised to a value which is several orders of magnitude smaller than MSS. The spatio-temporal structures also has some shorter wavelengths present similar to those in MSS. This analysis suggests that, as in the tangent formulation, the NV methods derived from the adjoint energy equation may not be able to find approximate Shadowing direction. This could be due to the large amount of control applied resulting in a discrepancy between the adjoint equation and non-linear equation, Ref. [49]. One other explanation could be that while these NV methods attempt to stabilise the adjoint solution whereas Shadowing minimise the tangent solution and then find the corresponding adjoint.

6.3.1 Similarity in adjoint co-state spatio-temporal structures

In this section the angle between solutions generated by MSS, OCS and NV is found. This provides more objective comparison between the solutions than comparing visually the solutions. In this section the metric used to compare the adjoint co-state solutions of OCS and NV with MSS is

$$\hat{\theta}_X(t) = \arccos\left(\frac{\langle \hat{\lambda}_{\text{MSS}}(x,t), \hat{\lambda}_X(x,t)\rangle}{\|\hat{\lambda}_{\text{MSS}}(x,t)\|\|\hat{\lambda}_X(x,t)\|}\right),$$

where $\hat{\lambda}_X(x,t)$ is the adjoint co-state solution generated by OCS or NV_P and $\hat{\lambda}_{\text{MSS}}(x,t)$ from MSS. This metric determines the angle between the two solutions where values of 0 mean the solutions are identical and values of $\frac{\pi}{2}$ mean the solutions are orthogonal and dissimilar. The solution generated by MSS is used as a reference for the approximate Shadowing direction. Similar behaviour is seen between the NV_P and NV_D methods. The comparison between MSS and OCS, $\hat{\theta}_{\text{OCS}}(t)$, for a range of α values is shown in panel (A) and the comparison between NV_P and MSS, $\hat{\theta}_{\text{NV}_P}(t)$, for a range of $\hat{\mu}_P$ values in panel (B) of Figure 6.5.

It can be seen that unlike the tangent OCS formulation the adjoint variant diverges away from MSS. The explanation for this is that MSS has initial and terminal constraints whereas OCS only has the terminal constraint. Therefore, the MSS solution is modified significantly to satisfy these conditions which leads to an OCS solution that is dissimilar to MSS. It is argued that adjoint OCS finds an "adjoint Shadowing direction" whereas adjoint MSS finds the adjoint corresponding to the tangent Shadowing direction. This difference leads to the two solutions, while finding the similar time averaged sensitivity values, producing different adjoint solutions. This is not necessarily an issue as the sensitivity generated by both methods are similar. Comparison of the OCS solution to the "adjoint Shadowing direction", discussed previously, may provide OCS solutions in better agreement with MSS.

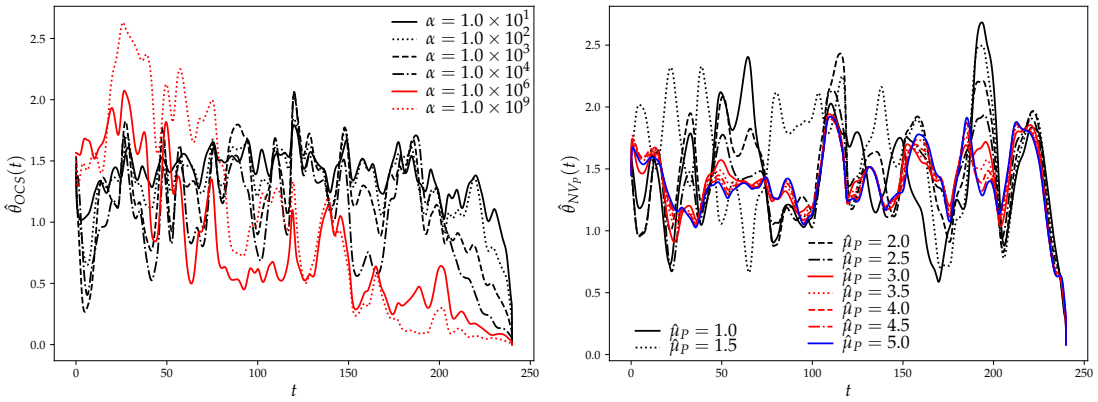

(A) (B)

FIGURE 6.5: $\hat{\theta}_{OCS}(t)$ for $\alpha = 1.0 \times 10^1$, solid black line, $\alpha = 1.0 \times 10^2$, dotted black line, $\alpha = 1.0 \times 10^3$, dashed black line, $\alpha = 1.0 \times 10^4$, dash dotted black line, $\alpha = 1.0 \times 10^5$, solid red line, and $\alpha = 1.0 \times 10^9$, dotted red line, panel (A), and $\hat{\theta}_{NV_P}(t)$ for $\hat{\mu}_P = 1$, solid black line, $\hat{\mu}_P = 1.5$, dotted black line, $\hat{\mu}_P = 2$, dashed black line, $\hat{\mu}_P = 2.5$, dash dotted black line, $\hat{\mu}_P = 3$, solid red line, $\hat{\mu}_P = 3.5$, dotted red line, $\hat{\mu}_P = 4$, dashed red line, $\hat{\mu}_P = 4.5$, dash dotted red line, and $\hat{\mu}_P = 5$, solid blue line, panel (B).

Similar to Figure 5.6b, there is very little similarity between the MSS and NV_P solutions for all values of $\hat{\mu}_P$ investigated for the majority of the time horizon. There is similarity towards the end of the time horizon which is caused by the similarity in terminal conditions. This, again, implies that these methods are non-optimal and potentially better control terms can be found.

6.4 Adjoint control spatio-temporal structures generated by OCS, NV and MSS

This section repeats the analysis of section 6.3 using the control terms instead. The rationale for this is to gain a better understanding of the methods along with showing the analysis presented is identical for the adjoint and tangent forms. Through examining Equation (3.31b) generated by OCS and comparing it to Equation (2.15), it can be seen that the main difference, disregarding the $\hat{\omega}(t)\mathbf{f}(\mathbf{u}(t,p),p)$ term, is $2\hat{\mathbf{v}}(t)$. This thesis refers to this term as the adjoint control term. The reason why this term is referred to as a control term is that it acts to stabilise the adjoint solution. This term is present both in MSS and OCS. In this section the spatio-temporal structures of the control term, $2\hat{v}(x,t)$, for MSS and the squared norm of this are shown in panel (A) and panel (B), respectively, of Figure 6.6. It can be seen that the amount of control applied by MSS is negligible across the entire domain. The implications are that MSS is applying control in a targeted and specific manner targeting certain features in the

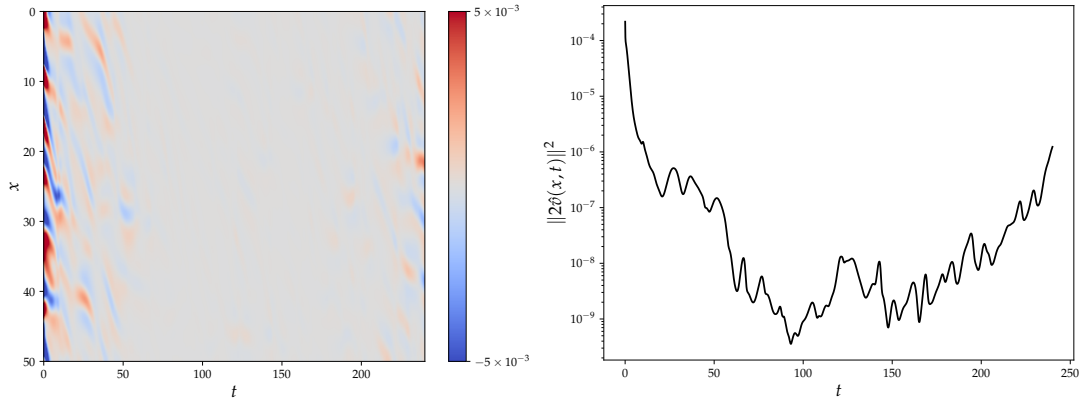

(A) (B)

FIGURE 6.6: $2\hat{v}(x,t)$, panel (A), and $\|2\hat{v}(x,t)\|^2$, panel (B), of the adjoint solution generated by MSS.

solution. It is argued that these features are the unstable sub-space. A larger amount is applied near the start of the time horizon and smaller towards the end.

The spatio-temporal structure, left column, of the control term, $2\hat{v}(x,t)$, for OCS and its squared norm, right column, are shown in Figure 6.7 for $\alpha \in \{50, 5000, 5 \times 10^6\}$, rows. The main feature across all values of α is the reduced amount of control applied compared to the tangent formulation. The argument for this is that the terminal conditions on the adjoint co-state between OCS and MSS are identical and, therefore, minimal amounts of control are required to keep the solution stable. It can be seen that the control applied when $\alpha = 50$ shares similar features to the non-linear solution. Similar to the co-state solution, the control applied by OCS shares no resemblance to the solution generated by MSS. Further, the amount of control is orders of magnitude larger than MSS, suggesting the solution is over-damped. Increasing α to 5000 results in a control solution that is starting to not resemble the non-linear solution. As in the tangent formulation, increasing α reduces the amount of control applied and is also the case here. Further, the amount of control applied is relatively constant throughout the time horizon. Finally, when $\alpha = 5 \times 10^6$ the control applied is reduced further for the majority of the time horizon and increases towards the end implying the solution is under-damped. The argument for this is that OCS stabilises the solution onto an "adjoint Shadowing direction". This is the inverse of MSS where the majority is applied initially. It can also be seen that, on average, the amount of control is orders of magnitude smaller than when $\alpha = 5000$ and is comparable to the amount of control applied by MSS. The implication of this is that MSS is applying control in a more targeted fashion. This is because OCS, while still applying similar amounts of control, has an under-damped co-state solution and inaccurate sensitivity values whereas MSS

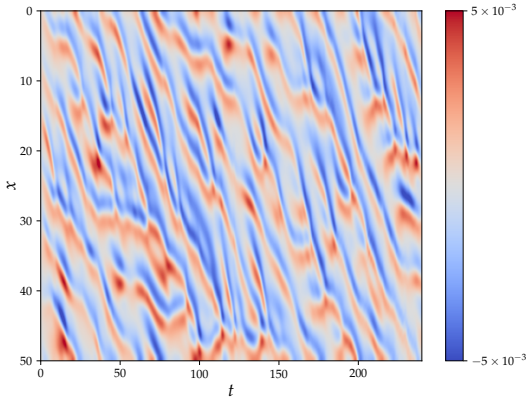

(A) $2\hat{v}(x,t)$ generated by OCS for $\alpha = 50$.

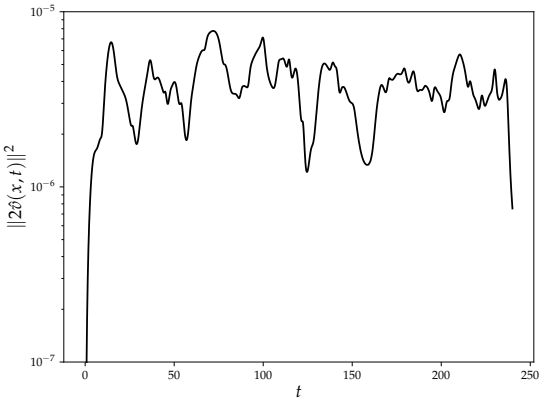

(B) $\|2\hat{v}(x,t)\|^2$ generated by OCS for $\alpha = 50$.

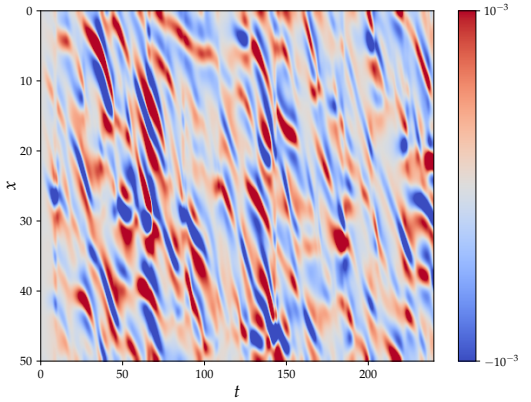

(C) $2\hat{v}(x,t)$ generated by OCS for $\alpha = 5000$.

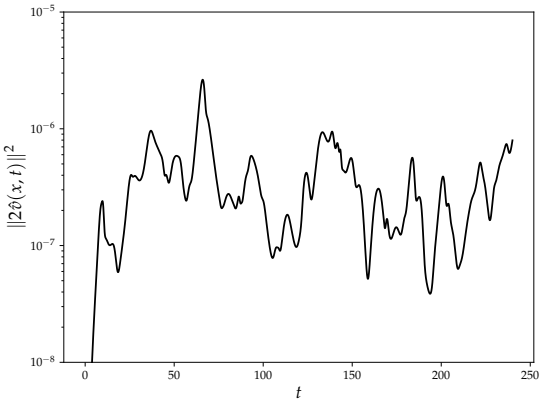

(D) $\|2\hat{v}(x,t)\|^2$ generated by OCS for $\alpha = 5000$.

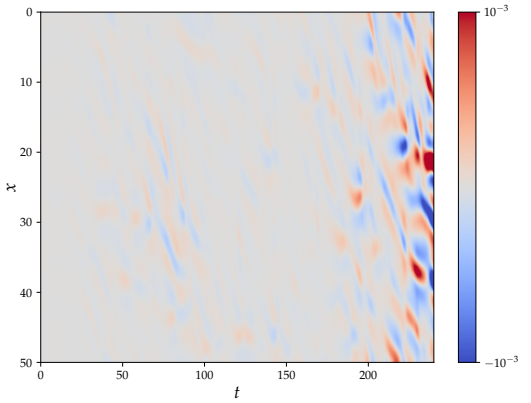

(E) $2\hat{v}(x,t)$ generated by OCS for $\alpha = 5 \times 10^6$.

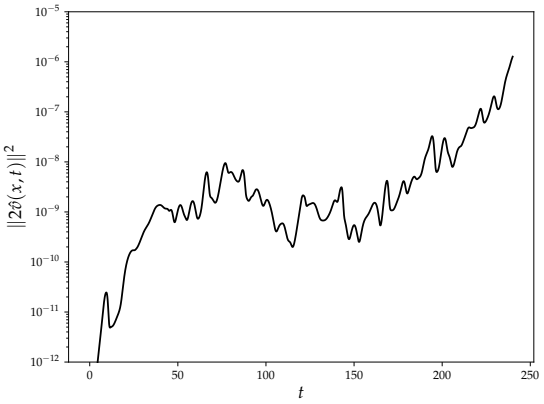

(F) $\|2\hat{v}(x,t)\|^2$ generated by OCS for $\alpha = 5 \times 10^6$.

FIGURE 6.7: $2\hat{v}(x,t)$, left column, and $\|2\hat{v}(x,t)\|^2$, right column, of the adjoint solution generated by OCS for $\alpha = 50$, top row, $\alpha = 5000$, middle row, and $\alpha = 5 \times 10^6$, bottom row.

has a stabilised solution and accurate sensitivity. This suggests that the adjoint OCS form is non-optimal.

Similarly, the spatio-temporal structures of the NV_P approach, $-\hat{\mu}_P \frac{\partial^2 \hat{\lambda}(x,t)}{\partial x^2}$, and its squared norm are shown in Figure 6.8 for $\hat{\mu}_P \in \{1, 2.5, 5\}$. As a general observation, the amount of control applied by NV_P is orders of magnitude larger than MSS. This suggests that NV methods, derived using the adjoint energy budget, are non-optimal and alternative methods can stabilise the solution for less control. As in the tangent formulation case, when $\hat{\mu}_P = 1$ there is insufficient control to stabilise the solution which is applied in a general sense. The implication of this is that the control does not target specific structures within the solution that contribute to production of adjoint energy. This leads to the amount of control being applied increasing exponentially backwards in time implying an under-damped solution. The control applied is also composed of shorter wavelengths in comparison to the adjoint co-state solution, which is related to the stable sub-space, Ref. [118], and more optimal control would apply control on the unstable sub-space.

Increasing $\hat{\mu}_P$ to 2.5 leads to a solution that does not exhibit such extreme exponential growth and some features in the control that are similar to Figure 4.7. There still, however, is a gradual increase in the amount of control applied backwards in time. Finally, when $\hat{\mu}_P = 5$ the control that is applied is able to stabilise the solution. The amount of control applied is orders of magnitude less than the other two cases but still larger than MSS or OCS. Further, the control applied strongly resembles that of Figure 4.7. This implies that the control, which acts at these shorter wavelength features, are not as optimal as those which apply control at longer wavelengths. The observation that control applied by NV methods investigated here is larger than OCS or MSS suggests that this approach of stabilisation could be improved and one which, as shown in the section 5.5, acts on the adjoint energy producing terms would be beneficial.

6.4.1 Similarity in adjoint control spatio-temporal structures

This thesis developed OCS as a bridge between Shadowing and NV methods. It was shown for the tangent formulation that OCS produces a solution similar to MSS. To help explain why the adjoint solutions are dissimilar between MSS, OCS and NV the angle between the control solutions is investigated. The angle between OCS and MSS is

$$\hat{\theta}^q_{OCS}(t) = \arccos\left(\frac{\langle 2\hat{v}_{MSS}(x,t), 2\hat{v}_{OCS}(x,t)\rangle}{\|2\hat{v}_{MSS}(x,t)\|\|2\hat{v}_{OCS}(x,t)\|}\right),$$

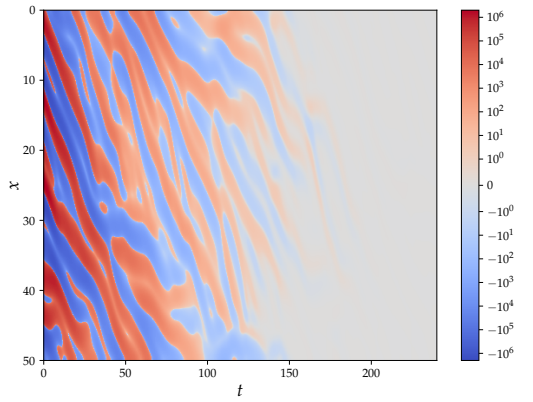

(A) $-\hat{\mu}_P \frac{\partial^2 \hat{\lambda}(x,t)}{\partial x^2}$ generated by adjoint NV_P for $\hat{\mu}_P = 1$.

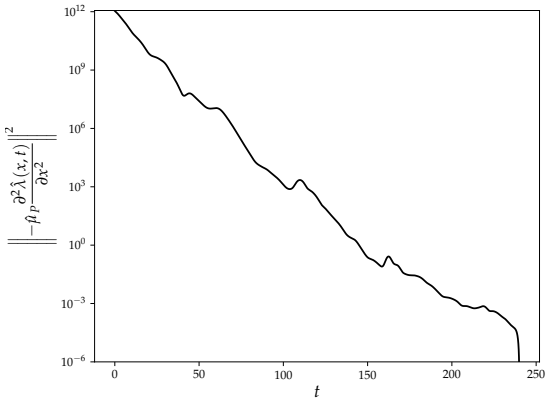

(B) $\left\| -\hat{\mu}_P \frac{\partial^2 \hat{\lambda}(x,t)}{\partial x^2} \right\|^2$ generated by adjoint NV_P for $\hat{\mu}_P = 1$.

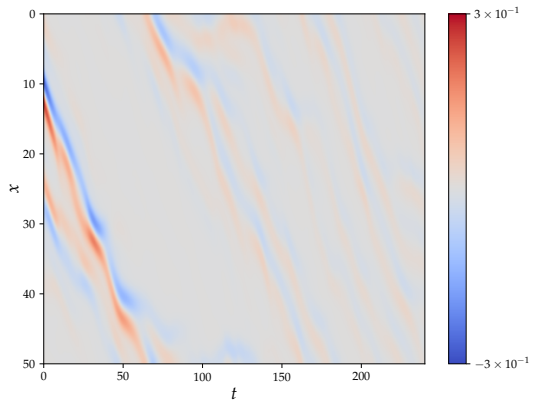

(C) $-\hat{\mu}_P \frac{\partial^2 \hat{\lambda}(x,t)}{\partial x^2}$ generated by adjoint NV_P for $\hat{\mu}_P = 2.5$.

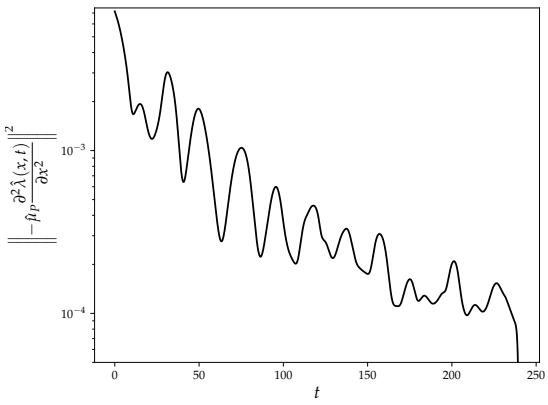

(D) $\left\| -\hat{\mu}_P \frac{\partial^2 \hat{\lambda}(x,t)}{\partial x^2} \right\|^2$ generated by adjoint NV_P for $\hat{\mu}_P = 2.5$.

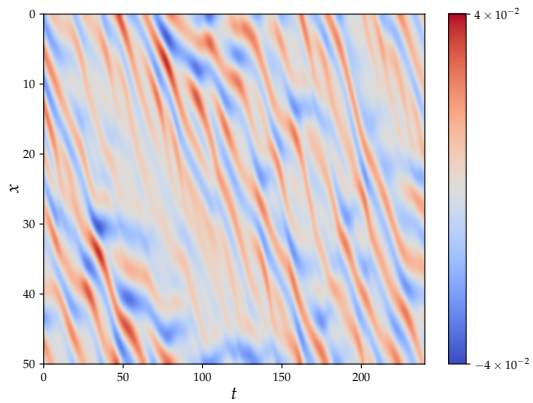

(E) $-\hat{\mu}_P \frac{\partial^2 \hat{\lambda}(x,t)}{\partial x^2}$ generated by adjoint NV_P for $\hat{\mu}_P = 5$.

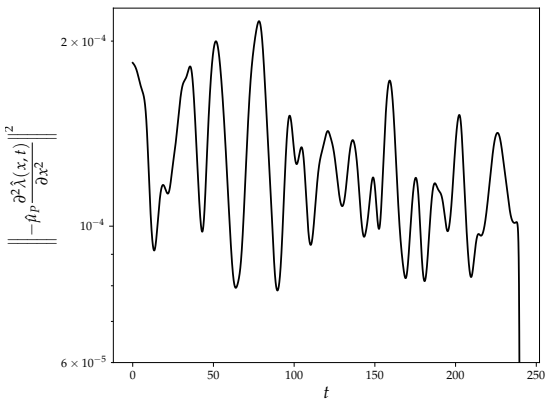

(F) $\left\| -\hat{\mu}_P \frac{\partial^2 \hat{\lambda}(x,t)}{\partial x^2} \right\|^2$ generated by adjoint NV_P for $\hat{\mu}_P = 5$.

FIGURE 6.8: $-\hat{\mu}_P \frac{\partial^2 \hat{\lambda}(x,t)}{\partial x^2}$, left column, and $\left\| -\hat{\mu}_P \frac{\partial^2 \hat{\lambda}(x,t)}{\partial x^2} \right\|^2$, right column, of the adjoint solution generated by NV_P for $\hat{\mu}_P = 1$, top row, $\hat{\mu}_P = 2.5$, middle row, and $\hat{\mu}_P = 5$, bottom row.

and for NV_P and MSS is

$$\hat{\theta}^q_{NV}(t) = \arccos\left(\frac{\left\langle 2\hat{v}_{MSS}(x,y,t), -\hat{\mu}_P \frac{\partial^2 \hat{\lambda}(x,t)}{\partial x^2}\right\rangle}{\|2\hat{v}_{MSS}(x,y,t)\| \left\|-\hat{\mu}_P \frac{\partial^2 \hat{\lambda}(x,t)}{\partial x^2}\right\|}\right).$$

These angles determines how similar the control solutions generated by OCS and NV are with MSS. An angle of 0 means the control solutions are identical and a value of $\frac{\pi}{2}$ means they are dissimilar. The results of these metrics can be seen for a range of α values for OCS, panel (A), and range of $\hat{\mu}_P$ values for NV_P, panel (B), in Figure 6.9. As

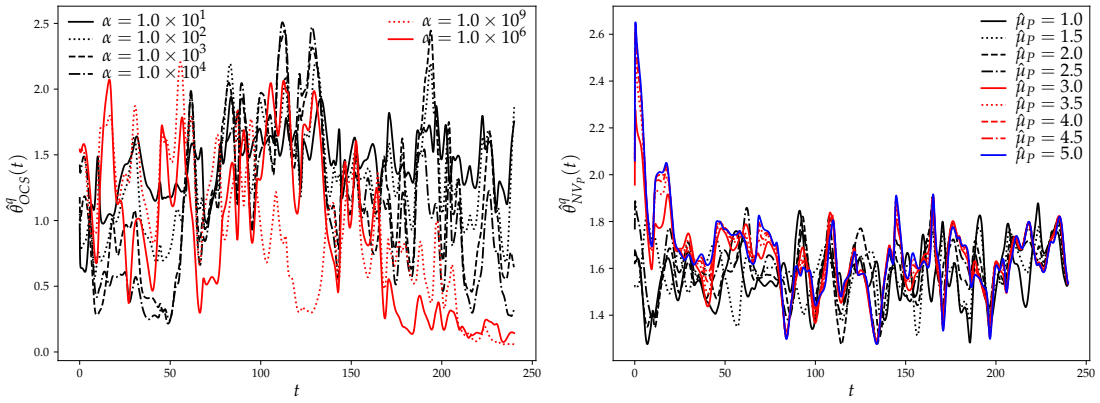

(A) (B)

FIGURE 6.9: $\hat{\theta}^q_{\mathrm{OCS}}(t)$ for $\alpha = 1.0 \times 10^1$, solid black line, $\alpha = 1.0 \times 10^2$, dotted black line, $\alpha = 1.0 \times 10^3$, dashed black line, $\alpha = 1.0 \times 10^4$, dash dotted black line, $\alpha = 1.0 \times 10^5$, solid red line, and $\alpha = 1.0 \times 10^9$, dotted red line, panel (A), and $\hat{\theta}^q_{\mathrm{NV}_P}(t)$ for $\hat{\mu}_P = 1$, solid black line, $\hat{\mu}_P = 1.5$, dotted black line, $\hat{\mu}_P = 2$, dashed black line, $\hat{\mu}_P = 2.5$, dash dotted black line, $\hat{\mu}_P = 3$, solid red line, $\hat{\mu}_P = 3.5$, dotted red line, $\hat{\mu}_P = 4$, dashed red line, $\hat{\mu}_P = 4.5$, dash dotted red line, and $\hat{\mu}_P = 5$, solid blue line, panel (B).

in the co-state similarity there is little to no resemblance of the control applied by OCS to MSS for the majority of the time horizon. There is a similarity in the final tenth of the time horizon, which is caused by OCS and MSS sharing the same terminal conditions. As in the co-state analysis it is argued that this difference is caused by the difference in temporal boundary conditions on the co-state solution. Regardless of which value for $\hat{\mu}_P$ selected there is no similarity between the control solution generated by MSS and NV_P as seen in the values of $\hat{\theta}^q_{\mathrm{NV}_P}(t)$ being, on average $\frac{\pi}{2}$. The interpretation of this is that the solutions are orthogonal and share no similar characteristics. This implies that NV methods, derived from the adjoint energy budget, are non-optimal suggesting that alternative methods would be beneficial.

6.5 Spectral analysis of the adjoint equation

In section 5.5 it was shown that the tangent OCS formulation applies control which acts on wavenumbers where production of tangent energy dominated dissipation. This, it is argued, is a feature of the method and relates to the application of control in the unstable sub-space. To show that this is a feature of the method spectral analysis is undertaken on the adjoint equation. In section 6.1, various terms ($\hat{I}(x,t)$, $\hat{C}(x,t)$, $\hat{P}(x,t)$, $\hat{D}(x,t)$ and $\hat{Q}(x,t)$) were derived. The wavenumber decomposition for each of these terms is presented in Figure 6.10 for MSS, panel (A), OCS, panel (B), NV_P, panel (C), and NV_D, panel (D). The value of the tuning parameters are $\alpha = 500$, $\hat{\mu}_P = 2.5$ and $\hat{\mu}_D = 31.0$ for consistency with the analysis drawn in section 5.5. In general,

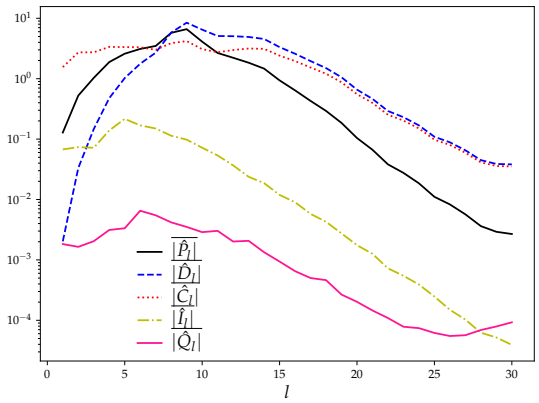

(A) Power spectra of the adjoint equation terms produced by MSS.

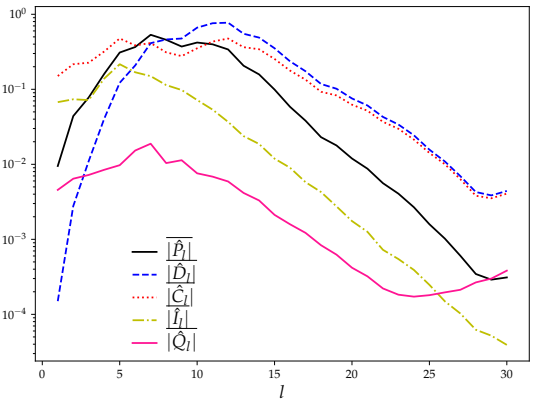

(B) Power spectra of the adjoint equation terms produced by OCS.

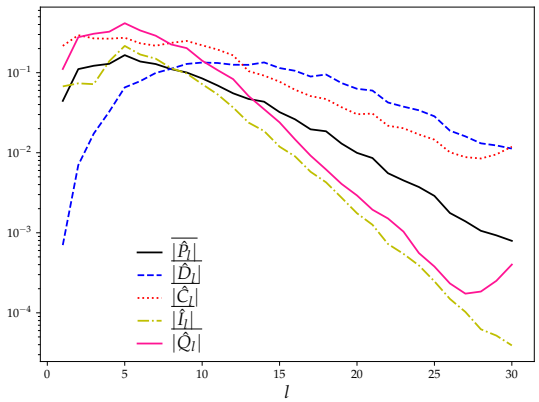

(C) Power spectra of the adjoint equation terms produced by NV_P.

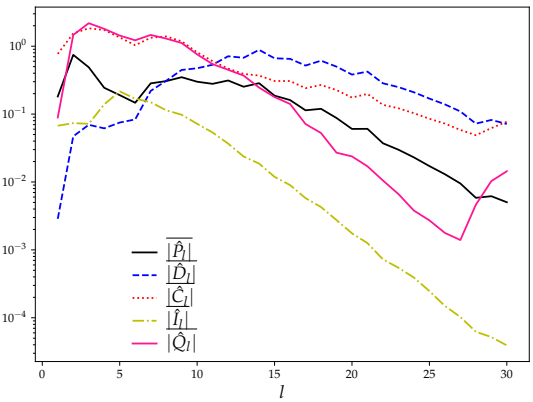

(D) Power spectra of the adjoint equation terms produced by NV_D.

FIGURE 6.10: Comparison of the power spectra of the adjoint equation produced by various methods. Panel (A) is generated by MSS, panel (B) by OCS, panel (C) by NV_P and panel (D) by NV_D.

$\hat{C}(x,t)$ along with $\hat{I}(x,t)$ act on the longest wavelengths and decrease for shorter

wavelengths. The wavenumber at which dissipation dominates production is, again, $l = 8$, similar to the tangent formulation, section 5.5. The control applied by MSS, $2\hat{v}(x,t)$, is predominantly in the wavenumbers where production dominates dissipation and reduced elsewhere. This, it is argued, implies MSS applies control targeting the unstable sub-space and minimal control is applied on the stable and neutral sub-spaces. The power spectra of the unstable sub-space, Figure 3 of Ref. [118], is dominant at smaller wavenumbers which are predominantly the modes which OCS and MSS apply control along implying OCS and MSS target and control these features. Similar to the tangent formulation, the control applied by OCS is in the wavenumbers where production of adjoint energy dominates dissipation. The wavenumbers where control is applied by OCS also shares similarities with MSS suggesting these methods are very similar in behaviour. Further, the amount of control applied by OCS is larger than MSS suggesting that OCS is non-optimal. For both the NV cases the amount of control applied is significantly larger than MSS or OCS and occasionally is the largest contribution along certain wavenumbers, $l = 5$ for example. The implication of this is that both NV methods apply control across all sub-spaces and do not specifically target the unstable sub-space. This suggests that the NV methods investigated here are non-optimal. In general, the main conclusion of this analysis is that, similar to the tangent formulation, the NV terms should act at wavelengths where production dominates dissipation and minimal elsewhere, *i.e.* targeting the unstable sub-space.

6.6 Summary

It was shown in chapter 5 that tangent OCS shares similar features with both Shadowing and NV methods. In industry, it is common to require the sensitivity of a function of interest with respect to multiple parameters. The tangent OCS formulation produces the sensitivity for a single parameter which led to the development of the adjoint OCS formulation. A comparison between the adjoint formulations of MSS, OCS and NV was undertaken to determine what, if any, features of Shadowing or OCS could provide a more optimal NV control term. This was undertaken through the comparison of the co-state and control fields generated by each method along with wavenumber analysis of the individual terms in the adjoint equation.

The adjoint energy equation was derived and utilised to determine two NV terms which were the adjoint variants of the NV terms used in the tangent OCS analysis. This approach is common in the literature. The sensitivity generated by these methods was compared against the expected values and showed similarities with the tangent formulation. There are differences in the sensitivity profile produced as a function of α compared to the tangent formulation of OCS and this was caused by the continuous adjoint approach being utilised instead of the discrete adjoint. It was found that as the

time step and grid spacing reduced, the discrete and continuous adjoint solutions, not reported here, produced identical results down to machine precision. This result is in good agreement with the literature, Ref. [87].

The co-state solutions generated by OCS were compared to solutions generated by MSS for a range of α values. Small values of α produced solutions which did not look visually similar to MSS. This was caused by the large amount of control applied which resulted in an over-damped solution. The solutions produced by OCS were an order of magnitude smaller than MSS. Increasing α led to solutions which visually resembled those of MSS along with the magnitudes being similar. On average, the angle between the solutions generated by OCS and MSS was $\frac{\pi}{2}$ throughout the entire time horizon. This suggests that the adjoint formulation of OCS finds an "adjoint Shadowing direction" whereas MSS finds an adjoint solution corresponding to the tangent Shadowing direction. The adjoint MSS formulation is derived from the tangent MSS formulation which minimises the tangent solution through modification of the tangent temporal boundary conditions and leads to two temporal boundary conditions on the adjoint solution. OCS, on the other hand, only has one temporal boundary condition on the adjoint solution and it is this difference that it argued to be the cause of the difference between solutions. One method to test this, which was not investigated here, is to formulate MSS to minimise the growth of the adjoint solution through relaxation on its temporal boundary conditions, *i.e.* find an "adjoint Shadowing direction". It was argued that this approach may lead to an increased similarity between the adjoint MSS and OCS solutions as in the tangent formulation. This analysis was repeated for NV where small values of the tuning parameter led to a solution which was not stabilised and visually dissimilar to MSS. Increasing the tuning parameter stabilised the solutions which did not look visually similar to MSS. Further, the angle between solutions generated by NV and MSS was, on average, $\frac{\pi}{2}$ similar to the tangent case. This suggests that NV methods derived using the adjoint energy budget are non-optimal. Further, the large amount of control produces an adjoint solution that relates to a slightly modified non-linear solution, Ref. [49], which could also be a cause of the discrepancy between MSS and NV solutions.

The analysis was repeated for the control terms. In the adjoint formulation there is a control term in the MSS solution and its structure is $2\hat{v}(x,t)$. Therefore, the control solutions that were generated by OCS for a range of α values were compared to MSS. The main feature is that the amount of control applied by the adjoint formulation is orders of magnitude smaller than the tangent formulation. This suggests that in some sense the temporal boundary conditions used in the adjoint formulation are more optimal and closer to a stabilised solution which requires smaller control. The reason for this is that the terminal condition on the co-state solution for OCS is identical to that of MSS and, therefore, minimal control is required to keep the solution stable. Further, the control applied by small values of α share some resemblance to the

non-linear solution and not MSS. The quantity of control applied is orders of magnitude larger than MSS for small values of α implying an over-damped solution. Increasing α further produced control of similar orders of magnitude to MSS with visually similar spatial structures except that the adjoint solution was under-damped. This result implies that, when OCS applied similar magnitude of control to MSS, the application of control in OCS is not as targeted as that in MSS and that its application could be improved further. MSS applied the majority of control towards the beginning of the time horizon whereas OCS applies the largest amount towards the end of the time horizon implying OCS stabilises the solution onto an "adjoint Shadowing direction".

As in the co-state solutions the angle between the control generated by OCS and MSS was around $\frac{\pi}{2}$. The outcome of this analysis is that, again, the control applied by OCS is non-optimal. This analysis was repeated for the NV control term where small values of the tuning parameter led to large amounts of control being applied which increased backwards in time. Increasing the tuning parameters led to smaller amounts of control being applied. The control applied by the NV methods was at a smaller wavelength than the adjoint solution. This suggested that the majority of the control is being applied in the stable sub-space. One interpretation of this is that the NV methods are applying general control and not in a targeted manner. Further benefits could be seen if control is developed to target specific features relating to production of adjoint energy. As in the co-state solutions the angle between the control terms generated by NV and MSS was $\frac{\pi}{2}$ throughout the time horizon implying sub-optimal control.

Finally, a wavenumber analysis of the adjoint equation was undertaken. The control applied by MSS was predominantly smaller than all other methods and acted on wavenumbers where production of adjoint energy dominated dissipation and was reduced outside this region. This suggests that MSS is applying control to target the unstable covariant Lyapunov vectors and specifically targeting the unstable sub-space. Further, the control applied by OCS shared the same behaviour as MSS but with a larger magnitude implying OCS is not as optimal in its application of control as MSS. Conclusions drawn for the adjoint case are similar to those for the tangent OCS formulation in that OCS applies targeted control with similar features to MSS. This implies that NV methods should also have this feature which was not found in the NV methods investigated here as control was applied across all wavelengths. Determination of the wavelengths of production and dissipation of adjoint energy may be computationally expensive and, therefore, prohibit the development of these methods. Further, this analysis was possible as spectra of the covariant Lyapunov vectors have been published prior. For systems where these are unfeasible would result in NV methods that could not apply control in the unstable sub-space.

Chapter 7

Decomposition of OCS onto covariant Lyapunov vectors for the KS system

It is well known, Ref. [125] and section 2.3, that the solutions generated by MSS decompose onto the covariant Lyapunov vectors (CLVs). These CLVs span the tangent/adjoint space and with help from the Lyapunov exponents (LEs) determine stable, unstable and neutral sub-spaces, Refs. [6, 7, 50, 51, 72, 95, 112, 131]. Various Shadowing methods, Refs. [14, 22, 65, 88, 91, 92, 93, 125], have been developed as linear combinations of these CLVs yet there has been little to no reporting of the composition of the generated tangent/adjoint solutions in terms of the CLVs. Here, it is argued that these CLVs could provide a deeper insight into the behaviour of these methods and could help inform structures or features of NV methods. In this section the CLVs and LEs are calculated for the Kuramoto-Sivashinsky (KS) system and analysis is provided. There has been limited research into adjoint CLVs in general and this section adds to this literature by providing details and analysis of the adjoint CLVs for the KS system. These CLVs are then used to decompose the solution fields generated by MSS, OCS and NV and are used to provide a deeper understanding of the methods.

7.1 Validation of covariant Lyapunov vectors and Lyapunov exponents

The Kuptsov and Parlitz algorithm, Ref. [72] and Appendix A, is used for the computation of CLVs, $\gamma_k(x,t)$ and $\hat{\gamma}_k(x,t)$, and LEs, Λ_k. This is undertaken on $T = 240$ time units on a domain size of $L = 50$ using $K_x = 60$ grid points. As

mentioned in section A.1, due to the method of selecting initial conditions for the CLVs/adjoint CLVs, $\gamma_k(t)$ and $\hat{\gamma}_k(t)$ for $k = 0, 1, \ldots, n_v - 1$, the 'spin up' time must be sufficiently long enough to allow them time to align with their respective sub spaces. Therefore, a method to determine when these have aligned is required.

One such approach is to fix the end of the 'spin up' time to $t_B = 1000$ and make multiple runs from $t_A \in (0, 950)$ and compare the values of $\gamma_k(t_B)$ from the different starting initial starting times. This can be seen in Figure 7.1. The metric used here to

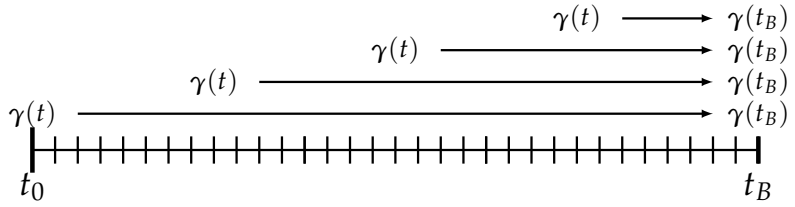

FIGURE 7.1: An approach to determing the 'spin up' time for backward CLV sub-space alignment.

determine convergence of the CLVs to their respective sub-spaces is to use the following metric

$$\theta_k = \arccos\left(\frac{\langle \gamma_k(x, t_B)_\tau, \gamma_k(x, t_B)_{1000} \rangle}{\|\gamma_k(x, t_B)_\tau\| \|\gamma_k(x, t_B)_{1000}\|}\right),$$

where $\gamma_k(x, t_B)_{1000}$ refers to the CLV at time t_B that has been simulated for a 'spin up' time of 1000 time units and $\gamma_k(x, t_B)_\tau$ to the CLV at time t_B that has a 'spin up' time of $\tau = 1000 - t_A$ time units. When θ_k is close to 0 it means the two CLVs are aligned and are assumed here to be converged to their respective sub-space. Conversely, when the value of θ_k is $\frac{\pi}{2}$ it means the CLVs are orthogonal and dissimilar and are determined to have not converged to their respective sub-spaces. The results of this convergence from $t_A \in (0, 950)$ are shown in Figure 7.2. When τ is small the CLVs are not aligned with the longest 'spin up' time case. It can be seen that when the τ is increased the CLVs are aligned with the longest 'spin up' time case. It can be concluded that when the 'spin up' time is 1000 time units the CLVs are aligned with their respective sub-spaces and are converged. The same process for the adjoint CLVs was undertaken, not reported here, but backwards in time and it was found that the time taken for the CLVs to align was very similar to the adjoint CLVs.

Having found the 'spin up' time that results in converged CLVs, the LE spectrum for the KS system is shown in Figure 7.3. This shows a very similar structures to that of Figure 1 presented in Ref. [132] and Figure 8 in Ref. [59]. Note at this point that here $L = 50$ is used, similar to that used in Ref. [59], whereas Ref. [132] uses $L = 96$. There are 6 positive exponents where $\Lambda_0 = 0.086$ is the largest. There are two neutral modes, $\Lambda_6 = \Lambda_7 = 0$ which theoretically correspond to $\gamma_6(x, t) = f(x, t)$ and $\gamma_7(x, t) = \frac{\partial u(x,t)}{\partial x}$. Here the value of $f(x, t)$ is the right hand side of Equation (4.3). This can be validated

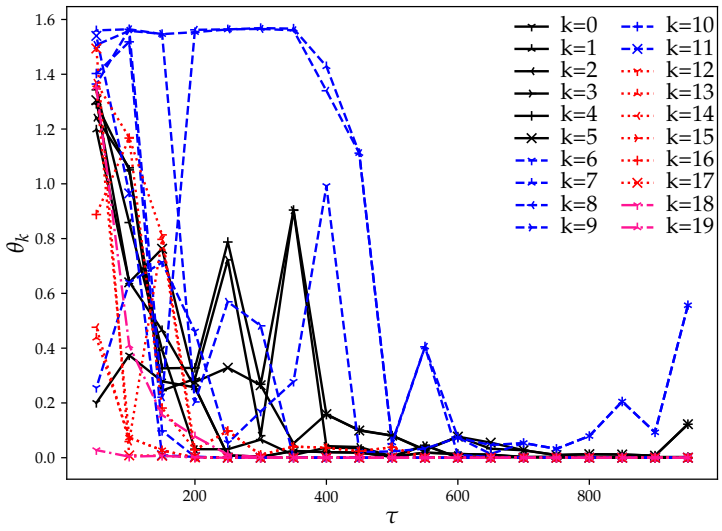

FIGURE 7.2: Convergence rates of $\gamma_k(x, t_B)_\tau$ for various 'spin up' times.

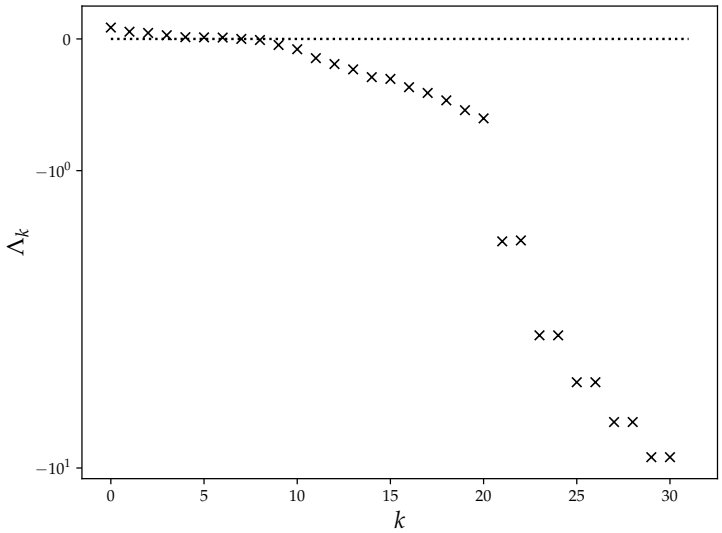

FIGURE 7.3: Lyapunov exponent, Λ_k, associated to each CLV mode.

by substitution of these into Equation (A.10). These CLVs can be thought of as being caused by the property of the system and to translational symmetry in the x direction. However, the algorithms used to generate these modes have difficulty in splitting the two neutral modes as their growth is identical, and the computed modes end up being a linear combination of the two theoretical modes and is the cause for the large angle at large τ values in Figure 7.2. Therefore, the space spanned by the computed neutral CLVs is the space spanned by the theoretical CLVs. There is a range of negative exponents, Λ_8 to Λ_{20}, which relate to physical and stable modes of the system, see Ref. [132]. Following this, the exponents come in pairs Λ_k and Λ_{k+1} having the same LE value for $k > 20$. This is caused by these modes being "isolated" and are high

frequency sine cosine pairs, see Ref. [132]. A range of spatio-temporal structures are shown in Figure 7.4 which, again, shows similar behaviours to those shown in Figure 2 in Ref. [118].

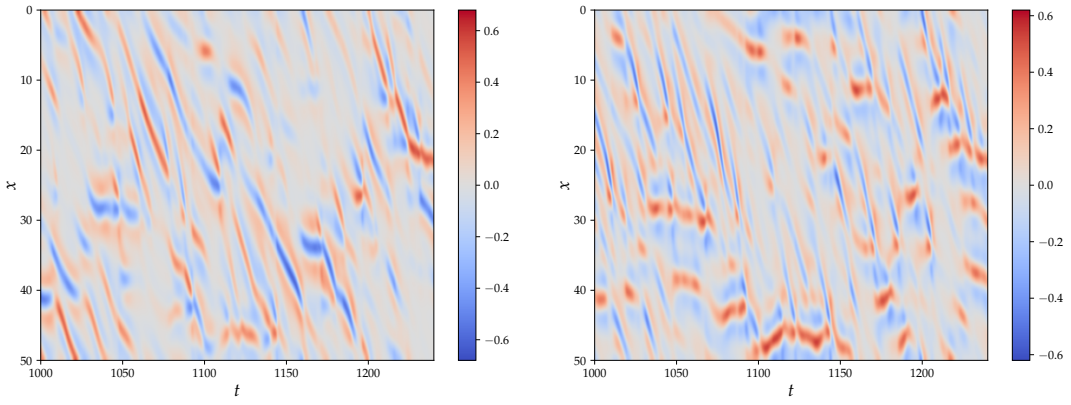

(A) Spatio-temporal structure of $\gamma_0(x,t)$.

(B) Spatio-temporal structure of $\gamma_5(x,t)$.

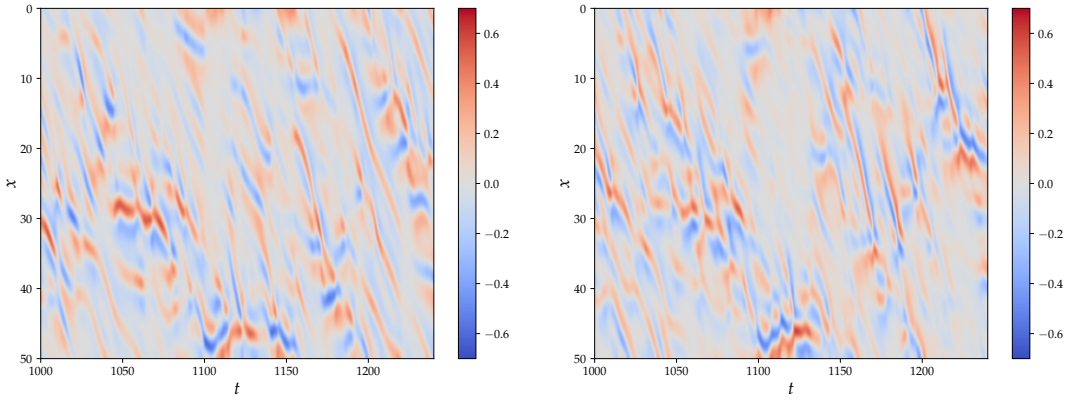

(C) Spatio-temporal structure of $\gamma_{10}(x,t)$.

(D) Spatio-temporal structure of $\gamma_{15}(x,t)$.

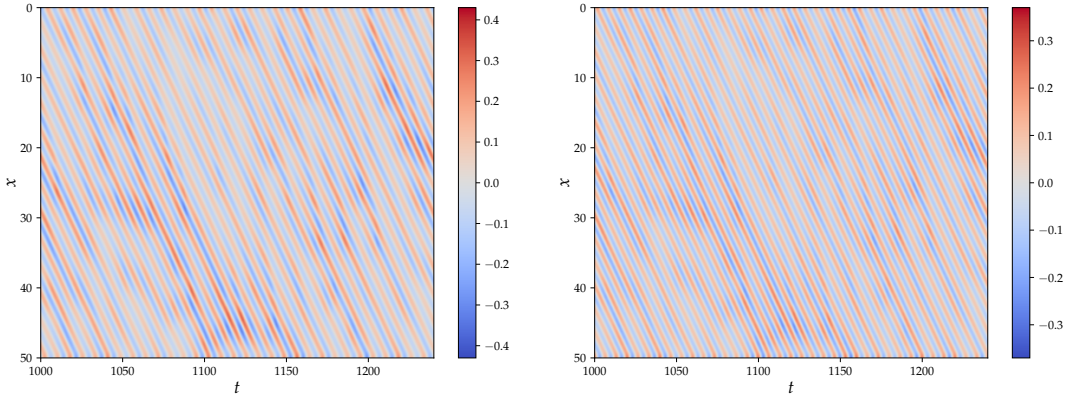

(E) Spatio-temporal structure of $\gamma_{25}(x,t)$.

(F) Spatio-temporal structure of $\gamma_{30}(x,t)$.

FIGURE 7.4: Spatio-temporal structures of $\gamma_k(x,t)$ for $k \in \{0,5,10,15,25,30\}$.

The spatial power spectra for the CLVs are also computed which shows similar

structures to that presented in Figure 3 of Ref. [118] and are shown in Figure 7.5. It can

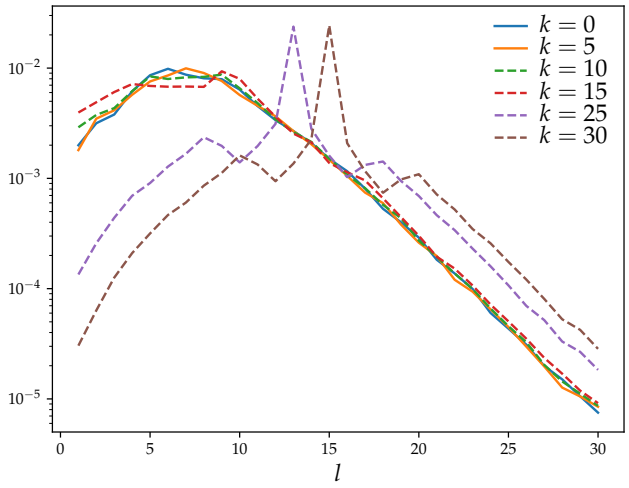

FIGURE 7.5: Power spectrum for each wavenumber, l, of $\gamma_k(x,t)$ for $k \in \{0,5,10,15,25,30\}$, where the solid lines represent a positive LE and the dashed represent a negative LE.

be seen that for large k the power spectrum is dominated by one wavenumber. As k increases this dominant wavenumber increases also. To provide further validation the time averaged angle between CLVs are shown in Figure 7.6. These angles are again in

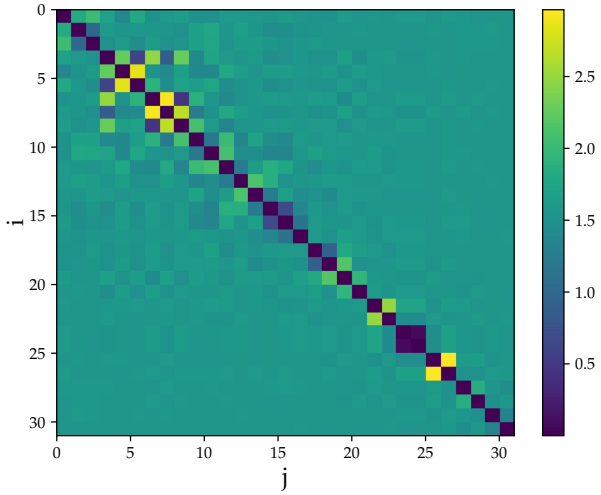

FIGURE 7.6: $\left|\arccos\left(\frac{\langle\gamma_i(x,t),\gamma_j(x,t)\rangle}{\|\gamma_i(x,t)\|\|\gamma_j(x,t)\|}\right)\right|$ between pairs of CLV modes.

very good agreement with Figure 4 in Ref. [118]. When the modes are in the physical region there is an angle between all pairs of CLVs. This is not the case when the

modes are in the "isolated" and high frequency regime and the only angle is between the sine cosine pairs.

As part of the Kuptsov and Parlitz algorithm the adjoint CLVs, $\hat{\gamma}_k(x,t)$, are also able to be computed. To the author's knowledge there has been no presentation of adjoint CLVs, $\hat{\gamma}_k(x,t)$, for this system and the spatio-temporal structures, Figure 7.7, their power spectra, Figure 7.8, and the time averaged angle between pairs of CLVs, Figure 7.9, are shown. The properties of $\hat{\gamma}_k(x,t)$ are very similar to that of $\gamma_k(x,t)$. It can be seen that, unlike the CLVs, the adjoint CLVs do not resemble the non-linear solution when $k < 20$. Outside of this region the CLVs are, again, dominated by high frequency structures similar to those of the CLVs. A similar argument can be made that these modes are "isolated" and not physical. This is, again, confirmed by the power spectra between the CLVs and the adjoint CLVs having a very similar structure. Further, the angle between the adjoint CLVs has a very similar profile to that of the CLVs.

One important characteristic of the covariant Lyapunov vectors is bi-orthogonality, Ref [72], where in general

$$\left\langle \gamma_i(t), \hat{\gamma}_j(t) \right\rangle = \delta_{ij} C_{ij}(t), \tag{7.1}$$

where δ_{ij} is the Kronecker delta and $C_{ij}(t)$ is a constant. The CLVs, in this thesis, are being utilised as a tool for understanding the behaviour of the Shadowing and NV methods. The implications of the bi-orthogonality is that as opposed to solving a large linear system of equations for the influence of each CLV on the solution the only CLV and associated adjoint CLV are required to compute the influence of the k^{th} CLV on the solution. This reduces the requirement for computation of all CLV modes, which can be computationally expensive. One other implication of this bi-orthogonality is that it is well known that orthogonality between the CLV and its adjoint are present when homoclinic tangencies are present, Ref. [72]. These tangencies correspond to CLVs becoming collinear, Ref. [50, 131]. The implications of this is that the accuracy of the influence of the CLVs when tangencies are present is reduced.

7.2 Decomposition of the solutions onto the covariant Lyapunov vectors

To gain better understanding of the structure of the forcing $\frac{\partial u(x,t)}{\partial x}$, tangent $v(x,t)$, and control $q(x,t)$ terms the decomposition of these onto the CLVs is computed. The rationale for undertaking this decomposition is to find if there are any structures or features present in MSS or OCS that can be utilised to inform a better choice of NV term. These features, if present, could produce a more accurate NV method, similar to the accuracy of Shadowing methods but without the computational cost, which

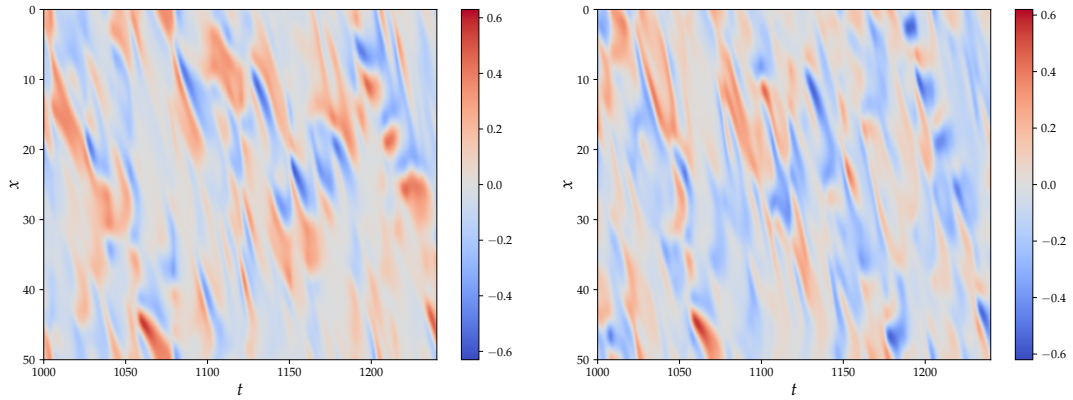

(A) Spatio-temporal structure of $\hat{\gamma}_0(x,t)$.

(B) Spatio-temporal structure of $\hat{\gamma}_5(x,t)$.

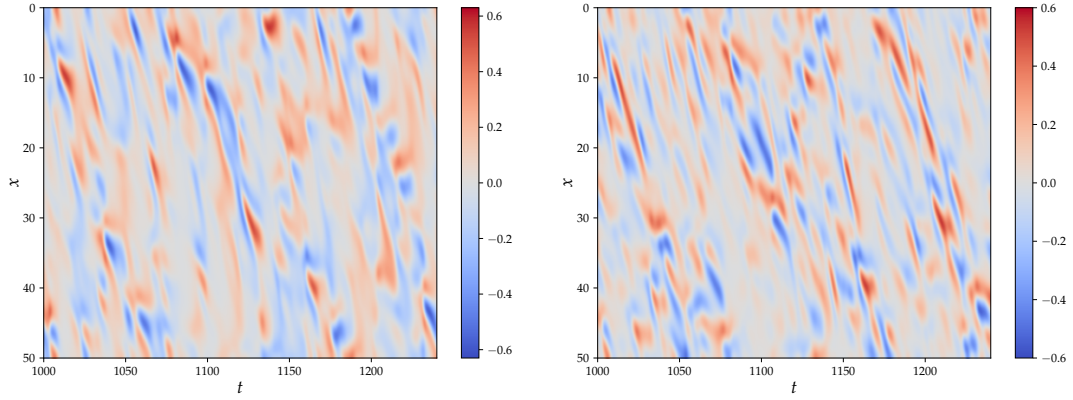

(C) Spatio-temporal structure of $\hat{\gamma}_{10}(x,t)$.

(D) Spatio-temporal structure of $\hat{\gamma}_{15}(x,t)$.

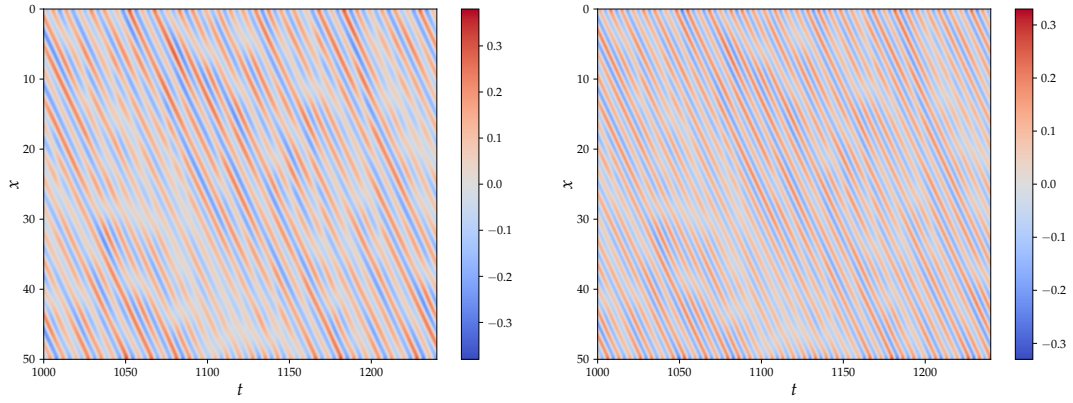

(E) Spatio-temporal structure of $\hat{\gamma}_{25}(x,t)$.

(F) Spatio-temporal structure of $\hat{\gamma}_{30}(x,t)$.

FIGURE 7.7: Spatio-temporal structures of $\hat{\gamma}_k(x,t)$ for $k \in \{0,5,10,15,25,30\}$.

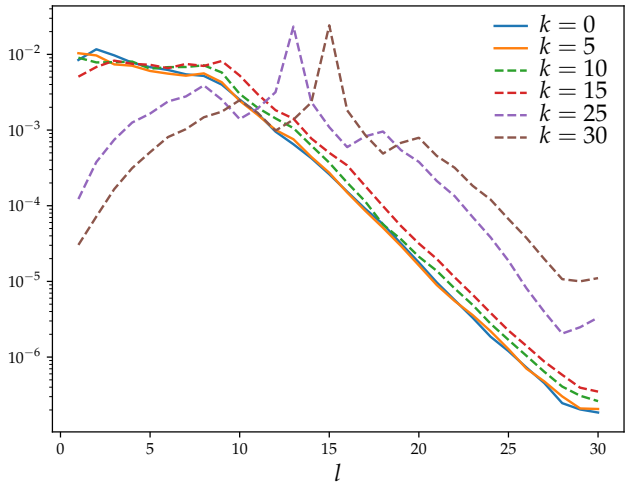

FIGURE 7.8: Power spectrum for each wavenumber, l, of $\hat{\gamma}_k(x,t)$ for $k \in \{0,5,10,15,25,30\}$, where the solid lines represent a positive LE and the dashed represent a negative LE.

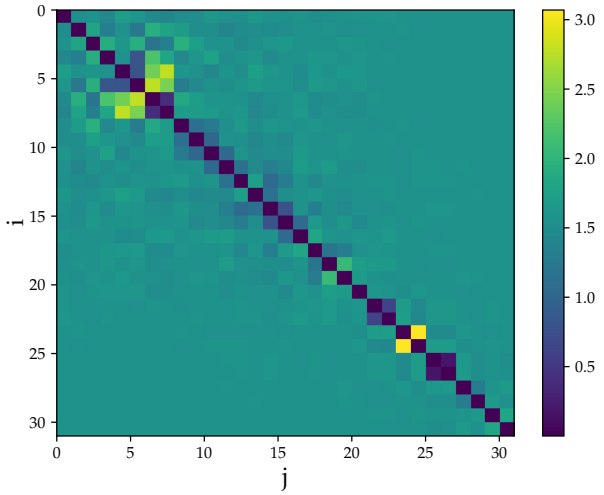

FIGURE 7.9: $\left|\arccos\left(\frac{\langle\hat{\gamma}_i(x,t),\hat{\gamma}_j(x,t)\rangle}{\|\hat{\gamma}_i(x,t)\|\|\hat{\gamma}_j(x,t)\|}\right)\right|$ between pairs of CLV modes.

would be beneficial to industry. A time horizon of $T = 240$ time units, following a 'spin up' time of 1000 time units, $L = 50$ and $K_x = 60$ are used. The mean of the decomposition is computed using 50 samples from different initial conditions along with computation of the standard error, $\frac{\sigma}{\sqrt{n}}$, where σ is the standard deviation and n is the number of samples. To ensure the decomposition is valid, MSS, OCS, and NV are computed on the same 240 time unit time horizon that the CLVs were computed on. The mean and standard deviation are computed from 50 different samples each with unique initial conditions so that analysis drawn in later sections are more general statements.

7.2.1 Decomposition of the forcing term onto the covariant Lyapunov vectors

This section finds the decomposition of the forcing term onto the CLVs by taking the inner product of Equation (2.19) with the adjoint CLVs and making use of Equation (7.1) which results in the forcing weighting factor

$$a_k^f(t) = \frac{\left\langle \hat{\gamma}_k(x,t), \frac{\partial u(x,t)}{\partial x} \right\rangle}{\langle \hat{\gamma}_k(x,t), \gamma_k(x,t) \rangle}. \tag{7.2}$$

The mean and standard error of the forcing term is shown in Figure 7.10. This shows

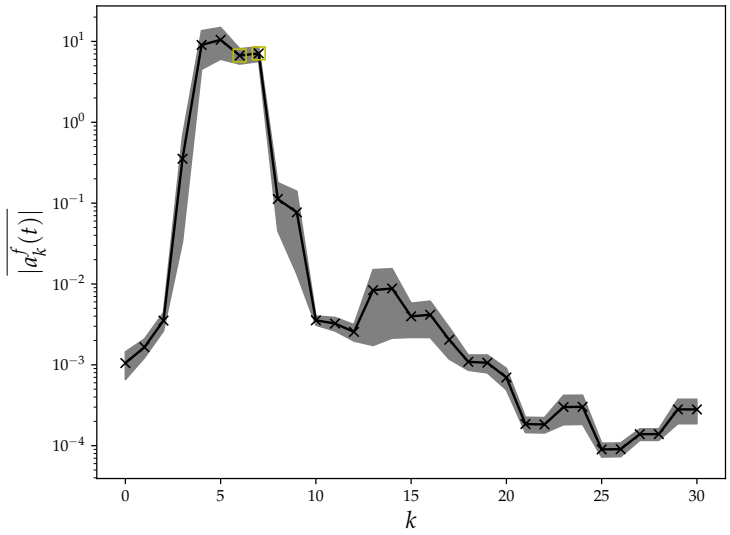

FIGURE 7.10: Mean and standard error of $\overline{|a_k^f(t)|}$. Yellow boxes denote the neutral CLV modes.

the decomposition is dominated by the modes in the $k = 3$ to $k = 9$ region. As can be seen from the LE spectrum, Figure 7.3, these modes relate to the near neutral CLVs, *i.e.* $\Lambda_k \approx 0$. The modes outside this region play a lesser role in the structure of the forcing

term. Figure 7.10 shows why the traditional sensitivity analysis methods fail, in that the forcing term drives the dynamics along all CLV modes, and as such the tangent solution is dominated by the unstable CLV.

One possible explanation for the peak around the near neutral modes is due to the denominator, $|\langle \hat{\gamma}_k(x,t), \gamma_k(x,t)\rangle|$, of Equation (7.2). The meaning of this term is the orthogonality between $\hat{\gamma}_k(x,t)$ and $\gamma_k(x,t)$. A value of zero means the vectors are orthogonal and larger values means the vectors are more aligned. In other words, having small value of orthogonality means that the adjoint CLV has a small component along the CLV. Equation (7.2) essentially finds the component of the solution down each CLV through finding the projection of the solution onto the adjoint CLV and performing a scaling which is related to the projection of the CLV onto its adjoint. It is clear that if the CLV and its corresponding adjoint are orthogonal then this method gives erroneous results. The time averaged value of this denominator is shown in Figure 7.11. The main feature to note is the large dip around

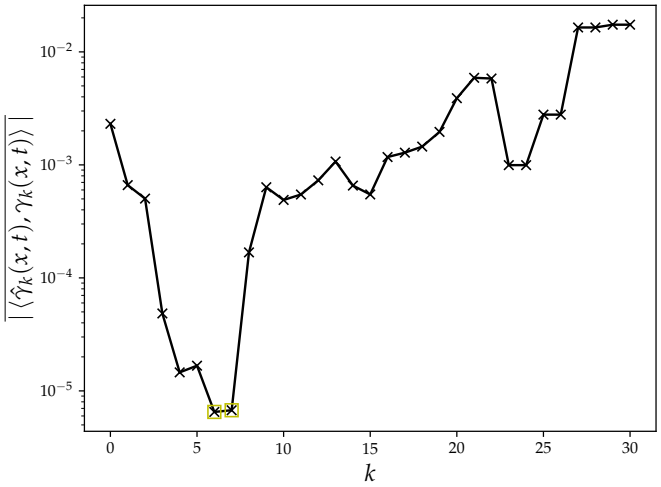

FIGURE 7.11: $\overline{|\langle \hat{\gamma}_k(x,t), \gamma_k(x,t)\rangle|}$ for each CLV mode. Yellow boxes denote the neutral CLV modes.

the near neutral modes meaning these modes are becoming orthogonal. This has the impact of increasing the influence of these modes when computing $a_k^f(t)$.

It is well known that orthogonality between $\hat{\gamma}_k(x,t)$ and $\gamma_k(x,t)$ is due to a homoclinic tangency, *i.e.* the intersection of the stable and unstable manifolds, Ref. [72]. Further, the tangency between $\gamma_k(x,t)$ and $\gamma_{k+1}(x,t)$ results in $\hat{\gamma}_{k+i}(x,t)$ and $\gamma_{k+i}(x,t)$ for $i = 0, 1$ being orthogonal, Ref. [72]. This is not observed in practice as these CLVs and their adjoints are subject to numerical round off error and do have a small component along each other. It can be seen that as the LEs get closer to zero, an increased tangency in the CLVs is observed and, therefore, the k^{th} CLV and its associated adjoint

become more orthogonal. It is for this reason that in the following sections the decomposition along the neutral CLVs are highlighted with yellow boxes to alert the reader that these decompositions are subject to orthogonality between the CLVs and their adjoints.

7.2.2 Decomposition of the tangent solution onto the covariant Lyapunov vectors

From Equation (2.23) it is expected that the tangent decomposition will follow something similar to that presented in section 7.2.1. Taking the inner product of Equation (2.18) with the adjoint CLVs and making use of Equation (7.1) results in

$$a_k(t) = \frac{\langle \hat{\gamma}_k(x,t), v(x,t) \rangle}{\langle \hat{\gamma}_k(x,t), \gamma_k(x,t) \rangle}. \tag{7.3}$$

Figure 7.12 shows the mean and standard error of the time average of the absolute value of $a_k(t)$ for MSS, OCS when $\alpha = 500$, NV_P when $\mu_P = 3.0$ and NV_D when $\mu_D = 30$. These tuning parameter values are selected because they produce sensitivity results that are in good agreement with the curve fit derivative and the along with the squared norm of the tangent solution not showing signs of exponential growth across the time horizon. It can be seen that the MSS tangent solution is primarily composed

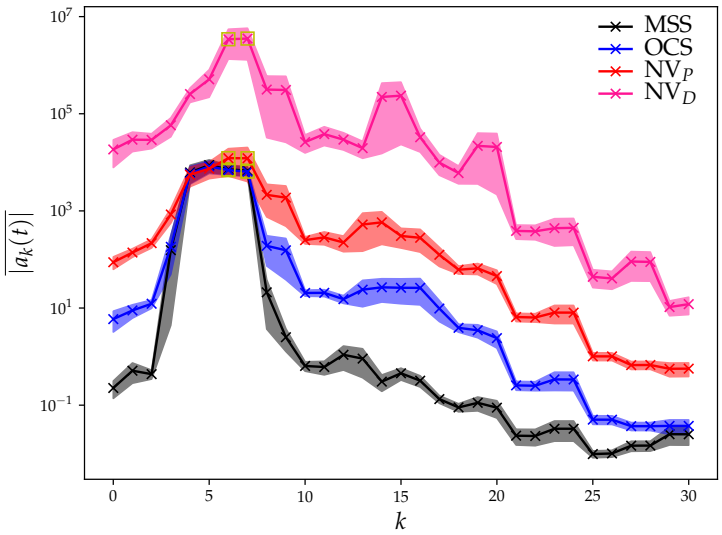

FIGURE 7.12: Mean and standard error of $\overline{|a_k(t)|}$ for MSS, black line, OCS, blue, NV_P, red and NV_D, pink. Yellow boxes denote the neutral CLV modes.

of the near neutral CLV modes and has reduced dependence on the modes outside this region. This is similar to Figure 7.10 as mentioned previously. This suggests that, as the tangent solution is used in the computation of the sensitivity, the near neutral modes also play an important role in the sensitivity calculated. Further, the solution

generated by OCS has a very similar structure to MSS in the near neutral CLV mode region. This implies that OCS is finding a similar solution and structure to MSS.

Outside this region OCS has more reliance on the CLVs than MSS. One argument for this is that this difference is caused by the addition of the control term that stabilises the solution onto the approximation of the Shadowing direction. NV_P has a similar peak around the near neutral CLV modes but is broader than MSS or OCS. Further, NV_P has an increased reliance on the other modes than MSS or OCS, which suggests that either the unstable CLVs are not completely being damped or the method is not optimal in its application of control. Finally, NV_D has the broadest peak around the near neutral modes and has increased dependence on all the CLV modes which, again, suggests that this approach is non-optimal.

It was noted in section 7.1 that, theoretically, the neutral modes should be $\gamma_6(x,t) = f(x,t)$ and $\gamma_7(x,t) = \frac{\partial u(x,t)}{\partial x}$. This should result in the sixth mode in Figure 7.12 being zero due to $\langle v(x,t), f(x,t)\rangle = 0$ for OCS and MSS. This is not the case as the computed neutral CLVs are a linear combination of the two theoretical modes which results in the tangent solution having a component down both modes.

It can be argued that knowing only these near neutral modes will produce a good approximation of $v(x,t)$ and the full solution is not required. To validate this, the modes are ordered by their decreasing value of $\overline{|a_k(t)|}$. The reconstruction of the solution with an increased number of ordered CLV modes is

$$v_{k^*}(x,t) = \sum_{i=0}^{k^*} a_i(t)\gamma_i(x,t),$$

where the CLVs are ordered such that $\overline{|a_i(t)|} > \overline{|a_{i+1}(t)|}$ for $i = 0, 1, \ldots, n_v - 2$. The angle between this reconstruction and the computed solution is

$$\theta_{k^*}(t) = \arccos\left(\frac{\langle v(x,t), v_{k^*}(x,t)\rangle}{\|v(x,t)\|\|v_{k^*}(x,t)\|}\right).$$

This analysis is undertaken for the MSS approach only as the results were similar between the methods. The angle between the actual and reconstructed MSS solutions, panel (A), and the ratio of norms of the reconstructed and MSS solution, panel (B), are given in Figure 7.13. It can be seen that there is exponential decay in the relationship between $\overline{\theta_{k^*}(t)}$ as k^* increases. This implies that the vast majority of the solution is a combination of the near neutral CLV modes. Addition of further modes just increases the accuracy of the solution. This implies that the near neutral CLV modes are important. Further, the magnitude of the reconstructed solution is significantly larger than the actual solution for the first $k^* < 6$ reconstruction cases. This is due to the large magnitude of the $a_i(t)$ terms. Above this the $a_i(t)$ terms result in a solution with similar norm to the MSS tangent solution.

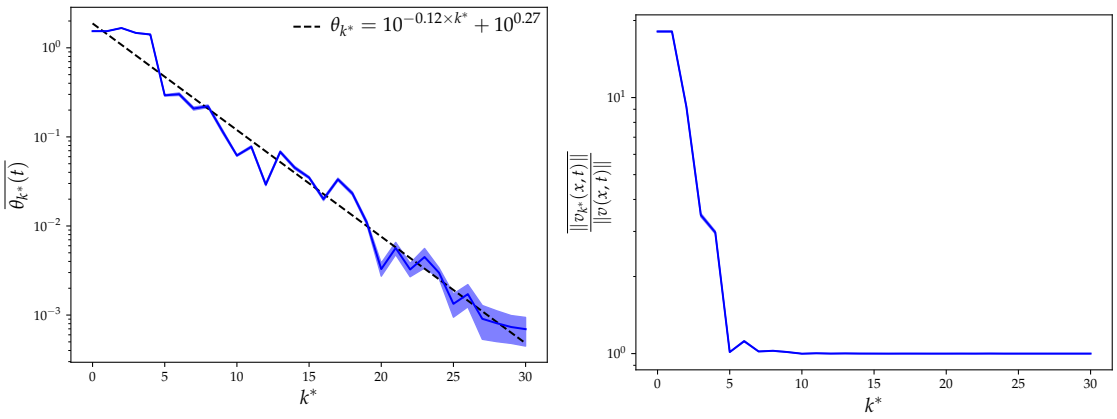

(A) Mean and standard error of $\overline{\theta_{k^*}(t)}$ generated for different values of k^*, blue line. The curve fit showing the exponential decay.

(B) Mean and standard error of $\overline{\frac{\|v_{k^*}(x,t)\|}{\|v(x,t)\|}}$ generated for different values of k^*, blue line.

FIGURE 7.13: Properties of the reconstructed tangent solution from the ordered CLV modes.

Investigating the linear combination further, the sensitivitiy computed from each reconstructed tangent solution, $\frac{\mathrm{d}\overline{J_{k^*}}}{\mathrm{d}c}$, is presented in Figure 7.14 along with the curve fit derivative of Figure 5.1. It can be seen that, similar to the computed angle and

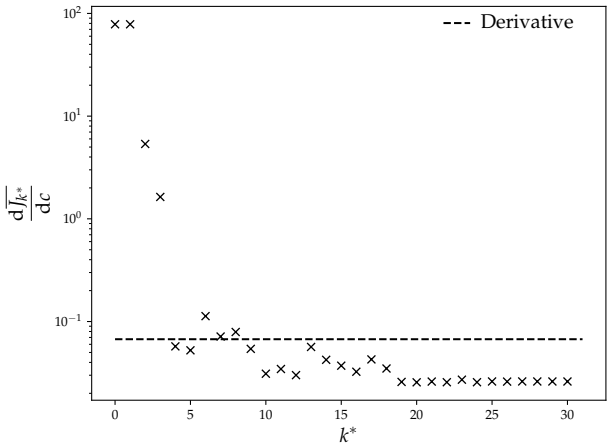

FIGURE 7.14: Sensitivitiy, $\frac{\mathrm{d}\overline{J_{k^*}}}{\mathrm{d}c}$, computed from the reconstructed tangent solution, $v_{k^*}(x,t)$. Curve fit derivative of Figure 5.1, dashed black line.

norm Figure 7.13, that when $k^* < 4$ the reconstructed sensitivity is inaccurate and only when more modes are utilised the accuracy of the sensitivity is increased. From Figure 7.12 it can be noted that the smallest influence CLVs are those that relate to the "isolated" region, $k > 20$. These have very little impact on the value of the sensitivity, as can be seen in Figure 7.14, and the majority of the accuracy come from the physical region of the CLVs.

7.2.2.1 Expected gain of the scalar ODE

To aid in the investigation of the CLVs it is useful to know how the output of a system is impacted by the input. To help with this analysis the state space gain of the ODE relating to each CLV mode is investigated. This also has the added benefit of removing the influence of the denominator, Figure 7.11, and its associated errors. This is achieved this as follows.

Firstly, consider Equation (2.23) which is restated here with a generic control term, $b_k(t) \in \mathbb{R}$, applied

$$\frac{\mathrm{d}a_k(t)}{\mathrm{d}t} = \Lambda_k a_k(t) + a_k^f(t) + b_k(t). \tag{7.4}$$

Taking the transfer function of this, see Refs. [99, 115] for details, results in

$$sA_k(s) = \Lambda_k A_k(s) + A_k^f(s) + B_k(s). \tag{7.5}$$

Investigating the ratio of output to input leads to

$$\frac{A_k(s)}{A_k^f(s)} = \frac{1 + \frac{B_k(s)}{A_k^f(s)}}{s - \Lambda_k}. \tag{7.6}$$

From this it is expected to see a large gain either when the denominator $s - \Lambda_k$ is small or when the control term $\frac{B_k(s)}{A_k^f(s)}$ is large. For MSS, $b_k(t) = 0$ and $\frac{B_k(s)}{A_k^f(s)} = 0$. Therefore, the magnitude of the gain of the system is found by finding the ratio of $a_k(t)$, Figure 7.12, to $a_k^f(t)$, Figure 7.10. The mean and standard error of this ratio generated by MSS, OCS and both NV methods for 50 samples is shown in Figure 7.15. The gain

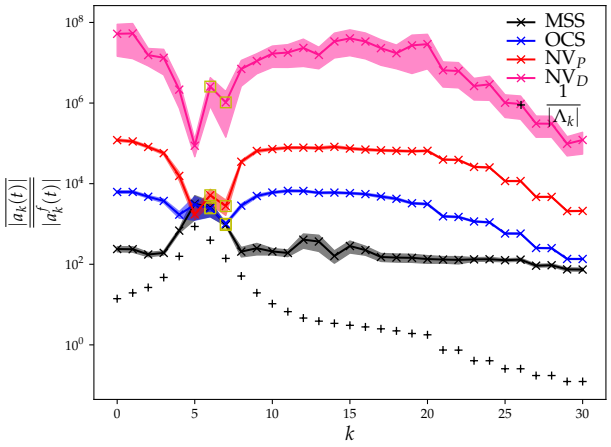

FIGURE 7.15: Mean and standard error of $\frac{\overline{|a_k(t)|}}{|a_k^f(t)|}$ for MSS, black line, OCS, blue line, NV$_P$, red line, NV$_D$, pink line, and the expected gain $\frac{1}{|\Lambda_k|}$, pluses. Yellow boxes denote the neutral CLV modes.

of MSS is very similar to $\frac{1}{|\Lambda_k|}$ and is in good agreement with the simple analysis provided. This implies that MSS is finding a very good approximation for the Shadowing direction. There is some bias outside the near neutral CLV modes for MSS. It is argued here that the explanation for this difference is that the solution is computed on a finite time horizon and it is expected that this causes some bias. Increasing the time horizon is expected to reduce this bias. Further, MSS generally has the lowest gain of all the methods implying that the solution found using these methods are more optimal. It can, therefore, be concluded that the most important modes are the near neutral CLV modes. As argued previously the increased value of the gain in the region outside the near neutral modes for OCS and both NV methods is due to the control term stabilising the solution which is shown in the following section.

7.2.3 Decomposition of the control solution onto the covariant Lyapunov vectors

The control term applied by OCS, $q(x,t)$, NV_P, $\mu_P \frac{\partial^2 v(x,t)}{\partial x^2}$, and NV_D, $-\mu_D \frac{\partial^4 v(x,t)}{\partial x^4}$, can also be decomposed onto the CLVs. This results in

$$\begin{aligned} q(x,t) &= \sum_{k=0}^{n_v-1} b_k(t)\gamma_k(x,t), \\ \mu_P \frac{\partial^2 v(x,t)}{\partial x^2} &= \sum_{k=0}^{n_v-1} b_k(t)\gamma_k(x,t), \\ -\mu_D \frac{\partial^4 v(x,t)}{\partial x^4} &= \sum_{k=0}^{n_v-1} b_k(t)\gamma_k(x,t). \end{aligned} \tag{7.7}$$

The decomposition of the control solution is computed by taking the inner product of Equation (7.7) with the adjoint CLVs and using Equation (7.1) which results in

$$\begin{aligned} b_k(t) &= \frac{\langle \hat{\gamma}_k(x,t), q(x,t)\rangle}{\langle \hat{\gamma}_k(x,t), \gamma_k(x,t)\rangle}, \\ b_k(t) &= \frac{\left\langle \hat{\gamma}_k(x,t), \mu_P \frac{\partial^2 v(x,t)}{\partial x^2}\right\rangle}{\langle \hat{\gamma}_k(x,t), \gamma_k(x,t)\rangle}, \\ b_k(t) &= \frac{\left\langle \hat{\gamma}_k(x,t), -\mu_D \frac{\partial^4 v(x,t)}{\partial x^4}\right\rangle}{\langle \hat{\gamma}_k(x,t), \gamma_k(x,t)\rangle}. \end{aligned} \tag{7.8}$$

Figure 7.16 shows the mean and standard error of $\overline{|b_k(t)|}$. It can be seen that of all the methods investigated OCS applies the least control. Further, OCS has a peak around the near neutral modes. There is some component of the control generated by OCS on the modes outside this region but this influence is several orders of magnitude smaller. This is again due to the control stabilising the solution onto the approximate

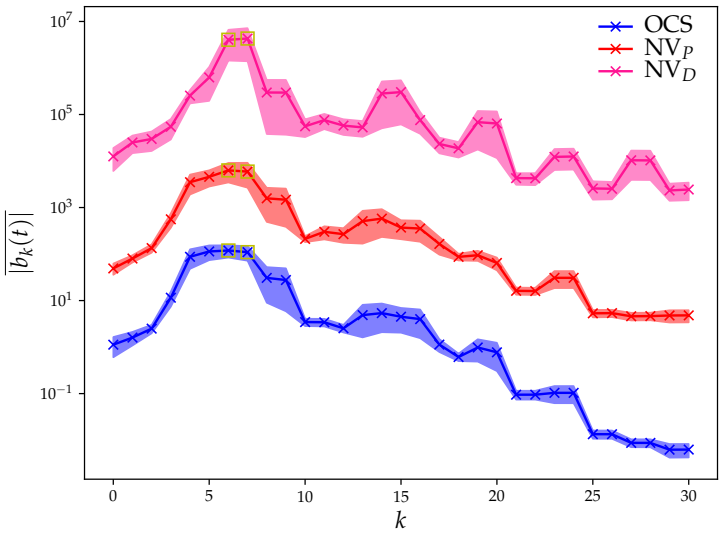

FIGURE 7.16: Mean and standard error of $\overline{|b_k(t)|}$ for OCS, blue line, NV$_P$, red and NV_D, pink. Yellow boxes denote the neutral CLV modes.

Shadowing direction. NV$_P$ has a larger component down each CLV mode than OCS implying this method is not as optimal as OCS and the application of control is not as targeted as OCS. There still remains a peak which is slightly broader than OCS around the near neutral modes.

NV$_D$ has the largest decomposition onto the CLVs out of all the methods investigated. There still is a peak around the near neutral modes but the influence of the other modes is still high, implying control is being applied in a non-optimal way. This is because NV does not produce a solution that is near the approximate Shadowing direction resulting in larger control than OCS. It can be concluded that the control term must also decompose onto the near neutral modes and have minimal contribution from the other modes. Selection of a control term that is along the near neutral modes is difficult because the CLVs are unknown *a priori* and, therefore, knowing if the control term selected is dominated by the near neutral modes is challenging.

7.2.3.1 Expected gain of the control term in the scalar ODE for Shadowing

In section 7.2.2.1 the scalar ODE gain was derived. There were some differences between OCS, NV$_P$, NV$_D$ and MSS which were argued to be due to the control term applied. The gains associated to the control term for OCS, NV$_P$ and NV$_D$ are shown in Figure 7.17. The profiles of the control gains are very similar to the differences between the tangent gain and expected gain shown in Figure 7.15. Further, the majority of the gain from the control term is outside the near neutral modes. An explanation for this is that the tangent initial condition is not on the approximation to

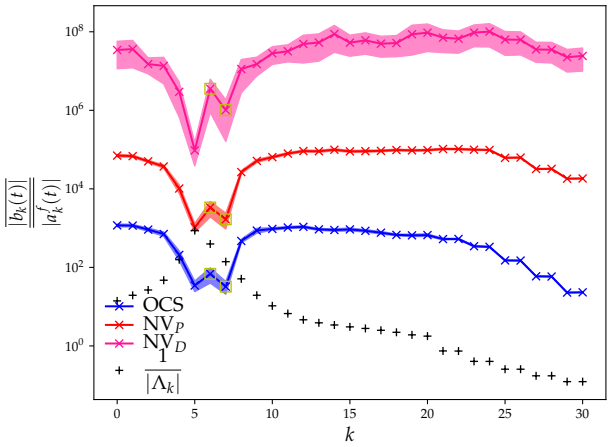

FIGURE 7.17: Mean and standard error of $\frac{\overline{|b_k(t)|}}{|a_k^f(t)|}$ for OCS, blue line, NV_P, red line, NV_D, pink line, and the expected gain $\frac{1}{|\Lambda_k|}$, pluses.

the Shadowing direction and, therefore, requires stabilising onto an estimate for the Shadowing direction for OCS, but is continually stabilised for NV. The process of stabilisation requires applying control down those modes outside the near neutral regime which leads to the large gain in these modes. Once the OCS solution is on the approximate Shadowing direction small nudges are required along each mode to keep it there hence the smaller control than NV. Selecting a value of α that results in a solution that remains closer to MSS, Figure 5.6a, for longer should reduce the gain seen along the modes outside of the near neutral mode regime.

7.3 Similarities in tangent decomposition between solutions on different domain sizes

The previous analysis has been undertaken on one single domain size. To show that the analysis is general the decomposition generated by MSS is computed for multiple domain sizes. The number of Fourier modes computed is scaled proportional to L such that the ratio $\frac{K_x}{L} = \frac{6}{5}$ is kept constant. This is undertaken such that the value of Δx is constant between the simulations. Further, the time horizon, $T = 240$ time units, is used for all domain sizes to ensure that the time horizon has no influence on the results. The 'spin up' times used for $L = 50$ is $10,000$ time units, for $L = 75$ is $12,500$ time units, for $L = 100$ is $15,000$ time units, for $L = 250$ is $20,000$ time units and for $L = 500$ is $40,000$ time units. The CLV calculation for $L = 500$ took several days on 6 compute nodes each with 20 CLVs computed per node.

Firstly, with appropriate normalisation the LE spectra of varying domain lengths collapse onto the same curve. This is shown by normalising the index of each mode

by the domain size, *i.e.* $\frac{k}{L}$, and the normalised LE spectrum is shown in Figure 7.18. This shows that changing the domain length does not increase the value of Λ_0 but

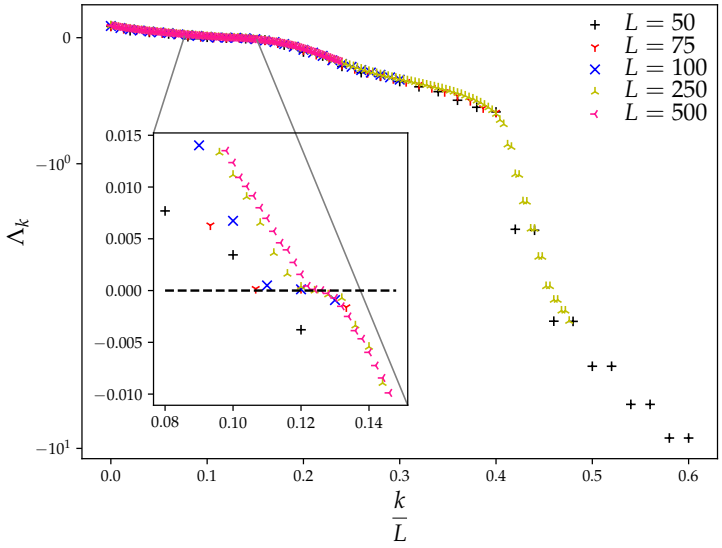

FIGURE 7.18: The LE spectrum, Λ_k for $L = 50$, black pluses, $L = 75$, red downwards tri, $L = 100$, blue crosses, $L = 250$, yellow upwards tri, and $L = 500$, pink left tri. The inset shows the region around the near neutral modes in more detail.

rather fills in the spectrum, meaning that the increased number of modes fill the gaps in between the LEs of the smaller domain cases. This results in the difference between LE values decreasing. The decrease between successive LE values results in a longer 'spin up' time required as these modes take longer to align with their respective sub-spaces. This is because it is more "difficult" to distinguish between modes that have similar exponents. This difference is only noticeable after longer simulation times. The projection of the MSS solution onto the normalised index of CLV modes results in the same gain profile as shown in Figure 7.19.

The main feature to notice is that as L increases the decomposition is dominated by the modes corresponding to $\frac{k}{L} = 0.13$. These are the modes which relate to the near neutral modes. This suggests that the analysis for $L = 50$ is directly translatable to other domain sizes. It is also found that as L increases the peak around $\frac{k}{L} = 0.13$ becomes narrower and taller. The reason for this is that around these modes the LEs are getting closer to zero and the expected gain is the inverse of this which leads to large values. One important issue to note is that the results are generally noisy in the region outside the near neutral modes. This is dissimilar to that presented in section 7.2 as the regions outside the near neutral modes are generally well-behaved. The reason for this is that the results presented here are for a single simulation and not an average over multiple simulations.

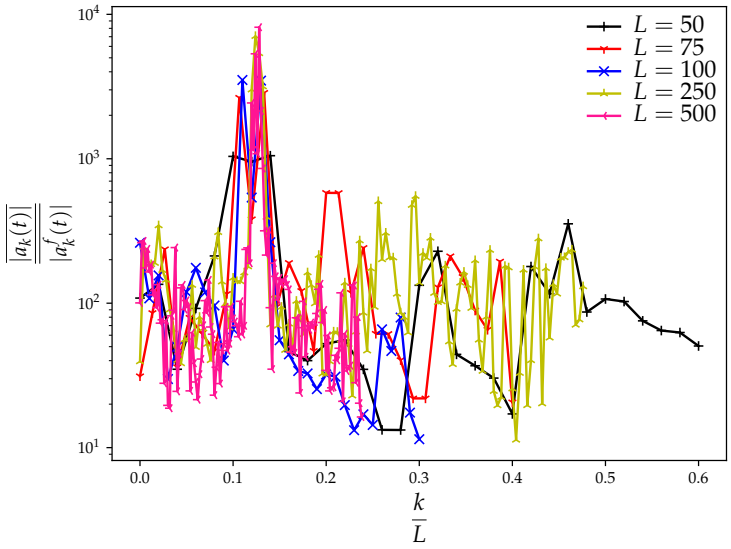

FIGURE 7.19: $\frac{\overline{|a_k(t)|}}{\overline{|a_k^f(t)|}}$ generated by MSS for $L = 50$, black pluses, $L = 75$, red downwards tri, $L = 100$, blue crosses, $L = 250$, yellow upwards tri, and $L = 500$, pink left tri.

7.4 Tuning parameters influence on the solution decomposition

It has been shown in chapter 5 that the tuning parameters have a large influence on the solutions generated by OCS and NV. In this section the influence that the tuning parameters has on the solutions generated by OCS and NV is investigated in terms of the decomposition of both the tangent and control solutions onto the CLVs. This is undertaken on the $L = 50$ domain size with $T = 240$ time units, a 'spin up' time of 1000 time units and $K_x = 60$. This analysis is undertaken for OCS and NV_P but similar features are present between NV_P and NV_D.

7.4.1 Impact of α on the decomposition

The role of α on the tangent and control decomposition is investigated in this section. Using the same tangent and control decomposition methods detailed previously the decomposition of the solutions generated using different α values onto the CLVs is shown in Figure 7.20 with MSS as a comparison. It can be seen that there is very similar projection in the near neutral modes regardless of which α value chosen. Increasing α from 1×10^1 to 1.0×10^4 moves the projection of the OCS tangent solution closer to that of MSS. There is little difference in the projection between $\alpha = 1.0 \times 10^3$ and $\alpha = 1.0 \times 10^4$ suggesting that there is a range of α values that all provide adequate control which results in a solution similar to that generated by MSS,

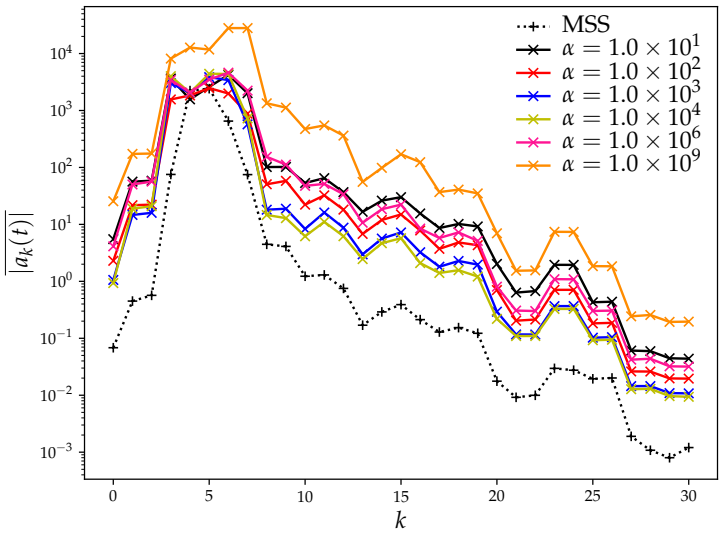

FIGURE 7.20: $\overline{|a_k(t)|}$ for $\alpha = 1.0 \times 10^1$, black line, $\alpha = 1.0 \times 10^2$, red, $\alpha = 1.0 \times 10^3$, blue, $\alpha = 1.0 \times 10^4$, yellow, $\alpha = 1.0 \times 10^6$, pink, $\alpha = 1.0 \times 10^9$, orange, and MSS, dotted, as a reference.

Figure 5.6a. Increasing α to 1.0×10^6 and beyond moves the projection away from the MSS projection. This suggests that the solution is prone to the exponential growth of perturbations as the control applied is unable to counteract the growth. Further, the implications are that regardless of what tuning parameter value selected OCS attempts to find the same Shadowing direction.

To validate this, a comparison of the projection of the control terms for a range of α valued is shown in Figure 7.21. A similar feature to the tangent decomposition is that

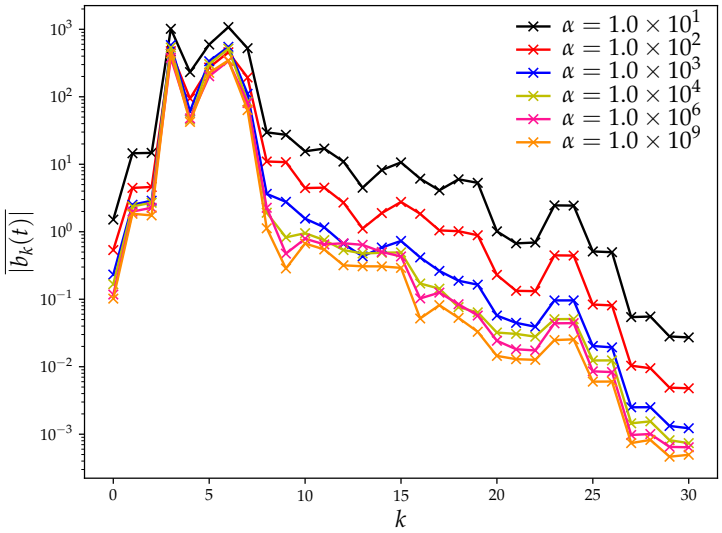

FIGURE 7.21: $\overline{|b_k(t)|}$ for $\alpha = 1.0 \times 10^1$, black line, $\alpha = 1.0 \times 10^2$, red, $\alpha = 1.0 \times 10^3$, blue, $\alpha = 1.0 \times 10^4$, yellow, $\alpha = 1.0 \times 10^6$, pink and $\alpha = 1.0 \times 10^9$, orange.

regardless of what value of α is chosen the decomposition in the near neutral modes is relatively constant. The main difference between control applied at each α is the projection onto each of the remaining CLV modes. Increasing α reduces the amount of control applied down each CLV. This suggests that when α is too large, inadequate control is applied to the remaining modes resulting in the tangent solution having exponential growth. Without knowing this decomposition *a priori* it is difficult to select an appropriate value of α. The point at which control becomes inadequate is not clear from Figure 7.21 as there is a general decrease in control along the region outside the near neutral modes as α is increased. As a final remark, this analysis suggests that the control term applied in the NV method, to be optimal, must be dominated by the near neutral modes.

7.4.2 Impact of μ_P on the decomposition

The analysis presented in section 7.4.1 is repeated here when μ_P is varied in the NV$_P$ approach. The results for the tangent solution decomposition when μ_P is varied are presented in Figure 7.22 with MSS as a comparison. It can be seen that with small

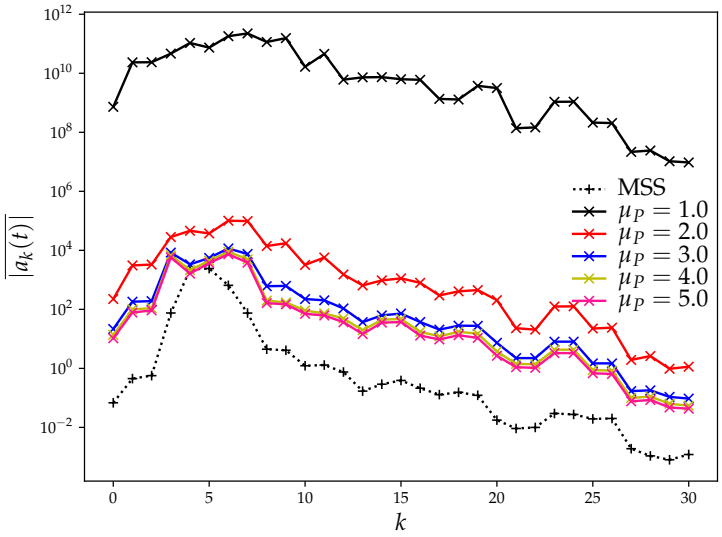

FIGURE 7.22: $\overline{|a_k(t)|}$ for NV$_P$ when $\mu_P = 1.0$, solid black line, $\mu_P = 2.0$, solid red, $\mu_P = 3.0$, solid blue, $\mu_P = 4.0$, solid yellow, $\mu_P = 5.0$, solid pink, and MSS, dotted black, for reference.

values of μ_P the tangent solution is equally composed of each CLV mode and is significantly larger influence than the other μ_P values investigated. This is due to the control being inadequate in stabilising the solution. As μ_P is increased, the tangent decomposition reduces on each mode along with emergence of the peak around the near neutral modes. The implication of this is that the value of the tuning parameter can be found when this peak emerges and not based on matching the sensitivity

values produced with that of the expected sensitivity. This suggests the increased influence of the near neutral modes in the solution determines the accuracy in the sensitivity produced. This is the case until increasing the value of μ_P further has very little impact on the decomposition suggesting that there is a limit to the solutions that are found by NV methods. An outcome is that the NV methods investigated with this simple control term are unable to find the Shadowing direction. The decomposition of the control solutions for the same μ_P values are shown in Figure 7.23. This control

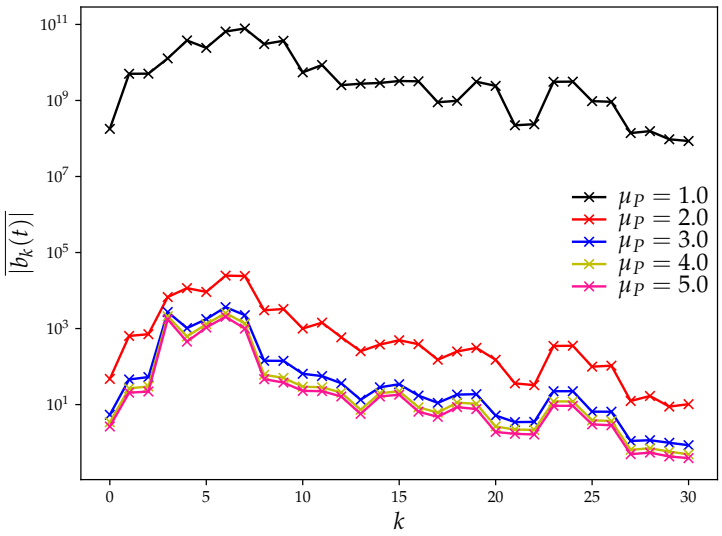

FIGURE 7.23: $\overline{|b_k(t)|}$ when $\mu_P = 1.0$, solid black line, $\mu_P = 2.0$, solid red, $\mu_P = 3.0$, solid blue, $\mu_P = 4.0$, solid yellow, and $\mu_P = 5.0$, solid pink.

term produces very different behaviour to OCS presented previously. The main difference is that the control solutions do not decompose onto the same near neutral modes regardless of which value of μ_P is selected. This behaviour is more akin to the tangent decomposition where μ_P is small a large decomposition of the control across all modes is seen. As μ_P is increased further the decomposition decreases along with an emergence of the peak around the near neutral modes. This implies, again, that this emergence could be utilised to determine the tuning parameter value. There is a point where the increase of μ_P has very little impact on the decomposition of the control term. This suggests there is a limit as to how similar the solution that these methods generate are to MSS.

7.5 Influence of the parameter of interest

The analysis undertaken until this point has been on the system

$$\frac{\partial u(x,t)}{\partial t} = -(u(x,t)+c)\frac{\partial u(x,t)}{\partial x} - \frac{\partial^2 u(x,t)}{\partial x^2} - \beta\frac{\partial^4 u(x,t)}{\partial x^4},$$
$$x \in [0, L),$$
$$u(0,t) = u(L,t),$$

when $c = 0.5$ is the parameter of interest. To show that the analysis presented previously is transferable between forcing terms this section focuses on analysing the system when $\beta = 1.0$ is the parameter of interest. A repeat of the analysis shown previously is not undertaken. Instead, the expected gain of MSS along each CLV is investigated.

Initially the value of $\bar{J}$ against β is presensted in Figure 7.24 for a time horizon $T = 2 \times 10^4$ and an average is taken over 50 different initial conditions $\mathbf{u}(t_s)$. The

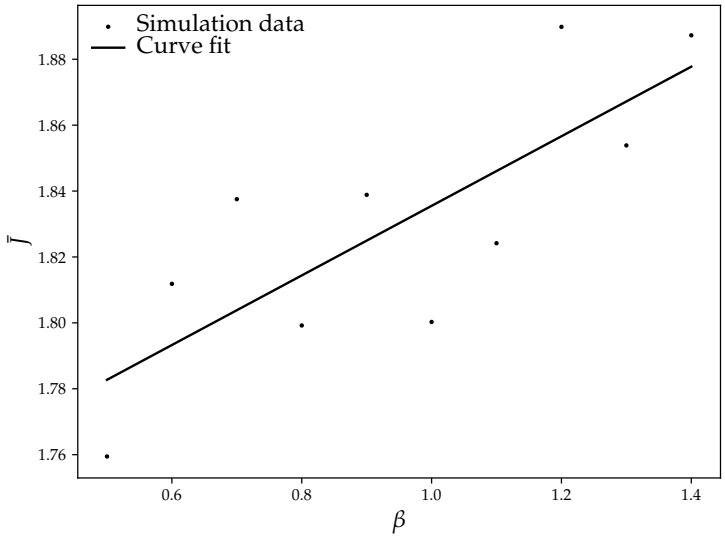

FIGURE 7.24: $\bar{J}$ against β and dashed line is the curve fit.

sensitivity computed using the curve fit is $\frac{\mathrm{d}\bar{J}}{\mathrm{d}\beta} \approx 1.055 \times 10^{-1}$. The value computed using MSS is 1.2789×10^{-1}.

The reason for this is that there is fundamentally a large amount of factors that are prevalent in the computation of the gain. To compute the gain, firstly the decomposition of the forcing term, which in this case is $-\frac{\partial^4 u(x,t)}{\partial x^4}$, onto these CLV is undertaken to compute $a_k^f(t)$. Secondly, the tangent solution generated by MSS, $v(x,t)$, is decomposed onto the CLV modes to produce $a_k(t)$. Finally, the ratio of $a_k(t)$ to $a_k^f(t)$ is the computed gain along each CLV mode. As before, the solution generated by MSS is computed on the same $T = 240$ time unit time horizon as the CLVs are

computed on using $K_x = 60$, $L = 50$ and a 'spin up' time of 1000 time units is used. The gain can be seen in Figure 7.25. The reader is reminded that the expected gain

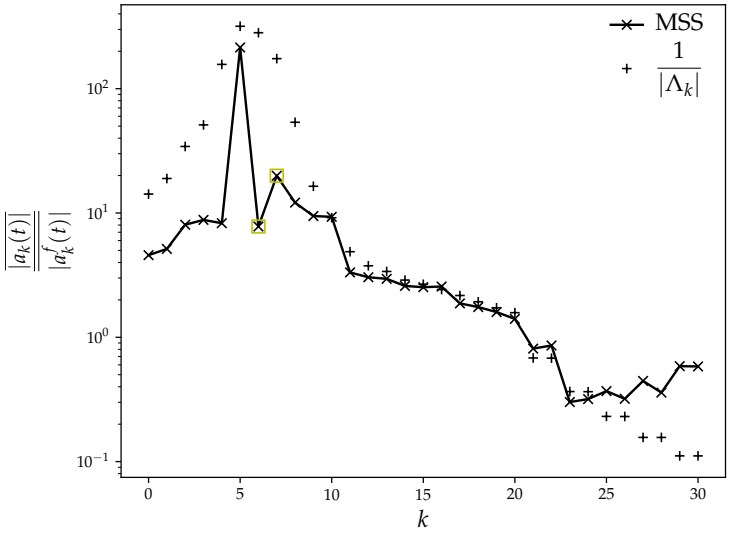

FIGURE 7.25: $\frac{\overline{|a_k(t)|}}{|a_k^f(t)|}$ for MSS, black line, and the expected gain $\frac{1}{|\Lambda_k|}$, pluses, when β is the parameter of interest. Yellow boxes denote the neutral CLV modes.

along each CLV mode is proportional to $\frac{1}{|\Lambda_k|}$. It is clear that the gain generated in this case when β is the parameter of interest is in very good agreement with the expected value. The implications of this is that the analysis drawn previously is generic for all parameters. This suggests that the same near neutral modes are also important between tuning parameters and that it is the difference linear combination of these modes that determine the sensitivity values for each tuning parameter. The reason why there is such similarity between the expected and computed gain is that the analysis provided in section 7.2.2.1 is generic. Therefore, it can be concluded that the analysis undertaken previously is common across all parameters of interest.

7.6 CLV decomposition of the adjoint solutions

The analysis undertaken for altering the domain size and parameter of interest are also valid for the adjoint formulation. Further analysis is required between the adjoint and tangent formulations to show that the conclusions drawn around the near neutral modes are common between the methods. In this section, the decomposition of the adjoint forcing $\frac{2u(x,t)}{T}$, co-state $\hat{\lambda}(x,t)$ and control terms $2\hat{v}(x,t)$ for MSS and OCS, $-\hat{\mu}_P \frac{\partial^2 \hat{\lambda}(x,t)}{\partial x^2}$ for NV_P and $\hat{\mu}_D \frac{\partial^4 \hat{\lambda}(x,t)}{\partial x^4}$ for NV_D onto the CLVs are investigated. The adjoint forcing term is found by taking the inner product of Equation (2.26) with

$\gamma_k(x,t)$ along with using Equation (7.1) resulting in

$$\hat{a}_k^f(t) = \frac{\left\langle \frac{2u(x,t)}{T}, \gamma_k(x,t) \right\rangle}{\langle \hat{\gamma}_k(x,t), \gamma_k(x,t) \rangle}.$$

Results of this decomposition are shown in Figure 7.26. The results of the adjoint

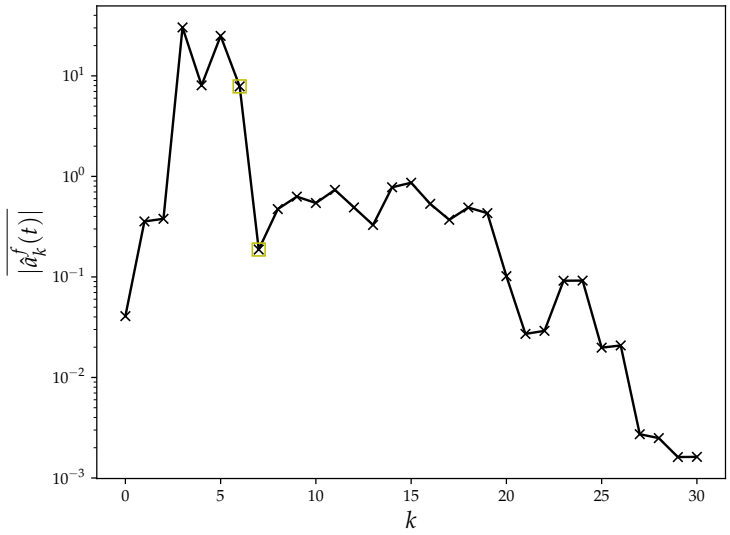

FIGURE 7.26: $\overline{|\hat{a}_k^f(t)|}$ for the adjoint formulation. Yellow boxes denote neutral CLV modes.

forcing decomposition produces a profile that is very similar to that presented in section 7.2.1. The forcing term is dominated by the near neutral CLV modes and reduced elsewhere which shows very similar features to the tangent forcing decomposition. The implications of this is that, as in the tangent case, the near neutral CLV modes are of importance for the adjoint case also.

7.6.1 CLV decomposition of the adjoint co-state solution

The decomposition of the co-state solution is achieved through taking the inner product of Equation (2.27) with $\gamma_k(x,t)$ along with using Equation (7.1) resulting in

$$\hat{a}_k(t) = \frac{\langle \hat{\lambda}(x,t), \gamma_k(x,t) \rangle}{\langle \hat{\gamma}_k(x,t), \gamma_k(x,t) \rangle}.$$

The results of this are shown in Figure 7.27 for MSS, OCS when $\alpha = 500$, NV_P when $\hat{\mu}_P = 3.0$ and NV_D when $\hat{\mu}_D = 30$. Again, these values are selected so that comparison between tangent and adjoint forms is consistent along with these values producing sensitivities in good agreement with the expected value and the adjoint solutions being adequately stabilised. It is clear that MSS, again, is dominated by the near

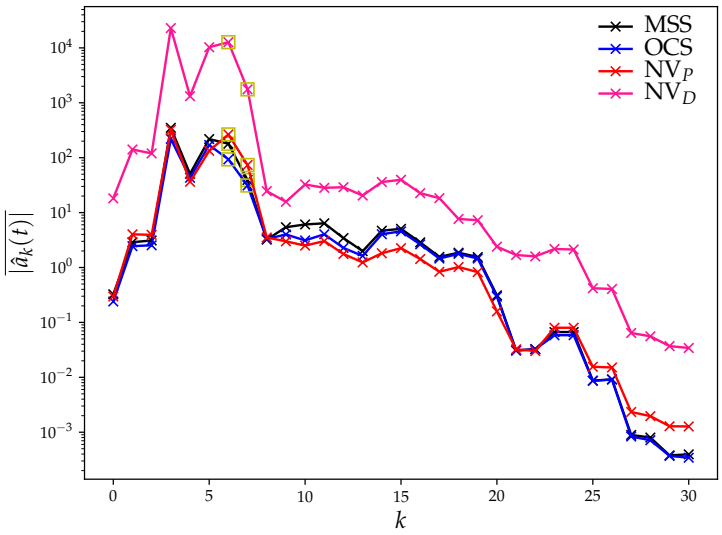

FIGURE 7.27: $\overline{|\hat{a}_k(t)|}$ for the adjoint formulations of MSS, black line, OCS, blue line, NV$_P$, red line, and NV$_D$, pink line. Yellow boxes denote neutral CLV modes.

neutral CLV modes. This is comparable to the investigation into the tangent formulation presented in section 7.2.2. It can be seen that OCS and MSS share very similar decomposition profiles across all CLV modes. This implies that OCS and MSS are acting in very similar ways and targeting the same features. There is even better agreement in the adjoint formulation than the tangent formulation with MSS.

The solution generated by NV$_P$ is in very good agreement with the solution produced by MSS and OCS. This is contrary to the analysis undertaken for the tangent formulations. The cause of this is due to the similarity in terminal conditions between OCS, NV and MSS in the adjoint formulation which results in smaller amounts of control being applied to stabilise the solution. The implications of this is that if a better tangent initial condition can be found for the tangent formulation then smaller amounts of control would be required to keep the solution stable. Further, there is a similarity between NV$_D$ and the other methods, however, the decomposition is larger across all modes. The peak around the near neutral modes still dominates the decomposition. This analysis suggests that using a NV term that is derived from a production of adjoint energy term is more optimal than one that is derived from dissipation of adjoint energy. Further, this analysis suggests that these NV terms derived for the adjoint formulation are more optimal than those developed for the tangent case. The reason for this is the reduced difference between the MSS and NV$_P$ terminal boundary condition. OCS is still more optimal than NV but the difference in the adjoint formulation is not as significant as in the tangent form.

Using the same reconstruction approach presented for the tangent formulation, the $\hat{a}_k(t)$ coefficients are ordered in descending order of importance. Following this, a

reconstruction of the adjoint co-state solution is generated by incorporation of an increased number of modes. It was argued in section 7.2.2 that knowing only these near neutral modes will produce a good approximation of $\hat{\lambda}(x,t)$ and the full solution is not required. The reconstruction of the solution with an increased number of ordered CLV modes is

$$\hat{\lambda}_{k^*}(x,t) = \sum_{i=0}^{k^*} \hat{a}_i(t)\hat{\gamma}_i(x,t).$$

The angle between this reconstruction and the computed solution is

$$\hat{\theta}_{k^*}(t) = \arccos\left(\frac{\langle \hat{\lambda}(x,t), \hat{\lambda}_{k^*}(x,t)\rangle}{\|\hat{\lambda}(x,t)\|\,\|\hat{\lambda}_{k^*}(x,t)\|}\right).$$

This analysis is undertaken for the MSS approach only. The time averaged angle between the actual and reconstructed MSS solutions, panel (A), and the time averaged ratio of norms of the reconstructed and MSS solution, panel (B), are given in Figure 7.28. It can be seen that a larger number of CLV modes are required to

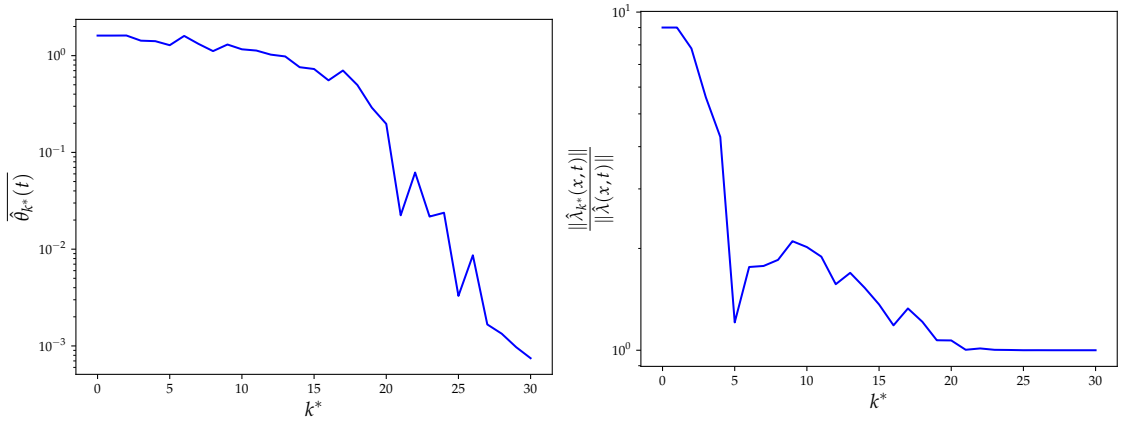

(A) $\overline{\hat{\theta}_{k^*}(t)}$ generated for different values of k^*.

(B) $\overline{\frac{\|\hat{\lambda}_{k^*}(x,t)\|}{\|\hat{\lambda}(x,t)\|}}$ generated for different values of k^*.

FIGURE 7.28: Properties of the reconstructed tangent solution from the ordered adjoint CLV modes.

reconstruct the solution for the adjoint formulation. In the adjoint formulation it takes around $k^* = 20$ modes to generate a solution that is similar to the computed solutions whereas for the tangent formulation is takes around $k^* = 6$ modes. The ratio of the reconstructed solution norm has a significant bump following $k^* = 6$. This feature is not present in the tangent case. It is unclear what is causing this bump only for the adjoint case in the solution norms but could potentially account for the increased number of modes required in the adjoint case. One possible explanation for this is that in the tangent formulation there was four orders of magnitude difference between the decomposition onto the near neutral CLV modes and the others. Here there are only

two orders of magnitude difference. Therefore, the other modes that are not the near neutral modes play a more important role which is why more of them are required to produce a reconstructed solution that is in good agreement with the computed solution. One possible explanation for this is that the adjoint MSS solution does not find an "adjoint Shadowing direction", rather the adjoint solution that equates to the tangent Shadowing direction. This difference has produced discrepancies in the adjoint OCS and MSS solutions presented in section 6. It is expected that if MSS is reformulated to find the "adjoint Shadowing direction" that this difference between the adjoint MSS and OCS forms decreases. The implications of this is that the number of CLV modes required to create an approximate adjoint solution would decrease and the analysis would be more in line with the tangent formulation.

7.6.1.1 Expected gain of the ODE

This section repeats the analysis of deriving the expected gain for the adjoint solution. Firstly, the addition of a generic control term, $\hat{b}_k(t) \in \mathbb{R}$, to Equation (2.25) results in

$$\frac{\mathrm{d}\hat{a}_k(t)}{\mathrm{d}t} = -\hat{a}_k(t)\Lambda_k + \hat{a}_k^f(t) + \hat{b}_k(t). \tag{7.9}$$

Taking the transfer function of this leads to

$$s\hat{A}_k(s) = -\hat{A}_k(s)\Lambda_k + \hat{A}_k^f(s) + \hat{B}_k(s). \tag{7.10}$$

The relationship between the output and the input is given by

$$\frac{\hat{A}_k(s)}{\hat{A}_k^f(s)} = \frac{1 + \frac{\hat{B}_k(s)}{\hat{A}_k^f(s)}}{(s + \Lambda_k)}. \tag{7.11}$$

The gain of the MSS, OCS, and NV systems are shown in Figure 7.29. It can, again, be seen that the MSS gain is in very good agreement with the expected gain. This was shown in the tangent MSS formulation also. Similar to the decomposition, the solution gain of OCS is very similar to that of MSS across all modes implying that OCS and MSS behave in similarly and it suggests that adjoint OCS is near optimal in its application of control. Further, NV_P is also in very good agreement with MSS again implying adjoint formulations are more optimal in application of control over their tangent counterparts. This was not the case for the tangent formulation. An explanation for this is that due to the terminal condition of the adjoint co-state being identical to that of MSS for OCS and similar for NV results in a solution that does not require significant control for stabilisation. This was shown in section 6.4. Therefore, the gain due to the control does not contribute as much to the solution compared to the tangent formulation. As seen previously NV_D has the largest gain.

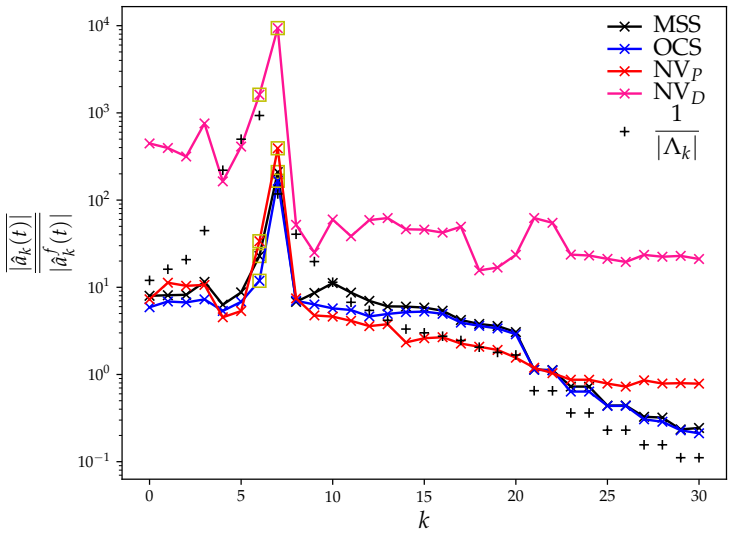

FIGURE 7.29: $\frac{\overline{|\hat{a}_k(t)|}}{|\hat{a}_k^f(t)|}$ for MSS, black line, OCS, blue line, NV$_P$, red line, and NV$_D$, pink line. The inverse absolute value of the LE, $\frac{1}{|\Lambda_k|}$, is also plotted with pluses. Yellow boxes denote the neutral CLV modes.

7.6.2 CLV decomposition of the adjoint control solution

The decomposition is repeated here for the control terms. The control for MSS and OCS is $2\hat{v}(x,t)$, NV$_P$ is $-\hat{\mu}_P\frac{\partial^2\hat{\lambda}(x,t)}{\partial x^2}$ and NV$_D$ is $\hat{\mu}_D\frac{\partial^4\hat{\lambda}(x,t)}{\partial x^4}$. Firstly, let these control terms be a linear combination of adjoint CLVs

$$\begin{aligned} 2\hat{v}(x,t) &= \sum_{k=0}^{n_v-1}\hat{b}_k(t)\hat{\gamma}_k(x,t), \\ -\hat{\mu}_P\frac{\partial^2\hat{\lambda}(x,t)}{\partial x^2} &= \sum_{k=0}^{n_v-1}\hat{b}_k(t)\hat{\gamma}_k(x,t), \\ \hat{\mu}_D\frac{\partial^4\hat{\lambda}(x,t)}{\partial x^4} &= \sum_{k=0}^{n_v-1}\hat{b}_k(t)\hat{\gamma}_k(x,t). \end{aligned} \tag{7.12}$$

Taking the inner product of these with $\gamma_k(x,t)$ along with using Equation (7.1) results in

$$\begin{aligned} \hat{b}_k(t) &= \frac{\langle 2\hat{v}(x,t),\gamma_k(x,t)\rangle}{\langle\hat{\gamma}_k(x,t),\gamma_k(x,t)\rangle}, \\ \hat{b}_k(t) &= \frac{\left\langle -\hat{\mu}_P\frac{\partial^2\hat{\lambda}(x,t)}{\partial x^2},\gamma_k(x,t)\right\rangle}{\langle\hat{\gamma}_k(x,t),\gamma_k(x,t)\rangle}, \\ \hat{b}_k(t) &= \frac{\left\langle \hat{\mu}_D\frac{\partial^4\hat{\lambda}(x,t)}{\partial x^4},\gamma_k(x,t)\right\rangle}{\langle\hat{\gamma}_k(x,t),\gamma_k(x,t)\rangle}. \end{aligned} \tag{7.13}$$

The results of this are shown in Figure 7.30 for MSS and OCS when $\alpha = 500$, NV_P when $\hat{\mu}_P = 3.0$ and NV_D when $\hat{\mu}_D = 30$. Again, these values are selected so that comparison between tangent and adjoint forms is consistent along with these values producing sensitivities in good agreement with the expected value and the adjoint solutions being adequately stabilised. It is clear that MSS, again, is dominated by the

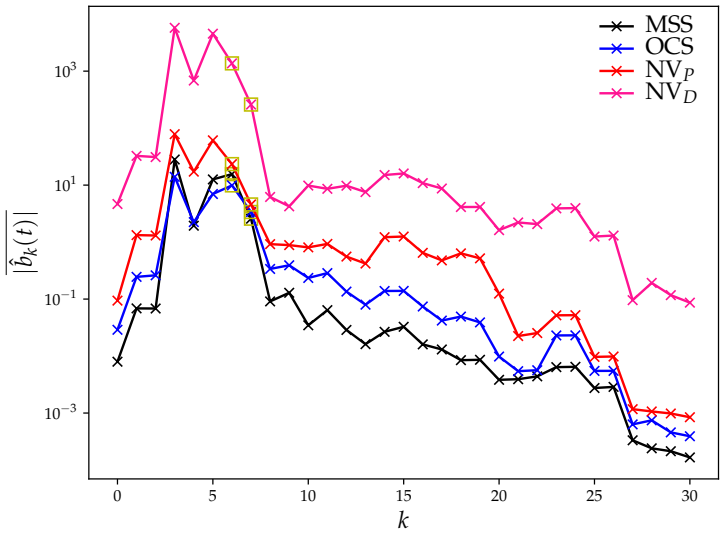

FIGURE 7.30: $\overline{|\hat{b}_k(t)|}$ for the adjoint formulations of MSS, black line, OCS, blue line, NV_P, red line, and NV_D, pink line. Yellow boxes denote neutral CLV modes.

near neutral CLV modes. Further, MSS applies the least control of all the methods investigated. OCS applies a similar amount of control as MSS along the near neutral CLVs, again, implying similarity between the methods. Outside this region the amount applied is larger than MSS. This is due to the difference in temporal boundary conditions between MSS and OCS. The solution generated by OCS can become unbounded if the control is small whereas the solution generated by MSS must satisfy terminal and initial constraints. This results in OCS applying more control than MSS. There is a larger difference in the amount of control applied between NV_P and MSS than is seen in the co-state solutions. This implies that NV methods are non-optimal and that smaller amounts of control can be applied in a more targeted fashion. Similar to the tangent analysis, to apply control in a more optimal manner the NV method should apply control that is composed predominantly of the near neutral modes.

The gain of the MSS, OCS, and NV control terms are presented in Figure 7.31. MSS, similar to the co-state gain, produces a control gain that has similar features as the expected gain albeit at a smaller value. Further, MSS has the largest gain around the near neutral modes again suggesting the importance of the near neutral modes. OCS also shows similar features to MSS with a peak around the near neutral CLVs and reduced gain outside this region contrary to the tangent formulation analysis. This implies that OCS, as in the tangent form, is finding similar features and structures to

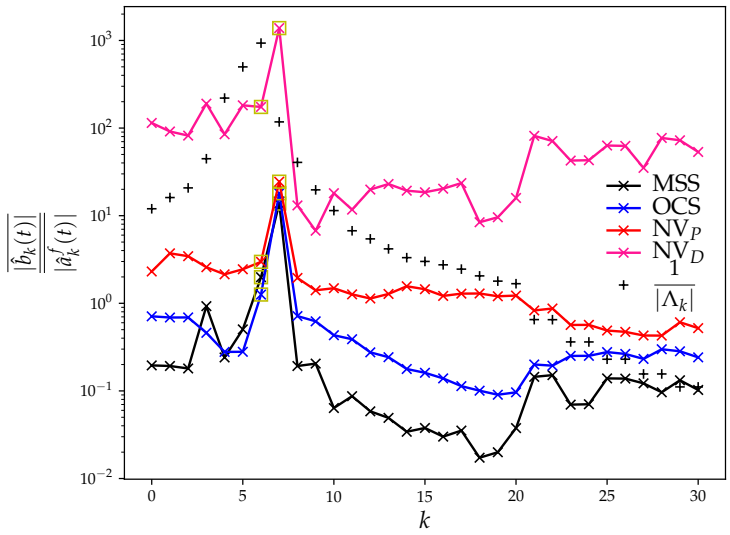

FIGURE 7.31: $\frac{\overline{|\hat{b}_k(t)|}}{\overline{|\hat{a}_k^f(t)|}}$ for MSS, black line, OCS, blue line, NV$_P$, red line, and NV$_D$, pink line. The inverse absolute value of the LE, $\frac{1}{|\Lambda_k|}$, is also plotted with pluses. Yellow boxes denote neutral CLV modes.

MSS and the Shadowing methods. These differences with the tangent formulation are due to the similarity in terminal conditions of the co-state equations between the methods which results in smaller control being applied to keep the solution stable. Similar to the values of $\overline{|\hat{b}_k(t)|}$, the control gain of OCS is similar to MSS in the near neutral region and larger than MSS elsewhere suggesting that OCS is not as optimal in its application of control as MSS.

Further, NV$_P$ has, in general, larger gain than MSS and OCS but shares the similar features of dominance in the near neutral region again implying the NV methods investigated here are non-optimal. This is also caused by the similarity in terminal conditions between NV and MSS resulting in smaller control being applied compared to the tangent formulation. NV$_P$ is still dominated by the near neutral CLV modes and all gains are larger than OCS and MSS. This is due to the control applied being larger than OCS and MSS. This implies that NV methods could apply control in a more targeted fashion which, in turn, could increase the accuracy of the methods. NV$_D$ has significantly larger amounts of gain due to the large amount of control applied. This suggests that, as in the tangent case, deriving control terms from terms which dissipate adjoint energy are not as optimal as those derived from production of adjoint energy.

7.7 Summary

This chapter presented the Lyapunov exponent (LE) spectrum and the covariant Lyapunov vectors (CLVs) generated for the KS system. As far as possible these were validated against previous CLVs and LEs presented in the literature. This was achievable for the CLVs as there is some work on these in the literature. However, validation of the adjoint CLVs was not possible as there has been no previous analysis on them in the literature. These adjoint CLVs did show similar features to the CLVs.

Following this, the decomposition of the solutions generated by the tangent MSS, OCS and NV formulations onto these CLVs was presented. This was undertaken to compare features present in MSS or OCS that could be transferred to NV. It was found that the main CLVs of importance were the near neutral modes. These were defined as the modes whose LEs are close to zero. This implies that any NV method should ensure that the tangent solution is predominantly comprised of the near neutral modes. This may be difficult to establish *a priori* as, in general, the CLV modes are computationally expensive to produce. Analysis of the expected gain, the ratio of output to input, was also presented for each mode and the computed gain showed similar features to the expected gain for MSS for two different parameters of interest. The expected gain along each CLV mode, which has been discovered through this investigation, is proportional to the inverse of the corresponding Lyapunov exponent, $\frac{1}{\Lambda_k}$. This suggests that a Shadowing solution should primarily be composed of the near neutral modes which is found in the MSS solution. This was not the case for OCS and NV. The reason why there was a large gain in the region outside the near neutral modes for OCS and NV was due to the tangent initial condition being away from the approximate Shadowing direction the solution required a large amount of stabilisation of these modes. If an initial condition that is closer to the Shadowing direction can be found then reduced control is required in the tangent formulations. This resulted in the larger than expected gains in this region. This suggests that the NV methods investigated here are non-optimal and better alternatives are available. The implications of this is that the control applied by NV should primarily damp the unstable CLV modes. This is in very good agreement with the conclusions drawn from the spectral analysis presented in the previous chapters. It was also shown that reconstruction of the MSS tangent solution using the six CLVs which had the largest influence which resulted in a solution that is in very good agreement with the computed solution. This implies that these near neutral CLV modes are important in the sensitivity of the system and that if they were known *a priori* then a reasonable approximation of the solution could be made using a linear combination of them. Further, this analysis was shown to be common between domain sizes given the correct scaling of the mode indices.

It was also shown that varying α produced solutions which are in good agreement with MSS in the near neutral CLV range for all values. Increasing α moved the decomposition closer to MSS until the control applied is too small then the solution diverges from MSS. This implies that OCS is applying control in such a manner that an approximation to the Shadowing direction is found. Further, OCS, regardless of tuning parameter used, it is argued attempts to find the same Shadowing direction. This, however, is unlike the NV methods investigated here. For small values of the tuning parameter in NV produced a decomposition that was dissimilar to MSS. Increasing this value brought the decomposition closer to one produced by MSS. The implications of this is that NV methods do not act in the same way for different tuning parameters.

The solutions generated by adjoint MSS, OCS and NV were decomposed onto the CLVs. It was shown that, as in the case of the tangent formulation, the near neutral CLV modes play an important role in the co-state solutions generated. A reconstruction of the MSS solution was generated using the most influential modes and twenty modes were required to produce a solution that is in good agreement with the computed solution. This is larger than the tangent formulation and one possible explanation why was due to the smaller difference between the decomposition of the near neutral modes compared to the modes outside this region. One other explanation for this difference is that tangent MSS finds the Shadowing direction and the adjoint form used here finds the adjoint solution which corresponds to the Shadowing direction. Reformulation of adjoint MSS to find an "adjoint Shadowing direction", *i.e.* find an adjoint solution that remains bounded through allowing the temporal boundary conditions to vary, could reduce the number of modes that are required to produce accurate sensitivity values. This would result in the analysis being more aligned with the tangent formulation.

The co-state solution generated by OCS decomposed onto the modes in a very similar manner to MSS with similar features and magnitudes. This implies that OCS and MSS are acting in very similar ways and that NV methods should also share this feature to be optimal. Further, NV_P also shared this behaviour whereas NV_D shared features but had larger magnitudes than all the other methods. The co-state gain along each CLV shared the same profile as the expected gain for all cases. This is different to the tangent investigation. This implies that the NV methods derived for the tangent formulation may be less optimal than those generated for the adjoint form. One reason for this is that the terminal conditions of the co-state equations are identical for OCS and MSS and similar for NV. This resulted in a smaller amount of control being applied which resulted in the control being applied down the modes outside the near neutral region being reduced. This implies that if an initial condition for the tangent solution is provided that is a better approximation to the Shadowing direction then

minimal control could be applied. Finding such a value may not be feasible as the computation of the Shadowing direction is expensive.

In the adjoint formulation the control solution decomposed predominantly onto the near neutral modes, similar to the tangent formulation, for all methods investigated. MSS applies the least control, followed by OCS and then the two NV methods. This implies that NV methods investigated here are not as optimal as OCS and that NV methods, of which OCS is an optimal version, may not be able to reproduce the exact solution found by Shadowing methods. The control gain was mainly dominated by the near neutral modes and reduced elsewhere for all methods. This was contrary to the tangent formulation and is caused by the similarity in terminal condition of the co-state equation which leads to minimal control being applied to stabilise the solution. This implies that depending on which formulation is being used potentially different NV methods should be utilised. The wider implications of this finding are that computing the CLVs beforehand is expensive and, therefore, knowing if the control term selected in the NV method acts in the near neutral modes is difficult and impractical.

Chapter 8

Behaviour of adjoint OCS on the Kolmogorov system

In this chapter, the behaviour of the adjoint OCS formulation on a 2D spatially distributed system is investigated to show that the analysis presented previously is common between systems. The Kolmogorov system, Refs. [29, 81, 102], which is a modification to the Navier-Stokes equations, is used as it provides a more industrially relevant test case than those used previously. The reason for this is that the Kolmogorov system is spatially two dimensional. The Navier-Stokes equations have been widely investigated for sensitivity analysis of chaotic systems, Refs [14, 16, 20, 21, 22, 23, 32, 33, 49, 90, 91, 92, 93, 120, 121, 127], however, to the author's knowledge sensitivity analysis has not been undertaken on the Kolmogorov system. In this chapter the analysis of the adjoint solutions generated by OCS and NV are compared to MSS to aid in the insight as to what features and structures the control term in the NV method should resemble. The solutions are also decomposed onto the CLVs for the system which, again, are utilised to provide insight into the structure of the NV methods.

8.1 Description of the Kolmogorov system

The Kolmogorov system, which is presented in detail in Ref. [29], is given by

$$\begin{aligned}\frac{\partial\chi(x,y,t)}{\partial t}+\frac{\partial\varphi(x,y,t)}{\partial y}\left(\frac{\partial\chi(x,y,t)}{\partial x}\right)-\frac{\partial\varphi(x,y,t)}{\partial x}\left(\frac{\partial\chi(x,y,t)}{\partial y}\right)=\\ \frac{1}{Re}\nabla^2\chi(x,y,t)-n\cos(ny),\\ x\in[0,L_x),\\ y\in[0,L_y),\\ \chi(0,y,t)=\chi(L_x,y,t),\\ \chi(x,0,t)=\chi(x,L_y,t),\end{aligned}\tag{8.1}$$

where $\chi(x,y,t)$ is the vorticity, $\varphi(x,y,t)$ is the stream function which is computed using $-\chi(x,y,t)=\nabla^2\varphi(x,y,t)$, ∇^2 is the Laplace operator and L_x and L_y are the domain lengths in the x and y co-ordinate directions, respectively. The terms $\frac{\partial\varphi(x,y,t)}{\partial y}$ and $-\frac{\partial\varphi(x,y,t)}{\partial x}$ are the velocity components in the x and y directions, respectively. The Reynolds number is $Re=40$ and $n=4$ is an integer determining the length scale of the forcing are used. Utilising periodic boundary conditions in x and y allows use of spectral methods where the solution can be decomposed as follows

$$\chi(x,y,t)=\sum_{l=-\infty}^{\infty}\sum_{m=-\infty}^{\infty}\tilde{\chi}_{(l,m)}(t)e^{i\left(\frac{2l\pi}{L_x}x+\frac{2m\pi}{L_y}y\right)},$$

where $\tilde{\chi}_{(l,m)}(t)\in\mathbb{C}$ and the solution is discretised in the x and y directions with $N_x=90$ and $N_y=90$ grid points, respectively. A domain of $L_x=2\pi$ and $L_y=2\pi$ in the x and y directions, respectively, is used. A 'spin up' time of $10,000$ time units is used. For numerical stability $\Delta t=5\times10^{-3}$ and $T=500$ time units are used. For time integration a third order Implicit-Explicit scheme, Ref. [70], for the linear and non-linear terms is used. An example of the solution at an instant in time is given in Figure 8.1. The inner product used for the Kolmogorov system between two spatially distributed variables $a(x,y,t)$ and $b(x,y,t)$ is

$$\langle a(x,y,t),b(x,y,t)\rangle=\frac{1}{L_xL_y}\int_0^{L_y}\int_0^{L_x}a(x,y,t)b(x,y,t)\mathrm{d}x\mathrm{d}y,$$

and the norm is

$$\|a(x,y,t)\|=\sqrt{\langle a(x,y,t),a(x,y,t)\rangle}.$$

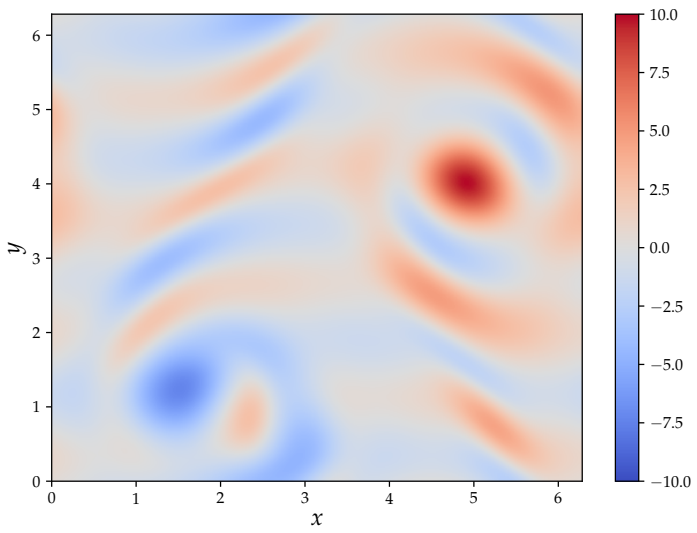

FIGURE 8.1: Example of a typical solution, $\chi(x, y, t)$, of the Kolmogorov equations when $t = 100$.

8.2 Numerical computation of the sensitivity for the Kolmogorov system

As in the previous cases the choice of the parameters and function of interest is free. The parameter of interest is chosen to be the Reynolds number, Re, and the function of interest is

$$J(\chi(x, y, t), p) = \|\chi(x, y, t)\|^2. \tag{8.2}$$

To find the relation between $\bar{J}$ and Re the value of $\bar{J}$ is computed for $Re \in (38, 42)$ with an interval of $\Delta Re = 0.2$ for a time horizon of $T = 25,000$ time units, preceded by a 'spin up' time of $10,000$ time units. The impact that varying Re has on $\bar{J}$, along with a curve fit, is shown in Figure 8.2. It can be seen that there is good correlation between the function of interest and parameter choice. The derivative of the curve fit gives an approximation to the sensitivity, which is $\frac{\mathrm{d}\bar{J}}{\mathrm{d}Re} \approx 0.179$.

Here, the NV term $\mu_s \nabla^2 \hat{\lambda}(x, y, t)$, Ref. [23], is utilised where μ_s is the tuning parameter. It is worth acknowledging that this NV term is derived from terms which dissipate adjoint energy. In sections 5, 6 and 7 it was shown that this approach is not as optimal as those derived from terms which contribute to production of adjoint energy. However, this approach has been developed and utilised in the literature, Refs. [23, 120], and is one of the simplest and most intuitive methods for sensitivity analysis and is for this reason that it is utilised here. Sensitivities generated by OCS, panel (A), and NV, panel (C), by varying their tuning parameters, α and μ_s, respectively, along with the squared norm of the solutions for a range of tuning parameters for OCS, panel (B), and NV, panel (D), can be seen in Figure 8.3. The behaviour seen here for both OCS

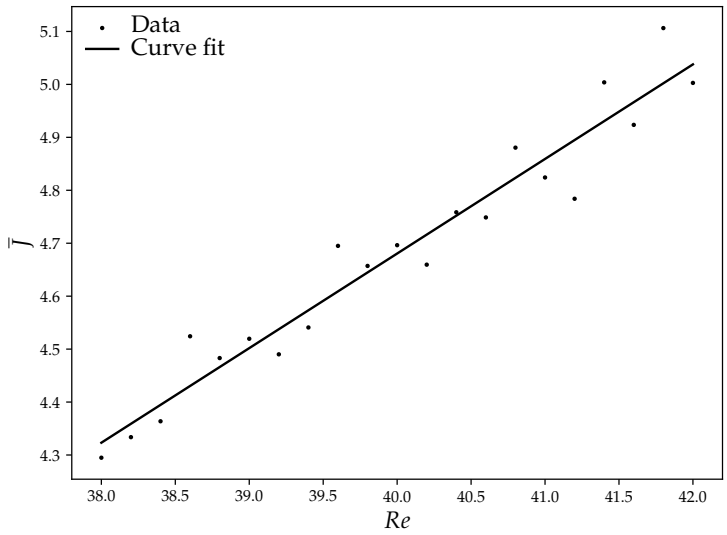

FIGURE 8.2: The relationship between $\bar{J}$ and Re and its curve fit.

and NV is similar to the behaviour shown for the previous cases. When $\alpha < 1 \times 10^2$ the solution is over-damped shown by the small solution norm and the reduced sensitivity value. Increasing α increases the solution norm and the sensitivity. Finally, when $\alpha \geq 1 \times 10^8$ the control is unable to stabilise the solution leading to an under-damped solution and inaccurate sensitivity values. These values of α are, again, system dependent. This implies that, while the features of OCS are common between system, the values at which the solutions is under or over-damped requires work in finding their values. This limits the applicability of the methods as a parameter sweep, to a certain fidelity, is required. Once this region has been determined the sensitivity values and solutions can then be utilised. For large systems, such as turbulent fluid flows, this parameter sweep approach will become unfeasible and alternative methods that do not require tuning should be utilised such as MSS.

For the NV case the solution is under-damped when $\mu_s < 6.0 \times 10^{-2}$. Increasing μ_s leads to a solution which does not show signs of exponential growth of perturbations and accurate sensitivity values. This feature is in very good agreement with the analysis provided for the KS case but again the value of the tuning at which the solution becomes stabilised is problem dependent. The saving grace of the NV methods is that the computation of these methods are cheaper than OCS or MSS and so a tuning parameter sweep may be more feasible.

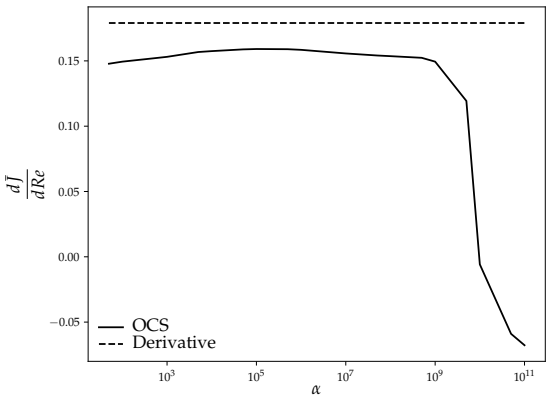

(A) $\frac{d\bar{J}}{dRe}$ against α generated by adjoint OCS, solid line, and the curve fit derivative, dashed line.

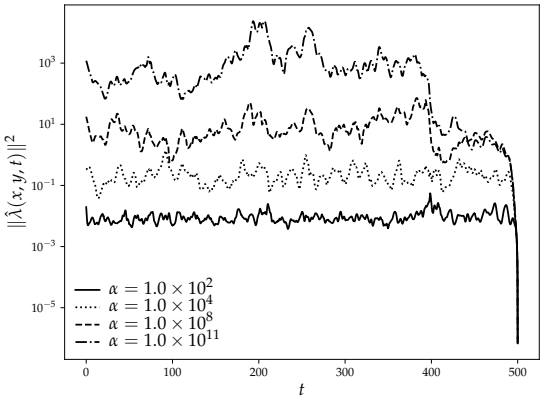

(B) $\|\hat{\lambda}(x,y,t)\|^2$ generated by OCS for $\alpha = 1.0 \times 10^2$, solid black line, $\alpha = 1.0 \times 10^4$, dotted black line, $\alpha = 1.0 \times 10^8$, dashed black line, and $\alpha = 1.0 \times 10^{11}$, dash dotted black line.

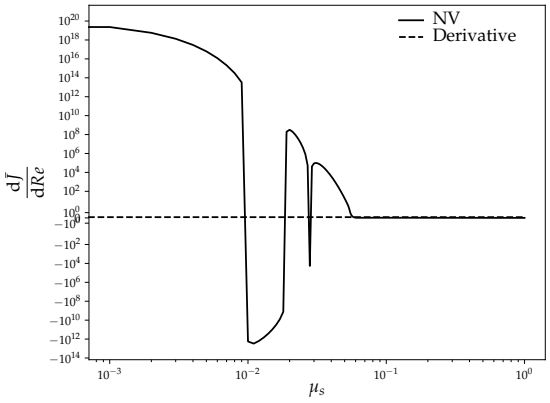

(C) $\frac{d\bar{J}}{dRe}$ against μ_s generated by adjoint NV, solid line, and the curve fit derivative, dashed line.

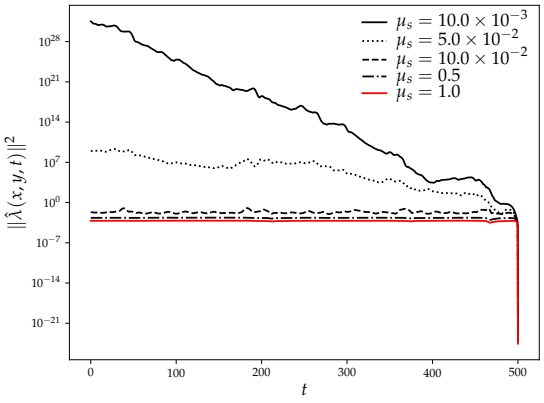

(D) $\|\hat{\lambda}(x,y,t)\|^2$ generated by OCS for $\mu_s = 10.0 \times 10^{-3}$, solid black line, $\mu_s = 5.0 \times 10^{-2}$, dotted black line, $\mu_s = 10.0 \times 10^{-2}$, dashed black line, $\mu_s = 0.5$, dash dotted black line, and $\mu_s = 1.0$, solid red line.

FIGURE 8.3: Sensitivity generated by the different methods, left column, and $\|\hat{\lambda}(x,y,t)\|^2$, right column, for OCS, top row, and NV, bottom row.

8.3 Influence of tuning parameters on the adjoint co-state solution

In this section the adjoint co-state solutions generated by OCS and NV are compared to those generated by MSS. The rationale is that, as before, features and structures may be present in OCS or MSS that can help inform better, more optimal, selection of NV terms. This is conducted for $L_x = L_y = 2\pi$, $N_x = N_y = 90$, $T = 500$ time units preceded by a 'spin up' time of 10,000 time units. Figure 8.4 shows the spatial solution generated by MSS at $t = 100$ time units, panel (A), and the squared norm of the solution, panel (B). Due to the formulation of the minimisation problem of MSS

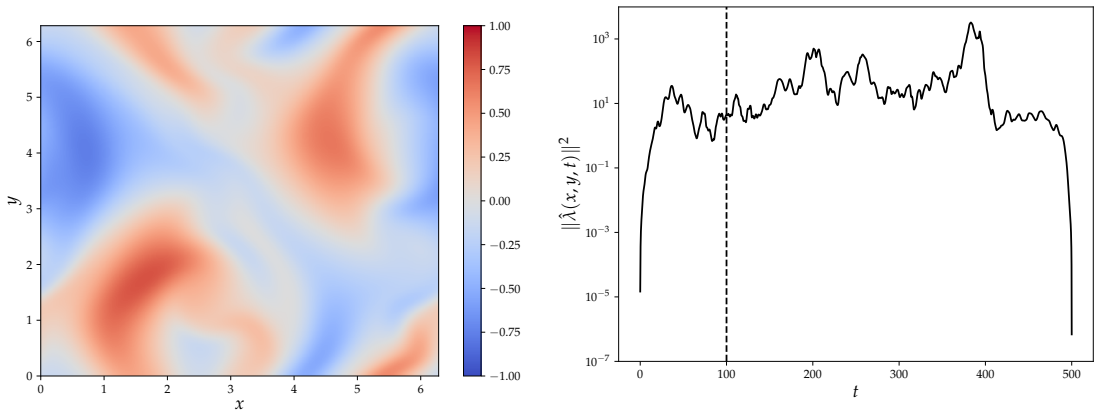

(A) Adjoint co-state solution, $\hat{\lambda}(x, y, t)$, when $t = 100$ time units.

(B) $\|\hat{\lambda}(x, y, t)\|^2$ generated by MSS. The dashed vertical line indicates where the solution in Figure 8.4a is plotted.

FIGURE 8.4: The solution generated by MSS at $t = 100$ time units, panel (A), and the squared norm of the solution, panel (B).

the adjoint co-state solution has both initial and terminal constraints on the solution. This causes the small squared norm values at the beginning and end of the time horizon. The MSS solution is the largest around the two vortex core regions of $x = y = 2$ and $x = y = 5$.

The solution generated by OCS for $\alpha \in \{100, 1 \times 10^4, 1 \times 10^{11}\}$, left column, and the squared norm of the solution, right column, can be seen in Figure 8.5. In general, OCS has a terminal condition identical to that of MSS. When $\alpha = 100$ the solution generated by OCS is several orders of magnitude smaller than that generated by MSS. This, again, is due to an over-damped solution. The two vortex core regions, found by MSS, are also present in the OCS solution, except there are higher frequency features present in OCS. One explanation for this is that, as in the KS case, the forcing term which is proportional to the non-linear solution, Figure 8.1, is dominating the solution hence why there are higher frequency features present in OCS. The squared norm of the solution remains, on average, around 1×10^{-2}, which is smaller than MSS suggesting signs of over-damping. Increasing α to 1×10^4 produces a solution which is very similar to one generated by MSS. This implies that this value of α is neither over or under-damped. This also impacts the squared norm of the solution where the average is increased to around 2×10^{-1}. Finally, when $\alpha = 1 \times 10^{11}$ the solution is larger than that generated by MSS which implies the solution is under-damped. In this instance the vortex cores have negative solutions compared to MSS. Further, the norm squared of the solution is, on average, larger than that of generated by MSS. The implication of this analysis is that OCS behaves in a very similar manner between systems and the concluisions drawn in the previous chapters are also valid here.

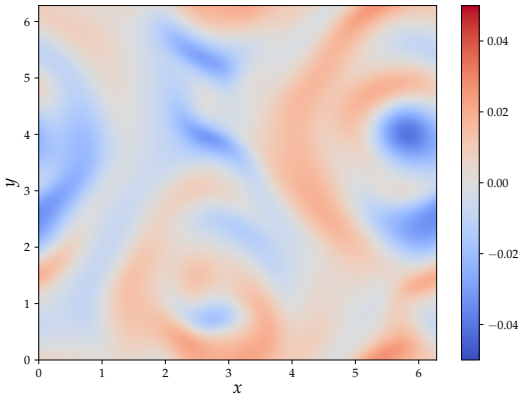

(A) Adjoint co-state solution, $\hat{\lambda}(x, y, t)$, when $t = 100$ time units and $\alpha = 100$.

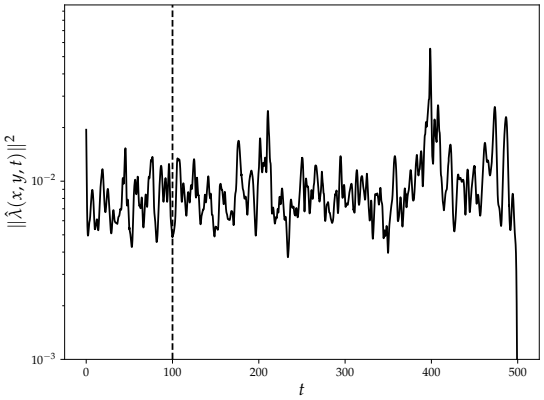

(B) $\|\hat{\lambda}(x, y, t)\|^2$ generated by OCS when $\alpha = 100$. The dashed vertical line indicates where the solution in Figure 8.5a is plotted.

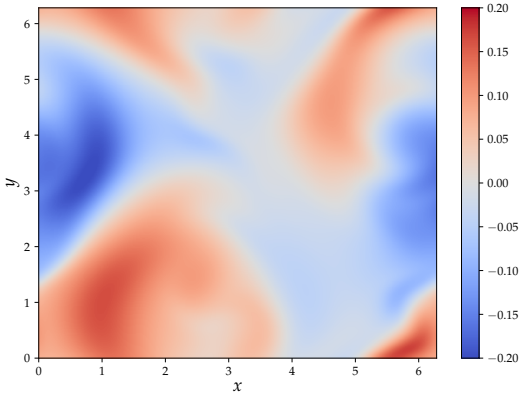

(C) Adjoint co-state solution, $\hat{\lambda}(x, y, t)$, when $t = 100$ time units and $\alpha = 1 \times 10^4$.

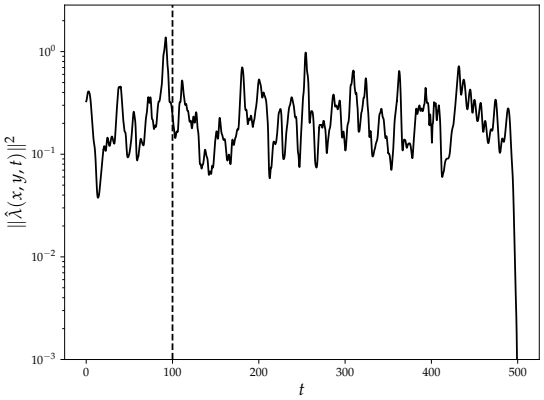

(D) $\|\hat{\lambda}(x, y, t)\|^2$ generated by OCS when $\alpha = 1 \times 10^4$. The dashed vertical line indicates where the solution in Figure 8.5c is plotted.

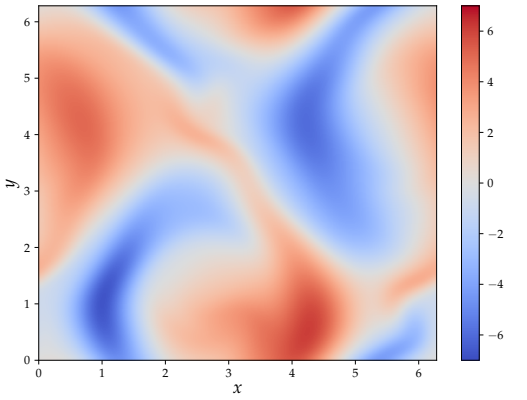

(E) Adjoint co-state solution, $\hat{\lambda}(x, y, t)$, when $t = 100$ time units and $\alpha = 1 \times 10^{11}$.

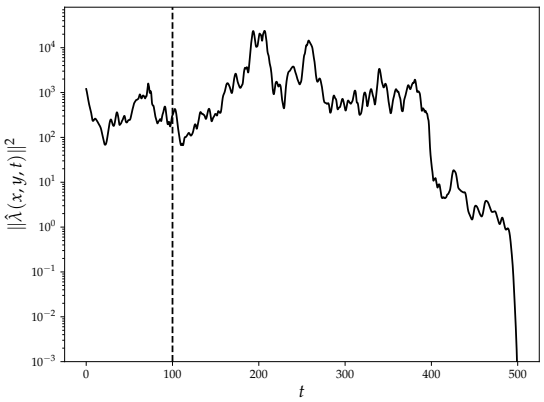

(F) $\|\hat{\lambda}(x, y, t)\|^2$ generated by OCS when $\alpha = 1 \times 10^{11}$. The dashed vertical line indicates where the solution in Figure 8.5e is plotted.

FIGURE 8.5: The solution generated by OCS at $t = 100$ time units, left column, and the squared norm of the solution, right column, when $\alpha = 100$, top row, $\alpha = 1 \times 10^4$, middle row, and $\alpha = 1 \times 10^{11}$, bottom row.

The solutions generated by NV for $\mu_s \in \{0.01, 0.05, 1.0\}$ are shown in Figure 8.6. When $\mu_s = 0.01$ the solution is under-damped and is several orders of magnitude larger than that generated by MSS or OCS. This suggests that this value is applying control in a non-optimal fashion and that more efficient methods are available. Further, the largest region in the solution is at $x = 0.5, y = 4.5$ and $x = y = 4.5$ which is dissimilar to the solution generated by MSS implying NV is not finding the same approximate Shadowing direction as MSS. The solution magnitude continues to grow backwards in time in contrast to OCS and MSS which remain constant. This suggests that NV is not applying control in an optimal or targeted fashion. Increasing μ_s to 0.05 produces a similar, albeit inverted, structure that, again, is still several orders of magnitude larger than MSS and OCS. In this instance the squared norm of the solution does grow backwards in time but to a lesser extent than the previous case implying the solution is still under-damped. Finally, when $\mu_s = 1.0$ the solution is stabilised and the squared norm of the solution remains of the order 5×10^{-4} which is significantly lower than both OCS and MSS. This may imply that the solution has been over-damped or the application of control is generic and not targeting specific structures that contribute to the production of adjoint energy and that more efficient methods are availabe. It is also clear that the solution does not resemble that of MSS or OCS. This could be due to the control term leading to an adjoint system being altered significantly and an alternative Shadowing direction is found which, in essence, relates to a slightly modified non-linear system, Ref. [49]. Further, the damping has removed the high frequency modes which is expected as these control terms act on high frequency modes. Finally, there are two main vortex structures at $x = 3, y = 1$ and $x = 6, y = 4$ that are not seen in the MSS or OCS cases.

8.3.1 Similarities in co-state solution with MSS

In this section the adjoint co-state solutions generated by OCS and NV are compared against MSS using the same metric used previously which is restated here

$$\hat{\theta}_X(t) = \arccos\left(\frac{\langle \hat{\lambda}_{MSS}(x,y,t), \hat{\lambda}_X(x,y,t)\rangle}{\|\hat{\lambda}_{MSS}(x,y,t)\|\|\hat{\lambda}_X(x,y,t)\|}\right).$$

The rationale is, again, to attempt to find structures and solutions that are present in the Shadowing approach that could provide more targeted control in NV methods. As in the KS case, a small value of this metric means the solutions are aligned and values close to $\frac{\pi}{2}$ means the solutions are dissimilar. The results of this decomposition for a range of value of α, panel (A), and μ_s, panel (B), are shown in Figure 8.7. All OCS solutions are aligned with MSS denoted by the small value of $\hat{\theta}_{OCS}(t)$ towards the end of the time horizon. This implies that the solutions are similar in this region. This, as mentioned previously, is due to the same terminal conditions. Working further

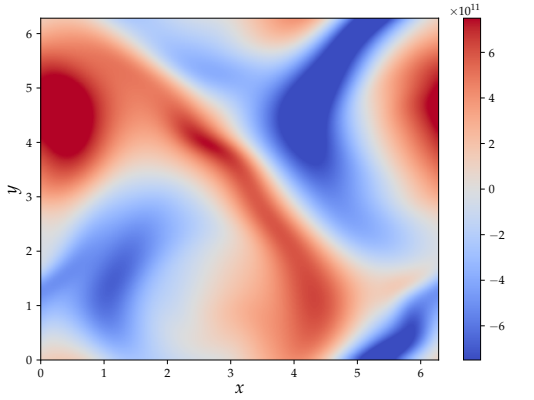

(A) Adjoint co-state solution, $\hat{\lambda}(x, y, t)$, when $t = 100$ time units and $\mu_s = 0.01$.

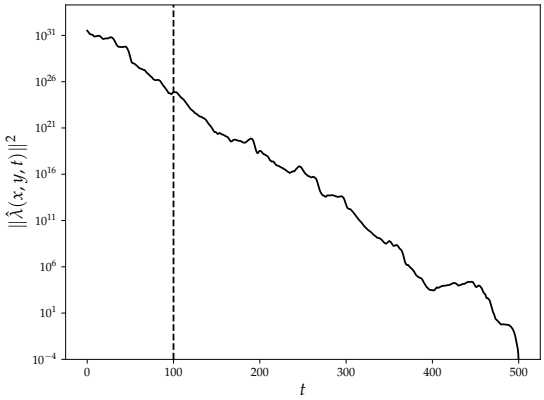

(B) $\|\hat{\lambda}(x, y, t)\|^2$ generated by NV when $\mu_s = 0.01$. The dashed vertical line indicates where the solution in Figure 8.6a is plotted.

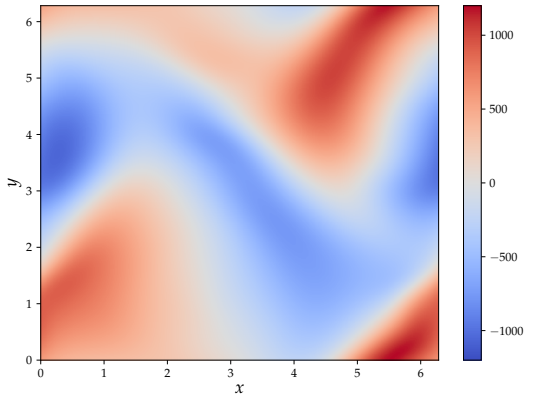

(C) Adjoint co-state solution, $\hat{\lambda}(x, y, t)$, when $t = 100$ time units and $\mu_s = 0.05$.

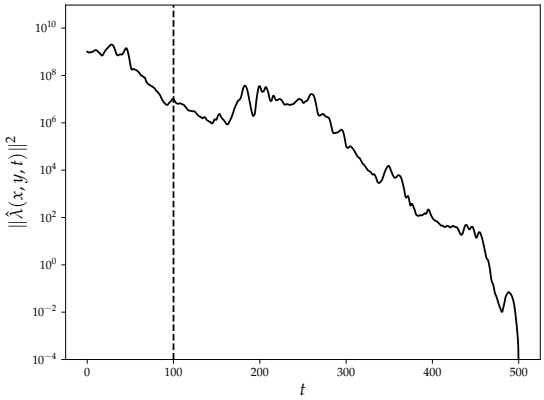

(D) $\|\hat{\lambda}(x, y, t)\|^2$ generated by NV when $\mu_s = 0.05$. The dashed vertical line indicates where the solution in Figure 8.6c is plotted.

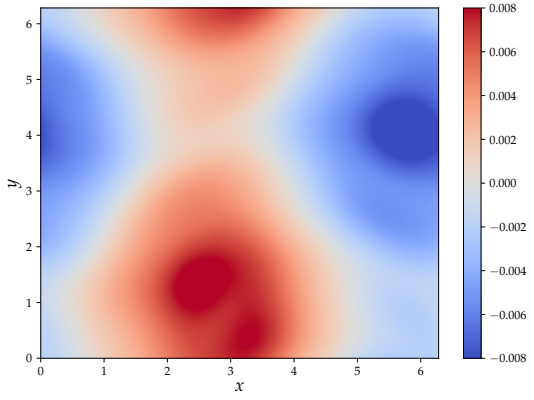

(E) Adjoint co-state solution, $\hat{\lambda}(x, y, t)$, when $t = 100$ time units and $\mu_s = 1.0$.

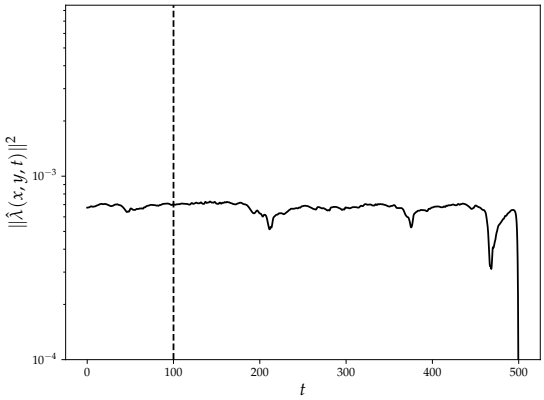

(F) $\|\hat{\lambda}(x, y, t)\|^2$ generated by NV when $\mu_s = 1.0$. The dashed vertical line indicates where the solution in Figure 8.6e is plotted.

FIGURE 8.6: The solution generated by NV at $t = 100$ time units, left column, and the squared norm of the solution, right column, when $\mu_s = 0.01$, top row, $\mu_s = 0.05$, middle row, and $\mu_s = 1.0$, bottom row.

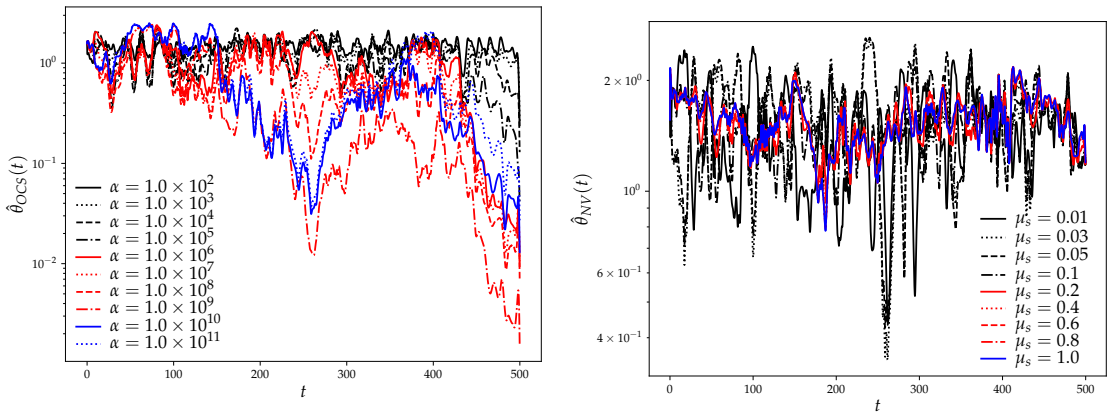

(A) $\hat{\theta}_{OCS}(t)$ for $\alpha = 1.0 \times 10^2$, solid black line, $\alpha = 1.0 \times 10^3$, dotted black line, $\alpha = 1.0 \times 10^4$, dashed black line, $\alpha = 1.0 \times 10^5$, dash dotted black line, $\alpha = 1.0 \times 10^6$, solid red line, $\alpha = 1.0 \times 10^7$, dotted red line, $\alpha = 1.0 \times 10^8$, dashed red line, $\alpha = 1.0 \times 10^9$, dash dotted red line, $\alpha = 1.0 \times 10^{10}$, solid blue line, and $\alpha = 1.0 \times 10^{11}$, dotted blue line.

(B) $\hat{\theta}_{NV}(t)$ for $\mu_s = 0.01$, solid black line, $\mu_s = 0.03$, dotted black line, $\mu_s = 0.05$, dashed black line, $\mu_s = 0.1$, dash dotted black line, $\mu_s = 0.2$, red solid line, $\mu_s = 0.4$, red dotted line, $\mu_s = 0.6$, red dashed line, $\mu_s = 0.8$, red dash dotted line, and $\mu_s = 1.0$, blue solid line.

FIGURE 8.7: $\hat{\theta}_X(t)$ for OCS, panel (A), for a range of α values and NV, panel (B), for a range of μ_s values.

backwards in time the solutions diverge. This means the solutions are orthogonal and share no similarities with each other. This, as mentioned in chapter 6, is caused by the difference in temporal boundary conditions between OCS and MSS. One interesting observation is that when α is small the values diverge away from MSS more rapidly than larger values. This is caused by the large amount of control being applied in these cases having a large influence on the solution. Implications of this are that OCS is finding an "adjoint Shadowing direction" which is different to the MSS method. One possible solution to this, as mentioned for the adjoint KS analysis, is to find the solution using MSS that minimises the adjoint solution through allowing the temporal boundary conditions to vary. This is different to the method used here where the adjoint solution has constrained temporal boundary conditions. All values of μ_s investigated showed no similarity with the MSS solutions, Figure 8.7b. The implications of this are that, as in the KS cases, the NV methods are non-optimal and more efficient methods of control are availabele. The dip in both OCS and NV around $t = 250$ is caused by a large vortex bursting event where it is well known that solutions align in these regions, see Refs. [4, 5, 26, 46, 47, 108, 123] for further details, hence the aligning of the solutions with MSS.

8.4 Influence of tuning parameters on the adjoint control solution

In this section the adjoint control solutions generated by OCS and NV are compared to those generated by MSS. This is undertaken using similar reasoning to before and to find potential structures or features that could improve NV methods. As mentioned in section 6.4, MSS also has a control term, $2\hat{v}(x, y, t)$, and is compared to those generated by OCS and NV. This is conducted for $L_x = L_y = 2\pi$, $N_x = N_y = 90$, $T = 500$ time units preceded by a 'spin up' time of $10,000$ time units which ensures the solution is on the attractor. Figure 8.8 shows the control spatial solution generated by MSS at $t = 100$, panel (A), and the squared norm of the solution, panel (B). Due to the

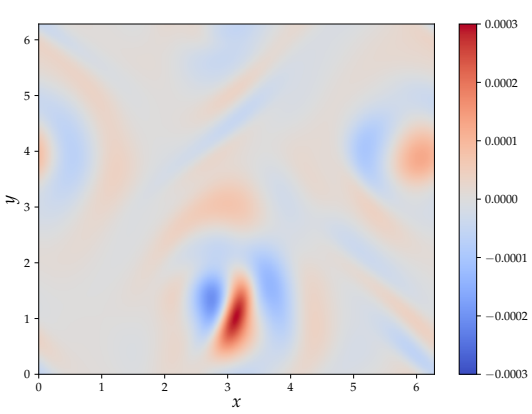

(A) Adjoint control solution, $2\hat{v}(x, y, t)$, when $t = 100$ time units.

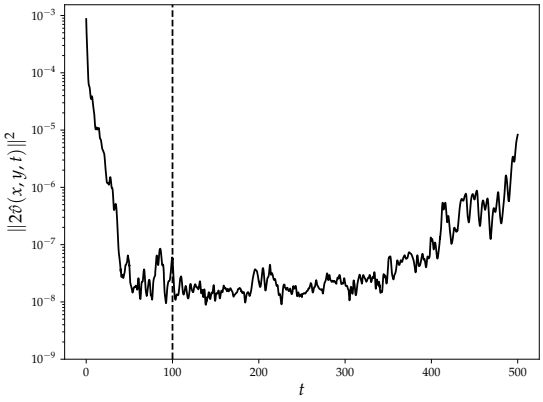

(B) $\|2\hat{v}(x, y, t)\|^2$ generated by MSS. The dashed vertical line indicates where the solution in Figure 8.8a is plotted.

FIGURE 8.8: The solution generated by MSS at $t = 100$ time units, panel (A), and the squared norm of the solution, panel (B).

formulation of the minimisation problem of MSS the adjoint control solution has no fixed initial and terminal constraints on the solution. The MSS solution is largest around the regions of $x = 3, y = 1$ and $x = 6, y = 4$ which relate to the vortex core regions in the non-linear solution at that instant in time.

The solution generated by OCS for $\alpha \in \{100, 1 \times 10^4, 1 \times 10^{11}\}$, left column, and the squared norm of the solution, right column, can be seen in Figure 8.9. It is clear that in all cases investigated the control solution shares common features, albeit of different magnitudes, with that of MSS. This implies that the control applied by OCS is very similar in feature and structure to MSS suggesting that OCS acts in a similar manner to MSS. The main two are the vortex cores at $x = 3, y = 1$ and $x = 6, y = 4$ and there are high frequency features present similar to MSS. When $\alpha = 100$ the solution generated by OCS is several orders of magnitude larger than that generated by MSS

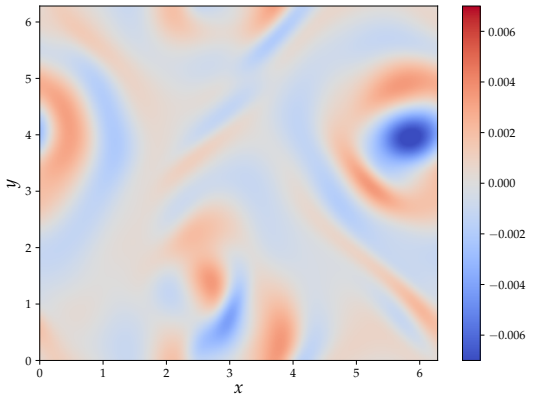

(A) Adjoint control solution, $2\hat{v}(x,y,t)$, when $t = 100$ time units and $\alpha = 100$.

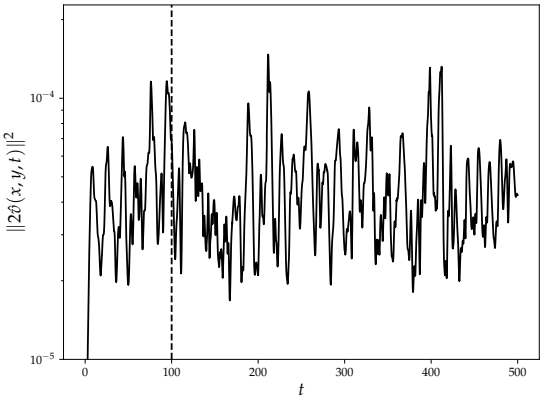

(B) $\|2\hat{v}(x,y,t)\|^2$ generated by OCS when $\alpha = 100$. The dashed vertical line indicates where the solution in Figure 8.9a is plotted.

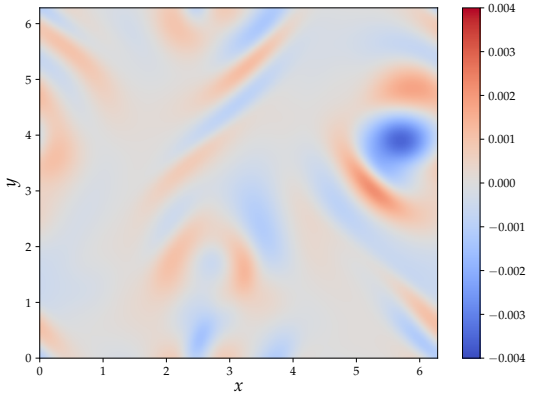

(C) Adjoint control solution, $2\hat{v}(x,y,t)$, when $t = 100$ time units and $\alpha = 1 \times 10^4$.

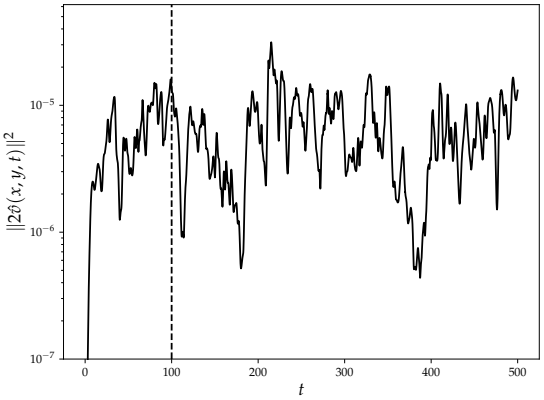

(D) $\|2\hat{v}(x,y,t)\|^2$ generated by OCS when $\alpha = 1 \times 10^4$. The dashed vertical line indicates where the solution in Figure 8.9c is plotted.

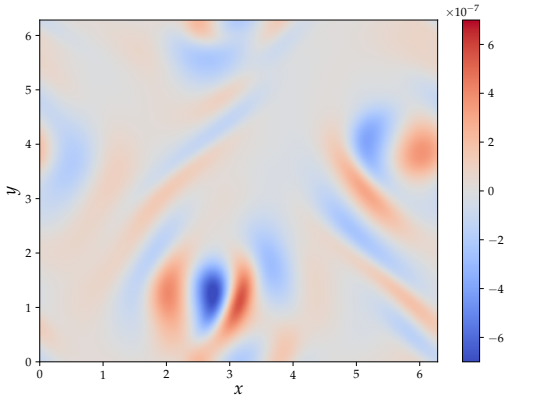

(E) Adjoint control solution, $2\hat{v}(x,y,t)$, when $t = 100$ time units and $\alpha = 1 \times 10^{11}$.

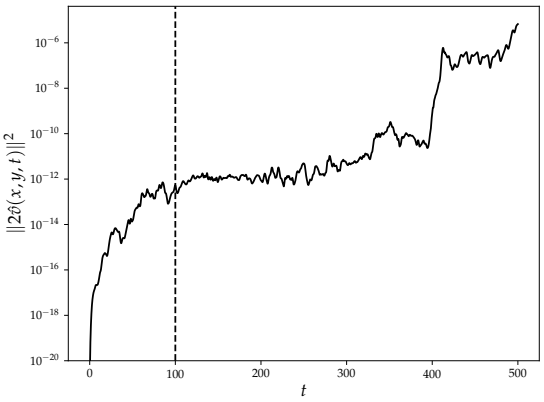

(F) $\|2\hat{v}(x,y,t)\|^2$ generated by OCS when $\alpha = 1 \times 10^{11}$. The dashed vertical line indicates where the solution in Figure 8.9e is plotted.

FIGURE 8.9: The solution generated by OCS at $t = 100$ time units, left column, and the squared norm of the solution, right column, when $\alpha = 100$, top row, $\alpha = 1 \times 10^4$, middle row, and $\alpha = 1 \times 10^{11}$, bottom row.

suggesting the solution is over-damped. This, again, is due to the control being cheap to apply. The squared norm of the solution remains, on average, around 5×10^{-5}, which is larger than MSS. Increasing α to 1×10^4 produces a solution which is very similar to one generated by MSS in structure suggesting that this value is producing a solution which is appropriately stabilised. This also impacts the squared norm of the solution where the average is decreased to around 5×10^{-6} which is comparable to MSS. When $\alpha = 1 \times 10^{11}$ the solution is smaller than that generated by MSS suggesting the solution generated is under-damped. Further, the norm squared of the solution is, on average, significantly smaller than that generated by MSS. When $\alpha \in \{100, 1 \times 10^4\}$ the squared norm remains constant throughout the time horizon whereas for $\alpha = 1 \times 10^{11}$ the solution increases exponentially. Selection of the value of α *a priori* is difficult as the value which appropriately stabilised the solution is system dependent and as such no rules of thumb can be produced. This suggests that an alternative approach should be utilised in industry, such as MSS.

The solutions generated by NV for $\mu_s \in \{0.01, 0.05, 1.0\}$ are shown in Figure 8.10. The first finding is that when $\mu_s = 0.01$ the squared norm of the control solution increases exponentially backwards in time. This implies the control is non-optimal and not targeting the unstable CLV modes. This behaviour was seen for small values of tuning parameter in the KS case also and suggests is a feature of certain NV methods. Further, the solution generated does not resemble the solution generated by MSS and is in the under-damped region. There is an emergence of the diagonal streaks that are not present in MSS or OCS. This, it is argued, is caused by the control applied altering the system significantly which results in a discrepancy between adjoint system and non-linear system, Ref. [49]. Increasing μ_s to 0.05 reduces the squared norm of the solution but still is unable to stabilise the solution. Further, the control solution is closer to that of $\mu_s = 0.01$ than MSS or OCS suggesting that the control is not being applied in a more appropriate manner. When $\mu_s = 1.0$ the control applied has a squared norm that remains constant throughout the time horizon. Finally, the solution shares similar features with MSS and OCS but is an order of magnitude larger. This analysis suggests that when $\mu_s = 1.0$ then this NV method may be close to optimal.

8.4.1 Similarities in control solution with MSS

In this section, the similarities between the control solutions generated by MSS are compared to OCS and NV. This additional analysis is used to determine if structures or features are present in OCS or MSS that could influence future selection of NV terms. The metric used to in the comparison between the adjoint control terms for MSS and OCS is

$$\hat{\theta}^q_{OCS}(t) = \arccos\left(\frac{\langle 2\hat{v}_{MSS}(x,y,t), 2\hat{v}_{OCS}(x,y,t)\rangle}{\|2\hat{v}_{MSS}(x,y,t)\|\|2\hat{v}_{OCS}(x,y,t)\|}\right),$$

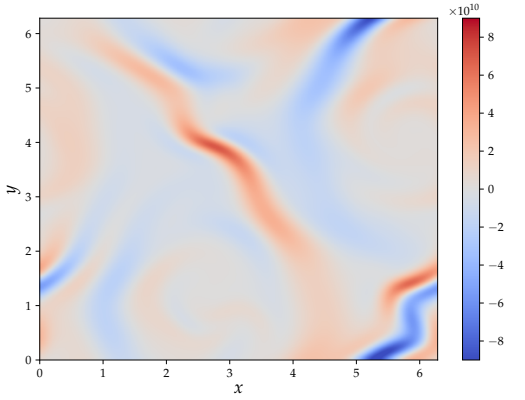

(A) Adjoint control solution, $\mu_s \nabla^2 \hat{\lambda}(x,y,t)$, when $t = 100$ time units and $\mu_s = 0.01$.

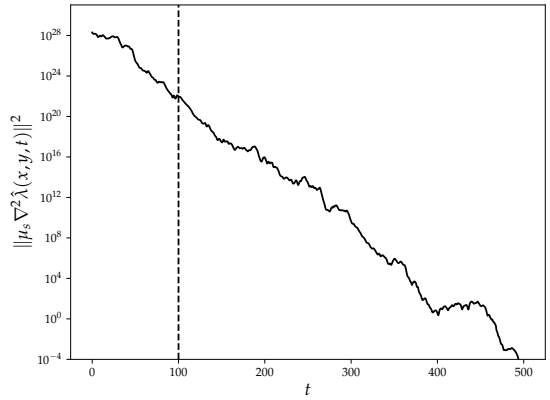

(B) $\|\mu_s \nabla^2 \hat{\lambda}(x,y,t)\|^2$ generated by NV when $\mu_s = 0.01$. The dashed vertical line indicates where the solution in Figure 8.10a is plotted.

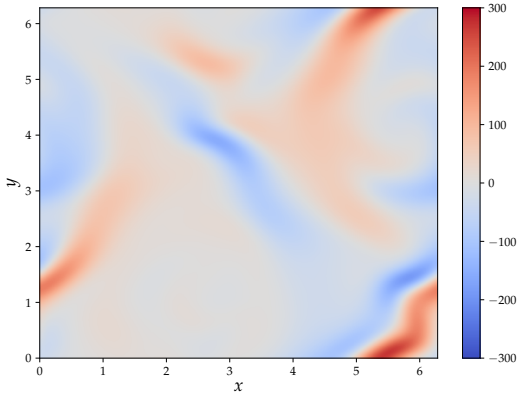

(C) Adjoint control solution, $\mu_s \nabla^2 \hat{\lambda}(x,y,t)$, when $t = 100$ time units and $\mu_s = 0.05$.

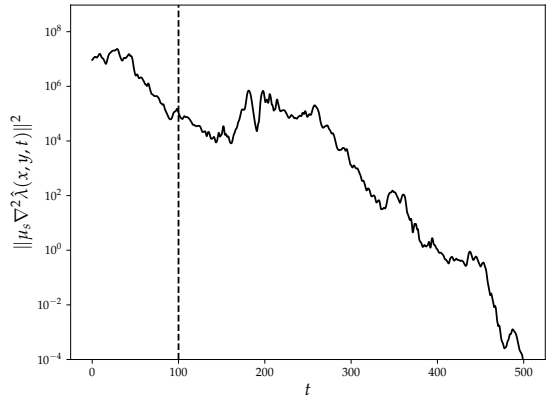

(D) $\|\mu_s \nabla^2 \hat{\lambda}(x,y,t)\|^2$ generated by NV when $\mu_s = 0.05$. The dashed vertical line indicates where the solution in Figure 8.10c is plotted.

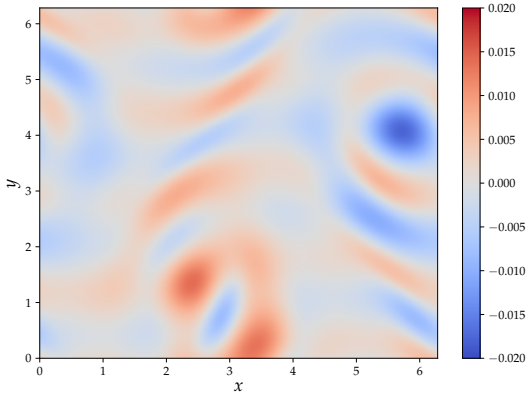

(E) Adjoint control solution, $\mu_s \nabla^2 \hat{\lambda}(x,y,t)$, when $t = 100$ time units and $\mu_s = 1.0$.

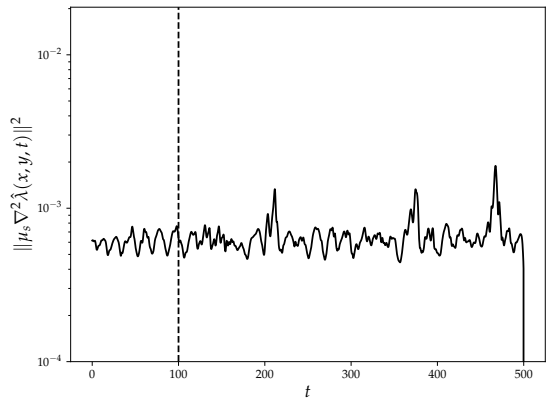

(F) $\|\mu_s \nabla^2 \hat{\lambda}(x,y,t)\|^2$ generated by NV when $\mu_s = 1.0$. The dashed vertical line indicates where the solution in Figure 8.10e is plotted.

FIGURE 8.10: The solution generated by NV at $t = 100$ time units, left column, and the squared norm of the solution, right column, when $\mu_s = 0.01$, top row, $\mu_s = 0.05$, middle row, and $\mu_s = 1.0$, bottom row.

and NV and MSS is

$$\hat{\theta}^q_{NV}(t) = \arccos\left(\frac{\langle 2\hat{v}_{MSS}(x,y,t), \mu_s\nabla^2\hat{\lambda}_{NV}(x,y,t)\rangle}{\|2\hat{v}_{MSS}(x,y,t)\|\|\mu_s\nabla^2\hat{\lambda}_{NV}(x,y,t)\|}\right).$$

As before values close to 0 for these metrics means solutions are aligned and values of $\frac{\pi}{2}$ mean the solutions are orthogonal and dissimilar. The results of this decomposition for a range of values of α, panel (A), and μ_s, panel (B), are shown in Figure 8.11. In the

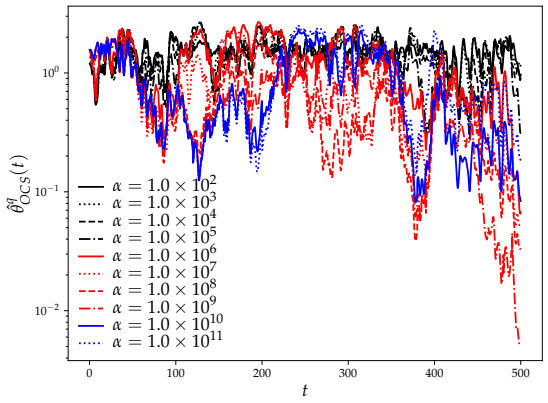

(A) $\hat{\theta}^q_{OCS}(t)$ for $\alpha = 1.0 \times 10^2$, solid black line, $\alpha = 1.0 \times 10^3$, dotted black line, $\alpha = 1.0 \times 10^4$, dashed black line, $\alpha = 1.0 \times 10^5$, dash dotted black line, $\alpha = 1.0 \times 10^6$, solid red line, $\alpha = 1.0 \times 10^7$, dotted red line, $\alpha = 1.0 \times 10^8$, dashed red line, $\alpha = 1.0 \times 10^9$, dash dotted red line, $\alpha = 1.0 \times 10^{10}$, solid blue line, and $\alpha = 1.0 \times 10^{11}$, dotted blue line.

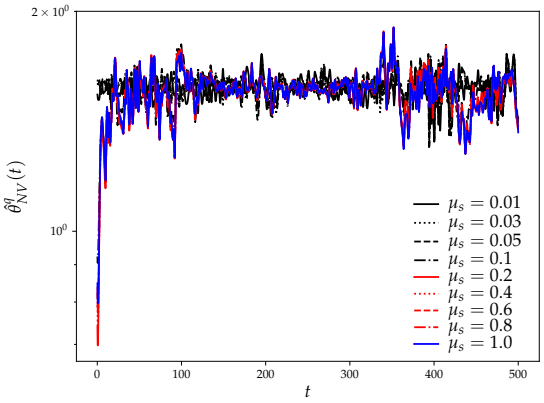

(B) $\hat{\theta}^q_{NV}(t)$ for $\mu_s = 0.01$, solid black line, $\mu_s = 0.03$, dotted black line, $\mu_s = 0.05$, dashed black line, $\mu_s = 0.1$, dash dotted black line, $\mu_s = 0.2$, red solid line, $\mu_s = 0.4$, red dotted line, $\mu_s = 0.6$, red dashed line, $\mu_s = 0.8$, red dash dotted line, and $\mu_s = 1.0$, blue solid line.

FIGURE 8.11: $\hat{\theta}^q_X(t)$ for OCS, panel (A), for a range of α values and NV, panel (B), for a range of μ_s values.

OCS case the control applied is fairly well aligned with that of MSS in the final 100 time units of the time horizon for large values of α. This implies that the control terms share some resemblance in this region. The reason for this is that OCS and MSS share identical terminal boundary conditions and, therefore, minimal control is applied in this region resulting in similar control between the methods. Outside this region there is no similarity between the OCS and MSS control terms as the angle between solutions is around $\frac{\pi}{2}$. This is again due to the initial condition on the co-state solution of MSS which is not present for OCS leading to differing control strategies between the methods. The initial condition on MSS modifies the control such that OCS is no longer similar. For NV, however, initially the control applied is similar to that of MSS for large values of μ_s. As time increases this similarity diverges until there is no similarity at all between solutions. The behaviour shown by NV is very similar to that presented in chapter 6 which implies this control method is non-optimal and does not apply control in a targeted manner.

8.5 Validation of the covariant Lyapunov vectors and Lyapunov exponents generated for the Kolmogorov system

There has been relatively little work on computation of the CLVs, $\gamma_k(x,y,t)$ and $\hat{\gamma}_k(x,y,t)$, on the Kolmogorov system. Work on computation of CLVs and LEs for fluid flow has been undertaken in Ref. [90] around a cylinder, Ref. [66] on a thermo-acoustic model, Ref. [58] for forced homogeneous turbulence and Ref. [94] in a turbulent channel. There are works investigating the LEs of the Kolmogorov system, Ref. [54]. More recently computation of the CLVs for the Kolmogorov system, Ref. [67], has taken place. This work presents the adjoint CLVs extending the work of Refs. [54, 67]

Firstly, as in the KS case, the 'spin up' time is determined such that the CLVs have aligned with their respective sub-spaces. This is achieved in a very similar manner to that presented in section 7.1 by simulating many CLVs from different starting times and finding when the angles between the CLVs reduces to zero or in reality below 1×10^{-7}. The angle metric used is

$$\theta_k = \arccos\left(\frac{\langle \gamma_k(x,y,t_B)_\tau, \gamma_k(x,y,t_B)_{10,000}\rangle}{\|\gamma_k(x,y,t_B)_\tau\|\,\|\gamma_k(x,y,t_B)_{10,000}\|}\right),$$

where $\gamma_k(x,y,t_B)_{10,000}$ is the CLV simulated for $10,000$ time units and $\gamma_k(x,y,t_B)_\tau$ the CLV simulated for $\tau = 10,000 - t_A$ time units. As before, small values of the metric mean the CLVs are similar and aligned and large values are dissimilar and not aligned. The results of this can be seen in Figure 8.12 for a range of different τ values. The two neutral CLVs do not converge with the same behaviour of the other modes.

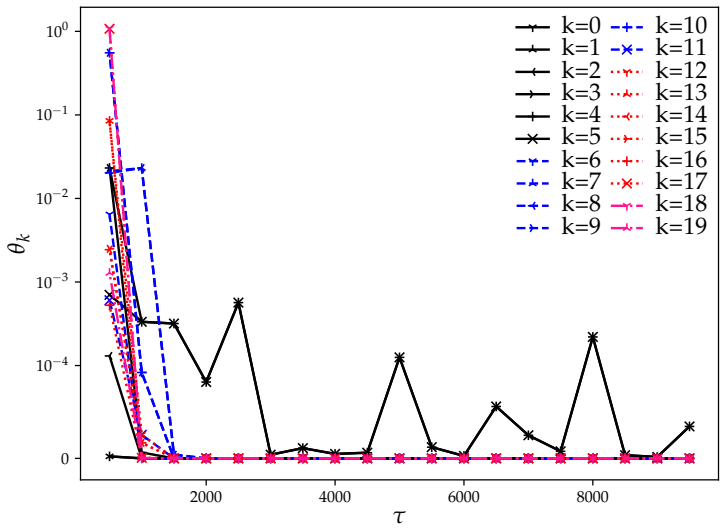

FIGURE 8.12: Convergence rates of $\gamma_k(x,y,t_B)_\tau$ for various τ values.

The reason for this is identical to the KS CLVs and is due to the computed neutral modes being a linear combination of the analytical neutral modes. Similar features are present here as with the KS CLVs in that small values of τ means the CLVs do not have time to align with their respective sub-spaces while large values allow time for alignment. Here, a 'spin up' time of $10,000$ time units is used.

As the 'spin up' time has been determined, the LE spectrum computed using the Kuptsov and Parlitz algorithm for the Kolmogorov system is shown in Figure 8.13 when $Re = 40$. While Ref. [67] uses a lower Reynolds number than investigated here

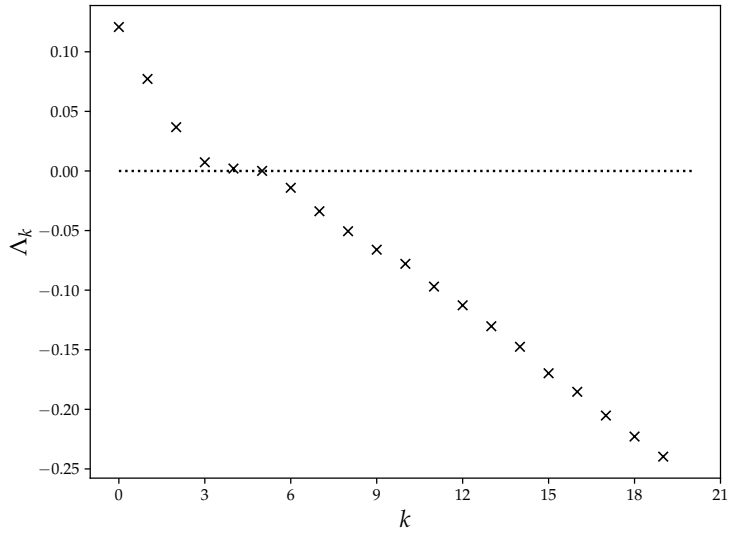

FIGURE 8.13: The Lyapunov exponent spectrum for the Kolmogorov system when $Re = 40$.

there are similarities between Figure 1 in Ref. [67] and Figure 8.13 presented here. It can, therefore, be concluded that the LE spectrum computed here is showing similar behaviour to that of previously published works. The LEs show there are four positive exponents, corresponding to four unstable CLV modes. The spectrum shows that there are two neutral CLV modes. These CLVs can be thought of as being caused by the property of the system and due to translational symmetry in the x direction respectively, Ref. [67]. As in the KS system, the Kuptsov and Parlitz algorithm struggles to disambiguate these modes and, therefore, the CLVs computed are linear combinations of the two theoretical modes. The remaining LEs are found to be negative. Unlike the KS system, the number of CLVs computed is argued here to be well within the physical mode region as the high frequency modes are not found. Further, due to the small domain investigated the resolution of the LE spectrum is relatively "coarse" and increasing the domain size will resolve further modes and likely lead to a reduced difference between consecutive LE values.

A range of CLVs, $\gamma_k(x, y, t)$, are shown for $k \in \{0, 6, 12, 18\}$ when $t = 100$ are shown in Figure 8.14. While Ref. [67] uses a lower Re it is worth noting that the main CLV

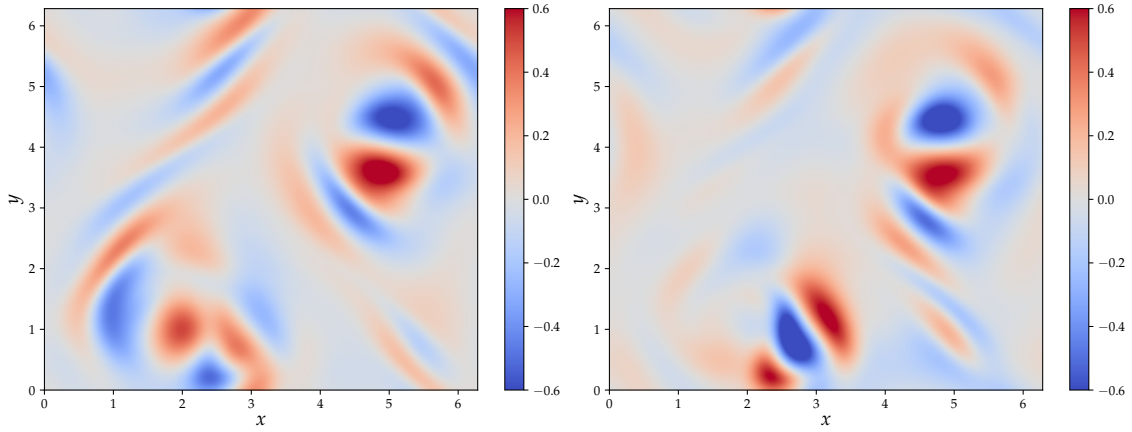

(A) Spatial structure of $\gamma_0(x, y, t)$ when $t = 100$.

(B) Spatial structure of $\gamma_6(x, y, t)$ when $t = 100$.

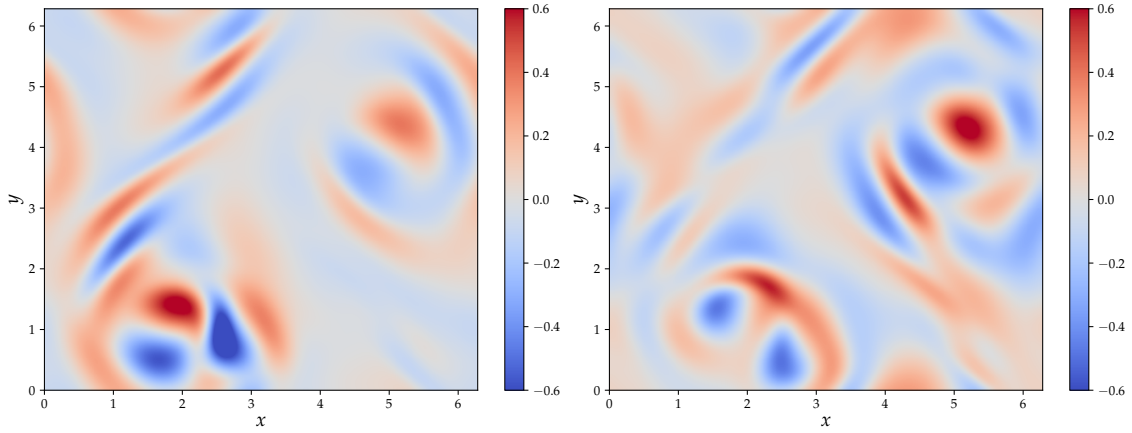

(C) Spatial structure of $\gamma_{12}(x, y, t)$ when $t = 100$.

(D) Spatial structure of $\gamma_{18}(x, y, t)$ when $t = 100$.

FIGURE 8.14: Spatial structures of $\gamma_k(x, y, t)$ for $k \in \{0, 6, 12, 18\}$ when $t = 100$.

structures presented in Figure 4b in Ref. [67] are located around the main structures in Figure 4a in Ref. [67]. There are similarities in the main CLV structures, Figure 8.14, being around the two main structures around the banding at $x = 2$ and $x = 5$ in Figure 8.1. These features are also shown in the KS CLVs presented in section 7.1. While there has been little comparison of the CLVs to those presented in literature, similar trends can be observed and the conclusion that CLVs computed here are accurate can be drawn.

To the author's knowledge there has been no publication of the adjoint CLVs, $\hat{\gamma}_k(x, y, t)$, for the Kolmogorov system and, therefore, these are presented in Figure 8.15 for $k \in \{0, 6, 12, 18\}$ when $t = 100$. As in the KS adjoint CLVs, there is very little similarity between the adjoint CLVs and the non-linear solution, Figure 8.1. The CLVs, which are computed with the forward/backward Lyapunov vectors, have been validated against literature. Further, the adjoint CLVs, which cannot be validated

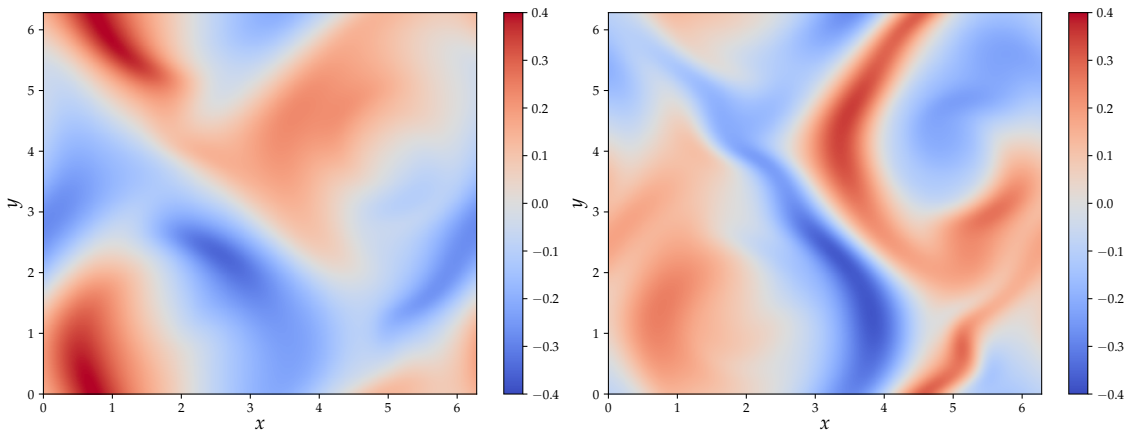

(A) Spatial structure of $\hat{\gamma}_0(x, y, t)$ when $t = 100$.

(B) Spatial structure of $\hat{\gamma}_6(x, y, t)$ when $t = 100$.

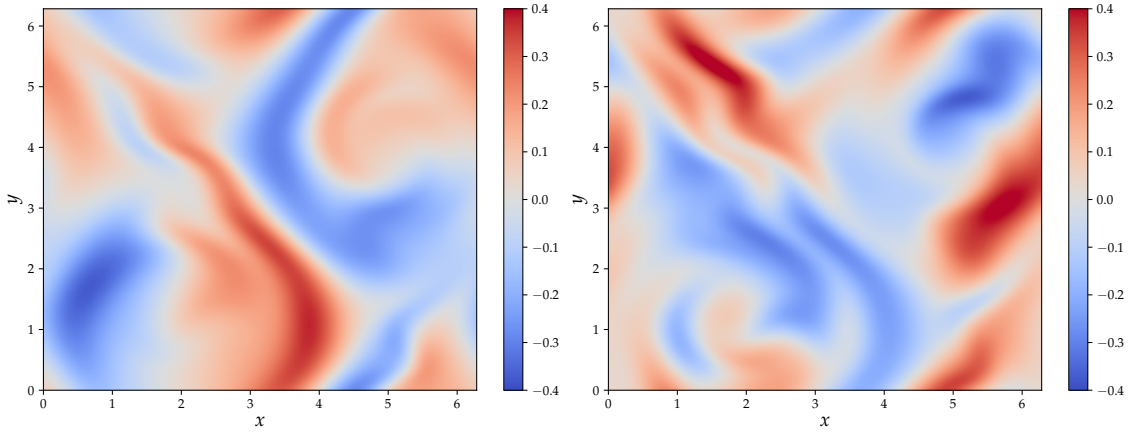

(C) Spatial structure of $\hat{\gamma}_{12}(x, y, t)$ when $t = 100$.

(D) Spatial structure of $\hat{\gamma}_{18}(x, y, t)$ when $t = 100$.

FIGURE 8.15: Spatial structures of $\hat{\gamma}_k(x, y, t)$ for $k \in \{0, 6, 12, 18\}$ when $t = 100$.

against literature as there has been no publication of them, are computed using the same forward/backward Lyapunov vectors. This provides reassurance that the adjoint CLVs are accurate also. The structure of the adjoint CLVs has large scale features and not the finer structures of those presented in Figure 8.14. This is similar to the relation between the adjoint CLVs and CLVs found for the KS system providing further validation that the adjoint CLVs presented here are accurate.

8.6 Impact of tuning parameters on the CLV decomposition

This section follows the analysis presented for the KS system where the forcing, co-state and control fields are decomposed onto the CLVs. The rationale for this analysis is to show that the conclusions drawn for the KS system and the statements made are generalised across systems and are features of the methods and not of

individual systems under investigation. Further analysis is also undertaken through varying the tuning parameters α and μ_s for OCS and NV respectively. It is worth noting that the forcing term of the adjoint formulation is $\frac{2\chi(x,y,t)}{T}$. Firstly, the value of the forcing is a linear combination of the adjoint CLVs

$$\frac{2\chi(x,y,t)}{T} = \sum_{k=0}^{n_v-1} \hat{a}_k^f(t)\hat{\gamma}_k(x,y,t).$$

Taking the inner product of this with $\gamma_k(x,y,t)$ along with using Equation (7.1) leads to

$$\hat{a}_k^f(t) = \frac{\left\langle \gamma_k(x,y,t), \frac{2\chi(x,y,t)}{T} \right\rangle}{\langle \gamma_k(x,y,t), \hat{\gamma}_k(x,y,t,) \rangle}.$$

The time average value of $|\hat{a}_k^f(t)|$ is presented in Figure 8.16. This decomposition

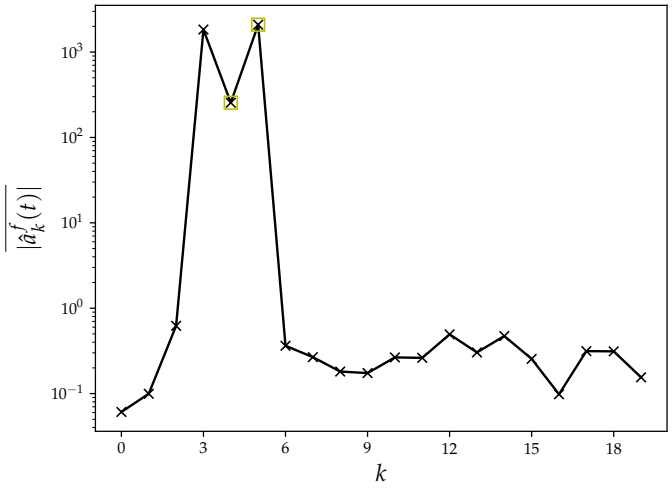

FIGURE 8.16: $\overline{|\hat{a}_k^f(t)|}$ for the Kolmogorov system. Yellow boxes denote the neutral CLV modes.

shares similar features with those presented for the KS system where the forcing term mainly decomposes onto the near neutral modes and has reduced influence outside this region. This is in very good agreement with the analysis undertaken on the KS system suggesting that the near neutral modes are important regardless of which system or parameter is selected. It is worth noting, at this point, that due to the relative coarseness of the LE spectrum that there are fewer near neutral modes, three in this case, than investigated in the KS system, where there are approximately 10. This results in fewer modes becoming dominant in the forcing term and likely in the co-state and control decomposition also. The argument for the reduced dominance of the near neutral modes is that the LE spectrum is relatively "coarse" in that there are large gaps between successive exponents. It was shown in section 7.3 that increasing the domain size "refines" the LE spectrum. Doing so resulted in the dominance

around the near neutral modes increasing. It is expected that this would also be beneficial here and the dominance around the near neutral modes would increase. This impact of increasing the domain size would be that a larger number of CLVs being required leading to an increase in 'spin up' time, computational cost and memory. However, these trends do not show significant differences with those observed for the KS system and can be concluded that these are features of the methods and not due to the system under investigation.

It was presented in section 7.2.1 that the denominator, $\langle \gamma_k(x,y,t), \hat{\gamma}_k(x,y,t,) \rangle$ also plays an important role in the decomposition. The time average of the absolute value of this denominator is shown in Figure 8.17. This shows that the denominator shares

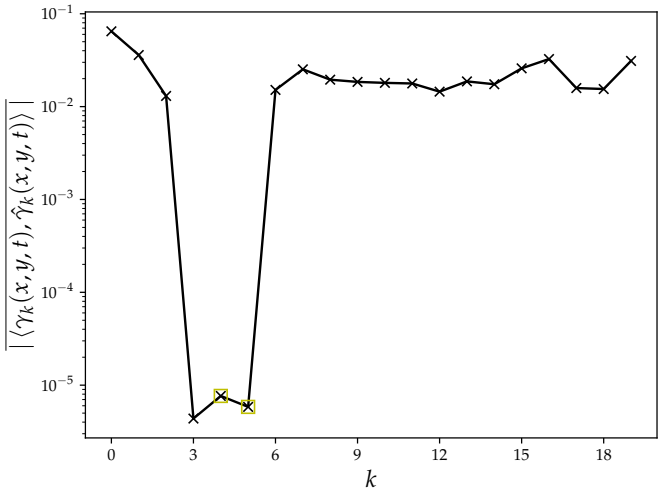

FIGURE 8.17: $\overline{|\langle \gamma_k(x,y,t), \hat{\gamma}_k(x,y,t) \rangle|}$ for the Kolmogorov system. Yellow boxes denote the neutral CLV modes.

similar features to that presented for the KS system. The reason for this is due to the tangency between the near neutral modes which results in orthogonality between the k^{th} CLV and its adjoint. Increasing the domain size, as suggested previously, would increase the "resolution" of the LE spectrum which would increase tangencies between the CLVs and their respective adjoints around the near neutral regime. This results in an increasing orthogonality between CLVs and their adjoints. This implies that this limitation is present regardless of which spatially distributed system is investigated. To overcome this limitation the expected gain of the system, ratio of output to input, are investigated as this removes the influence of the denominator.

The gain for the co-state for MSS, OCS when $\alpha = 500$ and NV when $\mu_s = 0.5$ is presented in Figure 8.18. The reader is reminded that the gain expected gain of the k^{th} mode is proportional to $\frac{1}{\Lambda_k}$. This implies that near neutral CLVs have a larger gain than those outside of the region. As in the previous cases, the gain is peaking around

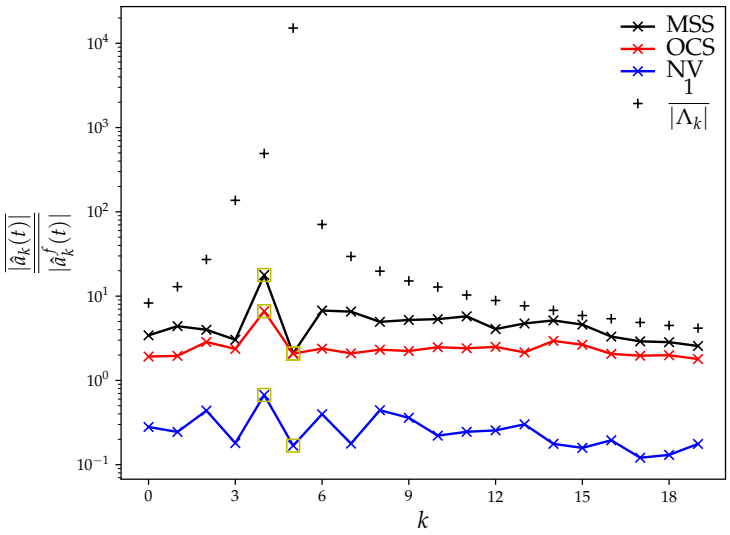

FIGURE 8.18: $\frac{\overline{|\hat{a}_k(t)|}}{|\hat{a}_k^f(t)|}$ for MSS, black line, OCS, red line, NV, blue line, for the Kolmogorov system. Yellow boxes denote the neutral CLV modes.

the near neutral modes for MSS and OCS. This implies that the expected gain is generic between systems and only relies on the LEs of the system. The dominance of the near neutral modes is smaller than that observed in the KS system. The reason for this is that, due to the relative "coarseness" of the LE spectrum there are fewer modes around the near neutral region and as such have larger LE exponents which results in a smaller gain. To overcome this, increasing the domain, which would increase the "resolution" of the LE spectrum would result in more modes with smaller Lyapunov exponents which would lead to larger gains along these modes. Increasing the time horizon is expected to increase the gain also and provide a bigger difference between the near neutral modes and those that are outside this region. It can still be seen that the expected gain seen here is similar to that seen in the KS system and the analysis and conclusions drawn for the KS system are also valid here. The similarity in expected gain between OCS and MSS is due to similarity in terminal conditions between the methods. This results in minimal control being required which results in the gain being similar to the expected value for both the methods, again similar to the adjoint KS findings. NV, on the other hand, has gain along all modes. This is due to the difference in terminal boundary conditions between MSS/OCS and NV which results in mode control being applied which results in additional damping. This implies that the NV methods investigated is non-optimal and the application of control is not targeting the unstable sub-space.

The reader is reminded that for the adjoint formulation the control term for MSS/OCS is $2\hat{v}(x, y, t)$. The control gain for MSS, OCS when $\alpha = 500$ and NV when $\mu_s = 0.5$ are shown in Figure 8.19. MSS has the least control gain along each CLV but still retains

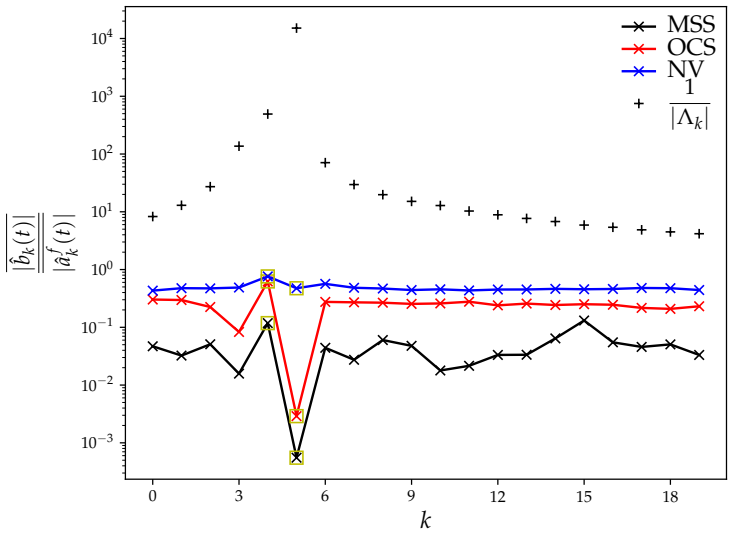

FIGURE 8.19: $\overline{\frac{|\hat{b}_k(t)|}{|\hat{a}_k^f(t)|}}$ for MSS, black line, OCS, red line, NV, blue line, for the Kolmogorov system. Yellow boxes denote the neutral CLV modes.

the peak in the near neutral modes. This suggests that MSS is providing a more optimal control over the OCS and NV methods. OCS shares features with MSS in that the largest gain is along the near neutral modes and decreasing slightly elsewhere. The analysis for the Kolmogorov system is not as clear as for the KS system. This again is due to the small domain investigated resulting in a "coarse" LE spectrum which results in a smaller number of near neutral modes. The implication of this reduced number of near neutral modes is that the dominance of the near neutral modes is reduced and trends are less obvious. Increasing the domain size would likely mean the near neutral gain becoming more dominant for the control terms also. Finally, NV has almost constant gain along each mode. This implies that NV methods are not targeting specific unstable sub-spaces and the NV method is non-optimal.

8.6.1 Influence of α on the CLV decomposition

In this section the tuning parameter α is varied and the impact on the solution decomposition onto the CLVs is investigated. This is to show that the influence of α is common between systems. Firstly, the value of the adjoint co-state is a linear combination of the adjoint CLVs

$$\hat{\lambda}(x,y,t) = \sum_{k=0}^{n_v-1} \hat{a}_k(t)\hat{\gamma}_k(x,y,t).$$

Taking the inner product of this with $\gamma_k(x,y,t)$ along with using Equation (7.1) leads to

$$\hat{a}_k(t) = \frac{\langle \gamma_k(x,y,t), \hat{\lambda}(x,y,t) \rangle}{\langle \gamma_k(x,y,t), \hat{\gamma}_k(x,y,t) \rangle}.$$

The time averaged value of $|\hat{a}_k(t)|$ is shown in Figure 8.20. In general, it can be seen

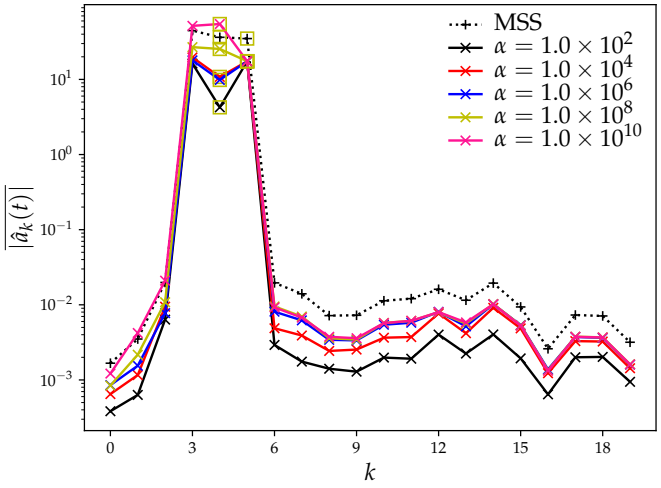

FIGURE 8.20: $\overline{|\hat{a}_k(t)|}$ generated by OCS for $\alpha = 1 \times 10^2$, black line, $\alpha = 1 \times 10^4$, red line, $\alpha = 1 \times 10^6$, blue line, $\alpha = 1 \times 10^8$, yellow line, $\alpha = 1 \times 10^{10}$, pink line, and MSS, black dotted line. Yellow boxes denote the near neutral modes.

that regardless of which value of α is selected, in the range investigated here, all the decompositions are again dominated by the near neutral modes. This implies that OCS is finding the similar Shadowing directions regardless of which value of α is selected. This is in very good agreement with that shown for the KS system. In comparison to KS, the peak around the near neutral modes is orders of magnitude, four or five, larger than the other modes whereas KS was only around two or three. This may contribute to the relative similarities between solution decompositions and decreased dependence on α.

When $\alpha = 1 \times 10^2$ it can be seen that the solution is reduced along each CLV mode. Further, this case is lower than that of MSS. This implies that the the solution is over-damped. As α is increased the solutions converge to MSS in the stable modes, $k > 6$. For the unstable modes, however, increasing α leads to increased projection which, when $\alpha \geq 1 \times 10^8$, is closer and sometimes above that of MSS. This suggests that OCS is unable to control the unstable modes which leads to them becoming dominant and the solution becoming under-damped. This peak around the near neutral modes is, again, due to $\langle \gamma_k(x,y,t), \hat{\gamma}_k(x,y,t,) \rangle$ and the time average of this value is shown in Figure 8.17.

Similarly, the control term, which for the adjoint formulation is $2\hat{v}(x,y,t)$ for both MSS and OCS, is a linear combination of the adjoint CLVs

$$2\hat{v}(x,y,t) = \sum_{k=0}^{n_v-1} \hat{b}_k(t)\hat{\gamma}_k(x,y,t).$$

The value of the weighting factor can be found using

$$\hat{b}_k(t) = \frac{\langle \gamma_k(x,y,t), 2\hat{v}(x,y,t)\rangle}{\langle \gamma_k(x,y,t), \hat{\gamma}_k(x,y,t)\rangle}.$$

The time averaged value of $|\hat{b}_k(t)|$ is shown in Figure 8.21. In general, it is found that,

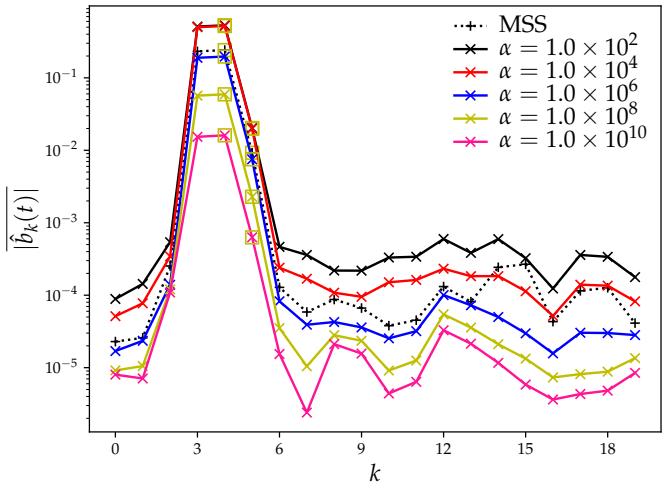

FIGURE 8.21: $\overline{|\hat{b}_k(t)|}$ generated by OCS for $\alpha = 1 \times 10^2$, black line, $\alpha = 1 \times 10^4$, red line, $\alpha = 1 \times 10^6$, blue line, $\alpha = 1 \times 10^8$, yellow line, $\alpha = 1 \times 10^{10}$, pink line, and MSS, black dotted line. Yellow boxes denote the near neutral modes.

again, the control solution is dominated by the near neutral modes for all values investigated. This implies that NV methods should follow this structure also to be optimal. In reality, it is difficult to know *a priori* if this will be the case for any NV method as the computation of CLVs is expensive and may not be feasible. It is also worth noting that the amount of control applied is orders of magnitude smaller than the co-state decomposition, Figure 8.20. This implies that the adjoint formulation is more optimal as the termporal boundary conditions are closer to a solution that has been stabilised. When $\alpha \in \{1 \times 10^2, 1 \times 10^4\}$ the amount of control applied is larger than that applied by MSS. This implies that the solution is over-damped. Conversely, when $\alpha \geq 1 \times 10^8$ the control applied is smaller than that of MSS. This implies that control is inadequate to stabilise the solution which results in under-damping. The wider implications are that NV methods should not apply a smaller amount of control than that applied by MSS. This may be difficult constraint to apply in practice as MSS

is also computationally expensive. In between these values the control applied is in good agreement with that applied by MSS. This suggests that OCS and MSS are very similar in their application of control, similar to that found for the KS system, and target control onto similar features of the unstable sub-space.

8.6.2 Influence of μ_s on the CLV decomposition

In this section the tuning parameter μ_s is varied and its impact on how the adjoint co-state and control solutions decomposes onto the CLVs is investigated. This is undertaken to increase the understanding of the NV methods and how they compare to OCS. The time averaged value of $|\hat{a}_k(t)|$ for multiple μ_s values is shown in Figure 8.22. It can be seen, again, that there is a peak in all solutions around the near

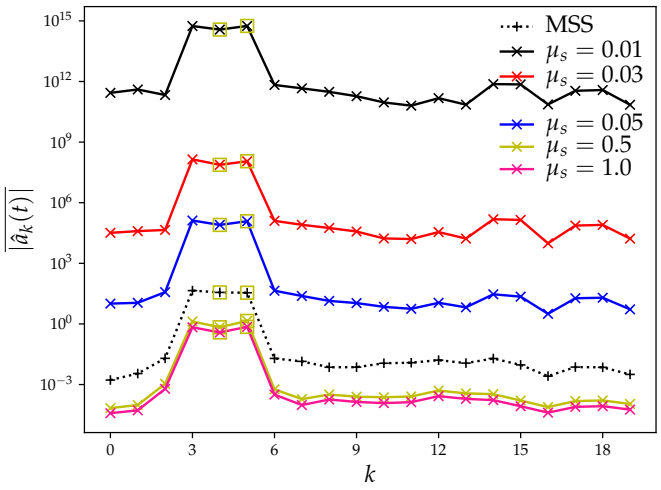

FIGURE 8.22: $\overline{|\hat{a}_k(t)|}$ generated by NV for $\mu_s = 10.0 \times 10^{-3}$, black line, $\mu_s = 3.0 \times 10^{-2}$, red line, $\mu_s = 5.0 \times 10^{-2}$, blue line, $\mu_s = 0.5$, yellow line, $\mu_s = 1$, pink line, and MSS, black dotted line. Yellow boxes denote the near neutral modes.

neutral modes for all values of μ_s investigated. When $\mu_s \in \{10 \times 10^{-3}, 3.0 \times 10^{-2}, 5.0 \times 10^{-2}\}$ the decomposition is larger than MSS, suggesting the solution is under-damped. As μ_s is increased the solution tends to that of MSS. Above a certain value the solution is lower than MSS which implies the solution is over-damped. It is worth noting that this approach has a higher dependence on the tuning parameter than OCS. The implication of this is that, where OCS finds the similar solution for a large range of values for α, the solution found by NV is highly dependent on the tuning parameter. This suggests that NV methods are non-optimal and do not target the same features for all values of the tuning parameter.

Similarly, the control term which for the adjoint formulation is $2\hat{v}(x, y, t)$ for MSS and $\mu_s \nabla^2 \hat{\lambda}(x, y, t)$ for NV is decomposed in a similar manner. The time averaged value of

$|\hat{b}_k(t)|$ is shown in Figure 8.23. In general, the control solution is found to be

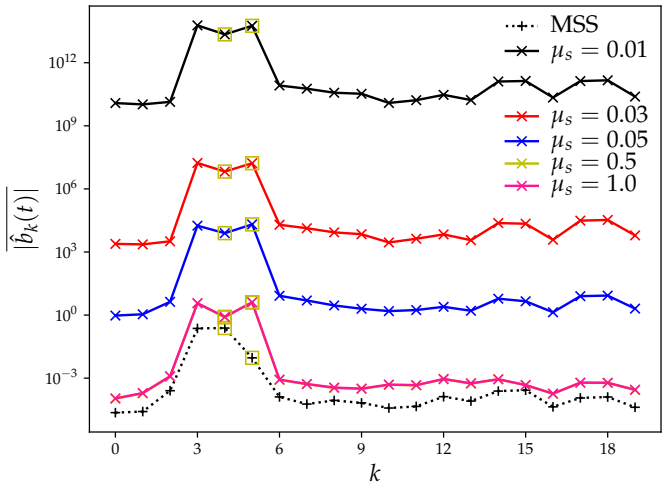

FIGURE 8.23: $\overline{|\hat{b}_k(t)|}$ generated by NV for $\mu_s = 10.0 \times 10^{-3}$, black line, $\mu_s = 3.0 \times 10^{-2}$, red line, $\mu_s = 5.0 \times 10^{-2}$, blue line, $\mu_s = 0.5$, yellow line, $\mu_s = 1$, pink line, and MSS, black dotted line. Yellow boxes denote the near neutral modes.

dominated by the near neutral modes for all cases investigated. For all values of μ_s the amount of control applied is larger than that applied by MSS. Even in the cases when the solution is adequately damped, $\mu_s = 1.0$, the amount of control is larger. This implies that the control applied by NV is non-optimal. It is also worth noting that the decompositions when $\mu_s = 0.5$ and $\mu_s = 1.0$ are almost identical suggesting a limit to the amount of control and solution stabilisation that these methods can achieve. The conclusions drawn here are in good agreement with those for the KS system and it can be concluded that the behaviour of NV methods are common between systems. This implies that NV methods may not be able to achieve the same solution as MSS or other Shadowing methods.

8.7 Summary

While the behaviour of OCS, MSS and NV on the Kolmogorov system is very similar to that presented for the KS system all previous analysis is valid. Moving to a more complex system leads to differences between the systems which are outlined here and analysis as to their impact on the OCS, MSS and NV methods drawn.

The first major difference between the the Kolmogorov and KS systems investigated is the correlation between $\bar{J}$ and the parameter of interest. For the KS system the sensitivity was approximately zero gradient, in the range of parameters investigated, while the Kolmogorov system showed stronger correlation along with positive

correlation between $\bar{J}$ and parameter Re. Fundamental assumptions of OCS and MSS rely on the attractor of the system being hyperbolic. The reason for this is that the Shadowing lemma is derived for hyperbolic attractors which MSS and OCS are built upon. For most engineering systems the attractor is quasi-hyperbolc which does not cause significant concern for the validity of the methods. The value of the gradient is not a significant concern as there are parameters which do not impact the value of $\bar{J}$ in the real world systems and these methods are able to accurately compute these.

The second major difference is the range of α for which accurate sensitivities are computed. The Kolmogorov system had a larger range of α values which produced accurate sensitivity than KS. One possible explanation is the increased dimension of the Kolmogorov system enabled a larger space of control that could leverage physical mechanisms to damp the unstable modes. The result of this is that a larger range of α values can be utilised. One implication of this is that for 3D turbulent flow systems the range of α values that produce accurate sensitivity values could increase and would remove one of the limitations of the method in *a priori* selection of α that would lead to accurate sensitivities.

One similarity between the systems was that both systems had two neutral CLV modes. For both systems these modes theoretically corresponded to a translation in time and a translation in the x coordinate. Kolmogorov does not have three neutral modes which correspond to translation in y due to the forcing term in the primal equations. OCS computes accurate sensitivities for systems with one neutral mode, Lorenz, and two, both KS and Kolmogorov. It is expected that increasing the number of neutral modes, from investigating a 3D Kolmogorov system for example, would not impact the behaviour or accuracy of the OCS method. Many engineering system do not have periodic boundaries and, therefore, would likely have only one neutral CLV mode which does not pose any issues for OCS.

Increasing from one spatial dimension, KS, to two, Kolmogorov, increased the degrees of freedom of the system leading to an increase in the memory requirements for the OCS algorithm without impacting the accuracy of the method. The result of this was twofold. Firstly, the number of segments required for Kolmogorov was larger than KS to ensure the memory requirement of each segment was not larger than the compute node. Computational time was increased due to more degrees of freedom and convergence was slower for the CG/GMRES solvers. Secondly, the larger degrees of freedom meant the CLVs required a longer 'spin up' time to converge to their respective sub spaces. For larger more industrially relevant systems could result in CLVs or OCS being too computationally expensive.

A major difference between KS and Kolmogorov was that for KS the smallest domain investigated generated both detailed information about the primal structures, accurate sensitivity and a large number of positive LEs. The Kolmogorov system, on

the other hand, produced accurate sensitivities along with detailed infromation about the primal structures but relatively few positive LEs. A result of this is that direct comparison between KS and Kolmogorov was not achievable due to the "coarse" LE spectrum for the Kolmogorov system. An appraoch to overcome this limitation is to increase the domain of the Kolmogorov system to ensure a smoother LE spectrum. The impact this would have on OCS is mainly time and memory related. A larger domain leads to a larger number of degrees of freedom resulting in a larger memory footprint. A result of this could be a larger number of segments being required which negatively impacts convergence rates, leading to an increased time to solution. Further, larger number of degrees of freedom will lead to a longer 'spin up' time required to ensure the CLVs have converged to their respective subspaces.

One final difference between KS and Kolmogorov is that Kolmogorov has rare bursting events whereas KS does not. The impact this has is that around these bursting events the CLVs all align. Sensitivities generated by OCS did not seem to be negatively impacted by the bursting events and the control term was not significantly altered by their presence. One argument as to why this was the case is that during the bursting event all the CLVs align which would mean control is easier determine. This could also be responsible for the larger range of α values that produce accurate sensitivity. An argument for this is that the bursting events essentially split the time domain in to sections determined by physical mechanisms which means a larger space of control is applicable.

Chapter 9

Conclusion

Traditional methods for sensitivity analysis either involve the tangent (forward) formulation or the adjoint (backward) formulation. In chaotic systems these methods fail due to the exponential growth of perturbations which is also known as the "butterfly effect". The sensitivity computed is unbounded and non-physical. To overcome this limitation two classes of sensitivity analysis have been developed in the literature.

The first approach is derived from the Shadowing lemma and are known as Shadowing methods. These methods either require the computation of the covariant Lyapunov vectors (CLVs), solve a minimisation problem in the case of LSS, MSS or NILSS, or solve a boundary value problem in the case of Periodic Shadowing without any *a priori* knowledge of the expected sensitivity. The limitation of these methods is that they are typically computationally expensive. The main benefit is that these approaches compute accurate sensitivities with no *a priori* knowledge of the expected value.

The second approach is the numerical viscosity (NV) method where terms are added to the linearised equations. The impact that these additional terms have is to stabilise the solutions and control the exponential growth of perturbations when tuned correctly. One of the main limitations of these methods is that a tuning parameter is altered until the sensitivities generated match the expected value. The benefit is that one non-linear solution is required along with one linear solution which makes these methods computationally cheap.

Several questions arise from analysing these various approaches: The first main question is how optimal are the current NV methods that have been proposed in the literature? This relates to the amount of control that is required to be applied to stabilise the solution and is there an alternative approach that could apply less and still stabilise the solution. Further, are there specific structures or characteristics of

control that could be utilised to provide a better, more selective NV term in stabilising the solution? The current NV literature selects terms which dissipate energy and it is unclear if this is the best strategy or is targeting production of energy terms more effective? Another question that arises is how similar or dissimilar are the solutions generated by the Shadowing approach to NV? It is clear that the two methods can produce the same sensitivities but how do the solutions compare? It is currently unclear if there are certain features of Shadowing that can be utilised to generate a more optimal NV term. As all the current NV method are reactive, *i.e.* the application of control is proportional to the linearised solution, is there an approach that is proactive, for example a NV term that can apply control based on the future dynamics of the non-linear solution?

9.1 Summary of findings and critical analysis

This thesis developed Optimal Control Shadowing, OCS, as a method to bridge the gap between the computationally expensive and accurate Shadowing methods, and the computationally cheap but potentially less accurate numerical viscosity, NV, methods if tuned incorrectly. This was achieved through the introduction of a generic control term into the tangent equation, and its structure is found utilising optimal control techniques. The tangent OCS formulation, valid for a single parameter, and the adjoint OCS formulation, valid for multiple parameters, were derived. For large systems the optimal control problem becomes very memory intensive and, in extreme cases, may not even fit on a compute node. To overcome this limitation, an approach that decomposed the time domain into segments, section 3.6, such that the solutions can be distributed across multiple compute nodes was derived for the tangent OCS form but is equally valid for the adjoint formulation. This has the added benefit of also conditioning the system. Finally, various algorithms and preconditioning methods for the numerical solution of the optimality conditions were presented for the tangent OCS formulation and the decomposed time domain formulation. These algorithms and preconditioning methods are also applicable to the adjoint formulations.

As part of the derivation of OCS a tuning parameter, α, was introduced and determines the accuracy of the method which is analogous to the tuning parameters in the NV methods. Small values of α lead to solutions which are over-damped. In the tangent OCS formulation these values lead to tangent solutions which are visually similar to ones produced by MSS along with the angle between these solutions being small, meaning they are aligned. It can, therefore, be concluded that OCS finds an approximation to the Shadowing direction that is very similar to one found by MSS. For the adjoint formulation, on the other hand, these values of α produced solutions which were not visually similar to MSS and the angles between solutions were on

average $\frac{\pi}{2}$. The reason why this was the case is due to the initial and terminal constraints on the MSS solutions impacting the solutions. One explanation for discrepancy between tangent and adjoint formulations is that two approaches for the adjoint form were presented for OCS. The first is to find the adjoint of the tangent formulation where the tangent is minimised, section 3.4, and the second is to minimise the adjoint, section 3.5. It was shown that, for OCS, these two are identical. However, this may not be the case for MSS and that the adjoint OCS should be compared to the equivalent MSS which minimised the adjoint field which could be a cause of the discrepancy between adjoint solutions. Increasing α lead to under-damped solutions. For the tangent formulation this led to solutions which shared no visual resemblance to MSS along with the angles between solutions being $\frac{\pi}{2}$. The adjoint formulation led to solutions which visually looked similar to MSS but the angles between solutions were again $\frac{\pi}{2}$. This suggests that adjoint OCS may not be as optimal in the application of control as the tangent formulation or MSS. For the NV methods investigated here the solutions generated results which did not look visually similar to MSS for both tangent and adjoint formulations, regardless of the tuning parameter value used. Further, the angles between solutions and MSS were all $\frac{\pi}{2}$ for both tangent and adjoint formulations and all tuning parameters investigated. The implications of this is that NV methods are not as optimal as OCS and that their control is applied that does not target the same features as OCS or MSS.

For the tangent formulation comparison between the control solutions generated by OCS and NV was presented. For the adjoint case, however, MSS has a control term and, therefore, comparison between MSS, OCS and NV control terms was undertaken. In the tangent formulation OCS applied control that was initially large and decreased throughout the time domain. For the adjoint formulation the control was largest towards the end of the time horizon and decreased backwards in time. This implies that OCS stabilises the solution onto the approximate Shadowing direction and then applies minimal control that keeps the solution stabilised. Further, all control terms shared visual similarities with MSS and the angle between OCS and MSS control was around $\frac{\pi}{2}$ implying that OCS and MSS are targeting slightly different features. In both tangent and adjoint formulations increasing α maintained this feature but reduced the magnitude of control applied. This implies that when α is large the control can then not stabilise the solution. Further, control was predominantly applied in wavenumbers where production of tangent/adjoint energy dominated dissipation. This suggests that as these wavelengths correspond predominantly to the unstable sub-spaces, as shown by the power spectra of the covariant Lyapunov vectors, that OCS and MSS target this sub-space and are minimal in the neutral and stable sub-spaces. This implies that as OCS predominantly targets the production terms future NV methods should have this feature. Increasing the wavenumber reduced the amount of control applied as dissipation began to dominate. This behaviour was seen in the adjoint MSS control term also but at a reduced magnitude. This suggests that

OCS and MSS share similar features in that the production terms are targeted. This analysis was repeated for the NV methods. In general, the amount of control applied is proportional to the tangent or co-state solution for all values of tuning parameter. When the tuning parameter is small the solutions are not stabilised and, therefore, the amount of control grows exponentially in time. Increasing the tuning parameter leads to smaller amount of control being applied which is able to control the solution. For the tangent formulation NV applies zero control initially and increases in time. This implies the NV methods are not finding the approximate Shadowing direction but some other direction which is related to a slightly modified non-linear solution, Ref. [49]. In the adjoint formulation control applied is zero at the terminal condition and increases backwards in time. For all values of tuning parameters the control solutions did not visibly resemble that of MSS and the angle between the control solutions was, on average, $\frac{\pi}{2}$. This implies that the NV methods investigated here are not targeting the unstable sub-space but applying general control across all sub-spaces.

From the decomposition of the solutions generated by the methods onto the CLVs it was discovered that the near neutral modes play an important factor in the solutions generated. A reconstructed solution was generated that was a linear combination of six of the most influential modes for the tangent formulation and twenty for the adjoint formulation. These reconstructions showed good agreement in the angle between the reconstructed and computed solutions along with the ratio of norms being around unity. This implies that having knowledge of these near neutral CLVs could be used to create a good approximation of the solutions generated by the various methods. The adjoint formulation required more modes was that the influence of the near neutral modes was smaller than that of the tangent formulation and the other modes play a larger role. One other reason was the difference in adjoint formulations between OCS and MSS. It is argued that the adjoint MSS formulation used in this thesis does not find an "adjoint Shadowing direction" but rather the adjoint solution corresponding to the tangent Shadowing direction whereas adjoint OCS finds an "adjoint Shadowing direction". This suggests that, if the CLVs were known *a priori* that a good approximation of the tangent/adjoint solution could be achieved. The further implications of this is that, as the tangent/adjoint solutions are used in the computation of the sensitivity, the near neutral modes also are important for the sensitivity of the system under investigation.

The impact that the tuning parameters on the CLV decomposition was then investigated. It was shown that for OCS that when α was small the decompositions were similar to MSS in the near neutral modes and larger outside this region. As α was increased the near neutral mode decomposition remained constant but the modes outside this region tended towards the MSS decomposition. When α was increased further the solution diverged away from MSS. The reason for this was that the amount

of control applied decreased which led to the solution being under-damped and led to the solution not being stabilised. Increasing α reduced the amount of control down each of the other modes which moves the solution from over-damped to adequately stabilised and, finally, under-damped solutions. This behaviour was not seen for NV. For small values of the tuning parameter the decomposition had no resemblance with MSS. Increasing the tuning parameter moved the decomposition closer to MSS until increasing the tuning parameter further had no impact on the solution. Similar behaviour was seen for the control decomposition. The suggestion for this is that OCS acts in a very similar manner to MSS for a large range of tuning parameters. This highlights that OCS and MSS are finding solutions with very similar features. Further, this result implies that OCS is attempting to find the same approximate Shadowing direction over a wide range of tuning parameters. The ramification is that this should be a feature at NV methods should incorporate which is not seen from the methods investigated here. Discovery of these features is computationally expensive as the CLVs are, in general, computationally expensive and often unfeasible.

Increasing the domain size did not increase the largest Lyapunov exponent (LEs) but reduced the difference between consecutive modes or, in other words, increased the resolution of the spectrum. With the correct scaling of the mode index it was shown that the LE spectra and decompositions collapsed onto the same curve. It was shown that the expected gain along each of the CLV modes was found to be proportional to $\frac{1}{\Lambda_k}$ which is the inverse of the Lyapunov exponent for mode k. This result had not been discovered prior to this work, is a key finding and highlights the importance of the near neutral modes in the Shadowing solution as they have smaller exponents leading to larger gain. MSS had good agreement with this expected gain for both tangent and adjoint formulations. This implies that MSS is targeting the unstable sub-space to remove its influence and that as OCS produces similar results has this feature also. Further, this gain was shown for two parameter of interest cases and similar features were seen between them. OCS and NV did not follow this expected gain profile for the tangent formulation due to the existence of the control terms in the equations. The gain of the control terms for tangent OCS and NV were along the modes outside the near neutral region. The reason for this was due to the initial condition on the tangent solutions that were far away from the approximate Shadowing direction. This resulted in the unstable modes requiring additional damping which lead to a larger than expected gain. This was not the case for the adjoint formulation as OCS and MSS shared identical terminal boundary conditions which, it was argued, led to an terminal condition that was closer to a stabilised solution which resulted in smaller amount of control being applied to stabilise the solution. This suggests that the adjoint OCS formulation is more optimal than the tangent formulation due to the terminal boundary condition. The implications of this is that if the tangent solution has an initial condition closer to the Shadowing direction, then smaller, more targeted amounts of control would be applied. In reality,

finding the Shadowing direction is computationally expensive and as such results in the modified initial condition being prohibitive. It was shown that increasing the domain size leads to the resolution of the Lyapunov exponents increasing, *i.e.* the difference between successive modes decreases. This led to an increased gain around this region, highlighting the importance of the near neutral modes. These results were shown on the Kuramoto-Sivashinsky system and to a lesser extent the Kolmogorov system. The reason why the Kolmogorov did not show such strong results was due to the number of CLVs calculated in the unstable sub-space regime. Increasing the domain size would lead to larger number of unstable CLVs being computed and as such should lead to more pronounced results.

In general, fewer segments used to decompose the time domain results in an algorithm with smaller computational cost. In practice, however, fewer segments results in the memory requirements of the optimal control problem on each segment potentially being larger than the compute node they are allocated to. Therefore, the number of segments is selected such that the memory requirements for the optimal control problem is below the memory limit of each node and that the optimal control problem on each segment is solved in a "reasonable" time. The value of α controls the condition number of the optimal control problem. Large values mean that the condition number is small and leads to fast convergence, whereas, small values leads to slow convergence. The implication of this is that, as the system determines the values of α that relate to under or over-damped solutions, the system impacts the conditioning of OCS through the value of α. Finally, Forward Gauss-Seidel (FGS) preconditioning, for the tangent formulation, produces the fastest convergence rates of the preconditioning methods investigated, followed by Backward Gauss-Seidel (BGS) and then Jacobi. The reason why FGS was fastest was due to an increased rate of "information" transfer between segments and at each iteration control can be applied more "appropriately". The limitation of FGS and BGS is that the segments must be solved sequentially whereas Jacobi and no preconditioning can be solved in parallel. Therefore, the increased rate of convergence of the FGS method may have a slower wall-clock time than Jacobi due to the parallel nature of Jacobi preconditioning.

In answer to the questions asked at the beginning of this thesis, the NV methods did decompose onto the near neutral CLV modes which is similar to that of OCS and MSS. The decomposition onto the modes outside of this region are larger than OCS and MSS suggesting that these methods are not optimal. Further, sensitivities were calculated which were in good agreement with the expected values. Comparison of the norm, wavenumber and angle between solutions with MSS showed that the NV methods investigated here were again not similar to MSS or OCS. The NV methods investigated here did not find a solution that is close to the approximate Shadowing direction where OCS did. It is clear that the NV methods are not optimal even though accurate and similar sensitivity values are produced between the methods. Further,

the OCS approach is "better" than the NV methods for the tangent and adjoint formulations on systems investigated here due to the smaller amount of control applied. As to specific characteristics and structures of the NV term, it was found that OCS applies control that is predominantly in the wavenumbers where production of energy dominates dissipation which relates to the unstable sub-space and implies that this feature should be incorporated into future NV methods. OCS also decomposes onto the near neutral CLVs in a more predictable manner than NV suggesting that OCS attempts to find a solution that is very similar to the Shadowing direction for a range of control solutions and should be a feature that NV methods have. Further, OCS applied control initially, for the tangent formulation, whereas NV applies control that is proportional to the linearised solution. This implies OCS attempts to stabilise the solution onto an approximate Shadowing direction and applies minimal control to ensure the solution remains close to the Shadowing direction. A recommendation for selection of an NV term should have a combination and aspects of these features.

9.2 Future work

There are several directions that future research could take. The obvious direction is to continue this investigation on larger, more complex and industrially relevant systems. This avenue may not be significantly fruitful as the behaviour of OCS was shown to be common between three different systems, and it is expected to have this behaviour on all systems. Another obvious direction is to determine a method to find the value of α with no *a priori* information of the expected sensitivity. Again, this avenue may not be beneficial as the cost of these OCS methods are more expensive than MSS and, therefore, if sensitivities are required then MSS would be a better suited method.

One of the major discrepancies between OCS and MSS was the difference in solution similarity between the two when considering the adjoint formulations. In the analysis of OCS it was shown that OCS and MSS find similar solutions in the tangent formulation but was not the case for the adjoint formulation which is counterintuitive. The adjoint OCS derived from the minimisation of the tangent solution has been shown to be identical to the adjoint OCS formulation derived from minimisation of the adjoint solution. It was argued that adjoint MSS derived from minimising the tangent solution is different from the adjoint MSS derived from minimising the adjoint solution, and that this difference could cause the difference in solution between the adjoint formulations of OCS and MSS. Therefore, a suggestion for future work is to compare adjoint OCS to adjoint MSS derived from the minimisation of the adjoint solution to investigate if the "adjoint Shadowing direction" generated by OCS has similar features with adjoint MSS.

This thesis described the computational aspects of the OCS algorithm. From the experience gained in this work two avenues of research have emerged. Firstly, conjugate gradient and GMRES linear solvers have been utilised in this work. There are a number of other linear system solvers available in the literature and selection of a more appropriate one could lead to reduced computational costs. Secondly, simple preconditioning methods were utilised which offered an increased convergence over the standard case. A range of other preconditioning methods are covered in the literature for alternative sectors/fields and some of these may be applicable to this work.

Optimal control was investigated here as the solution generated was the "best" that NV could achieve and provided a good measure of the NV methods. Alternative non-optimal control methods are available in the literature. Two avenues arise from using non-optimal control. Firstly, what is the impact that utilising non-optimal control have on the solutions generated by OCS? Secondly, what computational benefits does using non-optimal control generate? Are non-optimal control methods significantly cheaper computationally or do they provide a memory improvement? If these methods are beneficial then sensitivity analysis may be a step closer to being adopted in an industrial setting.

The formulation presented in this thesis assumes that a control term is available at every time-step. Two avenues of investigation arise from this. The first is what would the impact be in "coarsening" the control solution, *i.e.* only have the control every n time-steps or only at certain grid points if the solution is spatially distributed. The second avenue is that multi-grid methods have been shown to provide improved convergence rates in computational fluid dynamics and what, if any, benefit would these approaches have in the solution and convergence rates of OCS.

In this work it was discovered that the near neutral CLVs are important in the solutions generated by all methods. Several avenues of investigation arise from this.

Firstly, given a set of near neutral CLVs what is the best approach to combine these to produce a solution that is a good approximation to the Shadowing direction. Granted, this avenue is unlikely as the CLV are more computationally expensive than solving the MSS minimisation problem. Researching this combination of CLVs could be fruitful as it may provide insight into the structure of the solution.

Secondly, it is well known that the number of positive exponents is the main limitation of the Shadowing methods. A method that could potentially make NV a more attractive approach is to utilise information and structures within the first n unstable CLV modes, or a subset thereof, to generate a NV term which specifically targets the unstable subspace. This could be lead to a more generic NV approach that could require less tuning than the current approaches.

Thirdly, is there an approach to computation or extraction of the CLVs form the solutions generated by MSS. Throughout the course of this investigation MSS was significantly cheaper to compute than the CLVs. With this in mind and knowing that MSS decomposes onto the near neutral CLV modes would it be possible to extract these from the solution. This would be beneficial as having CLVs provides information about the solution, the sub-spaces of the tangent space and could lead to developments in understanding of turbulence, transition and vortex bursting for example.

Finally, this work has already discussed the convergence rates of OCS and could that convergence rate be improved by knowledge of the first n CLVs. This work has shown that the unstable CLVs are damped and incorporation of these into the algorithms could lead to faster convergence. Increased convergence would then mean that these methods are more attractive to industry.

Appendix A

Covariant Lyapunov vectors and Lyapunov exponents

The covariant Lyapunov vectors (CLVs) and Lyapunov exponents (LEs) have been proposed as a tool for analysis of the various time averaged sensitivity analysis methods investigated. While their exact derivation is not required for the analysis, their context and details which may not be well known are provided here. The CLVs, along with LEs, can be utilised to determine the unstable, neutral and stable sub-spaces, Ref. [72]. It is for this property that the CLVs are utilised as a tool for analysing the time averaged sensitivity methods investigated in this thesis. By decomposing the solutions generated onto these sub-spaces could inform features that NV methods should take. The mathematical derivation and algorithms provided here is a recap of the literature, Refs. [6, 7, 50, 51, 72, 95, 112, 131], and no additional development in understanding or algorithms is provided. This Appendix has been written in the form that is consistent with the remainder of this thesis. The CLVs were initially developed in the 1970s and early 80s, Refs. [6, 7, 112], but have gained more traction recently, Refs. [50, 51, 72, 95, 131], due to computational advancements.

Firstly, consider a linear perturbation, $\mathbf{v}(t) \in \mathbb{R}^{n_v}$, to the trajectory of Equation (2.1) which can be described by

$$\frac{\mathrm{d}\mathbf{v}(t)}{\mathrm{d}t} = \frac{\partial \mathbf{f}(\mathbf{u}(t,p),p)}{\partial \mathbf{u}(t,p)}\mathbf{v}(t). \tag{A.1}$$

Utilising Equation (A.1), a matrix of perturbations, $\mathbf{X}(t) \in \mathcal{R}^{n_v \times n_v}$, can be propagated as

$$\frac{\mathrm{d}\mathbf{X}(t)}{\mathrm{d}t} = \frac{\partial \mathbf{f}(\mathbf{u}(t,p),p)}{\partial \mathbf{u}(t,p)}\mathbf{X}(t), \tag{A.2}$$

where the initial conditions for Equation (A.2) is any non-singular matrix. From Appendix B it is known that this perturbation matrix, $\mathbf{X}(t)$, can be used to form the

state transition matrix

$$\mathbf{\Phi}(t_1, t_2) = \mathbf{X}(t_2)\mathbf{X}(t_1)^{-1}. \tag{A.3}$$

A singular value decomposition of $\mathbf{\Phi}(t_1, t_2)$ can be performed resulting in

$$\mathbf{\Phi}(t_1, t_2) = \mathbf{G}^{-}(t_1, t_2)\sigma(t_1, t_2)\mathbf{G}^{+}(t_1, t_2)^{T}, \tag{A.4}$$

where $\mathbf{G}^{-}(t_1, t_2) \in \mathcal{R}^{n_v \times n_v}$ and $\mathbf{G}^{+}(t_1, t_2) \in \mathcal{R}^{n_v \times n_v}$ are the left and right singular vectors respectively and $\sigma(t_1, t_2) \in \mathcal{R}^{n_v \times n_v}$ are the singular values. Since $\mathbf{\Phi}(t_1, t_2)$ determines the growth of the perturbations the singular values, $\sigma(t_1, t_2)$, determine the local stretching/contraction ratios of these perturbations.

It is expected that for infinitely large time horizons that there will be a limit to these stretching ratios and, therefore, the singular values, Ref. [72]. By taking $t_2 \to \infty$ the right singular vectors reach a limit also, which are referred to as the forward Lyapunov vectors, $\boldsymbol{\psi}_k^{+}(t) \in \mathcal{R}^{n_v}$ for $k = 0, 1, \ldots, n_v - 1$. By taking $t_1 \to -\infty$ the left singular vectors reach a limit as well, which are the backward Lyapunov vectors, $\boldsymbol{\psi}_k^{-}(t) \in \mathcal{R}^{n_v}$ for $k = 0, 1, \ldots, n_v - 1$. The action of $\mathbf{\Phi}(t_1, t_2)$ on the backwards Lyapunov vectors, $\mathbf{\Psi}^{-}(t) = [\boldsymbol{\psi}_0^{-}(t), \boldsymbol{\psi}_1^{-}(t), \ldots, \boldsymbol{\psi}_{n_v-1}^{-}(t)]$, is

$$\mathbf{\Phi}(t_1, t_2)\mathbf{\Psi}^{-}(t_1) = \mathbf{\Psi}^{-}(t_2)\mathbf{R}(t_1, t_2), \tag{A.5}$$

where $\mathbf{R}(t_1, t_2) \in \mathbb{R}^{n_v \times n_v}$ is an upper triangular matrix with non-zero diagonal. The values for $\mathbf{\Psi}^{-}(t_2)$ and $\mathbf{R}(t_1, t_2)$ can be computed using a QR decomposition of $\mathbf{\Phi}(t_1, t_2)\mathbf{\Psi}^{-}(t_1)$, Ref. [72]. The finite time Lyapunov exponents (LEs), Λ_k for $k = 0, 1, \ldots, n_v - 1$, are computed using

$$\Lambda_k(t_1, t_2) = \frac{\ln |\mathbf{R}_{kk}(t_1, t_2)|}{t_2 - t_1}. \tag{A.6}$$

For completeness, the LEs then can be thought of as the average rate at which the perturbations grow/decay. Similarly, the action of $\mathbf{\Phi}(t_1, t_2)^{-1}$ on the forward Lyapunov vectors, $\mathbf{\Psi}^{+}(t) = [\boldsymbol{\psi}_0^{+}(t), \boldsymbol{\psi}_1^{+}(t), \ldots, \boldsymbol{\psi}_{n_v-1}^{+}(t)]$, is

$$\mathbf{\Phi}(t_1, t_2)^{-1}\mathbf{\Psi}^{+}(t_2) = \mathbf{\Psi}^{+}(t_1)\mathbf{L}(t_1, t_2), \tag{A.7}$$

where $\mathbf{L}(t_1, t_2) \in \mathbb{R}^{n_v \times n_v}$ is lower triangular matrix. The values of $\mathbf{\Psi}^{+}(t_1)$ and $\mathbf{L}(t_1, t_2)$ can be found using a QL decomposition of $\mathbf{\Phi}(t_1, t_2)^{-1}\mathbf{\Psi}^{+}(t_2)$, Ref. [72]. Covariant Lyapunov vectors are defined as being covariant to the dynamics and invariant with respect to the time direction. The implication of this is that the forward and backward Lyapunov vectors are non-covariant with the dynamics of the system due to the presence of $\mathbf{R}(t_1, t_2)$ and $\mathbf{L}(t_1, t_2)$ in Equations (A.5) and (A.7), respectively.

This is behaviour is seen for the adjoint formulation also. Define the adjoint state transition matrix as $\hat{\mathbf{\Phi}}(t_1, t_2) = \mathbf{\Phi}(t_1, t_2)^{-T}$. The action of $\hat{\mathbf{\Phi}}(t_1, t_2)^{-1}$ on $\mathbf{\Psi}^{+}(t_2)$ and

$\hat{\mathbf{\Phi}}(t_1, t_2)$ on $\mathbf{\Psi}^-(t_1)$ is

$$\hat{\mathbf{\Phi}}(t_1, t_2)^{-1}\mathbf{\Psi}^+(t_2) = \mathbf{\Psi}^+(t_1)\hat{\mathbf{R}}(t_1, t_2) \tag{A.8}$$

and

$$\hat{\mathbf{\Phi}}(t_1, t_2)\mathbf{\Psi}^-(t_1) = \mathbf{\Psi}^-(t_2)\hat{\mathbf{L}}(t_1, t_2), \tag{A.9}$$

where $\hat{\mathbf{R}}(t_1, t_2) \in \mathbb{R}^{n_v \times n_v}$ and $\hat{\mathbf{L}}(t_1, t_2) \in \mathbb{R}^{n_v \times n_v}$ are upper and lower triangular matrices, respectively. Again, these are found with QR and QL decomposition. As before, the implication is that the forward and backward Lyapunov vectors are non-covariant with the dynamics due to $\hat{\mathbf{R}}(t_1, t_2)$ and $\hat{\mathbf{L}}(t_1, t_2)$ in Equations (A.8) and (A.9), respectively.

Additional work and formulation is required to compute vectors which are covariant to the dynamics and invariant with respect to the time direction. To achieve this let $\gamma_k(t) \in \mathcal{R}^{n_v}$ for $k = 0, 1, \ldots, n_v - 1$ be a covariant Lyapunov vector, Ref. [6, 7, 112], that satisfies

$$\frac{\mathrm{d}\gamma_k(t)}{\mathrm{d}t} = \frac{\partial \mathbf{f}(\mathbf{u}(t,p),p)}{\partial \mathbf{u}(t,p)}\gamma_k(t) - \Lambda_k\gamma_k(t) \quad k = 0, 1, \ldots, n_v - 1. \tag{A.10}$$

This derived in an identical manner to finding "eigenvector/value" pair for the operator Equation (A.1). The implication of Equation (A.10) is that the forward/backward Lyapunov vectors are found using Equation (A.1) and therefore the term $-\Lambda_k\gamma_k(t)$ is the main difference between the two which accounts for the non-covariance with the dynamics of the forward/backward Lyapunov vectors. The value of Λ_k is unknown *a priori* and is computed as part of the forward/backward Lyapunov vector calculation and cannot, therefore, be added beforehand. This implies that as the forward/backward Lyapunov vectors are utilised in the computation of Λ_k they can be used to compute the covariant Lyapunov vectors. There exist an upper triangular matrix, $\mathbf{A}^-(t) \in \mathbb{R}^{n_v \times n_v}$, and lower triangular matrix, $\mathbf{A}^+(t) \in \mathbb{R}^{n_v \times n_v}$, that satisfy

$$\mathbf{\Gamma}(t) = \mathbf{\Psi}^-(t)\mathbf{A}^-(t) = \mathbf{\Psi}^+(t)\mathbf{A}^+(t), \tag{A.11}$$

where $\mathbf{\Gamma}(t) = [\gamma_0(t), \gamma_1(t), \ldots, \gamma_{n_v-1}(t)]$, Ref [72]. Similarly, let $\hat{\gamma}_k(t) \in \mathcal{R}^{n_v}$ for $k = 0, 1, \ldots, n_v - 1$ be the adjoint covariant Lyapunov vector, Ref [72], that satisfies

$$-\frac{\mathrm{d}\hat{\gamma}_k(t)}{\mathrm{d}t} = \frac{\partial \mathbf{f}(\mathbf{u}(t,p),p)}{\partial \mathbf{u}(t,p)}^{\dagger}\hat{\gamma}_k(t) - \Lambda_k\hat{\gamma}_k(t) \quad k = 0, 1, \ldots, n_v - 1. \tag{A.12}$$

Equation (A.12) is found in an identical manner to finding the "eigenvector/value" pair for the adjoint of Equation (A.1). Using similar reasoning as that used in the computation of Equation (A.11) there exist an upper triangular matrix, $\mathbf{B}^+(t) \in \mathbb{R}^{n_v \times n_v}$, and lower triangular matrix, $\mathbf{B}^-(t) \in \mathbb{R}^{n_v \times n_v}$, that satisfy

$$\hat{\mathbf{\Gamma}}(t) = \mathbf{\Psi}^+(t)\mathbf{B}^+(t) = \mathbf{\Psi}^-(t)\mathbf{B}^-(t), \tag{A.13}$$

where $\hat{\mathbf{\Gamma}}(t) = [\hat{\gamma}_0(t), \hat{\gamma}_1(t), \ldots, \hat{\gamma}_{n_v-1}(t)]$, Ref [72]. Equations (A.11) and (A.13) give the relationship between the forward and backwards Lyapunov vectors and covariant Lyapunov vectors. These equations can be manipulated to give

$$\mathbf{P}(t)\mathbf{A}^-(t) = \mathbf{A}^+(t) \quad \text{and} \quad \mathbf{P}(t)^T\mathbf{B}^+(t) = \mathbf{B}^-(t),$$

where $\mathbf{P}(t) = \mathbf{\Psi}^+(t)^T\mathbf{\Psi}^-(t)$. Computation of $\mathbf{P}(t)$ is found using the forward/backward Lyapunov vectors and then LU factorisation is performed, Ref [72], to obtain $\mathbf{A}^-(t)$ and $\mathbf{A}^+(t)$ which can be utilised to then compute $\mathbf{\Gamma}(t)$. Similarly, the value of $\mathbf{P}(t)^T$ can be utilised, again through LU factorisation, to obtain $\mathbf{B}^+(t)$ and $\mathbf{B}^-(t)$ which can then be utilised to compute $\hat{\mathbf{\Gamma}}(t)$.

To see how the CLVs help determine the unstable, neutral and stable sub-spaces they are taken in conjunction with their Lyapunov exponent. It is known, Ref. [72], that

$$\|\mathbf{\Phi}(t_1, t_1 \pm t)\gamma_k(t_1)\| \sim e^{\pm\Lambda_k t},$$

as $t \to \infty$. This implies that when the k^{th} Lyapunov exponent is positive perturbations grow along this CLV suggesting an unstable direction. Similarly, when k^{th} Lyapunov exponent is zero this implies the perturbations along the corresponding CLV neither grows nor decays. Finally, when $\Lambda_k < 0$ this implies perturbations decay. Therefore, the unstable CLVs span the unstable sub-space, and similar behaviour is found for the neutral and stable CLVs and their respective sub-spaces also.

A.1 The Kuptsov and Parlitz algorithm for the computation of covariant Lyapunov vectors

While this thesis makes use of the CLVs/adjoint CLVs and the theory has been outlined previously, it is somewhat unclear how those translate into algorithms. This Appendix provides the algorithms, which have already been published, Ref. [72], to provide completeness for the reader. In the derivation of the CLVs an initial value for the backward Lyapunov vectors, $\mathbf{\Psi}^-(t_A)$, was provided, where t_A is a start time. This value was selected to ensure this matrix is non-singular. Random values are commonly utilised, Ref. [131], which implies the backward Lyapunov vectors are not aligned with their respective sub-spaces. To overcome this limitation they are propagated forwards in time to t_B under Equation (A.5) and a QR decomposition, or re-orthogonalisation, of these vectors is preformed every n time steps, or more formally when $t \pmod{n\Delta t} \equiv 0$. The difference between t_B and t_A is the 'spin up' time used in this thesis. This 'spin up' time must be sufficiently large to ensure the backward Lyapunov vectors have properly aligned with their sub-spaces and is

system dependent and required determining for each system investigated. This is presented in Algorithm 11.

Algorithm 11: An algorithm for marching $\mathbf{\Psi}^-$ forwards in time and computation of Λ_k.

Input: $\mathbf{u}(t_1, p)$, $\mathbf{\Psi}^-(t_1)$
Output: $\mathbf{\Psi}^-(t_2)$, $\Lambda_k(t_1, t_2)$

Store the solution of $\mathbf{u}(t, p)$ on the interval t_1 to t_2 by solving Equation (2.1) from initial condition $\mathbf{u}(t_1, p)$.
$t \leftarrow t_1$
while $t < t_2$ **do**
  for $k = 0, 1, \ldots, n_v - 1$ **do**
    March $\boldsymbol{\psi}_k^-(t)$, using Equation (A.1), one time step forwards in time.
  if $t \pmod{n\Delta t} \equiv 0$ **then**
    $\mathbf{\Psi}^-(t) = \boldsymbol{Q}(t)\boldsymbol{R}(t)$
    $\mathbf{\Psi}^-(t) \leftarrow \boldsymbol{Q}(t)$
    $\Lambda_k \leftarrow \Lambda_k + \ln|\boldsymbol{R}_{kk}|$
  $t \leftarrow t + \Delta t$
$\Lambda_k \leftarrow \frac{\Lambda_k}{t_2 - t_1}$

Similarly, the value of the forward Lyapunov vectors, $\mathbf{\Psi}^+(t_D)$, where t_D is the final time, are initialised as any non-singular matrix. This also implies that these vectors are not aligned with their respective sub spaces and are marched backwards in time under Equation (A.8) from t_D to t_C, where $t_C < t_D$, and is also referred to as the 'spin up' time. As in the forward case a QR, or re-orthogonalisation, is preformed every n time steps. As the k^{th} forward/backward Lyapunov vectors have the same Λ_k it follows that the 'spin up' times must be similar, *i.e.* $t_B - t_A \equiv t_D - t_C$. This is presented in Algorithm 12.

Algorithm 12: An algorithm for marching $\mathbf{\Psi}^+$ backwards in time.

Input: $\mathbf{u}(t_1, p)$, $\mathbf{\Psi}^+(t_2)$
Output: $\mathbf{\Psi}^+(t_1)$

Store the solution of $\mathbf{u}(t, p)$ on the interval t_1 to t_2 by solving Equation (2.1) from initial condition $\mathbf{u}(t_1, p)$.
Set $t \leftarrow t_2$
while $t > t_1$ **do**
  for $k = 0, 1, \ldots, n_v - 1$ **do**
    March $\boldsymbol{\psi}_k^+(t)$, using the adjoint of Equation (A.1), one time step backwards in time.
  if $t \pmod{n\Delta t} \equiv 0$ **then**
    $\mathbf{\Psi}^+(t) = \boldsymbol{Q}(t)\boldsymbol{R}(t)$
    $\mathbf{\Psi}^+(t) \leftarrow \boldsymbol{Q}(t)$
  $t \leftarrow t - \Delta t$

Once the forward/backward Lyapunov vectors have aligned with their respective sub-spaces the CLVs and their adjoint counterparts can be computed on the time span (t_B, t_C). The reason for this is that outside of this region the forward/backward Lyapunov vectors have not aligned with their sub-spaces leading to inaccurate CLVs. To compute the CLVs first the backward Lyapunov vectors are computed using Algorithm 11 on the time span (t_B, t_C) along with the forward Lyapunov vectors, Algorithm 12. This time domain can be seen in Figure A.1. Once the

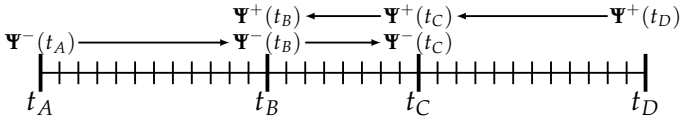

FIGURE A.1: A typical time domain for the computation of $\mathbf{\Gamma}(t)$ and $\hat{\mathbf{\Gamma}}(t)$

forward/backward Lyapunov vectors have been computed on the interval (t_B, t_C) the value of $\mathbf{P}(t)$ can be computed and performing its LU decomposition to $\mathbf{A}^+(t)$ and $\mathbf{A}^-(t)$ which can be used for computation of the CLVs, $\hat{\mathbf{\Gamma}}(t)$, using Equation (A.11). Similarly, performing the LU decomposition on $\mathbf{P}^T(t)$ leads to $\mathbf{B}^-(t)$ and $\mathbf{B}^+(t)$ which can be utilised to compute the adjoint CLVs, $\hat{\mathbf{\Gamma}}(t)$, through Equation (A.13). This is presented in Algorithm 13.

Algorithm 13: An algorithm for computation of $\mathbf{\Gamma}$ and $\hat{\mathbf{\Gamma}}$.

Input: $\mathbf{u}(t_1, p)$, $\mathbf{\Psi}^-(t_1)$, $\mathbf{\Psi}^+(t_2)$
Output: $\mathbf{\Gamma}$, $\hat{\mathbf{\Gamma}}$

March $\mathbf{\Psi}^-(t_1)$ forwards using Algorithm 11 and store every t_n
March $\mathbf{\Psi}^+(t_2)$ backwards using Algorithm 12 and store every t_n
$t \leftarrow t_1$
while $t < t_2$ **do**
    $\mathbf{P}_{ij}(t) \leftarrow \left\langle \boldsymbol{\psi}_i^+(t), \boldsymbol{\psi}_j^-(t) \right\rangle$
    $\mathbf{P}(t) = \mathbf{L}(t)\mathbf{U}(t)$
    $\mathbf{A}^-(t) \leftarrow \mathbf{U}(t)^{-1}$
    $\mathbf{\Gamma}(t) \leftarrow \mathbf{\Psi}^-(t)\mathbf{A}^-(t)$
    $t \leftarrow t + n\Delta t$
while $t > t_1$ **do**
    $\mathbf{P}_{ij}(t) \leftarrow \left\langle \boldsymbol{\psi}_i^+(t), \boldsymbol{\psi}_j^-(t) \right\rangle$
    $\mathbf{P}(t)^T = \mathbf{L}(t)\mathbf{U}(t)$
    $\mathbf{B}^+(t) \leftarrow \mathbf{U}(t)^{-1}$
    $\hat{\mathbf{\Gamma}}(t) \leftarrow \mathbf{\Psi}^+(t)\mathbf{B}^+(t)$
    $t \leftarrow t - n\Delta t$

Appendix B

Properties of the state transition matrix

Throughout the development of OCS the state transition matrix (STM) has been utilised. The exact properties of the STM are not required in the derivation, it is merely utilised as a tool. However, details are outlined here to provide context as to its meaning and behaviour. This Appendix recaps the basic information that has already been published in the literature, Ref [57], and no additional development in understanding is provided. This Appendix has been written in the form that is consistent with the remainder of this thesis. The STM is derived as follows. Given a system of the form

$$\frac{\mathrm{d}\mathbf{v}(t)}{\mathrm{d}t} = \mathbf{A}(t)\mathbf{v}(t) + \mathbf{g}(t), \tag{B.1}$$

where $\mathbf{v}(t) \in \mathbb{R}^n$ is the state. $\mathbf{A}(t) \in \mathcal{R}^{n\times n}$ and $\mathbf{g}(t) \in \mathbb{R}^n$ are known and continuous in time. The homogeneous equation is defined as

$$\frac{\mathrm{d}\mathbf{v}(t)}{\mathrm{d}t} = \mathbf{A}\mathbf{v}(t), \tag{B.2}$$

where the solution of this homogeneous equation is a linear combination of a set of solutions $\mathbf{v}_j(t)$ that satisfy Equation (B.2). Define the fundamental matrix solution, $\mathbf{X}(t) \in \mathbb{R}^{n\times n}$, as a matrix whose columns are solutions to Equation (B.2). A general solution is $\mathbf{v}(t) = \mathbf{X}(t)\mathbf{c}$, where $\mathbf{c}$ is a vector of arbitrary weights. One other important feature is $\mathbf{X}(t_0) = \mathbf{I}$. If $\mathbf{v}(t_1)$ is known then $\mathbf{c} = \mathbf{X}(t_1)^{-1}\mathbf{v}(t_1)$. The difference between the solution at time t_1 and t_2 of Equation (B.2) and Equation (B.1) is the influence of $\mathbf{g}(t)$ which can be written as

$$\mathbf{X}^{-1}\mathbf{v}\Big|_{t_1}^{t_2} = \int_{t_1}^{t_2} \mathbf{X}(\tau)^{-1}\mathbf{g}(\tau)\mathrm{d}\tau. \tag{B.3}$$

The solution to Equation (B.1) at t_2 is

$$\mathbf{v}(t_2) = \mathbf{X}(t_2)\left[\mathbf{X}(t_1)^{-1}\mathbf{v}(t_1) + \int_{t_1}^{t_2} \mathbf{X}(\tau)^{-1}\mathbf{g}(\tau)\mathrm{d}\tau\right]. \tag{B.4}$$

The state transition matrix is defined as

$$\mathbf{\Phi}(t_1, t_2) = \mathbf{X}(t_2)\mathbf{X}(t_1)^{-1} \tag{B.5}$$

and can be thought of moving the solution $\mathbf{v}(t_1)$ to $\mathbf{v}(t_2)$ under the influence of Equation (B.2) and is written $\mathbf{v}(t_2) = \mathbf{\Phi}(t_1, t_2)\mathbf{v}(t_1)$. The state transition matrix also satisfies Equation (B.2) and has the following relationships

$$\mathbf{\Phi}(t, t) = I, \tag{B.6}$$

$$\mathbf{\Phi}(t_1, t_2)\mathbf{\Phi}(t_0, t_1) = \mathbf{\Phi}(t_0, t_2), \tag{B.7}$$

$$\mathbf{\Phi}(t_1, t_2) = \mathbf{\Phi}(t_2, t_1)^{-1}, \tag{B.8}$$

and

$$\hat{\mathbf{\Phi}}(t_1, t_2) = \mathbf{\Phi}(t_1, t_2)^{-T}, \tag{B.9}$$

where $\hat{\mathbf{\Phi}}(t_1, t_2)$ is the adjoint state transition matrix.

Appendix C

Derivation of the closed form expression of $\hat{\eta}(t)$

Similar to the tangent formulation, the term $\hat{\eta}(t)$ was introduced as a Lagrange multiplier which is a free variable. To find a solution to the optimality conditions its value needs constraining and a closed form solution found. The solution to Equation (3.31a) at time t can be written using its state transition matrix, $\mathbf{\Phi}(t_1, t_2)$, which results in

$$\hat{\mathbf{v}}(t) = \hat{\boldsymbol{A}}\hat{\mathbf{v}}(t_s) + \left(\int_{t_s}^{t} \hat{\eta}(\tau)\mathrm{d}\tau\right)\mathbf{f}(\mathbf{u}(t,p),p) + \hat{\boldsymbol{B}}\hat{\mathbf{q}}(t), \tag{C.1}$$

where

$$\hat{\boldsymbol{A}}\hat{\mathbf{v}}(t_s) = \mathbf{\Phi}(t_s,t)\hat{\mathbf{v}}(t_s), \tag{C.2}$$

and

$$\hat{\boldsymbol{B}}\hat{\mathbf{q}}(t) = \int_{t_s}^{t} \mathbf{\Phi}(\tau,t)\hat{\mathbf{q}}(\tau)\mathrm{d}\tau. \tag{C.3}$$

By defining the solution to the tangent equation without the influence of the $\hat{\eta}(t)\mathbf{f}(\mathbf{u}(t,p),p)$ term as

$$\hat{\mathbf{v}}'(t) = \hat{\boldsymbol{A}}\hat{\mathbf{v}}(t_s) + \hat{\boldsymbol{B}}\hat{\mathbf{q}}(t), \tag{C.4}$$

Equation (C.1) can be re-written to give

$$\hat{\mathbf{v}}(t) = \hat{\mathbf{v}}'(t) + \left(\int_{t_s}^{t} \hat{\eta}(\tau)\mathrm{d}\tau\right)\mathbf{f}(\mathbf{u}(t,p),p). \tag{C.5}$$

Taking the inner product of Equation (C.5) with $\mathbf{f}(\mathbf{u}(t,p),p)$ and utilising constraint, Equation (3.31d), results in

$$\begin{aligned}\left\langle \hat{\mathbf{v}}(t), \mathbf{f}(\mathbf{u}(t,p),p)\right\rangle = 0 = \left\langle \hat{\mathbf{v}}'(t), \mathbf{f}(\mathbf{u}(t,p),p)\right\rangle + \\ \left(\int_{t_s}^{t} \hat{\eta}(\tau)\mathrm{d}\tau\right)\left\langle \mathbf{f}(\mathbf{u}(t,p),p), \mathbf{f}(\mathbf{u}(t,p),p)\right\rangle.\end{aligned} \tag{C.6}$$

Manipulation of Equation (C.6) leads to the closed form expression for $\hat{\eta}(t)$,

$$\int_{t_s}^{t} \hat{\eta}(\tau)\mathrm{d}\tau = -\frac{\langle \hat{\mathbf{v}}'(t), \mathbf{f}(\mathbf{u}(t,p),p)\rangle}{\langle \mathbf{f}(\mathbf{u}(t,p),p), \mathbf{f}(\mathbf{u}(t,p),p)\rangle}, \tag{C.7}$$

which can be substituted combined with Equation (C.4) to give the adjoint tangent solution at time t

$$\hat{\mathbf{v}}(t) = \hat{\mathbf{v}}'(t) - \frac{\langle \hat{\mathbf{v}}'(t), \mathbf{f}(\mathbf{u}(t,p),p)\rangle}{\langle \mathbf{f}(\mathbf{u}(t,p),p), \mathbf{f}(\mathbf{u}(t,p),p)\rangle}\mathbf{f}(\mathbf{u}(t,p),p). \tag{C.8}$$

Appendix D

Derivation of the closed form expression of $\hat{\omega}(t)$

Similar to the tangent formulation, the term $\hat{\omega}(t)$ was introduced as a Lagrange multiplier which is a free variable. To find a solution to the optimality conditions its value needs constraining and a closed form solution is found. This is achieved using a very similar approach as used for $\omega(t)$. The solution to Equation (3.31b) at time t can be written in terms of its adjoint state transition matrix, $\hat{\mathbf{\Phi}}(t_1, t_2)$, resulting in

$$\begin{aligned}\hat{\boldsymbol{\lambda}}(t) = -\int_t^{t_f} \hat{\mathbf{\Phi}}(t,\tau)^{-1}\left[2\hat{\mathbf{v}}(\tau)\right]\mathrm{d}\tau - \int_t^{t_f} \hat{\mathbf{\Phi}}(t,\tau)^{-1}\left[\frac{1}{T}\frac{\partial J(\mathbf{u}(\tau,p),p)}{\partial \mathbf{u}(\tau,p)}\right]\mathrm{d}\tau + \\ \hat{\boldsymbol{D}}\boldsymbol{\lambda}(t_f) + \left(\int_t^{t_f} \hat{\omega}(\tau)\mathrm{d}\tau\right)\mathbf{f}(\mathbf{u}(t,p),p),\end{aligned} \tag{D.1}$$

where to ease the notation the terms

$$\int_t^{t_f} \hat{\mathbf{\Phi}}(t,\tau)^{-1}\left[2\hat{\mathbf{v}}(\tau)\right]\mathrm{d}\tau \quad \text{and} \quad \int_t^{t_f} \hat{\mathbf{\Phi}}(t,\tau)^{-1}\left[\frac{1}{T}\frac{\partial J(\mathbf{u}(\tau,p),p)}{\partial \mathbf{u}(\tau,p)}\right]\mathrm{d}\tau$$

are denoted using the simplified notation

$$\hat{\boldsymbol{C}}\square = \int_t^{t_f} \hat{\mathbf{\Phi}}(t,\tau)^{-1}\square(\tau)\mathrm{d}\tau \quad \text{to give} \quad \hat{\boldsymbol{C}}\left[2\hat{\mathbf{v}}(t)\right] \quad \text{and} \quad \hat{\boldsymbol{C}}\left[\frac{1}{T}\frac{\partial J(\mathbf{u}(t,p),p)}{\partial \mathbf{u}(t,p)}\right]$$

and

$$\hat{\boldsymbol{D}}\boldsymbol{\lambda}_{t_f} = \hat{\mathbf{\Phi}}\left(t,t_f\right)^{-1}\hat{\boldsymbol{\lambda}}(t_f). \tag{D.2}$$

Defining the solution to the co-state equation without the influence of $\hat{\omega}(t)\mathbf{f}(\mathbf{u}(t,p),p)$ as

$$\hat{\boldsymbol{\lambda}}'(t) = -\hat{\boldsymbol{C}}\left[2\hat{\mathbf{v}}\right] - \hat{\boldsymbol{C}}\left[\frac{1}{T}\frac{\partial J(\mathbf{u}(t,p),p)}{\partial \mathbf{u}(t,p)}\right] + \hat{\mathbf{D}}\hat{\boldsymbol{\lambda}}(t_f), \tag{D.3}$$

Equation (D.1) can be rewritten as

$$\hat{\boldsymbol{\lambda}}(t) = \hat{\boldsymbol{\lambda}}'(t) + \left(\int_t^{t_f} \hat{\omega}(\tau) \mathrm{d}\tau \right) \mathbf{f}(\mathbf{u}(t,p),p). \tag{D.4}$$

By taking the inner product of Equation (D.4) with $\mathbf{f}(\mathbf{u}(t,p),p)$ and using the co-state constraint, Equation (3.31e), results in

$$\begin{aligned} \left\langle \hat{\boldsymbol{\lambda}}(t), \mathbf{f}(\mathbf{u}(t,p),p) \right\rangle - \frac{1}{T} \left(J(\mathbf{u}(t,p),p) - \bar{J} \right) = 0 = \left\langle \hat{\boldsymbol{\lambda}}'(t), \mathbf{f}(\mathbf{u}(t,p),p) \right\rangle + \\ \left(\int_t^{t_f} \hat{\omega}(\tau) \mathrm{d}\tau \right) \left\langle \mathbf{f}(\mathbf{u}(t,p),p), \mathbf{f}(\mathbf{u}(t,p),p) \right\rangle - \frac{1}{T} \left(J(\mathbf{u}(t,p),p) - \bar{J} \right). \end{aligned} \tag{D.5}$$

The closed form expression for $\hat{\omega}(t)$ is

$$\int_t^{t_f} \hat{\omega}(\tau) \mathrm{d}\tau = - \frac{\left\langle \hat{\boldsymbol{\lambda}}'(t), \mathbf{f}(\mathbf{u}(t,p),p) \right\rangle}{\left\langle \mathbf{f}(\mathbf{u}(t,p),p), \mathbf{f}(\mathbf{u}(t,p),p) \right\rangle} + \frac{1}{T} \frac{J(\mathbf{u}(t,p),p) - \bar{J}}{\left\langle \mathbf{f}(\mathbf{u}(t,p),p), \mathbf{f}(\mathbf{u}(t,p),p) \right\rangle}. \tag{D.6}$$

and can be substituted into Equation (D.4) to give the adjoint co-state solution at time t

$$\begin{aligned} \hat{\boldsymbol{\lambda}}(t) = \hat{\boldsymbol{\lambda}}'(t) - \frac{\left\langle \hat{\boldsymbol{\lambda}}'(t), \mathbf{f}(\mathbf{u}(t,p),p) \right\rangle}{\left\langle \mathbf{f}(\mathbf{u}(t,p),p), \mathbf{f}(\mathbf{u}(t,p),p) \right\rangle} \mathbf{f}(\mathbf{u}(t,p),p) + \\ \frac{1}{T} \frac{J(\mathbf{u}(t,p),p) - \bar{J}}{\left\langle \mathbf{f}(\mathbf{u}(t,p),p), \mathbf{f}(\mathbf{u}(t,p),p) \right\rangle} \mathbf{f}(\mathbf{u}(t,p),p). \end{aligned} \tag{D.7}$$

Appendix E

Analytical structure of the linear system from time domain decomposition

The structures of $\mathbf{F}$ and $\mathbf{c}$ are not required in the derivation or solution of the optimality conditions. This is due to the use of matrix-free methods and, therefore, their structure does not require explicit implementation. Rather, the action of $\mathbf{F}$ on $\mathbf{x}$ is found computationally and $\mathbf{F}$ is never constructed analytically. Similarly, $\mathbf{c}$ is found through the action of $\mathbf{F}$ on $\mathbf{x} = \mathbf{0}$ and never needs explicitly implementing. It is, however, useful to show their structure for those who wish to implement these terms which could be utilised in the development of alternative preconditioning methods, which is outside the scope of this thesis. The analytical structure of $\mathbf{F}$ is

$$\mathbf{F} = \begin{pmatrix} \mathbf{F}_{0,0} & \mathbf{F}_{0,1} & & & & & & \\ \mathbf{F}_{1,0} & & & & & & & \\ & \ddots & & & & & & \\ & & \mathbf{F}_{j,j-1} & \mathbf{F}_{j,j} & \mathbf{F}_{j,j+1} & & & \\ & & & & \ddots & & & \\ & & & & & & \mathbf{F}_{N-2,N-1} & \\ & & & & & \mathbf{F}_{N-1,N-2} & \mathbf{F}_{N-1,N-1} \end{pmatrix}, \tag{E.1}$$

with

$$\mathbf{F}_{0,0} = \begin{pmatrix} \mathbf{I} & \mathbf{A}_0 \\ 0 & 2\alpha\mathbf{I} + \mathbf{C}_0\left(2\mathbf{B}_0\right) \end{pmatrix}, \tag{E.2}$$

$$\mathbf{F}_{0,1} = \begin{pmatrix} 0 & 0 & 0 \\ 0 & 0 & -\mathbf{D}_0 \end{pmatrix}, \tag{E.3}$$

$$\mathbf{F}_{1,0} = \begin{pmatrix} -\mathbf{A}_1 & 0 \\ \mathbf{C}_1\left(2\mathbf{A}_1\right) & 0 \\ \mathbf{C}_1\left(2\mathbf{A}_1\right) & 0 \end{pmatrix}, \tag{E.4}$$

$$\mathbf{F}_{j,j-1} = \begin{pmatrix} -\mathbf{A}_j & 0 & 0 \\ \mathbf{C}_j\left(2\mathbf{A}_j\right) & 0 & 0 \\ \mathbf{C}_j\left(2\mathbf{A}_j\right) & 0 & 0 \end{pmatrix}, \tag{E.5}$$

$$\mathbf{F}_{j,j} = \begin{pmatrix} \mathbf{I} & -\mathbf{B}_j & 0 \\ 0 & 2\alpha\mathbf{I} + \mathbf{C}_j\left(2\mathbf{B}_j\right) & 0 \\ 0 & \mathbf{C}_j\left(2\mathbf{B}_j\right) & \mathbf{I} \end{pmatrix}, \tag{E.6}$$

$$\mathbf{F}_{j,j+1} = \begin{pmatrix} 0 & 0 & 0 \\ 0 & 0 & -\mathbf{D}_j \\ 0 & 0 & -\mathbf{D}_j \end{pmatrix}, \tag{E.7}$$

$$\mathbf{F}_{N-2,N-1} = \begin{pmatrix} 0 & 0 \\ 0 & -\mathbf{D}_{N-2} \\ 0 & -\mathbf{D}_{N-2} \end{pmatrix}, \tag{E.8}$$

$$\mathbf{F}_{N-1,N-2} = \begin{pmatrix} \mathbf{C}_{N-1}\left(2\mathbf{A}_{N-1}\right) & 0 & 0 \\ \mathbf{C}_{N-1}\left(2\mathbf{A}_{N-1}\right) & 0 & 0 \end{pmatrix}, \tag{E.9}$$

$$\mathbf{F}_{N-1,N-1} = \begin{pmatrix} 2\alpha\mathbf{I} + \mathbf{C}_{N-1}\left(2\mathbf{B}_{N-1}\right) & 0 \\ \mathbf{C}_{N-1}\left(2\mathbf{B}_{N-1}\right) & \mathbf{I} \end{pmatrix}. \tag{E.10}$$

The subscripts, $\mathbf{A}_j$, represent the operator $\mathbf{A}$ on segment j. Finally, the analytical structure of $\mathbf{c}$ is

$$\mathbf{c} = \left(\mathbf{c}_0, \ldots, \mathbf{c}_j, \ldots, \mathbf{c}_{N-1}\right)^T, \tag{E.11}$$

with

$$\mathbf{c}_0 = \begin{pmatrix} \mathbf{B}_0 \frac{\partial \mathbf{f}(\mathbf{u}(t,p),p)}{\partial p} + \left(\int_{t_0}^{t} \eta(\tau)\mathrm{d}\tau\right) \mathbf{f}(\mathbf{u}(t,p),p) \\ \alpha_0 \end{pmatrix} \tag{E.12}$$

where

$$\alpha_0 = \mathbf{C}_0 \left(2\left[\mathbf{B}_0 \frac{\partial \mathbf{f}(\mathbf{u}(t,p),p)}{\partial p} + \left(\int_{t_0}^{t_1} \eta(\tau)\mathrm{d}\tau\right) \mathbf{f}(\mathbf{u}(t_1,p),p)\right]\right) - \left[\int_{t_0}^{t_1} \omega_0(\tau)\mathrm{d}\tau\right] \mathbf{f}(\mathbf{u}(t_1,p),p),$$

$$\mathbf{c}_j = \begin{pmatrix} \mathbf{B}_j \frac{\partial \mathbf{f}(\mathbf{u}(t,p),p)}{\partial p} + \left(\int_{t_j}^{t_{j+1}} \eta(\tau)\mathrm{d}\tau\right) \mathbf{f}(\mathbf{u}(t,p),p) \\ \alpha_j \\ \beta_j \end{pmatrix}, \tag{E.13}$$

where

$$\alpha_j = \mathbf{C}_j \left(2 \left[\mathbf{B}_j \frac{\partial \mathbf{f}(\mathbf{u}(t,p),p)}{\partial p} + \left(\int_{t_j}^{t} \eta(\tau) \mathrm{d}\tau \right) \mathbf{f}(\mathbf{u}(t,p),p) \right] \right) - \left[\int_{t_j}^{t} \omega_j(\tau) \mathrm{d}\tau \right] \mathbf{f}(\mathbf{u}(t,p),p)$$

and

$$\beta_j = \mathbf{C}_j \left(2 \left[\mathbf{B}_j \frac{\partial \mathbf{f}(\mathbf{u}(t,p),p)}{\partial p} + \left(\int_{t_j}^{t_{j+1}} \eta(\tau) \mathrm{d}\tau \right) \mathbf{f}(t_{j+1}) \right] \right) - \left[\int_{t_j}^{t_{j+1}} \omega_j(\tau) \mathrm{d}\tau \right] \mathbf{f}(\mathbf{u}(t_{j+1},p),p)$$

$$\mathbf{c}_{N-1} = \begin{pmatrix} \delta \\ \gamma \end{pmatrix} \tag{E.14}$$

where

$$\delta = \mathbf{C}_{N-1} \left(2 \left[\mathbf{B}_{N-1} \frac{\partial \mathbf{f}(\mathbf{u}(t,p),p)}{\partial p} + \left(\int_{t_{N-1}}^{t} \eta(\tau) \mathrm{d}\tau \right) \mathbf{f}(\mathbf{u}(t,p),p) \right] \right) - \left[\int_{t_{N-1}}^{t} \omega_{N-1}(\tau) \mathrm{d}\tau \right] \mathbf{f}(\mathbf{u}(t,p),p)$$

and

$$\gamma = \mathbf{C}_{N-1} \left(2 \left[\mathbf{B}_{N-1} \frac{\partial \mathbf{f}(\mathbf{u}(t,p),p)}{\partial p} + \left(\int_{t_{N-1}}^{t_f} \eta(\tau) \mathrm{d}\tau \right) \mathbf{f}(\mathbf{u}(t_f,p),p) \right] \right) - \left[\int_{t_{N-1}}^{t_f} \omega_{N-1}(\tau) \mathrm{d}\tau \right] \mathbf{f}(\mathbf{u}(t_f,p),p)$$

Bibliography

[1] Usman Ali and Yorai Wardi. "Multiple shooting technique for optimal control problems with application to power aware networks". In: *IFAC-PapersOnLine* 48.27 (2015), pp. 286–290.

[2] Brian D. O. Anderson and John B. Moore. *Optimal Control: Linear Quadratic Methods*. USA: Prentice-Hall, Inc., 1990.

[3] Andrew T. Barker and Martin Stoll. "Domain decomposition in time for PDE-constrained optimization". In: *Computer Physics Communications* 197 (2015), pp. 136–143.

[4] Marcus W. Beims and Jason A. C. Gallas. "Alignment of Lyapunov vectors: A quantitative criterion to predict catastrophes?" In: *Scientific Reports* 6 (Nov. 2016).

[5] Marcus W. Beims and Jason A.C. Gallas. "Predictability of the onset of spiking and bursting in complex chemical reactions". In: *Physical Chemistry Chemical Physics* 20 (27 2018), pp. 18539–18546.

[6] Giancarlo Benettin et al. "Lyapunov characteristic exponents for smooth dynamical systems and for hamiltonian systems; A method for computing all of them. Part 1: Theory". In: *Meccanica* 15.1 (1980), pp. 9–20.

[7] Giancarlo Benettin et al. "Lyapunov characteristic exponents for smooth dynamical systems and for hamiltonian systems; A method for computing all of them. Part 2: Numerical application". In: *Meccanica* 15.1 (1980), pp. 21–30.

[8] Martin Berggren and Matthias Heinkenschloss. "Parallel solution of optimal-control problems by time-domain decomposition". In: 1997.

[9] John T. Betts. *Practical methods for optimal control and estimation using nonlinear programming*. Society for Industrial and Applied Mathematics, 2010.

[10] Thomas R. Bewley, Paolo Luchini, and Jan Pralits. "Methods for solution of large optimal control problems that bypass open-loop model reduction". In: *Meccanica* 51.12 (2016), pp. 2997–3014.

[11] Thomas R. Bewley, Parviz Moin, and Roger Temam. "DNS-based predictive control of turbulence: An optimal benchmark for feedback algorithms". In: *Journal of Fluid Mechanics* 447 (2001), pp. 179–225.

[12] Manav Bhatia and David Makhija. "Sensitivity analysis of time-averaged quantities of chaotic systems". In: *AIAA Journal* 57.5 (2019), pp. 2088–2099.

[13] Patrick J Blonigan and Qiqi Wang. "Multiple shooting Shadowing for sensitivity analysis of chaotic systems and turbulent fluid flows". In: *53rd AIAA Aerospace Sciences Meeting*. DOI: 10.2514/6.2015-1534.

[14] Patrick J. Blonigan. "Adjoint sensitivity analysis of chaotic dynamical systems with non-intrusive least squares Shadowing". In: *Journal of Computational Physics* 348 (2017), pp. 803–826.

[15] Patrick J. Blonigan. "Least squares Shadowing for sensitivity analysis of large chaotic systems and fluid flows". PhD Thesis. Massachusetts Institute of Technology, 2016.

[16] Patrick J. Blonigan, Steven A. Gomez, and Qiqi Wang. "Least squares Shadowing for sensitivity analysis of turbulent fluid flows". In: *52nd Aerospace Sciences Meeting* (Jan. 2014), pp. 1–23.

[17] Patrick J. Blonigan and Qiqi Wang. "Least squares Shadowing sensitivity analysis of a modified Kuramoto-Sivashinsky equation". In: *Chaos, Solitons and Fractals* 64.1 (2014), pp. 16–25.

[18] Patrick J. Blonigan and Qiqi Wang. "Multigrid-in-time for sensitivity analysis of chaotic dynamical systems". In: *Numerical Linear Algebra with Applications* 24 (2017), pp. 1–27.

[19] Patrick J. Blonigan and Qiqi Wang. "Multiple shooting Shadowing for sensitivity analysis of chaotic dynamical systems". In: *Journal of Computational Physics* 354 (2018), pp. 447–475.

[20] Patrick J. Blonigan et al. "A non-intrusive algorithm for sensitivity analysis of chaotic flow simulations". In: *AIAA SciTech Forum - 55th AIAA Aerospace Sciences Meeting* (2017), pp. 1–8.

[21] Patrick J. Blonigan et al. "Least-squares Shadowing sensitivity analysis of chaotic flow around a two-dimensional airfoil". In: *AIAA Journal* 56.2 (2018), pp. 658–672.

[22] Patrick J. Blonigan et al. "Toward a chaotic adjoint for LES". In: *arXiv* (2017). URL: http://arxiv.org/abs/1702.06809.

[23] Patrick J. Blonigan et al. "Towards adjoint sensitivity analysis of statistics in turbulent flow simulation". In: *2012 Summer Program, Center for Turbulence Research, Stanford Univ., Stanford, CA, 2012* (2012), pp. 229–239.

[24] Hans G. Bock and Karl J. Plitt. "Multiple shooting algorithm for direct solution of optimal control problems." In: *IFAC Proceedings Series* 17.2 (1985), pp. 1603–1608.

[25] J. Frédéric Bonnans. "The shooting approach to optimal control problems". In: *IFAC Proceedings Volumes (IFAC-PapersOnline)* 11 (2013), pp. 281–292.

[26] Eduardo L. Brugnago, Jason A. C. Gallas, and Marcus W. Beims. "Machine learning, alignment of covariant Lyapunov vectors, and predictability in Rikitake's geomagnetic dynamo model". In: *Chaos* 30 (8 Aug. 2020).

[27] Arthur E. Bryson and Yu-Chi Ho. *Applied Optimal Control*. New York: John Wiley and Sons, 1975.

[28] John C. Butcher. "A history of Runge-Kutta methods". In: *Applied Numerical Mathematics* 20.3 (1996), pp. 247–260.

[29] Gary J. Chandler and Rich R. Kerswell. "Invariant recurrent solutions embedded in a turbulent two-dimensional Kolmogorov flow". In: *Journal of Fluid Mechanics* 722 (2013), pp. 554–595.

[30] Nisha Chandramoorthy, Luca Magri, and Qiqi Wang. *Variational optimization and data assimilation in chaotic time-delayed systems with automatic-differentiated Shadowing sensitivity*. 2020. URL: http://arxiv.org/abs/2011.08794.

[31] Nisha Chandramoorthy and Qiqi Wang. "On the probability of finding nonphysical solutions through Shadowing". In: *Journal of Computational Physics* 440 (2021), p. 110389.

[32] Nisha Chandramoorthy et al. "Feasibility analysis of ensemble sensitivity computation in turbulent flows". In: *AIAA Journal* 57 (10 2019), pp. 4514–4526.

[33] Nisha Chandramoorthy et al. *Toward computing sensitivities of average quantities in turbulent flows*. Feb. 2019. URL: http://arxiv.org/abs/1902.11112.

[34] Yong Chang and S. Scott Collis. "Active control of turbulent channel flows based on large eddy simulation". In: *Proceedings of the 1999 3rd ASME/JSME Joint Fluids Engineering Conference, FEDSM'99, San Francisco, California, USA, 18-23 July 1999* (1999).

[35] Mario Chater et al. "Least squares Shadowing method for sensitivity analysis of differential equations". In: *SIAM Journal on Numerical Analysis* 55.6 (2017), pp. 3030–3046.

[36] Haecheon Choi, Michael Hinze, and Karl Kunisch. "Instantaneous control of backward-facing step flows". In: *Applied Numerical Mathematics* 31 (2 1999), pp. 133–158.

[37] Agata Comas. "Time domain decomposition methods for second order linear quadratic optimal control problems". Master's Thesis. Rice University, 2004.

[38] Agata Comas. “Time-domain decomposition preconditioners for the solution of discretized parabolic optimal control problems”. PhD Thesis. Rice University, 2005.

[39] “Conjugate Gradient Methods”. In: *Numerical Optimization*. New York, NY: Springer New York, 2006, pp. 101–134. ISBN: 978-0-387-40065-5. DOI: 10.1007/978-0-387-40065-5_5.

[40] John Crank and Phyllis Nicolson. “A practical method for numerical evaluation of solutions of partial differential equations of the heat-conduction type”. In: *Mathematical Proceedings of the Cambridge Philosophical Society* 43.1 (1947), pp. 50–67.

[41] Cvitanovic, Ruslan L. Davidchack, and Evangelos Siminos. “On the state space geometry of the Kuramoto-Sivashinsky flow in a periodic domain”. In: *SIAM Journal on Applied Dynamical Systems* 9 (1 Jan. 2010), pp. 1–33.

[42] Xiaodi Deng. “A parallel-in-time gradient-type method for optimal control problems”. PhD Thesis. Rice University, 2017.

[43] Byron DeVries et al. “Parallel implementations of FGMRES for solving large, aparse non-symmetric linear systems”. In: *Procedia Computer Science* 18 (2013). 2013 International Conference on Computational Science, pp. 491–500.

[44] Jocelyne Erhel. “A parallel GMRES version for general sparse matrices”. In: *ETNA* 3 (Aug. 1998).

[45] Gregory L. Eyink, Tom W. N. Haine, and Daniel J. Lea. “Ruelle’s linear response formula, ensemble adjoint schemes and Lévy flights”. In: *Nonlinearity* 17.5 (2004), pp. 1867–1889.

[46] Mohammad Farazmand and Themistoklis P. Sapsis. “A variational approach to probing extreme events in turbulent dynamical systems”. In: *Science Advances* 3 (9 Sept. 2017).

[47] Mohammad Farazmand and Themistoklis P. Sapsis. “Dynamical indicators for the prediction of bursting phenomena in high-dimensional systems”. In: *Physical Review E* 94 (3 Sept. 2016).

[48] R. Fletcher. “Conjugate gradient methods for indefinite systems”. In: *Numerical Analysis*. Ed. by G Alistair Watson. Berlin, Heidelberg: Springer Berlin Heidelberg, 1976, pp. 73–89. ISBN: 978-3-540-38129-7.

[49] Anirban Garai and Scott M. Murman. “Stabilization of the adjoint for turbulent flows”. In: *AIAA Journal* 59.6 (June 2021), pp. 2001–2013.

[50] Francesco Ginelli et al. “Characterizing dynamics with covariant Lyapunov vectors”. In: *Physical Review Letters* 99.13 (2007), pp. 2–5.

[51] Francesco Ginelli et al. “Covariant Lyapunov vectors”. In: *Journal of Physics A: Mathematical and Theoretical* 46.25 (2013).

[52] Sebastian Götschel and Michael L. Minion. "An efficient parallel-in-time method for optimization with parabolic PDEs". In: *SIAM Journal on Scientific Computing* 41.6 (2019), pp. C603–C626.

[53] Sebastian Götschel and Michael L. Minion. "Parallel-in-time for parabolic optimal control problems using PFASST". In: *Lecture Notes in Computational Science and Engineering* 125.May (2018), pp. 363–371.

[54] Roland Grappin and Jacques Léorat. "Lyapunov exponents and the dimension of periodic incompressible Navier-Stokes flows: Numerical measurements". In: *Journal of Fluid Mechanics* 222 (1991), pp. 61–94.

[55] Lars Grüne. "Numerical methods for nonlinear optimal control problems". In: *Encyclopedia of Systems and Control*. London: Springer London, 2019, pp. 1–8.

[56] Stefanie Günther, Nicolas R. Gauger, and Jacob B. Schroder. "A non-intrusive parallel-in-time approach for simultaneous optimization with unsteady PDEs". In: *Optimization Methods and Software* 34.6 (2019), pp. 1306–1321.

[57] Jack K. Hale. *Ordinary Differential Equations*. Dover Books on Mathematics Series. Dover Publications, 2009. ISBN: 9780486472119.

[58] Malik Hassanaly and Venkat Raman. "Lyapunov spectrum of forced homogeneous isotropic turbulent flows". In: *Phys. Rev. Fluids* 4 (11 Nov. 2019), p. 114608.

[59] Malik Hassanaly and Venkat Raman. "Numerical convergence of the Lyapunov spectrum computed using low Mach number solvers". In: *Journal of Computational Physics* 386 (June 2019), pp. 467–485.

[60] Matthias Heinkenschloss. "A time-domain decomposition iterative method for the solution of distributed linear quadratic optimal control problems". In: *Journal of Computational and Applied Mathematics* 173.1 (2005), pp. 169–198.

[61] Michael Hinze and Karl Kunisch. "On suboptimal control strategies for the Navier-Stokes equations". In: *ESAIM: Proceedings* 4 (1998), pp. 181–198.

[62] Michael Hinze and Stefan Volkwein. "Analysis of instantaneous control for the Burgers equation". In: *Nonlinear Analysis, Theory, Methods and Applications* 50 (1 2002), pp. 1–26.

[63] L. Stephen Hou and Y. Yan. "Dynamics and approximations of a velocity tracking problem for the Navier-Stokes flows with piecewise distributed controls". In: *SIAM Journal on Control and Optimization* 35 (6 1997).

[64] Oscar Hugues-Salas and Stephen P. Banks. "Optimal control of nonhomogeneous chaotic systems". In: *IFAC Proceedings Volumes (IFAC-PapersOnline)* 1.PART 1 (2006), pp. 203–208.

[65] Francisco Huhn and Luca Magri. "Optimisation of chaotically perturbed acoustic limit cycles". In: *Nonlinear Dynamics* 100.2 (2020), pp. 1641–1657.

[66] Francisco Huhn and Luca Magri. “Stability, sensitivity and optimisation of chaotic acoustic oscillations”. In: *Journal of Fluid Mechanics* 882 (Jan. 2020).

[67] Masanobu Inubushi et al. “Covariant Lyapunov analysis of chaotic Kolmogorov flows”. In: *Physical Review E - Statistical, Nonlinear, and Soft Matter Physics* 85 (1 Jan. 2012).

[68] Antony Jameson. “Aerodynamic shape optimization using the adjoint method”. In: *VKI Lecture Series on Aerodynamic Drag Prediction and Reduction, von Karman Institute of Fluid Dynamics, Rhode St Genese*. 2003, pp. 3–7.

[69] Morteza Khodabin et al. “Numerical solution of stochastic differential equations by second order Runge-Kutta methods”. In: *Mathematical and Computer Modelling* 53.9 (2011), pp. 1910–1920.

[70] Toshiyuki Koto. “IMEX Runge-Kutta schemes for reaction-diffusion equations”. In: *Journal of Computational and Applied Mathematics* 215.1 (2008), pp. 182–195.

[71] Nathaniel Kroeger. “ADMM based methods for time-domain decomposition formulations of optimal control problems”. Master’s Thesis. Rice University, 2020.

[72] Pavel V. Kuptsov and Ulrich Parlitz. “Theory and computation of covariant Lyapunov vectors”. In: *Journal of Nonlinear Science* 22.5 (2012), pp. 727–762.

[73] Yoshiki Kuramoto. “Diffusion-induced chaos in reaction systems”. In: *Progress of Theoretical Physics Supplement* 64 (1978), pp. 346–367.

[74] Yoshiki Kuramoto and Toshio Tsuzuki. “Persistent propagation of concentration waves in dissipative media far from thermal equilibrium”. In: *Progress of Theoretical Physics* 55.2 (Feb. 1976), pp. 356–369.

[75] Felix Kwok. “On the time-domain decomposition of parabolic optimal control problems”. In: *Lecture Notes in Computational Science and Engineering* 116 (2017), pp. 55–67.

[76] John E. Lagnese and Guenter Leugering. “Time-domain decomposition of optimal control problems for the wave equation”. In: *Systems and Control Letters* 48.3-4 (2003), pp. 229–242.

[77] Davide Lasagna. “Sensitivity and stability of long periodic orbits of chaotic systems”. In: *Physical Review E* 102 (5 2020).

[78] Davide Lasagna, Ati Sharma, and Johan Meyers. “Periodic Shadowing sensitivity analysis of chaotic systems”. In: *Journal of Computational Physics* 391.September 2019 (2019), pp. 119–141.

[79] Daniel J. Lea, Myles R. Allen, and Thomas W.N. Haine. “Sensitivity analysis of the climate of a chaotic system”. In: *Tellus, Series A: Dynamic Meteorology and Oceanography* 52.5 (2000), pp. 523–532.

[80] Edward N. Lorenz. "Deterministic nonperiodic flow". In: *Journal of the Atmospheric Sciences* 20.2 (Mar. 1963), pp. 130–141.

[81] Dan Lucas and Rich R. Kerswell. "Spatiotemporal dynamics in two-dimensional Kolmogorov flow over large domains". In: *Journal of Fluid Mechanics* 750 (July 2014), pp. 518–554.

[82] Yvon Maday, Mohamed-Kamel Riahi, and Julien Salomon. "Parareal in time intermediate targets methods for optimal control problems". In: *Control and Optimization with PDE Constraints* (2013), pp. 79–92.

[83] Yvon Maday, Julien Salomon, and Gabriel Turinici. "Monotonic parareal control for quantum systems". In: *SIAM Journal on Numerical Analysis* 45.6 (Jan. 2007), pp. 2468–2482.

[84] K R Meyer and George R Sell. "An analytic proof of the shadowing lemma". In: *Funkcialaj Ekvacioj* 30 (1987), pp. 127–133.

[85] Bruce C. Moore. "Principal component analysis in linear systems: Controllability, observability, and model reduction". In: *IEEE Transactions on Automatic Control* 26.1 (1981), pp. 17–32.

[86] Hiro Mukai. "Parallel algorithms for unconstrained optimization". In: *Proceedings of the IEEE Conference on Decision and Control* 1 (1979), pp. 451–454.

[87] Siva Nadarajah and Antony Jameson. "A comparison of the continuous and discrete adjoint approach to automatic aerodynamic optimization". In: American Institute of Aeronautics and Astronautics, Jan. 2000.

[88] Angxiu Ni. *Adjoint Shadowing directions in hyperbolic systems for sensitivity analysis*. 2018. arXiv: 1807.05568 [math.DS].

[89] Angxiu Ni. *Approximating Ruelle's linear response formula by Shadowing methods*. 2020. arXiv: 2003.09801 [math.DS].

[90] Angxiu Ni. "Hyperbolicity, Shadowing directions and sensitivity analysis of a turbulent three-dimensional flow". In: *Journal of Fluid Mechanics* 863 (Mar. 2019), pp. 644–669.

[91] Angxiu Ni and Chaitanya Talnikar. "Adjoint sensitivity analysis on chaotic dynamical systems by Non-Intrusive Least Squares Adjoint Shadowing (NILSAS)". In: *Journal of Computational Physics* 395 (2019), pp. 690–709.

[92] Angxiu Ni and Qiqi Wang. "Sensitivity analysis on chaotic dynamical systems by Non-Intrusive Least Squares Shadowing (NILSS)". In: *Journal of Computational Physics* 347 (2017), pp. 56–77.

[93] Angxiu Ni et al. "Sensitivity analysis on chaotic dynamical systems by Finite Difference Non-Intrusive Least Squares Shadowing (FD-NILSS)". In: *Journal of Computational Physics* 394 (2019), pp. 615–631.

[94] Nikolay Nikitin. "Characteristics of the leading Lyapunov vector in a turbulent channel flow". In: *Journal of Fluid Mechanics* 849 (Aug. 2018), pp. 942–967.

[95] Florian Noethen. "Computing covariant Lyapunov vectors: A convergence analysis of Ginelli's algorithm". PhD Thesis. Hamburg, 2019.

[96] Roel Nottrot. *Optimal processes on manifolds*. Vol. 963. Lecture Notes in Mathematics. Berlin, Heidelberg: Springer Berlin Heidelberg, 1982.

[97] *Optimal Control: Calculus of Variations, Optimal Control Theory and Numerical Methods*. International Series of Numerical Mathematics. Birkhäuser Basel, 1993.

[98] Bernard Pagurek and C. Murray Woodside. "The conjugate gradient method for optimal control problems with bounded control variables". In: *Automatica* 4 (5-6 Nov. 1968), pp. 337–349.

[99] Sankaran Palani. *Signals and Systems*. Springer International Publishing, 2022. ISBN: 978-3-030-75741-0.

[100] George Papadakis, Liang Lu, and Pierre Ricco. "Closed-loop control of boundary layer streaks induced by free-stream turbulence". In: *Phys. Rev. Fluids* 1 (4 Aug. 2016), p. 043501.

[101] Sergei Y. Pilyugin. *Shadowing in dynamical systems*. Lecture Notes in Mathematics. Springer Berlin Heidelberg, 1999. ISBN: 978-3-540-66299-0.

[102] Nathan Platt, Lawrence Sirovich, and Nessan Fitzmaurice. "An investigation of chaotic Kolmogorov flows". In: *Physics of Fluids A* 3 (4 1991), pp. 681–696.

[103] Lev S. Pontryagin. *Mathematical theory of optimal processes*. Classics of Soviet Mathematics. Taylor & Francis, 1987.

[104] James B. Rawlings, David Q. Mayne, and Moritz M. Diehl. *Model Predictive Control: Theory, Computation, and Design*. Nob Hill Publishing, 2017. ISBN: 9780975937730.

[105] James Reuther et al. "Constrained multipoint aerodynamic shape optimization using an adjoint formulation and parallel computers". In: *35th Aerospace Sciences Meeting and Exhibit* (1997).

[106] Youcef Saad and Martin H Schultz. "GMRES: A generalized minimal residual algorithm for solving nonsymmetric linear systems". In: *SIAM Journal on Scientific and Statistical Computing* 7.3 (1986), pp. 856–869.

[107] Yousef Saad. *Iterative Methods for Sparse Linear Systems*. Second. Society for Industrial and Applied Mathematics, 2003.

[108] Themistoklis P. Sapsis. "New perspectives for the prediction and statistical quantification of extreme events in high-dimensional dynamical systems". In: *Philosophical Transactions of the Royal Society A: Mathematical, Physical and Engineering Sciences* 376 (2127 Aug. 2018).

[109] Christian E. Schaerer, Tarek Mathew, and Marcus Sarkis. "Block iterative algorithms for the solution of parabolic optimal control problems". In: *Lecture Notes in Computer Science (including subseries Lecture Notes in Artificial Intelligence and Lecture Notes in Bioinformatics)* 4395 LNCS (2007), pp. 452–465.

[110] Karim Shawki and George Papadakis. "A preconditioned multiple shooting Shadowing algorithm for the sensitivity analysis of chaotic systems". In: *Journal of Computational Physics* 398 (2019).

[111] Karim Shawki and George Papadakis. "Feedback control of chaotic systems using multiple shooting Shadowing and application to Kuramoto Sivashinsky equation". In: *Proceedings of the Royal Society A: Mathematical, Physical and Engineering Sciences* 476.2240 (2020).

[112] Ippei Shimada and Tomomasa Nagashima. "A numerical approach to ergodic problem of dissipative dynamical systems". In: *Progress of Theoretical Physics* 61.6 (1979), pp. 1605–1616.

[113] Gregory I. Sivashinsky. "Nonlinear analysis of hydrodynamic instability in laminar flames-I. Derivation of basic equations". In: *Acta Astronautica* 4.11-12 (Nov. 1977), pp. 1177–1206.

[114] Gregory I. Sivashinsky and Daniel M. Michelson. "On irregular wavy flow of a liquid film down a vertical plane". In: *Progress of Theoretical Physics* 63.6 (June 1980), pp. 2112–2114.

[115] Steven W. Smith. *The Scientist and Engineer's Guide to Digital Signal Processing*. USA: California Technical Publishing, 1997. ISBN: 0966017633.

[116] Josef Stoer and Roland Bulirsch. *Introduction to numerical analysis*. Texts in applied mathematics. Springer, 2002.

[117] Endre Süli and David F. Mayers. *An Introduction to Numerical Analysis*. Cambridge University Press, 2003.

[118] Kazumasa A. Takeuchi et al. "Hyperbolic decoupling of tangent space and effective dimension of dissipative systems". In: *Physical Review E - Statistical, Nonlinear, and Soft Matter Physics* 84.4 (2011), pp. 1–19.

[119] Chaitanya Talnikar and Qiqi Wang. "A two-level computational graph method for the adjoint of a finite volume based compressible unsteady flow solver". In: *Parallel Computing* 81 (2019), pp. 68–84.

[120] Chaitanya Talnikar and Qiqi Wang. "Adjoint-based trailing edge shape optimization of a transonic turbine vane using large eddy simulations". In: *arXiv* (Nov. 2020), pp. 1–34. URL: http://arxiv.org/abs/2011.06744.

[121] Chaitanya Talnikar, Qiqi Wang, and Gregory M. Laskowski. "Unsteady adjoint of pressure loss for a fundamental transonic turbine vane". In: *Journal of Turbomachinery* 139.3 (2017).

[122] Andreas Thune. "A parallel in time method for optimal control algorithm". Master's Thesis. University of Oslo, 2017.

[123] Stéphane Vannitsem and Wansuo Duan. "On the use of near-neutral backward Lyapunov vectors to get reliable ensemble forecasts in coupled oceanatmosphere systems". In: *Climate Dynamics* 55 (5-6 Sept. 2020), pp. 1125–1139.

[124] Qiqi Wang. "Convergence of the least squares Shadowing method for computing derivative of ergodic averages". In: *SIAM Journal on Numerical Analysis* 52.1 (2014), pp. 156–170.

[125] Qiqi Wang. "Forward and adjoint sensitivity computation of chaotic dynamical systems". In: *Journal of Computational Physics* 235 (2013), pp. 1–13.

[126] Qiqi Wang. "Uncertainty quantification for unsteady fluid flow using adjoint-based approaches". PhD Thesis. Stanford University, 2008.

[127] Qiqi Wang and Jun Hui Gao. "The drag-adjoint field of a circular cylinder wake at Reynolds numbers 20, 100 and 500". In: *Journal of Fluid Mechanics* 730 (2013), pp. 145–161.

[128] Qiqi Wang, Rui Hu, and Patrick J. Blonigan. "Least squares Shadowing sensitivity analysis of chaotic limit cycle oscillations". In: *Journal of Computational Physics* 267 (2014), pp. 210–224.

[129] Qiqi Wang et al. "Towards scalable parallel-in-time turbulent flow simulations". In: *Physics of Fluids* 25.11 (Nov. 2013), p. 110818.

[130] Markus Widhalm, Arno Ronzheimer, and Martin Hepperle. "Comparison between gradient-free and adjoint based aerodynamic optimization of a flying wing transport aircraft in the preliminary design". In: *Collection of Technical Papers - AIAA Applied Aerodynamics Conference* 1.June 2014 (2007), pp. 727–747.

[131] Christopher L. Wolfe and Roger M. Samelson. "An efficient method for recovering Lyapunov vectors from singular vectors". In: *Tellus, Series A: Dynamic Meteorology and Oceanography* 59.3 (2007), pp. 355–366.

[132] Hong Liu Yang et al. "Hyperbolicity and the effective dimension of spatially extended dissipative systems". In: *Physical Review Letters* 102.7 (2009), pp. 1–4.

[133] Xiong You, Xinmeng Yao, and Xin Shu. "An optimized fourth order Runge-Kutta method". In: *2010 Third International Conference on Information and Computing*. Vol. 3. 2010, pp. 46–49.

[134] Lilia Ziane Khodja et al. "Parallel sparse linear solver with GMRES method using minimization techniques of communications for GPU clusters". In: *The Journal of Supercomputing* 69 (Mar. 2014).